Instabilités cinétiques dans les plasmas : des fluctuations électromagnétiques aux chocs non-collisionnels

Charles Ruyer

UNIVERSITÉ PARIS SUD

Comprendre le monde, construire l'avenir®

DE LA RECHERCHE À L'INDUSTRIE

cea

Université Paris-Sud

École Doctorale : Ondes et Matière
Laboratoire Interaction Rayonnement-Matière

Discipline : Physique des Plasmas

Thèse de doctorat

Soutenue le 11/12/2014 par

Charles RUYER

Kinetic instabilities in plasmas: from electromagnetic fluctuations to collisionless shocks

Directeur de thèse :	Guy BONNAUD	Professeur INSTN (CEA/INSTN)
Encadrant :	Laurent GREMILLET	Chercheur (CEA/DAM)

Composition du jury :

Président du jury :	Jean-Marcel RAX	Professeur (Université de Paris-Sud, LOA)
Rapporteurs :	Mark DIECKMANN	Professeur associé (Université de Linköping, Suède)
	Andrea MACCHI	Chercheur (CNR/INO, Pise, Italie)
Examinateurs :	Laurent GREMILLET	Chercheur (CEA/DAM)
	Guy BONNAUD	Professeur INSTN (CEA/INSTN)
	Vladimir TIKHONCHUK	Professeur (Université de Bordeaux, CELIA)
	Jean-Marcel RAX	Professeur (Université de Paris-Sud, LOA)

À mon père

Remerciements

J'ai effectué cette thèse au CEA, DAM, DIF grâce à une bourse CFR. Je veux donc tout d'abord remercier les différents chefs de laboratoire, de service et de département Erik, Luc, Laurence, Franck et Daniel pour leur accueil chaleureux, leur accéssibilité et les excellentes conditions de travail dont ils m'ont fait bénéficier durant ces trois années.

Je tiens à remercier tout particulièrement mon encadrant Laurent Gremillet sans qui cette thèse n'aurait pas eu lieu. J'ai eu la chance de bénéficier de son encadrement scientifique qui fut parfait et essentiel au déroulement de cette thèse. Il a su me transmettre une partie de son immense savoir, de son sens physique aigu et peut être même une partie de l'impressionnante culture bibliographique qu'il possède. Il est l'un des plus grands scientifiques avec qui j'ai pu travailler et son sens de l'humour, son ouverture d'esprit et sa patience sont autant de qualités qui ont rendu la recherche avec lui agréable. Tout simplement, merci Laurent ! Je remercie tout particulièrement mon directeur de thèse, Guy Bonnaud, pour ses conseils et pour sa grande chaleur humaine. Sa présence fut précieuse, notamment pendant les difficultés et les moments de doute que j'ai pu traverser.

Tous les collègues du CEA ont été présents et très accessibles pour répondre aux différentes questions qui peuvent passer par le tête d'un étudiant. La bonne ambiance qui règne au service leur est due. Merci donc à Xavier pour sa disponiblité et sa patience, à Benoit pour ses qualités de surfeur scientifique, à Michel, Stéphane, et Patricia pour leur sens de l'humour, à Didier pour son facteur deux, à Alain et Serge pour leur application quotidienne à briser toute trace de monotonie au sein du service. Je n'oublierai aucun des étudiants et plus généralement l'ensemble des précaires qui se sont succédés pendant ma thèse : Julien mon co-bureau, Jérémy, Alexandre, Julien, Guillaume, Grégoire, et Aurélie... Il y a aussi Mathieu et Arnaud, membres de mon équipe rapprochée, que j'espère revoir très bientôt, que ce soit autour d'une bière ou d'une équation. Merci enfin à Brigitte et Sylvie pour leur sourires et leur compétences essentielles à la vie du département.

Ma gratitude va aussi aux membres du jury de cette thèse qui, de par leurs remarques et leurs questions, ont permis d'améliorer la qualité du manuscrit et du travail associé.

Au cours de ma thèse j'ai eu la chance, en plus de l'équipe du CEA, de côtoyer et travailler avec des personnes formidables. Je me souviendrai toujours des soirées passées avec Antoine Bret, acharnées à corriger des équations par mails interposés. Comment ne pas avoir une pensée pour Martin Lemoine, Emmanuel d'Humières et Mickael Grech avec qui j'aurai toujours plaisir à échanger. Anne Stockem, Frederico Fiuza, Ramesh Narayan et Lúis Silva ont aussi contribué à ce travail et je les en remercie.

Merci à tous mes amis pour leur soutient. J'ai une pensée toute particulière pour Aymeric, Charlène, Etienne, Valentin, Emilia, pour les membres du 3615 Brass Band et tout ces très bons moments passés en leur présence. Et merci à toi que j'ai oublié !

Je tiens à exprimer aussi ma profonde gratitude à ma mère et mon frère et l'ensemble de ma famille pour leur soutient indéfectible. Je finis ces remerciements par toi, Aurélie, mon épouse, à qui je dois mon bonheur quotidien mais aussi la prise de recul nécessaire à tous travaux de recherche. Tu as su me remonter le moral aux moments les plus durs et partager mon exaltation lorsque mes efforts payaient. J'ai pu, grâce à toi, garder en tête l'essentiel durant ces trois années de thèse.

Merci aussi pour ton soutien et toute l'aide précieuse que tu m'as apportée.

Abstract

Collisionless shocks play a major role in powerful astrophysical objects (e.g., gamma-ray bursts, supernova remnants, pulsar winds, etc.), where they are thought to be responsible for non-thermal particle acceleration and radiation. Numerical simulations have shown that, in the absence of an external magnetic field, these self-organizing structures originate from electromagnetic instabilities triggered by high-velocity colliding flows. These Weibel-like instabilities (Bret *et al.* 2010b) are indeed capable of producing the magnetic turbulence required for both efficient scattering and Fermi-type acceleration (Kato & Takabe 2008; Spitkovsky 2008b). Along with rapid advances in their theoretical understanding, intense effort is now underway to generate collisionless shocks in the laboratory using energetic lasers (Fox *et al.* 2013).

Relativistic electron-positron collisionless shocks In a first part we study the (ω,k)-resolved electromagnetic thermal spectrum sustained by a drifting relativistic plasma. In particular, we obtain analytical formulae for the fluctuation spectra, the latter serving as seeds for growing magnetic modes in counterstreaming plasmas (Ruyer *et al.* 2013). Distinguishing between subluminal and supraluminal thermal fluctuations, we derived analytical formulae of their respective spectral contributions. Comparisons with particle-in-cell (PIC) simulations are made, showing close agreement in the subluminal regime along with some discrepancy in the supraluminal regime.

Our formulae are then used to estimate the saturation time of the Weibel instability of relativistic pair plasmas. Our predictions are shown to match 2-D particle-in-cell (PIC) simulations over a three-decade range in flow energy (Bret *et al.* 2013).

Ion-electron Weibel-induced collisionless shocks: analytical model for formation and propagation We then develop a predictive kinetic model of the nonlinear phase of the Weibel instability induced by two counter-streaming, symmetric and non-relativistic ion beams. This self-consistent, fully analytical model allows us to follow the evolution of the beams'properties up to a stage close to complete isotropization and thus to shock formation. Its predictions are supported by 2D and 3D particle-in-cell (PIC) simulations of the ion Weibel instability in uniform geometries, as well as shock-relevant non-uniform configurations. Moreover, they are found in correct agreement with a recent laser-driven plasma collision experiment (Fox *et al.* 2013). Along with this comparison, we pinpoint the important role of electron screening on the ion-Weibel dynamics, which may affect the results of simulations with artificially high electron mass.

We subsequently address the shock propagation resulting from the magnetic Weibel turbulence generated in the upstream region. Generalizing the previous symmetric-beam model to the upstream region of the shock, the profile of the magnetic turbulence in the shock-front has been analytically and self-consistently characterized. Comparison with simulations validates the model.

Weibel induced collisionless shocks by high-intensity lasers The interaction of high-energy, ultra-high intensity lasers with dense plasmas is known to produce copious amounts of suprathermal

particles. Their acceleration and subsequent transport trigger a variety of Weibel-like electromagnetic instabilities, acting as additional sources of slowing down and scattering. Their understanding is important for the many applications based upon the energy deposition and/or field generation of laser-driven particles (Bret *et al.* 2010b). We investigate the ability of relativistic-intensity laser pulses to induce Weibel instability-mediated shocks in overdense plasma targets, as first proposed in Ref. (Fiuza *et al.* 2012). By means of both linear theory and 2D PIC simulations, we demonstrated that in contrast to the standard astrophysical scenario previously addressed, the early-time magnetic fluctuations (Weibel instability) generated by the suprathermal electrons (and not ions) are strong enough to isotropize the target ions and, therefore, induce a collisionless electromagnetic shock (Ruyer *et al.* 2014).

Contents

Nomenclature

- Mathematical quantities: vectors and tensors are in bold symbols.

x, y, z	Axes of the three-dimensional frame
θ	Angle counted from the x-axis
$(\widehat{\mathbf{x}}, \widehat{\mathbf{y}}, \widehat{\mathbf{z}})$	Unity vectors in the x, y and z direction
$\partial_x f$, $d_x f$	Partial, straight derivative of the function f with respect to the variable x (scalar or vector)
$\mathbf{1}$	Unity tensor
i	Imaginary unity: $i^2 = -1$
$\Re(x)$	Real part of the complex x
$\Im(x)$	Imaginary part of the complex x
$H(x)$	Step function: $H(x < 0) = 0$ and $H(x > 0) = 1$
$I_n(z)$	Modified Bessel function of the first kind
$K_n(z)$	Modified Bessel function of the second kind
$\mathcal{Z}$	Plasma dispersion function
$\mathrm{erfi}(x) = \int_0^x e^{t^2} dt$	complex error function:
$\delta(x)$	Dirac function
A, B, C, D	Quadratures used in the susceptibility tensor of a Maxwell-Jüttner-distributed beam (see Sec. 2)
$\mathcal{G}_1$, $\mathcal{G}_2$	Functions used in the resolution of the general electromagnetic dispersion relation (see Sec. 1)
$\lvert\mathbf{M}\rvert$	Norm of the complex vector $\mathbf{M}$
$\mathbf{M}^\dagger$	Hermitian conjugate of the $\mathbf{M}$ tensor
$\mathrm{Res}(f)_a$	Functional residue of $f(x)$ at $x = a$
$\otimes$	Tensorial product between two vectors, $\mathbf{a} \otimes \mathbf{b}$ is a tensor.
$\max_x(f)$	Maximum of f over x
$\min_x(f)$	Minimum of f over x
$TF[f(\mathbf{r})] = f(\mathbf{k})$	Fourier transform

The Fourier transform is defined as follows:

$$g_{\mathbf{k},\omega} = \iiiint_{\mathbb{R}^4} d^3r dt\, g(\mathbf{r}, t) \exp\left[i(\omega t - \mathbf{k}\cdot\mathbf{r})\right], \tag{1}$$

$$g(\mathbf{r}, t) = \iiiint_{\mathbb{R}^4} \frac{d^3k d\omega}{(2\pi)^4}\, g_{\mathbf{k},\omega} \exp\left[i(\mathbf{k}\cdot\mathbf{r} - \omega t)\right]. \tag{2}$$

- Physical quantities

$k_B = 1,3807 \times 10^{-23}\,\mathrm{J}\cdot\mathrm{K}^{-1}$	Boltzmann constant
$c = 2,9979 \times 10^{8}\,\mathrm{m}\cdot\mathrm{s}^{-1}$	Light speed in vacuum
$\varepsilon_0 = 8,8542 \times 10^{-12}\cdot\mathrm{m}^{-3}\cdot\mathrm{kg}^{-1}\cdot\mathrm{s}^{4}\cdot\mathrm{A}^{2}$	Permittivity of vacuum
$\mu_0 = 4\pi \times 10^{-7}\cdot\mathrm{kg}\cdot\mathrm{m}\cdot\mathrm{A}^{-2}\cdot\mathrm{s}^{-2}$	Magnetic permittivity of vacuum
$m_e = 9.1 \times 10^{-31}\mathrm{kg}$	Electron mass
$m_p = 1836.15 m_e$	Proton mass
$q_e = 1.602 \times 10^{-19}\mathrm{C}$	Electron charge
q_s	Charge of the sth particle species
Z_s	Atomic number of the sth particle species
Γ_{ad}	Adiabatic index
$c_s = \sqrt{Z_i T_e / m_i}$	Speed of sound
β	Normalized velocity, $\beta = v/c$
γ	Lorentz factor, $\gamma = (1-\beta^2)^{-1/2}$
p	Relativistic momentum, $p = m\gamma\beta$
n_s	Density of the sth species
ρ	Charge density $\rho = \sum_s q_s n_s$
$\mathbf{J}$	Current density
f_s	Distribution function of the sth species
$\mathbf{E}$	Electric field vector
Φ	Scalar potential, $\mathbf{E} = -\nabla\Phi$
$\mathbf{B}$	Magnetic field vector
$\mathbf{A}$	Vector potential, $\mathbf{B} = \nabla \times \mathbf{A}$
T_s	Temperature of the sth species
K_{xs}, K_{ys}, K_{zs},	Kinetic energy of the sth species on the x, y, z axis
E_c	Total kinetic energy, $E_c = K_{xs} + K_{ys} + K_{zs}$
$K_{\theta_i} = K_{xs} + \theta_i K_{ys}$	Typical energy used in Sec. 3 and 4
$W_E = \epsilon_0 E^2/2$	Electric energy
$W_B = B^2/2\mu_0$	Magnetic energy
$S_p = q_e^2 \sum_{k_y} \lvert A_{k_y}\rvert$	Transverse energy of the vector potential (Secs. 3 and 4)
a_s	Anisotropy ratio of the sth population: $a_s = \frac{K_{xs}}{K_{ys}} - 1$
$\theta_i = \partial_t K_{xs} / \partial_t T_{ys}$	Dimensionless quantity used in Secs. 3 and 4
$\boldsymbol{\epsilon}$	Dielectric tensor
$\boldsymbol{\chi}_s$	Susceptibility tensor of the sth species, $\boldsymbol{\epsilon} = \mathbf{1} + \sum_s \boldsymbol{\chi}_s$
$\mathbf{X}_s$	Modified susceptibility tensor of the sth species, $\boldsymbol{\chi} = \sum_s \omega_s^2 \boldsymbol{\xi}_s / \omega^2$
μ_s	Normalized inverse temperature (Secs. 1 and 2)
μ_s	Normalized inverse temperature (Secs. 1 and 2)
$\mu_a = \cos\theta \sin\theta \left(\frac{m_s}{T_{xs}} - \frac{m_s}{T_{ys}}\right)$	Parameter used in a bi-Maxwellian susceptibility tensor (Sec. 1)
$\mu_\parallel = m_s \frac{\cos^2\theta}{T_{xs}} + m_s \frac{\sin^2\theta}{T_{ys}}$	Parameter used in a bi-Maxwellian susceptibility tensor (Sec. 1)
$\mu_\perp = m_s \frac{\sin^2\theta}{T_{xs}} + m_s \frac{\cos^2\theta}{T_{ys}}$	Parameter used in a bi-Maxwellian susceptibility tensor (Sec. 1)

$\xi_s = (\omega/k - v_d \cos\theta)\sqrt{\mu_\parallel/2}$	Argument of the plasma dispersion function for a bi-Maxwellian plasma
$\alpha_i = [1 + \xi_{\rm sat}\mathcal{Z}(\xi_{\rm sat})] \simeq 0.5$	Dimensionless quantity used in Secs. 3 and 4
t	Time
t_*	Time of the saturation of the ion-Weibel instability
$\tau_{\rm sh}$	Shock formation time
$\Delta t_{\rm form}$	Time to achieve an ion anisotropy ratio of $a_i = 2$, assimilated to "quasi-shock formation" time(Secs. 3 and 4)
$t_{\rm front}(x)$	Time at which the shock front has reached abscissa x
τ_0	Collective coalescence time of the symmetric ion Weibel instability (Sec. 3)
τ_1	Collective coalescence time of the ion Weibel instability in the upstream of a propagating collisionless shock (Secs. 4)
τ_2	Collective coalescence time of the ion Weibel instability in the upstream of a propagating collisionless shock (Secs. 4)
τ_s	Electron Weibel saturation time (Sec. 2)
L_B	Length of the non-linear Weibel region, in the front shock (Sec. 4)
λ_{Ds}	Debye length of a plasma, $\lambda_D = \sqrt{\epsilon_0 T_e/n_e q_e^2}$
$\lambda_{\rm mfp}$	Collisionnal mean free path
$\lambda_{\rm sat}$	Dominant magnetic wavelength at saturation of the Weibel instability (Secs. 3 and 4)
$\lambda_c = 2^{1/2}\pi c/\omega_{pi}\eta_i$	Critical magnetic wavelength of the Weibel instability (Secs. 3 and 4)
$\lambda_{\rm front}$	Dominant magnetic wavelength of the Weibel instability at the shock front (Sec. 4)
$\lambda_* = \lambda_{\rm sat}(t = t_*)$	Dominant magnetic wavelenth at saturation of the ion-Weibel instability (Secs. 3 and 4)
$k_{\rm sat}$	Dominant magnetic wavevector at saturation of the Weibel instability (Secs. 3 and 4)
$k_{\rm max}$	Maximum magnetic wavevector of the Weibel-unstable domain ($\Gamma_{k_y} > 0$ for $k_y < k_{\rm sat}$) (Secs. 3 and 4)
$\eta_i \simeq 0.5$	Approximate value of the ratio between $k_{\rm sat}$ and $k_{\rm max}$ (Secs. 3 and 4)
$k_* = k_{\rm sat}(t = t_*)$	Dominant magnetic wavevector at saturation of the ion-Weibel instability (Secs. 3 and 4)
$\xi_{\rm sat} = \xi_i(\omega = 0, k_y = k_{\rm sat})$	Argument of the plasma dispersion function for a bi-Maxwellian ion beam, applied to the saturation of the Weibel instability (Secs. 3 and 4)
ω_{ps}	Plasma frequency, $\omega_{ps} = \sqrt{n_s q_s^2/m_s\varepsilon_0}$
Γ	Growth rate
ω_0	Laser frequency
$n_c = m_e\varepsilon_0\omega_0^2/q_e^2$	Laser critical density at the laser frequency ω_0
$A_0 = q_e E_0/m_e\omega_0 c$	Normalized amplitude of the laser wave
R_L	Laser reflectivity

- Simulation parameters

(X_i, Z_j, Y_k)	Position of the mesh point (i, j, k).
N_g	Total number of mesh points
N_p	Total number of macroparticules
Δx, Δy, Δz et Δt,	Spatial and temporal step size
L_x, L_y, L_z,	Length of the simulation box in the x, y and z direction.
$((E_x)^n_{i+\frac{1}{2},j,k}, (E_y)^n_{i,j+\frac{1}{2},k}, (E_z)^n_{i,j,k+\frac{1}{2}})$	Electric field at the mesh point (i, j, k) and time step n
$((B_x)^{n+\frac{1}{2}}_{i,j+\frac{1}{2},k+\frac{1}{2}}, (B_y)^{n+\frac{1}{2}}_{i+\frac{1}{2},j,k+\frac{1}{2}}, (B_z)^{n+\frac{1}{2}}_{i+\frac{1}{2},j+\frac{1}{2},k})$	Magnetic field at the mesh point (i, j, k), and time step n

The discrete Fourier Transform (DFT) calculation is defined as:

$$g_k = DFT_x(g) = \frac{1}{N-1} \sum_{n=0}^{N} g_n \exp\left(-ik_x x_n\right), \tag{3}$$

$$g_n DFT^{-1}_{k_x}(g) = \sum_{j=0}^{N-1} g_k \exp\left(ik_j x_n\right), \tag{4}$$

with $x_n = n\Delta x$ and $k_j = j2\pi/L_x$.
The continuity limit links the continuous and the discrete Fourier transform: for $L \to \infty$,

$$FFT_x(g) \equiv \frac{1}{\Delta_x} \int_{\mathbb{R}} dx\, g(x) \exp\left[-ik_x x\right], \tag{5}$$

$$iFFT_{k_x}(g) \equiv \frac{L_x}{2\pi} \int_{\mathbb{R}} dk_x\, g(k_x) \exp\left[ik_x x\right]. \tag{6}$$

Introduction

Studying high energy density physics

This theoretical work is incorporated within the vast and general framework of high-energy density physics. "High-energy density" is commonly defined as an energy density exceeding 10^{11}J.m^{-3}, which corresponds to a pressure above 1Mbar. Such conditions are reached, for example, in systems of densities close to that of liquid water (1g.cm^{-3}) and temperatures in excess of 10eV (10^5K). The study of high-energy density physics has a very wide range of applications, encompassing the production and characterization of matter under extreme conditions, laser plasma interactions, thermonuclear fusion and the generation of intense particle and radiation sources. Such a knowledge is also crucial for understanding the process of star formation, the structure of massive and planetary stellar objects, or the dynamics of energetic astrophysical events such as the origin of gamma-ray bursts or highly-energetic cosmic rays. A possible mechanism of generation of the latter could be the acceleration of particles by the self-amplified fields in collisionless shocks.

The main goal of physicists is to understand and predict the processes at stake. For this purpose, four cornerstones are able to lead the researcher on the path to progress: theory, simulation, experiments and observations. Therefore, models and theories can be built in order to provide insights on the studied phenomena. They are used to predict values/ranges of some quantities, to relate some parameters or qualitatively explain a process. In all these cases, they have to be compared to measurements, observations or numerical simulations in order to be validated.

A powerful tool commonly used by physicists is numerical simulations, or "numerical experiments". A "simulation code" refers to a software which can predict the evolution of matter, particles or radiation under well-defined conditions. The recent development of high-performance computers (as, for example, the CCRT and CINES facilities in France) has opened the possibility of large-scale numerical experiments aiming at reproducing an extensive part of the physical processes involved in high-energy phenomena. These supercomputers enable to run simulations over thousands of processors running at the same time (in parallel) on a regular basis. The world's record in this respect is a laser-plasma interaction simulation using the particle-in-cell code OSIRIS, performed at the Lawrence Livermore National Laboratory over 1.6 million processors (Fonseca *et al.* 2013). These large-scale simulations require a high level of optimization of the simulation code. Note that even the most complete (*i.e.*, first principles) simulation codes use approximate models, reduced geometries and discretization. Hence their results are tarnished by errors and uncertainties. This is why, as for an experiment, the simulation results must be interpreted with a careful critical mind.

Since theories and simulation results have to be verified, an experimental approach must be adopted. In the case of high-energy astrophysical phenomena, one of the major issues is linked to the difficulty of observing and characterizing matter under extreme conditions. Experiments are thus built in order to reproduce the physical conditions of the studied phenomena and can

give precious constraints on the processes at stake. Nonetheless, the design and the measurements in an experiment can be very complex, involving a wide range of expertise, the control of initial conditions and their reproducibility cannot be taken for granted. Many of the experiments in high-energy-density physics make use of high-intensity lasers to heat, compress and/or accelerate samples of matter as well as to probe them. These systems generate concentrated sources of light through spatial and temporal compression of energetic pulses. They represent powerful tools which open the possibility to probe matter under unprecedented physical conditions.

The observations of energetic astrophysical events can be at the origin of all the research process by pointing, for example, to an unexplained event. However, measuring or characterizing these phenomena making use of satellites or telescopes gives access to a limited set of data, although crucial for the study. Cosmic-rays are representative of the scientific problematic we have just addressed. Extremely energetic particles have been observed on Earth, leading to the questions: which astrophysical event is able to produce such energetic particles, and what are the mechanisms at play? As we will detail later, these observations could be explained in the framework of collisionless shocks. Yet, no direct observations are able to capture unequivocally the physical processes predicted by the theory. Assessing the underlying physics of cosmic-rays in a truly reliable way would require to produce some in controlled experiments and effectively observe them. For this purpose, we need a deep understanding of the processes at stake, the ability of predicting the required collisionless shock formation conditions, of reproducing them in an experiment, and of accurately measuring the produced "cosmic-rays". Each one of these four steps are very challenging. However, large-scale simulations have provided insights and made possible many of the recent developments in this domain. They suggest that, under specific conditions, such energetic particles can be generated during the propagation of an instability-mediated collisionless shock. To clarify this point, we will first briefly recall the basis of plasma kinetic theory and collisionless micro-instabilities, with a focus on the Weibel-filamentation instability. We will then introduce the physics of shocks in plasmas and finally show how the Weibel instability can give rise to turbulent shocks of properties similar to those of hydrodynamic shocks.

Kinetic description of a plasma and instabilities

Plasma is the fourth state of matter where a large amount of the particles are charged. Hence, it is generally made of free electrons and ions and possibly neutral species as atoms. In this manuscript, only fully ionized plasmas will be considered.

The Debye length, $\lambda_D = \sqrt{\epsilon_0 T/nq^2}$, characterizes the screening spatial scale of a charge in a plasma. We introduced the permitivity of vacuum, ϵ_0, the temperature, T, particle density, n and charge q (see nomenclature). As a simple illustration, a positive charge in a plasma (such as an ion) tends to be surrounded by an electron shell of typical radius λ_D, called the "Debye sphere". The interaction of two particles on a scale smaller than the Debye length is called a "collision". The mean-free-path, λ_{mfp}, represents the typical distance over which, owing to cumulative small-angle collision, a particle is deflected. In the so called collisional plasmas, short-range interactions dominate the evolution of the particle populations. They tend to establish locally a Maxwellian velocity distribution of particles, which reads for the sth species in a non-relativistic system

$$f_s^{(0)}(\mathbf{v}) = \left(\frac{m_s}{2\pi T_s}\right)^{\frac{3}{2}} \exp\left(-\frac{m_s \mathbf{v}^2}{2T_s}\right), \tag{7}$$

where m_s is the mass of the particles and $\mathbf{v}$ is the velocity vector. The above equation represents

the statistical velocity distribution of particles (normalized to unity, $\int d\mathbf{v} f^{(0)}(\mathbf{v}) = 1$) of a system at equilibrium if its parameter, the temperature T_s, is the same for all the species of the system for a neutral plasma (here $\sum_s q_s n_s = 0$).

When the mean free path becomes larger than the density or temperature gradient scale-lengths of the system, it is more likely to deviate from the Maxwellian equilibrium. A kinetic effect is an effect which tends to deviate the system from this equilibrium, either when the temperature of the species are not equal or when the velocity distributions differ from the Maxwellian. This is possible when the particle interaction is dominated by interactions of range much larger than the Debye length. These "long-range collisions" are called "collective effects" since their typical range involves many Debye spheres. In such systems, short-range collisions are rare hence, the mean free path is long and the collision frequency is short compared with the typical spatial and temporal scales of variation of the distribution functions. This characterizes the collisionless plasmas, as explained in Sagdeev (1966) that will be studied in this manuscript, namely a plasma dominated by long-range interactions. The relaxation processes in a highly non-equilibrium collisionless plasma frequently involve kinetic instabilities. Such processes generate long-range plasma oscillations through growing electric and magnetic fluctuations. Hence, the system tends to return to equilibrium via the feedback of the self-generated fields on particles.

Collisionless plasmas are described by the Vlasov equation, which predicts the evolution of the distribution function:

$$\delta_t f_s + \frac{\mathbf{p}}{m_s \gamma} \cdot \delta_{\mathbf{r}} f_s + \mathbf{F} \cdot \delta_{\mathbf{p}} f_s = 0\,, \tag{8}$$

where $\mathbf{F}$ is the Lorentz force which reads $\mathbf{F} = q_s\,(\mathbf{E} + \mathbf{v} \times \mathbf{B})$. The electric and magnetic fields, $\mathbf{E}$ and $\mathbf{B}$, are described by the Maxwell set of equations

$$\nabla \cdot \mathbf{E} = \frac{\rho}{\epsilon_0}\,, \tag{9}$$

$$\nabla \times \mathbf{E} = -\partial_t \mathbf{B}\,, \tag{10}$$

$$\nabla \cdot \mathbf{B} = 0\,, \tag{11}$$

$$\nabla \times \mathbf{B} = \mu_0 \mathbf{j} + c^{-2} \partial_t \mathbf{E}\,. \tag{12}$$

In Eqs. (9), (10), (11) and (12), respectively the Maxwell-Gauss, Maxwell-Thomson, Maxwell-Faraday and Maxwell-Ampère equations, we introduced the light speed in vacuum, permitivity of vacuum and magnetic permitivity c, ϵ_0 and μ_0 respectively. They can be combined with Eq. (8), using the definition of the charge and current density ρ and $\mathbf{j}$:

$$\rho = \sum_s n_s q_s \int f_s(\mathbf{v}) d\mathbf{v}\,, \tag{13}$$

$$\mathbf{j} = \sum_s n_s q_s \int \mathbf{v} f_s(\mathbf{v}) d\mathbf{v}\,. \tag{14}$$

The trivial solution of the above set of equations corresponds to a neutral and homogeneous plasma ($\rho = 0$ and $\mathbf{j} = 0$), with vanishing fields ($\mathbf{E} = 0$ and $\mathbf{B} = 0$). Note that, while $\rho = 0$ and $\mathbf{j} = 0$ in a homogeneous system, any initial distribution function can verify, at least initially, this field-free solution of the Vlasov-Maxwell equations. Yet, as a function of the initial particle distribution functions, this solution may prove unstable with respect to infinitesimal perturbations in the momentum distributions or the fields. In the most general case, non-equilibrium plasma states result in the growth of coupled electromagnetic and kinetic fluctuations. Various kinetic instabilities can be iden-

tified according to their spectral properties and the nature and number of the particle species at play.

Most of the instabilities can be decomposed in tree steps. The first one is the seed of the instability and corresponds to the initial state of the plasma which deviates from the equilibrium. An homogeneous free-field system with a anisotropic distribution, as two counter-propagating beams, represents an unstable equilibrium. More specifically, some components of the fields are unstable. External seeds can originate from the action of a laser or a particle beam, while thermal fluctuations inherent to finite-temperature plasmas exemplify spontaneous seeds. The second stage is the unstable loop during which the field grows and creates a wave usually described (making use of the Fourier transform) by its dominant wavevector $\mathbf{k}$ and complex frequency $\omega = \omega_r + i\Gamma$. The unstable mode then propagates along $\mathbf{k}$ at the phase speed $v_\phi = \omega_r/|\mathbf{k}|$, following an exponential growth $\propto \exp(2\Gamma t)$ (where Γ is the growth rate) of the electromagnetic energy. Since the energy is bounded in any physical system, this growth cannot last indefinitely. It stops when the fields are strong enough to significantly affect the particle velocities and trajectories, which will mitigate the unstable loop between the fields and the particles. This final step is called the nonlinear saturation stage of the instability and is usually the most complex part to describe theoretically.

Then, the system may subsequently relax to an equilibrium state or into another unstable one. In this last case, another instability occurs following the same three steps, and this cycle repeats until the system finally reach equilibrium. According to whether the growing electric field is parallel or perpendicular to the wavevector, we speak of an electrostatic or an electromagnetic instability respectively. Well-known examples are the electron two-stream electrostatic instability (Bohm & Gross 1949) and the Weibel electromagnetic instability (Weibel 1959), studied in this manuscript. The general case, however, is that of "mixed" electrostatic and electromagnetic instabilities (Bret *et al.* 2008, 2010b).

Most of this study concerns the common configuration of two counter-propagating electron-ion beams. The associated instabilities can be sorted according to two criteria: the orientation of their wavevector compared to the flow direction, and their complex frequency. At the very beginning of the interaction, the first particles to react are the electrons which have the largest plasma frequency $\omega_{ps} = \sqrt{n_s q_s^2/m_s\epsilon_0}$. They will trigger the first instabilities, on a time-scale larger than ω_{pe}^{-1}. During this electronic phase, the ion motion is usually neglected as a first approximation. Figure 1 presents three electron-driven instabilities: the fully electrostatic longitudinal electron-electron two-stream, the mostly electrostatic oblique two stream and the electron transverse electromagnetic Weibel instabilities Note that the system can successively go through these three instabilities before it evolves into an ionic stage (Bret *et al.* 2008, 2010b). After their growth and saturation, the ion-driven modes will occur on time-scales larger than ω_{pi}^{-1}. During this ionic phase, both the ions and electrons react to the waves. Three types of ion instabilities are indicated in Fig. 1 in the case of isotropic (stable) electrons. We summarized not exhaustively the different kind of instabilities along with there possible order of apparition in Fig. 1. We highlight that this sketch does not mention all the possible plasma instabilities and omits the potentially important families of electron-ion driven instabilities, such as the Buneman or electron-ion acoustic modes (Gary *et al.* 1985). Secondly, there exists many shades between a pure electronic and purely ionic instabilities. While important, this wavevector-based classifiaction may also hide the connections between the instability classes. The ion longitudinal and oblique modes may then be viewed as a unique instability class, their orientation depending upon their subsonic or supersonic character (Gary *et al.* 1985).

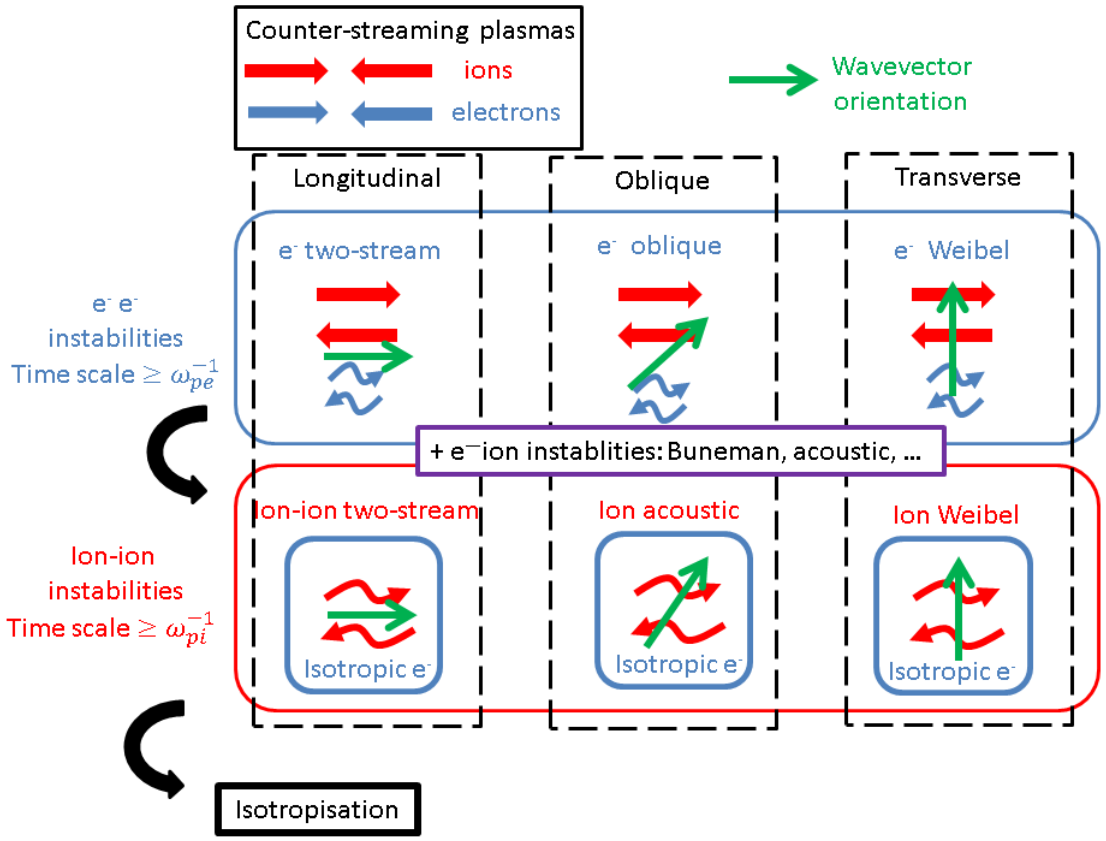

Figure 1. Not exhaustive list of plasma instabilities driven by counter-steaming electron-ion beams, sorted according to their propagation direction (wavevector orientation) and the plasma species driving them. The wavy arrows highlight which population drives and reacts to the instability

Shocks in plasmas

In the case of inhomogeneous systems characterized, for instance, by the overlapping of two counter-streaming, bounded plasma beams, the non-linear stage of the triggered instability may generate shock waves. Shock waves are usually characterized by a discontinuity in the spatial profile of physical quantities (particle density, temperature,...). It can be driven by any supersonic disturbance as, for example, two flows colliding with a velocity faster than the speed of waves in the medium. In such a case, the matter is being compressed (and heated) so fast that no relaxation of the compressed region can occur in the un-compressed medium through wave propagation. If a wave was able to propagate faster than the shock discontinuity, the system would be able to relax through its propagation and the shock would vanish. Colliding plasma flows are expected to be common sources of shocks in high-energy astrophysical environments such as pulsars, active galactic nuclei, supernovae. Shocks can also be generated when a large-amplitude wave propagates with a phase speed faster in its anti-nodes than in its nodes. These non-linear effects, although not addressed in this manuscript, result in a steepening of the wave and thus to a shock or shock-like structures.

Turbulent shocks and Rankine-Hugoniot conditions

In a collisional system, the typical thickness of the shock discontinuity is of the order of the mean free-path λ_{mfp} of the heaviest particles. In the collisionless systems addressed in this manuscript,

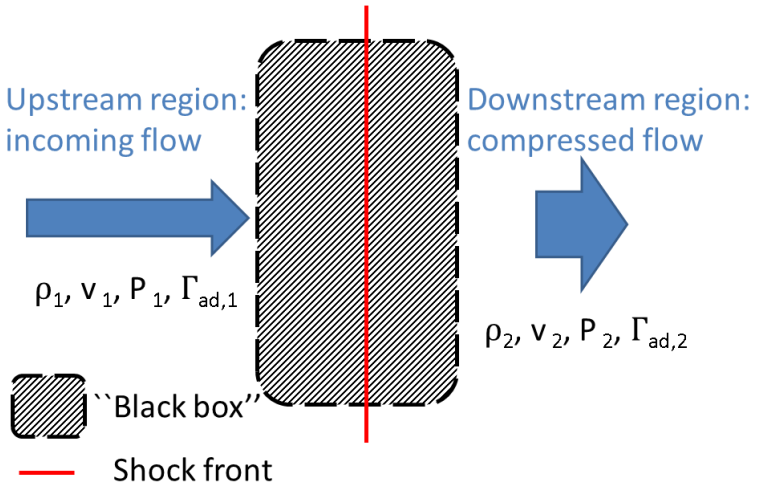

Figure 2. Sketch of a shock as derived in the Rankine-Hugoniot conditions.

the discontinuity develops over scales comparable to the Debye length or the electron/ion skin depth. For both cases, general relations can be derived between the incoming and the compressed flows, within a simple framework. Derived in Axford *et al.* (1977); Blandford & Ostriker (1978), they are called the Rankine-Hugoniot conditions. In the frame where the shock discontinuity is stationary, we will study the two flows lying on each sides of the shock front (subscript $s \equiv 1$ or 2). As will be shown, this calculation does not imply the knowledge of the interaction physics in the discontinuity region. This region is therefore considered as a "black box", outside of which the flows can be considered at equilibrium and characterized by their mass densities, flow velocities, pressures, adiabatic index and internal energy ρ_s v_s, P_s, $\Gamma_{ad,s}$ and ψ_s respectively [Fig. 2]. The Rankine-Hugoniot conditions relate ρ_1 and ρ_2, v_1 and v_2, P_1 and P_2, making use of the density, momentum, kinetic and internal energy conservation across the "black-box" region. Note that in this section and in this section only, ρ stands for the mass density. Everywhere else, it is a charge density as precised in the nomenclature. For a stationary system ($\partial_t \equiv 0$ in the shock frame), we obtain

$$\partial_x(\rho v) = 0\,, \tag{15}$$

$$\rho v \partial_x v = -\partial_x P\,, \tag{16}$$

$$\partial_x(\rho\psi v) = -P\partial_x v\,, \tag{17}$$

$$\partial_x\left(\frac{\rho v^2}{2}v\right) = -v\partial_x P\,. \tag{18}$$

From Eq. (15) it follows that the flux ρv is constant across the shock front. Combined with Eq. (16), we can show that $\rho v^2 + P$ is also conserved. Finally, adding Eq. (17) to (18) gives that $\rho v^2/2 + \rho\psi + P$ is also a constant. Assuming equilibrium for the two flows, obeying a polytropic equation of state, $\psi_s = P_s/\rho_s(\Gamma_{ad,s} - 1)$, one obtains the shock jump conditions

$$\frac{\rho_2}{\rho_1} = \frac{v_1}{v_2} = \frac{(\Gamma_{ad}+1)M_1^2}{(\Gamma_{ad}-1)M_1^2+2}\,, \tag{19}$$

$$\frac{P_2}{P_1} \simeq \frac{\rho_2 T_2}{\rho_1 T_1} = \frac{2\Gamma_{ad}M_1^2 - \Gamma_{ad} + 1}{\Gamma_{ad}+1}\,, \tag{20}$$

for $\Gamma_{ad,1} = \Gamma_{ad,1} = \Gamma_{ad}$. We have introduced the upstream Mach number M_1 which is the ratio of the shock speed (v_1 in frame of the downstream) to the upstream sound speed ($c_{s,1}$)

$$M_1 = \frac{v_1}{c_{s,1}}\,. \tag{21}$$

Plugging $M_1 = 1$ into Eqs. (19) and (20) gives the trivial solution $\rho_1 = \rho_2$ and $v_1 = v_2$. Shock formation therefore requires $M_1 > 1$, that is supersonic upstream flows. Consequently, following Eqs. (19) and (20), the slowed down downstream flow ($v_2 < v_1$) is compressed ($n_2 > n_1$, $P_2 > P_1$).

Taking the limit $M_1 \to \infty$ leads to the so-called strong-shock conditions:

$$\frac{\rho_2}{\rho_1} \simeq \frac{v_1}{v_2} = \frac{\Gamma_{ad}+1}{\Gamma_{ad}-1}\,, \tag{22}$$

$$P_2 \simeq \frac{2}{\Gamma_{ad}+1}\rho_1 v_1^2\,. \tag{23}$$

In this regime, the density jump is independent of the Mach number, and thus of the upstream flow. It verifies $n_2/n_1 = 4$ for a non-relativistic 3D (mono-atomic) gaz ($\Gamma_{ad} = 5/3$), $n_2/n_1 = 3$ for a non-relativistic 2D gaz ($\Gamma_{ad} = 2$). Overall, the above jump conditions are valid independently of the physical processes occurring in the black box, provided the system is stationary in the shock frame and the downstream and upstream regions fulfill polytropic equations of state. Such shocks are called "turbulent", and may originate from the dissipation induced via either Coulomb or wave-particle scattering. The latter dissipation can be provided by Weibel-type instabilities, which can trigger a strong magnetic turbulence in front of the shock able to scatter off the incoming particles. In this manuscript, we will study the ability of the Weibel-filamentation instability to generate and propagate these strong shocks. Note that generalized Rankine-Hugoniot conditions can also be derived in a more general framework: for oblique shocks propagating in a magnetized medium (Drury 1983). Equation (23) evidences that most of the incoming upstream kinetic energy is dissipated into thermal energy in the downstream. This is possible only if a strong dissipation process takes place in the "black box" of Fig. 2. Such dissipation can be provided by Weibel-type instabilities, which can trigger a strong magnetic turbulence in front of the shock able to scatter off the incoming particles. In this manuscript, we will study the ability of the Weibel-filamentation instability to generate and propagate these strong shocks.

Laminar shocks

Collisionless plasmas may sustain another kind of shocks called laminar, associated with electrostatic boundary layers and usually, to weak Mach numbers ($M \lesssim 3$). In the collisionless limit these weak shocks can be induced by electrostatic instabilities and described in a purely 1D model (depending only on x) by the electrostatic potential (Moiseev & Sagdeev 1963) as sketched in Fig. 3 (black plain line). Let first consider the downstream where matter is characterized by a higher pressure than in the upstream. Therefore, the lighter particles at the shock front (the electrons) tend to escape in the upstream. They are attracted back by the downstream ions through an electrostatic field (E_x) which lies at the shock front, and points to the upstream. Hence, the electric field potential rises from the upstream value Φ_1, to a value $\Phi_{\rm max}$ in the downstream [Fig. 3]. The larger the pressure jump (P_2/P_1 in Eq. (20)) s, the larger $\Phi_{\rm max}$ is. This electric field represent a perturbation which can initiate an electrostatic wave and thus a plasma oscillation. Its phase speed is smaller than the shock velocity, otherwise the shock would not exist. This is illustrated in Fig. 3 where Φ oscillates between $\Phi_{\rm max}$ and Φ_2 in the downstream. Far from the shock front, collisions, or any other dissipating process, will eventually damp this wave. Note that if the wave is not damped, the Rankine Hugoniot conditions cannot be applied since a polytropic equilibrium is not fulfilled.

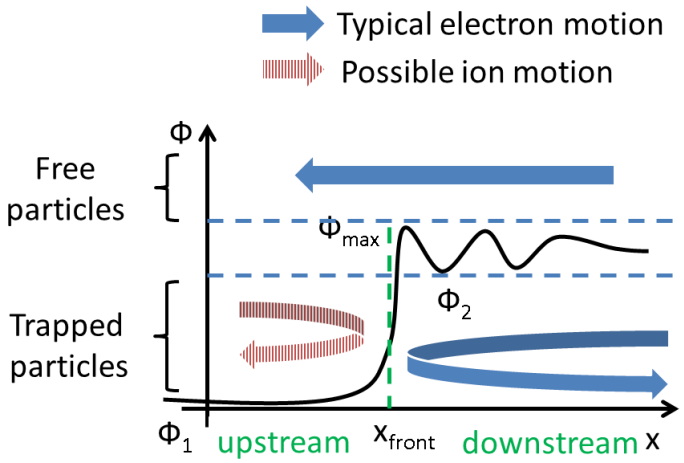

Figure 3. Sketch of an electrostatic shock

The particles with a kinetic energy lager than $q_e\Phi_{\max}$ are free. When the downstream particle's kinetic energy is smaller than $q_e\Phi_2$, they are trapped and cannot reach the upstream. The value of Φ_2 characterizes the dissipation of the directed kinetic energy of the upstream flow into thermal (pressure) energy in the downstream.

Qualitative evidence of different regimes of electrostatic shocks can be distinguished, as a function of the velocity of the upstream flow. For small upstream velocities (Mach number close to unity) the pressure jump of the shock is weak [Eq. (20)] which implies that $\Phi_{\max}$ is small. Since the ion kinetic is much larger than the electrons' (by a factor $m_i/m_e \geq 1836$), most of the ions cross the potential barrier, being thus slowed down and compressed. In this case, because dissipation is weak, Φ_2 is close to Φ_1 (Moiseev & Sagdeev 1963; Montgomery & Joyce 1969). Increasing the Mach number, increases P_2/P_1 and thus $\Phi_{\max}$ (as mentioned above) and some of the upstream ions can be reflected back in the upstream by the potential jump at the shock front. In this case, a more important part of the electrons are trapped in the downstream (larger dissipation) and the electric oscillations in the downstream can affect significantly the ions. Between $q_e\Phi_2$ and $q_e\Phi_{\max}$, the downstream particles are trapped by the electrostatic wave. This can creates characteristic density and velocity oscillations of all the plasma (electrons and ions) in the downstream (Sagdeev 1966).

At higher velocities, the amount of reflected ions at the shock front can be significant, which creates a region in the upstream where two counter-propagating ion populations overlap. This can trigger kinetic instabilities in the upstream such as the oblique ion-ion instability (Forslund & Shonk 1970) which may disrupt the propagation of the shock (Kato & Takabe 2010b; Dieckmann *et al.* 2013). In this regime, the electric fields are not limited to their sole longitudinal component E_x. A proper description of these effects requires multi-dimensional systems.

Collisionless shocks induced by the Weibel-filamentation instability

We will now focus on the shocks mediated by the Weibel instability. For this purpose, we will outline the properties of the latter and present the processes at stake.

The Weibel-filamentation instability

This manuscript addresses the particular case of the Weibel-filamentation (or current-filamentation) kinetic instability. Two kinds of Weibel instabilities can be defined: the Weibel-thermal instability (Weibel 1959) and the Weibel-filamentation (or current-filamentation) instability (Fried 1959) further studied in this manuscript. The first one occurs when a system has a strong temperature anisotropy ($T_x \neq T_y$). The second requires two counter-propagating beams (or one beam in a plasma at rest). Let us summarize the amplifying mechanism of the instability in the case of two counter-propagating high speed ($v \gtrsim 0.1c$) flows.

The development of the Weibel-filamentation instability can be decomposed into the three phases mentioned earlier: the seed, the unstable loop and the saturation. As mentioned previously, the initial perturbation seed of the instability can originate from an external source (laser, particle beam) or the field fluctuations inherent to finite temperature plasmas. We will now explain within a very simplified framework, the physical mechanism which can generate a small initial magnetic modulation. The overlap region of the two beams is characterized by two particle populations with opposite mean velocities. Since the charged particles are drifting at high velocities, each one generates a strong loop-like magnetic field. Thus, the interaction between all of the particles of same charge signs, drifting in the same direction is attractive through their induced magnetic field as illustrated in Fig. 4(a). This is true if the attractive magnetic interaction overcomes the electric (Coulomb) repulsion which is possible if the drift velocity is high enough. Consequently, if particles drift in the x direction, their magnetic interaction tends to segregate them in the y direction according to their current sign through the Lorentz force $q\mathbf{v} \times \mathbf{B}$. This creates a magnetic modulation in the y direction, thus transverse to the flow direction which is standing (*i.e.* non propagating, vanishing phase speed) and electromagnetic since the magnetic field is perpendicular to the wavevector.

Then, the unstable loop occurs, and the transverse magnetic modulations grow. The magnetic modulation segregates the drifting particles as illustrated on Fig. 4(b) which results in an increase of the current modulation. This current modulation thus amplifies the B-field which segregates even more the particles, amplifying the current again. The red curves of 4(b) stands for the trajectories of positively charged particles initially in the anti-nodes which tend to be segregated according to their current signs. This amplification can be driven by the electrons (electron-Weibel) or by the ions (ion-Weibel), or by both. During this phase, the system is usually modeled assuming the fields small enough to neglect their influence on the distribution function: the Vlasov-Maxwell set of equation can be linearized with respect to the fields. The obtained y-averaged magnetic energy grows exponentially with time, following $< B^2 >_y \propto \exp(2\Gamma t)$, where Γ is the growth rate. Details for the calculation of Γ will be given in the fist chapter of this manuscript, however, we will give here its basic scalings. The simplest way to derive the Weibel dispersion relation, is to consider two counter-propagating infinitely cold electron beams with no ion motion ($m_i = \infty$) and of plasma frequency ω_{pe}. In this case all the electrons have the exact same velocity, v_d and Lorentz factor $\gamma_d = (1 - v_d^2)^{-1/2}$. Making use of a Fourier transform, we can relate the growth rate Γ, with a given wavevector of the magnetic modulation, $\Gamma(k_y)$. As crudely sketched in Fig. 5, $\Gamma(k_y)$ is proportional to k_y for $k_y < \omega_{pe}/c\sqrt{\gamma_d}$: $\Gamma \simeq v_d k_y/\sqrt{\gamma_d}$. It then remains constant for $k_y > \omega_{pe}/c\sqrt{\gamma_d}$. This gives an infinitely large spectrum, and the maximum wavevector of the unstable domain, $k_{\max}$, tends to infinity, $k_{\max} \to \infty$. However, simulations (Bret *et al.* 2013) evidence that most of the magnetic energy is located at $k_y \sim \omega_{pe}/c\sqrt{\gamma_d}$ which corresponds to a growth rate of $\Gamma \sim \omega_{pe} v_d/c\sqrt{\gamma_d}$. This may be explained by a small heating of the electron distribution, at the beginning of the field growth. Solving the dispersion relation for two electron beams with non-vanishing initial temperature (*i.e.* all the electrons of a beam do not have the exact same velocity) results in a growth rate which eventually decreases and vanishes for large wavevectors, $k_{\max} < \infty$ [red dashed lines in Fig. 5].

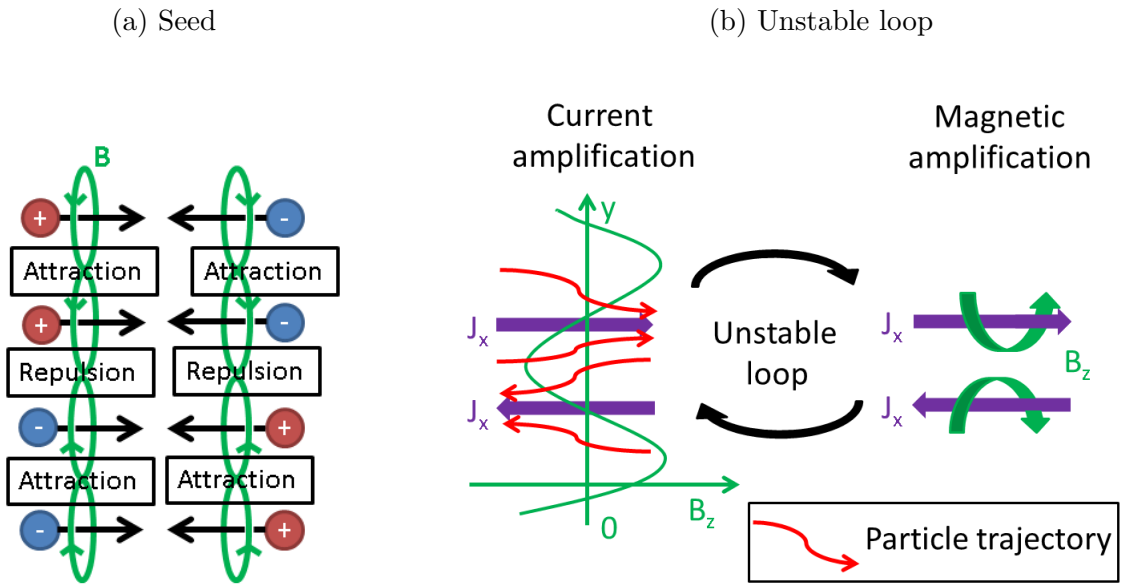

Figure 4. (a) Attraction and repulsion of charged drifting particles (positively in red, negatively in blue) through their magnetic interaction, if it overcomes the electric interaction. (b) Mechanism of current and magnetic amplification by the Weibel-filamentation instability

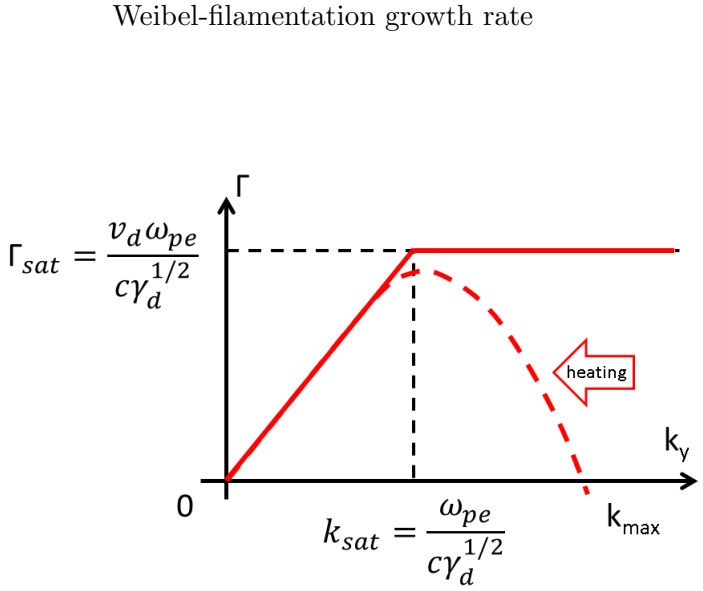

Figure 5. Typical dependence of the Weibel-filamentation growth rate upon the transverse wavevector: comparison of the cold (plain line) and warm case (dashed line) for two counter-propagating beams.

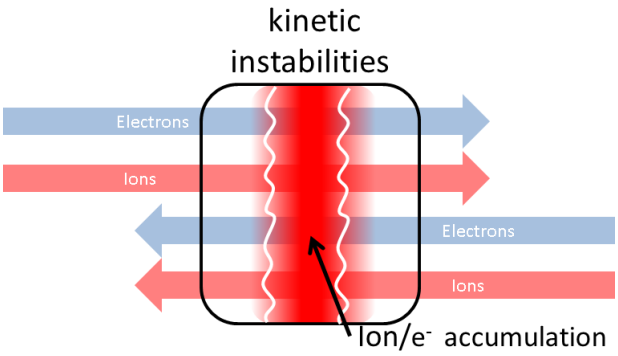

Figure 6. Sketch of shock formation. The white wavy lines represent the Weibel transverse modulations (B-field and current density).

Consequently, while the fields grow, a small heating of the electrons results in a narrowing of the unstable spectrum which may explain why the numerical simulations usually evidence a dominant magnetic wavevector of $k_y > \omega_{pe}/c\sqrt{\gamma_d}$.

The saturation occurs when the magnetic field is strong enough to affect significantly the distribution function. This implies that the Vlasov-Maxwell set of equations cannot be linearized anymore. Various approximate nonlinear models have been proposed, yet with limited range of validity and usually only capable of qualitative predictions (Davidson *et al.* 1972; Califano *et al.* 1998; Lyubarsky & Eichler 2006; Achterberg *et al.* 2007). In the weakly non-linear regime, the saturation stage can be treated through quasi-linear kinetic theory (Davidson *et al.* 1972; Pokhotelov & Amariutei 2011). The strongly non-linear regime has been addressed assuming that the filaments dynamics is governed by merging events (Medvedev *et al.* 2005; Achterberg *et al.* 2007) or secondary kink-like instabilities (Milosavljević & Nakar 2006). All these non-linear dynamics and their effects on the evolution of the plasma require further understanding.

Plasma subjects to the Weibel or Weibel-filamentation instability may be called self-magnetized since the magnetic fluctuations spontaneously develop in the absence of external magnetic field. This contrasts with most of the astrophysical plasmas which are immersed in an external magnetic field. First-principles numerical simulations have shown that the Weibel filamentation instability in its saturation stage is able to heat the system, transferring the bulk kinetic energy into thermal energy (Spitkovsky 2005; Kato & Takabe 2008). Qualitatively, the particles scatter off the self-amplified magnetic field, which eventually leads to the isotropization of the system. Once it is achieved, the instability is no longer sustained and the matter is no longer flowing.

If the initial beam velocities are large enough ($v \gtrsim 0.01c$), the ion-Weibel instability will always eventually be triggered. Moreover, for $v \gtrsim 0.4c$, the electron Weibel-filamentation is the fastest instability (Bret 2009; Bret *et al.* 2010a). In these cases, simulations show that this instability is able to isotropize the system and cause the formation of a collisionless shock (Spitkovsky 2008b; Keshet *et al.* 2009).

Weibel-mediated collisionless shocks

Let us now consider two counter-propagating high-velocity plasma beams of infinite spatial extension. The beams overlap, trigger the Weibel-filamentation instability which leads to local isotropization of the particles. This generates a rapidly growing magnetic turbulence. The resulting scattering

and slowing down (by the induced electric field) of the particles lead to a local density increase [Fig. 6]. The strong isotropization of the particles in the accumulation region (downsteam) tends to supress the Weibel instability. Particles will therefore accumulate until Rankine-Hugoniot jump conditions are reached. The resulting shock is strong as the Weibel-filamentation instability ensure nearly complete dissipation of the bulk kinetic energy into thermal energy is ensured by the Weibel-filamentation instability. Hence, Eqs. (19) and (20) can be applied and the matter is compressed by a factor three or four in 2D or 3D respectively. Moreover, in the downstream frame, the shock propagates at a velocity of $v_1/2$ (2D) and $v_1/3$ (3D), where v_1 is the unperturbed upstream flow velocity. Large scale first-principles simulations have validated these predictions (Kato & Takabe 2008; Spitkovsky 2008b).

In order to understand the processes responsible for shock propagation and the role of the Weibel-filamentation instability, we will lift the veil on the "black box" of Fig. 2. Figure 7(a) represents the qualitative evolution of the transverse averaged electric potential and magnetic energy in the shock front region. Since the shock is strong, no electrostatic oscillations are sustained in the downstream and Φ rises monotonically from the upstream to the downstream. An electrostatic field E_x lies at the shock front which contributes to the reflection of a part of the incoming ions back into the upstream, as illustrated in Fig. 7(a). Part of the downstream protons can leak from the downstream into the upstream with identical result. This creates a region close to the shock front where two counter-propagating ion populations overlap, thus triggering a Weibel-filamentation instability. Unlike in purely electrostatic shocks [Fig. 3], self-amplified magnetic fields are thus sustained close to the shock front [green line in Fig. 7(a)]. In the downstream where the particle populations are assumed to be essentially isotropic, the magnetic energy decays away far from the shock front (dashed green lines). Once again, the upstream incoming particles scatter or reflect off these magnetic fluctuations and the populations eventually get isotropized across the shock front. Hence, the incoming particles accumulate in the downstream and the shock front propagates.

Figure 7(b) sketches the spatial repartition of the electric and magnetic fields during the shock propagation. As shown above, an electrostatic potential jump lies at the shock front (red to blue region) while transverse magnetic modulations (orange and purple island) is sustained in the shock front region. In addition, the nonlinear feature of the magnetic filaments can sustain electric fluctuations (E_y and/or E_x) which makes the shock front region difficult to model. In such systems, numerical simulations (Spitkovsky 2008a) have demonstrated that an efficient Fermi-type acceleration can take place. This can be explained, considering a particle of the downstream streaming on the direction of the shock front. When the particle arrives at the shock front, it is accelerated by the local electric fields and its energy increases. Once in the upstream, although very close to the shock front, it may be deflected back into the downstream by the magnetic field surrounding Weibel filaments. During this step, it appears that no significant increase of the kinetic energy results, as shown by the particle trajectory of Fig. 7(c). This might be due to the interplay of the longitudinal electric field at the shock front with the electromagnetic fluctuations (magnetic and electric) of the Weibel-filaments. Now the particle can be scattered off the downstream magnetic fluctuations, close to the shock front (dashed green line of Fig. 7(b)). Hence the particle can be accelerated a second time across the shock front in the direction of the upstream. Each time the particle crosses the shock front from the downstream to the upstream, it gains a significant amount of energy [Fig. 7(c)]. When the Lorentz factor of the particle becomes too large, the fields become too weak to deflect the particle and the Fermi process stops. Once the Fermi-accelerated particles drift out of the shock front with relativistic energies, they can be slowed down in the upstream or the downstream of the shock, by the electromagnetic fields or any dissipation process (Lemoine 2013). This creates a synchrotron-type radiation. But the more energetic particles can also leave

(a) (b)

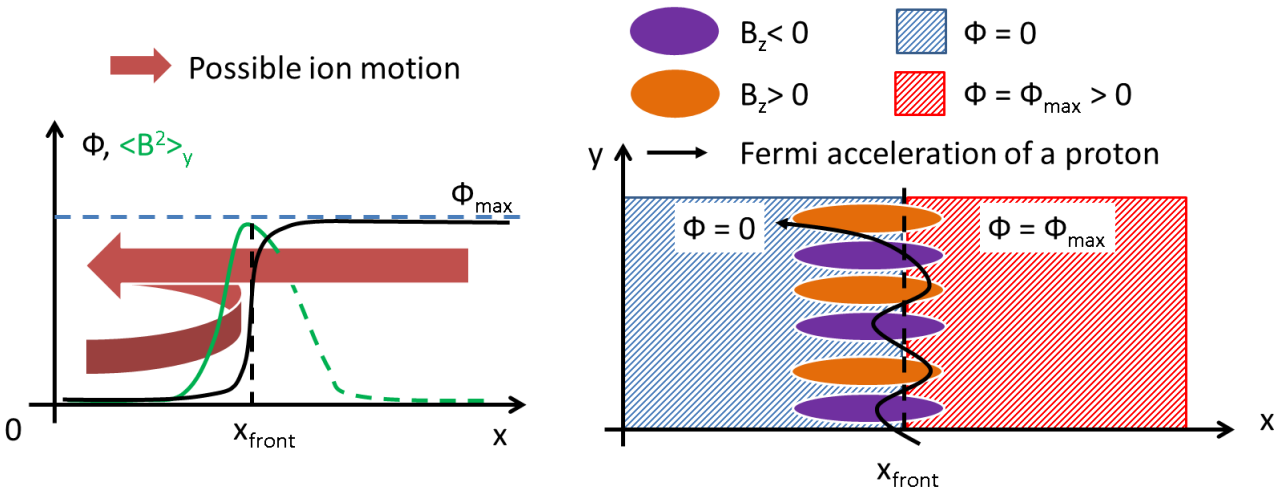

(c) Particle trajectories at the shock front in PIC simulation

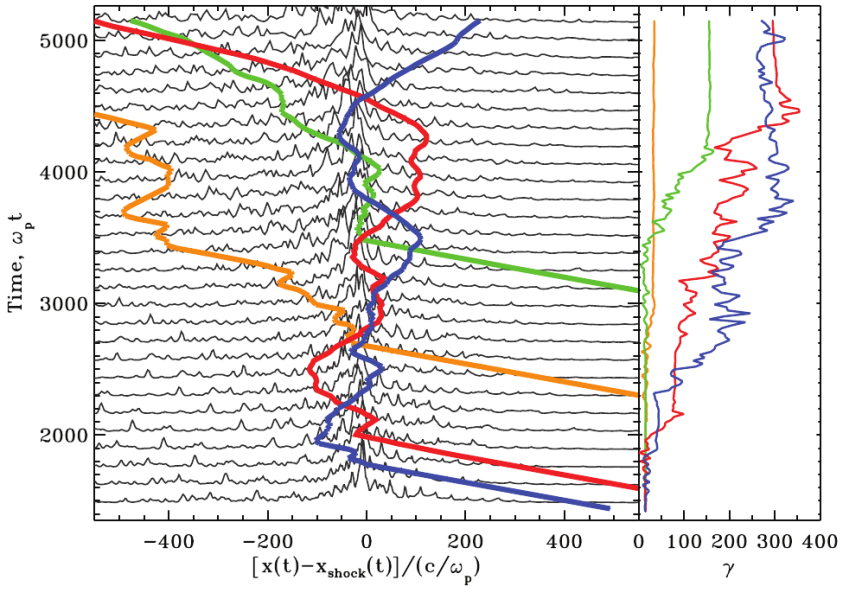

Figure 7. (a) Sketch of the fields in a Weibel-mediated ion-electron collisionless shock. (b) Fermi acceleration of positively charged particle (black arrow) at the shock front. (c) Left panel: particle trajectory close to the shock front (located at $x - x_{\rm shock} = 0$) in colorlines. Right panel: evolution of the particle's Lorentz factor, γ, in the abscissa (Spitkovsky 2008b)

the shock and drift on astronomical distances. If these particles could cross the Earth on their path, they would constitute ideal candidates for the cosmic rays explanation.

Many questions on Weibel-mediated collisionless shocks remain unanswered. From a plasma-physics point of view, even before studying the shock propagation, the formation of the shock requires a deeper understanding. How the magnetic or electric turbulence triggered by the particle distribution degenerates into a shock is still an open question, even in a very simplified framework (Lyubarsky & Eichler 2006). As an example, there was no model predicting an accurate self-magnetized shock formation time until recently (Bret *et al.* 2014). The underlying instability, the different processes of field growth, the saturation stage and evolution of the distribution functions, the heating processes and how all these effects lead to a shock need further understanding. Another issue concerns the propagation of the shock on long time-scales, which is poorly understood. A few large-scale simulations have already started to tackle this issue (Keshet *et al.* 2009). However, even for the longest simulations performed so far, less than one thousandth of the typical time of astrophysical interest is captured. Moreover, these shocks usually take place within external magnetic fields imposed by a massive stellar object, such as a white dwarf or an accretion disk. Hence, the effect of the external magnetic field on the formation and evolution of the shock should be addressed. Finally, collisionless shock are generally studied in a simplified framework where the interaction is driven by two symmetric plasma slabs, a quite unlikely configuration in the Universe.

We will now give more details on the experiments on kinetic instabilities and the simulations of collisionless shocks which will be used in this manuscript.

Tools for studying collisionless shocks

Laser experiments

The laser intensities and energies accessible nowadays open the possibility to create high-energy-density states of matter comparable to various astrophysical objects (Drake & Gregori 2012). Two regimes of laser-plasma interaction can be identified according to the energy and duration of the laser driver: the nanosecond (ns) and picosecond types (ps), which duration are respectively larger than 1ns and of the order of 1ps or smaller.

All the high energy ($E \gtrsim 1$kJ) nanosecond facilities use roughly the same general scheme to reach intensities of $I_0 \lesssim 10^{16}$W.cm^{-2}. A first long-duration laser pulse of a few nanoseconds is amplified until an energy of the order of 1-10kJ is reached. During the amplification stage, the pulse transverse section is enlarged up to a range [1-40]cm so that the intensity stays low and does not damage the optics. High-energy nanosecond laser pulses have given way to the development and study of inertial confinement fusion and recently to high-velocity collision experiments (Drake & Gregori 2012; Park *et al.* 2012; Kugland *et al.* 2012b). The study of the different instabilities which can arise in such system is of clear interest regarding our work. The usual experimental set-up consists of two solid foils irradiated by two symmetric high-intensity lasers. Two expanding plasmas are generated, which collide between the foils. The instabilities triggered in such systems depend on the laser-plasma parameters and thus on the laser parameters. Recent experiments have evidenced the formation of filamentary field structures in the overlap region. However, an accurate characterization of these filaments (wavelength, field amplitude) is still missing, which complicates the clear understanding of these results (Kugland *et al.* 2012b; Yuan *et al.* 2013; Fox *et al.* 2013; Huntington *et al.* 2013).

When a ns-pulse has been amplified, and after cleaning the phase front and its shape, it may be compressed temporally and spatially, to reach the picosecond regime. The temporal compression of a kilo-joule-class laser pulse use the "chirped pulse amplification" (CPA) proposed in (Strickland &

Mourou 1985). This drastically shortens the pulse duration from a few nanoseconds down to one picosecond or smaller, and increases the laser intensity. At this point, the laser pulse can be tightly focused onto $10-100\mu$m, reaching on-target intensities of $I_0 > 10^{18}$W.cm^{-2} for $E \lesssim 1$kJ (and often $E \ll 1$kJ). Such high-intensity pulses can generate energetic ion beams (Fuchs *et al.* 2003; Macchi *et al.* 2005) of critical importance for probing strong electromagnetic field with unprecedented space-time resolution (Mackinnon *et al.* 2004; Kugland *et al.* 2012a). Such a diagnostic has already been used in some of the plasma collision experiments previously mentioned (Kugland *et al.* 2012b; Fox *et al.* 2013). The generation of electrostatic shocks has also been observed for moderately-relativistic laser intensities $I \sim 10^{18-19}$W.cm^{-2} (Silva *et al.* 2004; Macchi *et al.* 2012) by means of simulations. These shocks can become self-magnetized for higher intensities and comparable to the Weibel-induced collisionless shocks of astrophysical interest ($I_L \geq 10^{21}$ W.cm^{-2}) (Fiuza *et al.* 2012) as we will study in Chapter 5.

Simulation of collisionless plasmas: particle-in-cell codes

Simulation codes have become crucial tools in modern research fields. For our study, we used the "particle-in-cell" (PIC) code CALDER (except in Sec. 2.6 where we have interpreted OSIRIS simulations). The PIC simulation scheme (Birdsall & Langdon 1985), detailed in Sec. 6.1, aims to describe the evolution of charged macroparticles (which represent a great number of real particles) which undergo self-generated or external fields. It then solves at each time-step Maxwell's set of equations combined with the equations of motion for each macroparticle in a discretized space.

The simulation of the kinetic instabilities involved in collisionless shocks usually considers neutral plasmas composed of electrons and positrons (pair plasmas) or electrons and fully ionized ions. In contrast to the pair plasma case, the dynamics of electron-ions shocks involves two different scales: given, respectively, by the electron and ion plasma frequencies ω_{pe} and ω_{pi} and inertial lengths c/ω_{pe} and c/ω_{pi}. Since $\omega_{pe}/\omega_{pi} \propto \sqrt{m_i/m_e}$, the smallest realistic value of this ratio is given by the proton mass, $\sqrt{m_i/m_e} \simeq 42$. Hence, an accurate simulation must resolve the electron scales, in a simulation box several times larger than the ion skin-depth. Since this involves very large and expensive simulations. This is why most of the collisionless shock simulations use a reduced ion mass (an ion mass smaller than the proton mass) in order to reduce the computational cost. The simulation is still expected to qualitatively capture the main physical processes if the ion dynamics remains sufficiently slower than the electron dynamics ($\omega_{pi}^{-1} \gg \omega_{pe}^{-1}$). Conversely, one can also increase artificially the electron mass (for fixed ion mass) to achieve the same goal of reducing the computation time (Fox *et al.* 2013). In this case, the temporal and spatial resolution of the simulation can be cruder. As will be seen in chapter 3, the Weibel instability dominates for relativistic counter-propagating plasma beams. However, in the non-relativistic regime ($v_i \lesssim 0.5c$), the analysis is complicated by other instabilities, such as the ion oblique (Forslund & Shonk 1970) or the electron oblique instability (Watson *et al.* 1960a,c). Moreover, the dominant instability depends on the ion mass ratio as evidenced in Bret (2009). This obviously increases the complexity of the analysis.

Outline

This manuscript is organized to ensure a progressive transition from the theoretical and academic questions addressed in the first chapters to more applied considerations such as the feasibility of collisionless shocks experiments considered in the last chapter. Care has also been taken to make each chapter understandable as an isolated entity. For this purpose, the nomenclature gathers the main mathematical, physical and numerical quantities as well as the mathematical conventions used

in the following. Moreover, the parts of this Manuscript which does not originate from our work, are pointed out by adding the corresponding reference in the titles of the section or subsection.

The dispersion relation of an unmagnetized, neutral and homogeneous relativistic plasma will be addressed in Chapter 1. We will evidence that it rules the propagation and growth of electromagnetic waves in collisionless plasmas. A very general resolution scheme will be introduced and applied to various distribution functions such as the relativistic Maxwell-Jüttner and waterbag distributions, and the non-relativistic bi-Maxwellian distribution. We will also introduce a simple fitting scheme able to decompose a given distribution function in a sum of waterbags (multi-waterbag). This technique will allow us to solve the dispersion relation associated with arbitrary distributions, such as the distributions given by a PIC simulation. This theoretical chapter represents the cornerstone of the following developments. The introduced tensorial elements and resolution schemes will be extensively used in the next chapters. However, it is not essential, in a first read, to the understanding of the physical processes addressed in this manuscript.

Chapter 2 addresses the equilibrium electromagnetic fluctuation spectrum of a relativistic drifting equilibrium plasma. The field fluctuations are crucial to the understanding of the deviation from equilibrium of a system. Moreover, the first comparison between the theoretical field fluctuations and their numerical counterparts in the relativistic regime will be made for various field polarizations. Finally an application of the obtained analytical formulae to the study of the growth of the electron-positron Weibel instability in a simple geometry will be addressed at the end of the chapter. This final part has been published in a collaboration with A. Bret, A. Stockem and collaborators (Bret *et al.* 2013).

Chapter 3 focuses on the kinetic instabilities triggered by two symmetric, non-relativistic and counter-propagating electron-ion plasma beams in a simple geometry. We will show that two different electrostatic instabilities can precede the Weibel stage, making use of the dispersion relations developed in the first chapter. Then, the saturation stage of the ion Weibel instability will be addressed and a predictive and analytic model of the evolution of the plasma parameters will be developed. A good agreement with PIC simulations will be evidenced for various plasma parameters.

In Chapter 4, our Weibel saturation model will be applied to the central overlap region of two colliding symmetric electron-ion plasma beams. Fair agreement until quasi-isotropization of the particle population will be evidenced. Qualitative and quantitative comparison with experiments (Kugland *et al.* 2012b; Fox *et al.* 2013) will also be made. in a second part we will address the phase of shock propagation. A kinetic model of the particle populations in the upstream and downstream region of the shock will be made. The upstream magnetic turbulence will then be addressed. An analytical formulation of the magnetic turbulence taking place upstream of the shock will be worked out. The profiles of the particle populations will also modeled by a set of differential equations. This predictive model of the upstream turbulence will be successfully compared with various shock simulations.

Chapter 5 will study the feasibility of driving collisionless shock experiments using the interaction of high intensity lasers with overdense plasmas. For intensities of $I_0 > 10^{20}\mathrm{W.cm}^{-2}$, the laser can induce a magnetic turbulence inside the target, possibly leading to a Weibel-mediated collisionless shock (Fiuza *et al.* 2012). Under these specific laser-plasma conditions, we will demonstrate that shock formation may result from the sole electron-induced turbulence, in contrast to the standard scenario ruled by ion Weibel instability.

Finally, the last part of this manuscript will gather our conclusions and prospective remarks.

Part I

Kinetic theory of a relativistic collisionless plasma

Chapter 1

Linear dispersion relation of a collisionless relativistic plasma

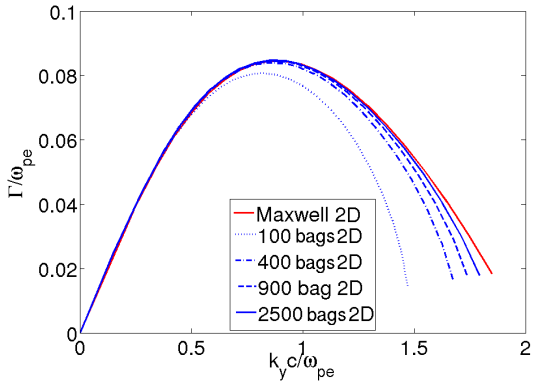

Figure 1.1. Weibel-filamentation growth rate in two counter-propagating Maxwellian electron plasma ($\beta_d = \pm 0.2$, $T = m_e c^2/100$ with fixed ions, red solid line) and comparison to a multi-waterbag calculation (blue lines).

1.1 The susceptibility tensor

1.1.1 The linearized Maxwell-Vlasov formula (Rostoker & Rosenbluth 1960; Ichimaru 1973)

The susceptibility tensor is the key ingredient ruling the stability properties of a plasma. It can be calculated exactly for various distribution functions in the linear approximation (Rostoker & Rosenbluth 1960; Ichimaru 1973). We start with a free-field (*i.e.* no external magnetic or electric field in a neutral plasma), homogeneous and infinite system of particles. Each plasma species obeys an initial momentum distribution $f_s^{(0)}(\mathbf{p})$ normalized to unity in the momentum space. In the linear approximation, we will assimilate the $\mathbf{E}$ and $\mathbf{B}$-fields to first-order quantities. The Vlasov equation on the sth total distribution function $f_s = f_s^{(0)} + f_s^{(1)}$ is

$$\delta_t f_s + \mathbf{v}\cdot\delta_{\mathbf{r}} f_s + \frac{q_s}{m_s}\left(\mathbf{E}+\mathbf{v}\times\mathbf{B}\right)\cdot\delta_{\mathbf{p}} f_s = 0\,. \tag{1.1}$$

We will know linearize this equation, and hence neglect the second-order quantities as $Ef^{(1)}$. Consequently, we neglect the feedback of the fields upon the initial distribution function $f_s^{(0)}$. This approximation breaks as soon as the distribution has varied significantly from its initial value. Since the initial distribution $f_s^{(0)}$ verifies Vlasov equation and Eq. (1.1) becomes:

$$\delta_t f_s^{(1)} + \mathbf{v}\cdot\delta_{\mathbf{r}} f_s^{(1)} + \frac{q_s}{m_s}\left(\mathbf{E}+\mathbf{v}\times\mathbf{B}\right)\delta_{\mathbf{p}} f_s^{(0)} = 0\,. \tag{1.2}$$

After a Fourrier transform using the convention presented in Nomenclature, we obtain

$$f_s^{(1)} = \frac{i\frac{q_s}{m_s}}{\mathbf{k}\cdot\mathbf{v}-\omega}\left(\mathbf{E}+\mathbf{v}\times\mathbf{B}\right)\cdot\delta_{\mathbf{p}} f_s^{(0)}\,, \tag{1.3}$$

There results the density current $\mathbf{j}$:

$$\mathbf{j}^{(1)} = \sum_s n_s q_s \int d\mathbf{p}\mathbf{v} f_s^{(1)}\,. \tag{1.4}$$

Plugging $\mathbf{j}^{(1)}$ into the Fourrier-transformed Maxwell-Ampère and Maxwell-Faraday equations, one gets:

$$\mathbf{j}^{(1)} = i\omega\left[\mathbf{E} + \frac{\mathbf{k}}{\omega}\times\left(\frac{\mathbf{k}}{\omega}\times\mathbf{E}\right)\right]\,, \tag{1.5}$$

Using Eq. (1.3):

$$i\sum_s \frac{q_s^2 n_s}{m_s}\int d\mathbf{p}\frac{\mathbf{p}}{\gamma}\frac{\delta_{\mathbf{p}} f_s^{(0)}}{\mathbf{k}\cdot\mathbf{v}-\omega}\cdot\left(\mathbf{1}+\mathbf{v}\times\frac{\mathbf{k}}{\omega}\times\right)\cdot\mathbf{E} + i\omega\left(1+\frac{\mathbf{k}}{\omega}\times\frac{\mathbf{k}}{\omega}\times\right)\cdot\mathbf{E} = 0\,. \tag{1.6}$$

We know introduce the tensorial product $\otimes$. Given the relations

$$\mathbf{v}\times\frac{\mathbf{k}}{\omega}\times\mathbf{E} = \left(\frac{\mathbf{k}}{\omega}\otimes\mathbf{v} - \mathbf{v}\cdot\frac{\mathbf{k}}{\omega}\right)\cdot\mathbf{E} \tag{1.7}$$

$$\frac{\mathbf{k}}{\omega}\times\frac{\mathbf{k}}{\omega}\times\mathbf{E} = \left(\frac{\mathbf{k}}{\omega}\otimes\frac{\mathbf{k}}{\omega} - \frac{k^2}{\omega^2}\right)\cdot\mathbf{E}\,, \tag{1.8}$$

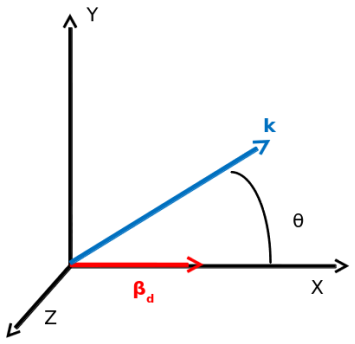

Figure 1.2. Frame adopted in this manuscript. The wavevector is taken in the xy plane while the plasma mean drift velocity $\boldsymbol{\beta}$ lies on the x axis.

we can recast Eq. (1.6) as

$$\left\{\omega^2\left[\mathbf{1}+\sum_s \frac{q_s^2 n_s}{m_s}\int d\mathbf{p}\frac{\mathbf{p}}{\gamma}\frac{\delta_{\mathbf{p}} f_s^{(0)}}{\omega-\mathbf{k}\cdot\mathbf{v}}\cdot\left(\mathbf{1}+\frac{\mathbf{k}\otimes\mathbf{v}-\mathbf{k}\cdot\mathbf{v}}{\omega}\right)\right]+\mathbf{k}\otimes\mathbf{k}-k^2\right\}\cdot\mathbf{E}=0\,. \tag{1.9}$$

This equation has non-zero solutions for $\mathbf{E}$ if and only if the determinant of the tensor in braces vanishes. We will now suppose that the distribution functions are gyrotropic, that is, of the form $(f(p_x, p_y^2+p_z^2))$. The y axis is chosen in the plane made by the x axis and the wavevector so that the wavevector lies in the xy plane. We introduce the angle θ between the wavevector $\mathbf{k}$ and the x axis. The frame is illustrated in Fig. 1.2. The z axis is taken out of the $(\widehat{\mathbf{x}},\,\mathbf{k})$ plane. The symmetry of Eq. (1.9) shows us that the xz and yz components of the bracketed expression are equal to zero. The dispersion relation, relating the wavevector $\mathbf{k}$ to the frequency ω, is deduced from the determinant of the resulting non-linear system:

$$\omega^2\epsilon_{zz}-k^2c^2=0\,, \tag{1.10}$$

$$(\omega^2\epsilon_{xx}-k_y^2c^2)(\omega^2\epsilon_{yy}-k_x^2c^2)-(\omega^2\epsilon_{xy}+k_yk_xc^2)^2=0\,. \tag{1.11}$$

We have introduced the dielectric tensor

$$\boldsymbol{\epsilon}=1+\sum_s \boldsymbol{\chi}_s\,, \tag{1.12}$$

where the susceptibility tensor $\boldsymbol{\chi}_s$ for the sth species is

$$\boldsymbol{\chi}_s=\frac{\omega_{ps}^2}{\omega^2}\iiint d^3p\,\frac{\mathbf{p}}{\gamma}\otimes\partial_{\mathbf{p}}f_s^{(0)}+\sum_s\frac{\omega_{ps}^2}{\omega^2}\iiint d^3p\left[\mathbf{v}\otimes\frac{\mathbf{p}}{\gamma}\right]\frac{\mathbf{k}\cdot\partial_{\mathbf{p}}f_s^{(0)}}{\omega-\mathbf{k}\cdot\mathbf{v}}\,, \tag{1.13}$$

and $\omega_{ps}=\sqrt{n_s q_s^2/m_s}$ is the plasma frequency of the sth species.

1.1.2 Mode solving using the generalized Fried and Gould method

In the following, we will look for the temporal instabilities of a given plasma system. These instabilities are characterized by real wavevectors and complex frequencies, solutions $D(\omega(\mathbf{k}),\mathbf{k})=0$ where $D(\omega,\mathbf{k})$ denotes the left-hand side of either (2.6) of (1.11). To compute $\omega(\mathbf{k})$, a numerical scheme originally proposed by Fried and Gould (Fried & Gould 1961) in the non-relativistic electrostatic regime has been generalized to the relativistic regime. This method is based on the formulation of the real wavevector as a function of the complex phase speed. For a given set of (gyrotropic)

distribution functions $f_s^{(0)}$ and their associated plasma frequencies ω_{ps}, we introduce a modified susceptibility tensor

$$\mathbf{X}_s = \frac{\omega^2}{\omega_{ps}^2}\boldsymbol{\chi}_s = \iiint d^3p\, \frac{\mathbf{p}}{\gamma} \otimes \partial_{\mathbf{p}} f_s^{(0)} + \sum_s \frac{\omega_{ps}^2}{\omega^2} \iiint d^3p \left[\mathbf{v} \otimes \frac{\mathbf{p}}{\gamma}\right] \frac{\cos\alpha \partial_{p_x} f_s^{(0)} + \sin\alpha \partial_{p_y} f_s^{(0)}}{v_\phi - v_x \cos\alpha - v_y \sin\alpha}\,. \tag{1.14}$$

We emphasize that $\mathbf{X}_s$ does not depend on the wavevector modulus k, but only on the phase speed β_ϕ and the orientation of the wavevector through the last term of Eq. (1.14). The dispersion relation Eq. (1.11) can be recast as a polynomial equation in $k^2 = |\mathbf{k}|^2$ using the angle θ defined as $k_y = k\sin\theta$ and $k_x = k\cos\theta$ (Fig. 1.2):

$$ak^4 + bk^2 + c = 0\,, \tag{1.15}$$

with

$$a = (\beta_\phi^2 - \sin^2\theta)(\beta_\phi^2 - \cos^2\theta) - \cos^2\theta\sin^2\theta\,, \tag{1.16}$$

$$b = (\sin^2\theta - \beta_\phi^2)\sum_s \omega_{ps}^2 X_{yy}(\cos^2\theta - \beta_\phi^2)\sum_s \omega_{ps}^2 X_{xx} + 2\cos\theta\sin\theta\sum_s \omega_{ps}^2 X_{yx}\,, \tag{1.17}$$

$$c = \left(\sum_s \omega_{ps}^2 X_{yy}\right)\left(\sum_s \omega_{ps}^2 X_{xx}\right) - \left(\sum_s \omega_{ps}^2 X_{yx}\right)^2\,, \tag{1.18}$$

$$\Delta = \sqrt{b^2 - 4ac}\,. \tag{1.19}$$

In Eqs. (1.16), (1.17) and (1.18), the subscript s has been omitted on the tensor elements $X_{\alpha\beta}$ for the sake of clarity. The wavevector modulus is then given by:

$$k^2 = \frac{-b(\beta_\phi) + \sqrt{\Delta(\beta_\phi)}}{2a(\beta_\phi)} \equiv \mathcal{G}_1(\beta_\phi)\,, \tag{1.20}$$

$$k^2 = \frac{-b(\beta_\phi) - \sqrt{\Delta(\beta_\phi)}}{2a(\beta_\phi)} \equiv \mathcal{G}_2(\beta_\phi)\,. \tag{1.21}$$

This formulation, in which $k^2(>0)$ is a function of β_ϕ only, lends itself to the efficient numerical scheme introduced by Fried and Gould (Fried & Gould 1961) in a non-relativistic framework. This technique consists, first, in determining the locus of the zeroes of $\Im\mathcal{G}_{1,2}(\beta_\phi)$. This can be readily performed by means of a contour plot in a finely discretized portion of the complex β_ϕ plane. Then, we retain those zeroes fulfilling $\Re\mathcal{G}_{1,2}(\beta_\phi) > 0$ and identify $k = \sqrt{\Re\mathcal{G}_{1,2}(\beta_\phi)}$. Depending on the β_ϕ domain considered, this method allows us to simultaneously solve for a set of discrete solutions $\omega_n(k,\theta)$. We highlight that no hypothesis has been made on the form of the gyrotropic distribution function and on the particles' properties. This scheme is then valid for any gyrotropic distribution function (relativistic or not) for which X_s is tractable. It has been presented and exploited in (Ruyer *et al.* 2013) for a Maxwell-Jüttner type distribution function. We will now derive the susceptibility tensors for three different distribution functions used in this manuscript.

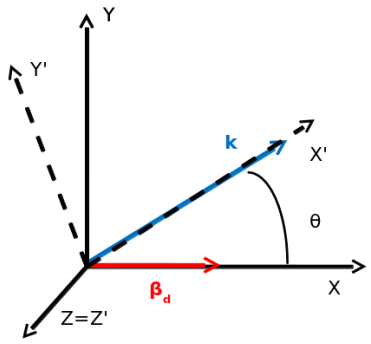

Figure 1.3. First step of Sec. 1.2 changing the xyz-frame to the $x'y'z'$-frame.

1.2 The susceptibility tensor for a 3D Maxwell-Jüttner distribution (Bret *et al.* 2010a)

1.2.1 Derivation

The particle species are assumed to obey drifting Maxwell-Jüttner distribution functions (Wright & Hadley 1975; Bret *et al.* 2010a):

$$f_s^{(0)}(\mathbf{p}) = F_s \exp\left[-\mu_s(\gamma - \beta_{ds} p_x)\right], \tag{1.22}$$

where $\gamma = \sqrt{1 + p^2/(m_s c)^2}$ is the relativistic factor, $\mu_s = m_s c^2/T_s$ the normalized inverse temperature and $\beta_{ds} = \langle v_z/c \rangle$ the z-aligned mean velocity. Moreover, in all Sec. 1.2, the momenta are normalized to mc. We have introduced the normalization factor $F_s = \mu_s/4\pi(m_s c)^3 \gamma_{ds}^2 K_2(\mu_s/\gamma_{ds})$, with $\gamma_{ds} = (1-\beta_{ds}^2)^{-1/2}$ and K_2 the modified Bessel function of the second kind. The distribution functions are normalized to unity: $\int f_s^{(0)}(\mathbf{p}) d^3p = 1$.

This distribution can be obtained by maximizing the specific entropy of a relativistic system for fixed values of the particle number, total momentum and total energy. Hence it represents the correct generalization to the relativistic framework of the usual Maxwellian distribution and thus characterizes the equilibrium distribution of a relativistic plasma. Note that this theoretical result has been recently confirmed by mean of molecular dynamics simulations (Cubero *et al.* 2007).

The related susceptibility tensors have been published in Refs. (Bret *et al.* 2010a; Ruyer *et al.* 2013). We will detail here the three main calculation steps, (omitting the s subscript) and assuming a wavevector lying in the xy plane (with $k_x = k\cos\theta$ and $k_y = k\sin\theta$):

$$X_{\alpha\beta} = -\mu_s F_s \iiint d^3p \left[\frac{p_\alpha}{\gamma}\left(\frac{p_\beta}{\gamma} - \beta_d \delta_{\beta,z}\right) + v_\alpha \frac{p_\beta}{\gamma} \frac{\cos\theta(p_x/\gamma - \beta_d) + \sin\theta \frac{p_y}{\gamma}}{\beta_\phi - v_x\cos\theta - v_y \sin\theta}\right] \exp\left[-\mu_s(\gamma - \beta_{ds} p_x)\right]. \tag{1.23}$$

Since the calculations are similar for all the tensor components, we will only present the calculation for the X_{yy} component. All the results will be gathered at the end of the section.

First step: alignment of the x-axis with k. Taking the yy component of Eq. (1.23) and changing the xyz-frame to the $x'y'z'$-frame where the x'-axis is aligned with the wavevector $\mathbf{k}$, as illustrated by Fig. 1.3:

$$X_{yy} = -\mu_s F_s(\beta_\phi - \beta_d\cos\theta) \iiint d^3p' \frac{(\frac{p'_y}{\gamma}\cos\theta + \frac{p'_z}{\gamma}\sin\theta)^2}{\gamma\beta_\phi - p'_z} \exp\left[-\mu_s(\gamma - \beta_{ds} p'_z\cos\theta - \beta_{ds} p'_y \sin\theta)\right]. \tag{1.24}$$

Only p'_z appears in the Landau pole of Eq. (1.24), simplifying the complex analysis of Sec. 1.2.2.

Second step: from the momentum space to velocity space. The second variable substitution consists in shifting from Cartesian momentum space to a cylindrical velocity space:

$$p'_x = \gamma v_\parallel \,, \tag{1.25}$$
$$p'_y = \gamma v_\perp \sin\alpha \,, \tag{1.26}$$
$$p'_z = \gamma v_\perp \cos\alpha \,. \tag{1.27}$$

The determinant of the Jacobian is here $|J| = \gamma^5 v_\perp$, giving:

$$\begin{aligned} X_{yy} = &- \mu_s F_s(\beta_\phi - \beta_d \cos\theta) \int_{-1}^{1} dv_\parallel \int_0^{\sqrt{1-v_\parallel^2}} dv_\perp \int_0^{2\pi} d\alpha \\ &\frac{(v_\perp \cos\theta \sin\alpha + v_\parallel \sin\theta)^2}{\beta_\phi - v_\parallel} \gamma^5 v_\perp \exp\left[-\mu_s(\gamma - \beta_{ds}\gamma v_\parallel \cos\theta - \beta_{ds}\gamma v_\perp \sin\alpha \sin\theta)\right] . \end{aligned} \tag{1.28}$$

We now introduce the phase speed functions A, B and C, yielding

$$X_{yy} = -2\pi\mu_s F_s(\beta_\phi - \beta_d \cos\theta)\left[\cos\theta^2 A + \sin\theta^2 B + 2\cos\theta\sin\theta C\right] \,, \tag{1.29}$$

with

$$A = \frac{1}{2\pi}\int_{-1}^{1} dv_\parallel \frac{1}{\beta_\phi - v_\parallel} \int_0^{\sqrt{1-v_\parallel^2}} dv_\perp \gamma^5 v_\perp^3 e^{-\mu_s\gamma(1-\beta_d\cos\theta v_\parallel)} \int_0^{2\pi} d\alpha \sin\alpha^2 e^{-\mu_s\gamma\beta_d v_\perp \sin\theta\sin\alpha} \,, \tag{1.30}$$

$$B = \frac{1}{2\pi}\int_{-1}^{1} dv_\parallel \frac{v_\parallel^2}{\beta_\phi - v_\parallel} \int_0^{\sqrt{1-v_\parallel^2}} dv_\perp \gamma^5 v_\perp e^{-\mu_s\gamma(1-\beta_d\cos\theta v_\parallel)} \int_0^{2\pi} d\alpha e^{-\mu_s\gamma\beta_d v_\perp \sin\theta\sin\alpha} \,, \tag{1.31}$$

$$C = \frac{1}{2\pi}\int_{-1}^{1} dv_\parallel \frac{v_\parallel}{\beta_\phi - v_\parallel} \int_0^{\sqrt{1-v_\parallel^2}} dv_\perp \gamma^5 v_\perp^2 e^{-\mu_s\gamma(1-\beta_d\cos\theta v_\parallel)} \int_0^{2\pi} d\alpha \sin\alpha e^{-\mu_s\gamma\beta_d v_\perp \sin\theta\sin\alpha} \,. \tag{1.32}$$

The integrals over α are now tractable using the formula (Ref. (Abramowitz & Stegun 1964)):

$$\int d\alpha \exp\left(-\mu_s\gamma\beta_d v_\perp \sin\theta\sin\alpha\right) = 2\pi I_0(\mu\gamma\beta_d v_\perp \sin\theta) \,. \tag{1.33}$$

In the above equation, I_n stands for the modified Bessel function of the first kind. Taking the derivative of Eq. (1.33) with respect to γ gives:

$$\int d\alpha \sin\alpha \exp\left(-\mu_s\gamma\beta_d v_\perp \sin\theta\sin\alpha\right) = -2\pi I_1(\mu\gamma\beta_d v_\perp \sin\theta) \,, \tag{1.34}$$

$$\int d\alpha \sin\alpha^2 \exp\left(-\mu_s\gamma\beta_d v_\perp \sin\theta\sin\alpha\right) = \pi\left(I_0(\mu\gamma\beta_d v_\perp \sin\theta) + I_2(\mu\gamma\beta_d v_\perp \sin\theta)\right) \,. \tag{1.35}$$

Plugging Eqs. (1.33), (1.34) and (1.35) into (1.30), (1.31) and (1.31) yields:

$$A = \frac{1}{2}\int_{-1}^{1} dv_\parallel \frac{1}{\beta_\phi - v_\parallel} \int_0^{\sqrt{1-v_\parallel^2}} dv_\perp \gamma^5 v_\perp^3 e^{-\mu_s\gamma(1-\beta_d \cos\theta v_\parallel)} \left(I_0(\mu\gamma\beta_d v_\perp \sin\theta) + I_2(\mu\gamma\beta_d v_\perp \sin\theta)\right) , \tag{1.36}$$

$$B = \int_{-1}^{1} dv_\parallel \frac{v_\parallel^2}{\beta_\phi - v_\parallel} \int_0^{\sqrt{1-v_\parallel^2}} dv_\perp \gamma^5 v_\perp e^{-\mu_s\gamma(1-\beta_d \cos\theta v_\parallel)} I_0(\mu\gamma\beta_d v_\perp \sin\theta) , \tag{1.37}$$

$$C = -\int_{-1}^{1} dv_\parallel \frac{v_\parallel}{\beta_\phi - v_\parallel} \int_0^{\sqrt{1-v_\parallel^2}} dv_\perp \gamma^5 v_\perp^2 e^{-\mu_s\gamma(1-\beta_d \cos\theta v_\parallel)} I_0(\mu\gamma\beta_d v_\perp \sin\theta) . \tag{1.38}$$

Third step The final step consists in changing the variable $v_\perp$ of the quadratures Eqs. (1.39), (1.40) and (1.41) to $t = \gamma(1-v_\parallel^2)^{\frac{1}{2}}$. Given $v_\perp dv_\perp = dt(1-v_\parallel^2)/t^3$ and $v_\perp^2 = (1-t^{-2})(1-v_\parallel^2)$, we get

$$A = \frac{1}{2}\int_{-1}^{1} dv_\parallel \frac{f_A(\beta_\phi)}{\beta_\phi - v_\parallel} , \tag{1.39}$$

$$B = \int_{-1}^{1} dv_\parallel \frac{f_B(\beta_\phi)}{\beta_\phi - v_\parallel} , \tag{1.40}$$

$$C = -\int_{-1}^{1} dv_\parallel \frac{f_C(\beta_\phi)}{\beta_\phi - v_\parallel} , \tag{1.41}$$

with

$$f_A(\beta_\phi) = \frac{\gamma_\parallel}{2}\int_1^{+\infty} dt(t^2-1)\left[I_0(\nu(t^2-1)^{1/2}) + I_2(\nu_s(t^2-1)^{1/2})\right] e^{-\rho_s t} , \tag{1.42}$$

$$f_B(\beta_\phi) = v_\parallel^2\gamma_\parallel^3 \int_1^{+\infty} dt I_0(\nu_s(t^2-1)^{\frac{1}{2}}) t^2 e^{-\rho_s t} , \tag{1.43}$$

$$f_C(\beta_\phi) = -v_\parallel\gamma_\parallel^2 \int_1^{+\infty} dt \sqrt{\frac{t-1}{t+1}}(t+1) t I_1(\nu_s(t^2-1)^{1/2}) e^{-\rho_s t} . \tag{1.44}$$

We have defined:

$$\nu_s = \mu_s\beta_{ds}\sin\theta \tag{1.45}$$

$$\rho_s = \mu_s\gamma_\parallel(1-\beta_{ds}v_\parallel\cos\theta) \tag{1.46}$$

$$\gamma_\parallel = (1-v_\parallel^2)^{\frac{-1}{2}} . \tag{1.47}$$

The quadratures of Eqs. (1.42), (1.43) and (1.44) can be performed exactly using the formula (Abramowitz & Stegun 1964):

$$\int_1^{+\infty} dt \left(\frac{t-1}{t+1}\right)^{\frac{N}{2}} I_N\left(\nu\sqrt{t^2-1}\right) e^{-\rho t} = \left(\frac{\nu}{\rho+\sqrt{\rho^2-\nu^2}}\right)^N \frac{e^{-\sqrt{\rho^2-\nu^2}}}{\sqrt{\rho^2-\nu^2}} = g_N(\rho) , \tag{1.48}$$

where N is a natural number. The functions f_A, f_B and f_C of Eqs. (1.42), (1.43) and (1.44) can be related to the derivatives of $g_N(\rho)$ (defined above). We obtain:

$$f_A(\beta_\phi) = \frac{\gamma_\parallel}{2}\left(\partial_\rho^2 - 1\right) g_0(\rho) + \frac{\gamma_\parallel}{2}\left(\partial_\rho^2 - 2\partial_\rho + 1\right) g_1(\rho)\,, \tag{1.49}$$

$$f_B(\beta_\phi) = v_\parallel^2 \gamma_\parallel^3 \partial_\rho^2 g_0(\rho)\,, \tag{1.50}$$

$$f_C(\beta_\phi) = -\, v_\parallel \gamma_\parallel^2 \left(\partial_\rho^2 - \partial_\rho\right) g_1(\rho)\,. \tag{1.51}$$

Plugging Eq. (1.48) into Eqs. (1.49), (1.50) and (1.51) gives the tensor X_{yy}. Proceeding along the same lines, the tensor elements X_{xy} and X_{xx} can be expressed as functions of the quadratures A, B and C, while the calculation of X_{zz} involves another quadrature D. The final results, (given $\epsilon_{\alpha,\beta} = \delta_{\alpha,\beta} + \sum_s \omega_{ps}^2 X_{\alpha,\beta}/\omega^2$) yields

$$X_{zz} = -2\pi F_s \mu_s \left(\beta_\phi - \beta_{ds}\cos\theta\right) D_s\,, \tag{1.52}$$

$$X_{yy} = -2\pi F_s \mu_s \left(\beta_\phi - \beta_{ds}\cos\theta\right)\left(A_s \cos^2\theta + 2C_s\cos\theta\sin\theta + B_s\sin^2\theta\right)\,, \tag{1.53}$$

$$X_{xx} = -2\pi F_s \mu_s \left(\beta_\phi - \beta_{ds}\cos\theta\right)\left(A_s \sin^2\theta - 2C_s\cos\theta\sin\theta + B_s\cos^2\theta\right) + \mu_s\beta_{ds}^2\,, \tag{1.54}$$

$$X_{yx} = -2\pi F_s \mu_s \left(\beta_\phi - \beta_{ds}\cos\theta\right)\left[(B_s - A_s)\cos\theta\sin\theta + C_s(\cos^2\theta - \sin^2\theta)\right]\,. \tag{1.55}$$

Each function $X \in \{A_s, B_s, C_s, D_s\}$ is defined as

$$X(\beta_\phi) = \int_{-1}^{1} d\beta\, \frac{f_X(\gamma, \rho_s, \nu_s)}{\beta_\phi - \beta} \quad (\Im\beta_\phi > 0)\,, \tag{1.56}$$

with

$$\begin{aligned}
f_{A_s} &= \frac{\gamma e^{-h_s}}{h_s^5}\left[(h_s+1)(\rho_s^2 + 2\nu_s^2) + \nu_s^2 h_s^2\right]\,,\\
f_{B_s} &= \frac{\beta^2\gamma^3 e^{-h_s}}{h_s^5}\left[(h_s+1)(2\rho_s^2 + \nu_s^2) + \rho_s^2 h_s^2\right]\,,\\
f_{C_s} &= -\nu_s\frac{\beta\gamma^2\rho_s e^{-h_s}}{h_s^5}\left[3(h_s+1) + h_s^2\right]\,,\\
f_{D_s} &= \frac{\gamma e^{-h_s}}{h_s^3}(h_s+1)\,,
\end{aligned} \tag{1.57}$$

where

$$\rho_s = \mu_s\gamma(1 - \beta_{ds}\beta\cos\theta)\,, \tag{1.58}$$

$$\nu_s = \mu_s\beta_{ds}\sin\theta\,, \tag{1.59}$$

$$h_s = (\rho_s^2 - \nu_s^2)^{1/2}\,. \tag{1.60}$$

1.2.2 Branch cuts

In order to compute Eqs. (1.52)-(1.55) for $(\omega, k) \in \mathbb{C}\times\mathbb{R}$, the function $Z \in \{A, B, C, D\}$ (the index s is omitted for the sake of clarity) must be analytically continued to the $\Im\beta_\phi \leq 0$ complex half-plane. To this goal, it is convenient to use the following expression

$$Z(\beta_\phi) = -\int_{-1}^{1} d\beta\, \frac{f_Z(\beta) - f_Z(\beta_\phi)}{\beta - \beta_\phi} - f_Z(\beta_\phi)\ln\left(\frac{\beta_\phi - 1}{\beta_\phi + 1}\right)\,, \tag{1.61}$$

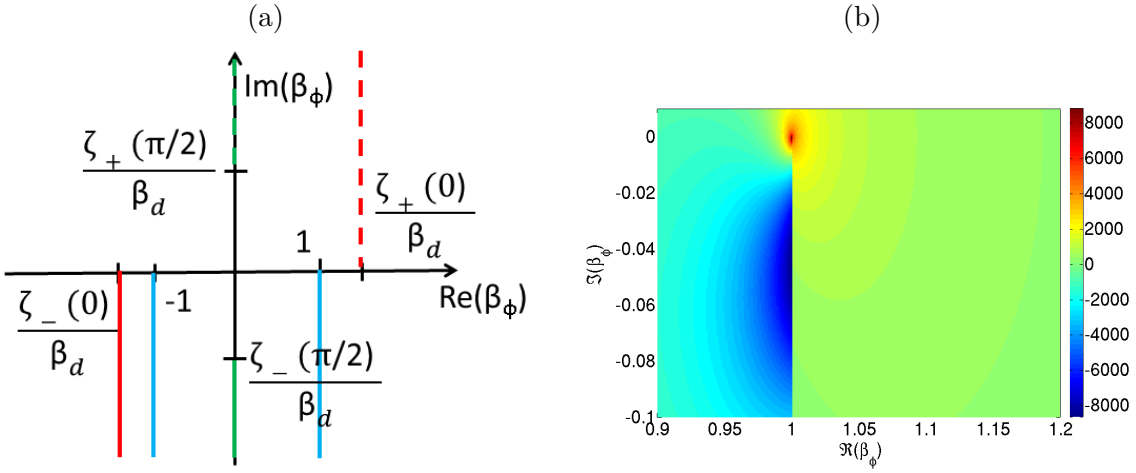

Figure 1.4. (a) Branch cuts (colored solid lines) of the function $Z \in \{A, B, C, D\}$ in the complex β_ϕ plane for $\theta = 0$ and $\theta = \pi/2$. (b) Map of $\Re B$ in the complex β_ϕ plane for $\mu = 1$, $\beta_d = 0.9$ and $\theta = 0$ which evidence the branch cut $]+1, +1 - i\infty[$.

where ln denotes a particular branch of the complex logarithm to be defined. The integrand of Eq. (1.61) has no singularity, and therefore lends itself to a standard numerical integration scheme. Because Z has to be computed on the real β_ϕ axis, the logarithm's branch cuts are chosen to be $]-1-i\infty, -1[\cup]+1, +1-i\infty[$. They are illustrated as blue plain lines in Fig. 1.4(a). The calculation of $\Re B$ Eq. (1.40) in the complex β_ϕ-plane, displayed in Fig 1.4(b), evidences the discontinuity caused by these branch cuts. This implies that the phase angles $\theta_{\beta\pm1} = \arg(\beta \pm 1)$ lie within the interval $-\pi/2 < \theta_{\beta\pm1} < 3\pi/2$. This specification leads to the same branch cuts for the multivalued relativistic factor

$$\gamma = i(|\beta - 1||\beta + 1|)^{-1/2} \exp\left[-i(\theta_{\beta+1} + \theta_{\beta-1})\right] . \tag{1.62}$$

Similarly, the analytical continuation of the function $h(\beta)$ (1.60) follows from its factorized form

$$h(\beta) = \mu\gamma\sqrt{(\beta_d\beta - \zeta_+)(\beta_d\beta - \zeta_-)}\,, \tag{1.63}$$

$$\zeta_\pm = \cos\alpha \pm i\frac{\sin\theta}{\gamma_d} . \tag{1.64}$$

The phase angles $\theta_{\beta_d\beta-\zeta_\pm} = \arg(\beta_d\beta - \zeta_\pm)$ are now restricted to the intervals $-\pi/2 < \theta_{\beta_d\beta-\zeta_-} < 3\pi/2$ and $-3\pi/2 < \theta_{\beta_d\beta-\zeta_+} < \pi/2$, which leads to the branch cuts $]-1-i\infty, -1[\cup]+1, +1-i\infty[\cup]\zeta_- - i\infty, \zeta_-[\cup]\zeta_+ + i\infty, \zeta_+[$. They are plotted as red and green lines in Fig. 1.4(a). Equation (1.56) shows that the function Z inherits the branch cuts $]-1-i\infty, -1[\cup]\zeta_- - i\infty, \zeta_-[$ in the lower half β_ϕ plane. By contrast, it is of the Cauchy type in the upper half β_ϕ plane, and therefore everywhere holomorphic.

As an example, we now make use of the generalized Fried and Gould solver for two symmetric Maxwell-Jüttner electron distribution functions of parameters $\mu = 10$ ($T = 51$keV) and $\beta_d = \pm 0.9$. We only discretize the upper part of the complex phase-speed plane ($\Im(\beta_\phi) > 0$). Hence, we only solve the unstable eigenmodes of the system. We thus obtain a map displaying the growth rate [Figs. 1.5(a)] and real frequency [Figs. 1.5(b)] in the (k_x, k_y) plane. Due to our finite resolution of the complex β_ϕ-plane, we solve neither the small nor the negative values of $\Im(\beta_\phi)$. These unresolved parts of the complex β_ϕ-plane result in the white areas of Figs. 1.5(a,b).

Figure 1.5(a) evidences that a significant part of the ($k_y\omega_p/c$, $k_x\omega_p/c$)-plane is unstable (positive value $\Im(\omega)$). The fastest-growing mode ($\Gamma/\omega_{pe} \sim 0.35$) is found at $k_y c/\omega_{pe} = 0.8$, and thus corresponds to a transverse instability ($\mathbf{k} \perp \boldsymbol{\beta}_d$). This mode is non-propagating since $\Re(\omega) = 0$

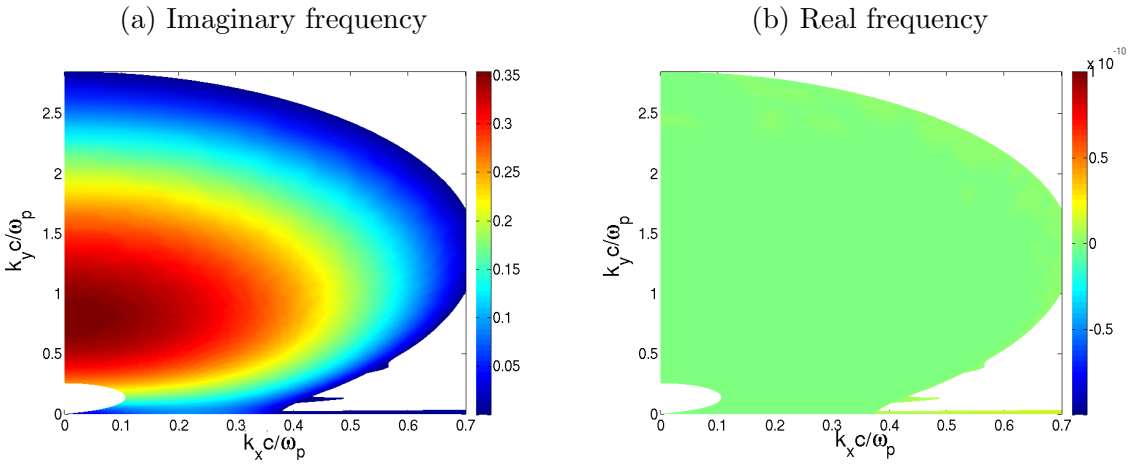

Figure 1.5. (a) Growth rate $\Im(\omega)$ and (b) real frequency $\Re(\omega)$ normalized to the plasma frequency in the $(k_y\omega_p/c,\ k_x\omega_p/c)$-plane for two Maxwell-Jüttner distributed electron beams of parameters $\mu = 10$ and $\beta_d = \pm 0.9$. The dispersion relation solved is Eq. (1.21).

[Fig. 1.5(b)] and solution of Eq. (1.21) which corresponds to the propagation of the E_x-component of the electric field. A wavevector along the y-axis, thus transverse to E_x, corresponds to an electromagnetic wave ($\mathbf{E} \perp \mathbf{k}$). Hence the most unstable part of the $(k_y\omega_p/c,\ k_x\omega_p/c)$-plane [Fig. 1.5(a)] corresponds to a non-propagating and transverse electromagnetic instability, namely the Weibel-filamentation instability (Weibel 1959).

1.3 The susceptibility tensor of a 2D bi-Maxwellian distribution

1.3.1 The susceptibility tensor components

The particle distribution is now taken to be a 2D non-relativistic bi-Maxwellian distribution function defined as:

$$f_s^{(0)} = \frac{1}{2\pi\sqrt{T_x T_y}} \exp\left(-\frac{m_s(v_x - v_d)^2}{2T_x} - \frac{m_s v_y^2}{2T_y}\right). \tag{1.65}$$

The parameters are the x-aligned drift velocity v_d and the axial and transverse temperature T_x and T_y. The $\mathbf{X}$ tensor of Eq. (1.23) can be linked to the plasma dispersion function $\mathcal{Z}$ (Fried *et al.* 1960). These calculations being simpler than in Sec. 1.2, we will only present the main stages of the calculation. At first, we will make a variable substitution which consists in aligning the x axis with the wavevector as in Sec. 1.2.1. The integration on the variable perpendicular to the wavevector is now tractable and involve Gaussian integrals. The last integral will then be linked to the derivatives of $\mathcal{Z}$ using:

$$\int_{-\infty}^{+\infty} dt \frac{e^{-t^2}}{t-x} = \sqrt{\pi}\mathcal{Z}(x)\,, \tag{1.66}$$

$$\int_{-\infty}^{+\infty} dt \frac{te^{-t^2}}{t-x} = \sqrt{\pi}\left(1 + x\mathcal{Z}(x)\right) = -\frac{\sqrt{\pi}}{2}\partial_x\mathcal{Z}(x)\,, \tag{1.67}$$

$$\int_{-\infty}^{+\infty} dt \frac{t^2e^{-t^2}}{t-x} = -\frac{\sqrt{\pi}}{2}x\partial_x\mathcal{Z}(x)\,, \tag{1.68}$$

$$\int_{-\infty}^{+\infty} dt \frac{t^3e^{-t^2}}{t-x} = \frac{\sqrt{\pi}}{2}\left(1 - x^2\partial_x\mathcal{Z}(x)\right)\,. \tag{1.69}$$

We thus obtain:

$$X_{xx} = -1 + \left[\cos^2(\theta) + \sin^2(\theta)\frac{\mu_a^2}{\mu_\perp^2} - \sin(2\theta)\frac{\mu_a}{\mu_\perp}\right]\left[1 - \xi^2\mathcal{Z}'(\xi)\right] + 2\sqrt{\frac{\mu_\parallel}{2}}\sin(\theta)\frac{\mu_a}{\mu_\perp}\beta_d\mathcal{Z}(\xi)$$
$$- \left[\beta_d^2\mu_\parallel + \frac{\mu_\parallel}{\mu_\perp}\sin^2(\theta) - 2\sin^2(\theta)\frac{\mu_a^2}{\mu_\perp^2} + 2\sin(2\theta)\frac{\mu_a}{\mu_\perp}\right]\frac{\mathcal{Z}'(\xi)}{2}$$
$$- 2\sqrt{\frac{\mu_\parallel}{2}}\beta_d\left[\cos(\theta) - \sin(\theta)\frac{\mu_a}{\mu_\perp}\right]\xi\mathcal{Z}'(\xi)\,, \tag{1.70}$$

$$X_{yy} = -1 - \left[\frac{\mu_\parallel}{\mu_\perp}\cos^2(\theta) - 2\cos^2(\theta)\frac{\mu_a^2}{\mu_\perp^2} - 2\sin(2\theta)\frac{\mu_a}{\mu_\perp}\right]\frac{\mathcal{Z}'(\xi)}{2}$$
$$+ \left[\sin^2(\theta) + \cos^2(\theta)\frac{\mu_a^2}{\mu_\perp^2} + \sin(2\theta)\frac{\mu_a}{\mu_\perp}\right]\left[1 - \xi^2\mathcal{Z}'(\xi)\right]\,, \tag{1.71}$$

$$X_{xy} = -\left[\cos(\theta)\sin(\theta)(1 - \frac{\mu_a^2}{\mu_\perp^2}) + \cos(2\theta)\frac{\mu_a}{\mu_\perp}\right]\xi\left[\mathcal{Z}(\xi) + \xi\mathcal{Z}'(\xi)\right] - \frac{\mu_a}{\mu_\perp}\sqrt{\frac{\mu_\parallel}{2}}\beta_d\cos(\theta)\mathcal{Z}(\xi)$$
$$- \cos(\theta)\sin(\theta)\left[\frac{\mu_\parallel}{\mu_\perp} - 1 - \frac{\mu_a^2}{\mu_\perp^2}\right]\frac{\mathcal{Z}'(\xi)}{2} - \left[\sin(\theta) + \cos(\theta)\frac{\mu_a}{\mu_\perp}\right]\beta_d\sqrt{\frac{\mu_\parallel}{2}}\xi\mathcal{Z}'(\xi)\,. \tag{1.72}$$

We have introduced μ_a, $\mu_\parallel$, $\mu_\perp$ and ξ:

$$\mu_a = \cos(\theta)\sin(\theta)\left(\frac{m}{T_x} - \frac{m}{T_y}\right) \tag{1.73}$$

$$\mu_\parallel = \frac{m\cos^2(\theta)}{T_x} + \frac{m\sin^2(\theta)}{T_y} \tag{1.74}$$

$$\mu_\perp = \frac{m\sin^2(\theta)}{T_x} + \frac{m\cos^2(\theta)}{T_y} \tag{1.75}$$

$$\xi = \sqrt{\frac{\mu_\parallel}{2}}\left(\frac{\omega}{k} - v_d\cos(\theta)\right) \tag{1.76}$$

Equations (1.70), (1.71) and (1.72) make use of the plasma dispersion function $\mathcal{Z}$ and its argument ξ [Eq. (1.76)]. We emphasize that the above tensor elements depend only on the plasma parameters, complex phase velocity and propagation angle and are therefore adapted to the resolution scheme introduced previously.

Note that the plasma dispersion function can be accurately approximated using a rational expansions (Weideman 1995), thus allowing fast computations of the dielectric tensor elements.

1.3.2 Particular cases of longitudinal and transverse modes

Longitudinal modes We will now derive the dispersion relation of a two counter-streaming bi-Maxwellian plasmas (for $s = 1$ or 2: $T_{x1} = T_{x2}$, $T_{y1} = T_{y2}$, $\omega_{p1} = \omega_{p2}$ and $v_{d1} = -v_{d2}$). The tensor component associated with the mode $\mathbf{k} \parallel \mathbf{E}$ along the x axis, is obtained by plugging $\theta = 0$ into Eq. (1.70)

$$X_{xx}(\theta = 0) = -\sum_s \frac{\omega_{ps}^2}{k_x^2c^2}\frac{m_s}{2T_{xs}}\partial_{\xi_s}\mathcal{Z}(\xi_s)\,, \tag{1.77}$$

where $\xi_s = (\omega/k_x - v_{ds})\sqrt{m_s/2T_{xs}}$. Moreover, under these conditions, one can show that the X_{xy} component vanishes, which results in $\epsilon_{xy} = 0$. Hence, the longitudinal dispersion relation [Eq.

(1.11)] writes $\epsilon_{xx} = 0$, that is,

$$1 - \sum_s \frac{\omega_{ps}^2}{k_x^2 c^2} \frac{m_s}{2T_{xs}} \partial_{\xi_s} \mathcal{Z}(\xi_s) = 0\,, \tag{1.78}$$

as derived a long time ago in Fried & Gould (1961) and (Bohm & Gross 1949).

Transverse modes For the same two-stream bi-Maxwellian system, we now consider the elctromagnetic dispersion relation of transverse modes (with $\mathbf{k} \perp \boldsymbol{\beta}_d$). For an anisotropic enough system, these modes correspond to the non-relativistic Weibel instability. Plugging $\alpha = \pi/2$ into Eq. (1.71) yields the susceptibility tensor component X_{xx}

$$X_{xx}(\theta = \pi/2) = + \sum_s \frac{\omega_{ps}^2}{\omega k_y c} \left[1 + \frac{m_s v_{ds}^2 + T_{sx}}{T_{sy}} (1 + X_s \mathcal{Z}(X_s)) \right]\,, \tag{1.79}$$

where $\xi_s = \sqrt{m_s/2T_{xs}}\omega/k_y$. In the symmetric system we consider, X_{xy} vanishes [Eq. 1.72] and the electromagnetic dispersion relation simplifies to $\omega^2 \epsilon_{xx} - k_y^2 c^2 = 0$. It now reads

$$\omega^2 - k_y^2 c^2 - \sum_s \omega_{ps}^2 \left[1 + \frac{m_s v_{ds}^2 + T_{sx}}{T_{sy}} (1 + \xi_s \mathcal{Z}(\xi_s)) \right] = 0\,, \tag{1.80}$$

consistently with Davidson *et al.* (1972).

1.4 The susceptibility tensor for 2D relativistic multi-waterbag distribution

1.4.1 Analytical expression of the dielectric tensor (Bret *et al.* 2010b)

The 2D relativistic waterbag distribution function is (Gremillet *et al.* 2007; Bret *et al.* 2010b):

$$f^{(0)} = \frac{1}{4 p_\perp p_\parallel} H(p_\parallel - |p_x - p_d|) H(p_\perp - |p_y|)\,, \tag{1.81}$$

where H is the Heaviside function. This distribution is characterized by two momentum spreads, $p_\parallel$ and $p_\perp$, respectively in the directions x and y and a mean momentum p_d aligned with the x axis. The derivatives of the distribution function in Eq. (1.14) are equal to zero except at the borders of the distribution:

$$\partial_{p_x} f^{(0)} = -\frac{1}{4 p_\perp p_\parallel} H(p_\perp - |p_y|) \delta\left(\frac{p_\parallel}{2} - |p_x - p_d| \right) \mathrm{sgn}(p_x - p_d)\,, \tag{1.82}$$

$$\partial_{p_x} f^{(0)} = -\frac{1}{4 p_\perp p_\parallel} H(p_\parallel - |p_x - p_d|) \delta\left(p_\perp - |p_y| \right) \mathrm{sgn}(p_y)\,. \tag{1.83}$$

Plugging Eqs. (1.82) and (1.83) into (1.23) yields the susceptibility tensors published in (Bret *et al.* 2010b):

$$X_{\alpha\beta} = \mathcal{A}_{\alpha\beta} + \cos(\theta)\mathcal{B}_{\alpha\beta} + \sin(\theta)\mathcal{C}_{\alpha\beta}\,. \tag{1.84}$$

The tensorial elements $\mathcal{A}_{\alpha\beta}$ and $\mathcal{B}_{\alpha\beta}$ write

$$\mathcal{A}_{xx} = -\frac{1}{2p_\perp}\ln\left[\frac{p_d+p_\parallel+\sqrt{1+(p_d+p_\parallel)^2+p_\perp^2}}{p_d-p_\parallel+\sqrt{1+(p_d-p_\parallel)^2+p_\perp^2}}\right], \tag{1.85}$$

$$\mathcal{A}_{yy} = \frac{p_d-p_\parallel}{4p_d p_\perp}\ln\left[\frac{p_\perp+\sqrt{1+(p_d-p_\parallel)^2+p_\perp^2}}{-p_\perp+\sqrt{1+(p_d-p_\parallel)^2+p_\perp^2}}\right] - \frac{p_d+p_\parallel}{4p_d p_\perp}\ln\left[\frac{p_\perp+\sqrt{1+(p_d+p_\parallel)^2+p_\perp^2}}{-p_\perp+\sqrt{1+(p_d+p_\parallel)^2+p_\perp^2}}\right], \tag{1.86}$$

$$\mathcal{A}_{xy} = 0\,. \tag{1.87}$$

$$\mathcal{B}_{xx} = \frac{p_\perp}{4p_\parallel\sqrt{1+p_\perp^2}}\left[\mathcal{F}_0\left(x,\frac{\sin(\theta)p_\perp}{\sqrt{1+p_\perp^2}},v_\phi,-\cos(\theta)\right)-\mathcal{F}_0\left(x,-\frac{\sin(\theta)p_\perp}{\sqrt{1+p_\perp^2}},v_\phi,-\cos(\theta)\right)\right]_{\sinh^{-1}\left(\frac{p_d-p_\parallel}{\sqrt{1+p_\perp{}^2}}\right)}^{\sinh^{-1}\left(\frac{p_d+p_\parallel}{\sqrt{1+p_\perp{}^2}}\right)}, \tag{1.88}$$

$$\mathcal{B}_{yy} = \frac{\sqrt{1+p_\perp^2}}{4p_\parallel p_\perp}\left[\mathcal{F}_2\left(x,\frac{\sin(\theta)p_\perp}{\sqrt{1+p_\perp^2}},v_\phi,-\cos(\theta)\right)-\mathcal{F}_2\left(x,-\frac{\sin(\theta)p_\perp}{\sqrt{1+p_\perp^2}},v_\phi,-\cos(\theta)\right)\right]_{\sinh^{-1}\left(\frac{p_d-p_\parallel}{\sqrt{1+p_\perp{}^2}}\right)}^{\sinh^{-1}\left(\frac{p_d+p_\parallel}{\sqrt{1+p_\perp{}^2}}\right)}, \tag{1.89}$$

$$\mathcal{B}_{xy} = -\frac{1}{4p_\parallel}\left[\mathcal{F}_1\left(x,\frac{\sin(\theta)p_\perp}{\sqrt{1+p_\perp^2}},v_\phi,-\cos(\theta)\right)-\mathcal{F}_1\left(x,-\frac{\sin(\theta)p_\perp}{\sqrt{1+p_\perp^2}},v_\phi,-\cos(\theta)\right)\right]_{\sinh^{-1}\left(\frac{p_d-p_\parallel}{\sqrt{1+p_\perp{}^2}}\right)}^{\sinh^{-1}\left(\frac{p_d+p_\parallel}{\sqrt{1+p_\perp{}^2}}\right)}. \tag{1.90}$$

The tensorial elements of $\mathcal{C}_{\alpha\beta}$ verify:

$$\begin{aligned}\mathcal{C}_{xx} =& \frac{\sqrt{1+(p_d-p_\parallel)^2}}{4p_\parallel p_\perp}\left[\mathcal{F}_2\left(x,-\cos(\theta)\frac{p_d-p_\parallel}{\sqrt{1+(p_d-p_\parallel)^2}},v_\phi,-\sin(\theta)\right)\right]_{-\sinh^{-1}\left(\frac{p_\perp}{\sqrt{1+(p_d-p_\parallel)^2}}\right)}^{\sinh^{-1}\left(\frac{p_\perp}{\sqrt{1+(p_d-p_\parallel)^2}}\right)}\\ &-\frac{\sqrt{1+(p_d+p_\parallel)^2}}{4p_\parallel p_\perp}\left[\mathcal{F}_2\left(x,-\cos(\theta)\frac{p_d+p_\parallel}{\sqrt{1+(p_d+p_\parallel)^2}},v_\phi,-\sin(\theta)\right)\right]_{-\sinh^{-1}\left(\frac{p_\perp}{\sqrt{1+(p_d+p_\parallel)^2}}\right)}^{\sinh^{-1}\left(\frac{p_\perp}{\sqrt{1+(p_d+p_\parallel)^2}}\right)},\end{aligned} \tag{1.91}$$

$$\mathcal{C}_{yy} = \frac{(p_d - p_\parallel)^2}{4p_\parallel p_\perp \sqrt{1+(p_d-p_\parallel)^2}} \left[\mathcal{F}_0 \left(x, -\cos(\theta)\frac{p_d-p_\parallel}{\sqrt{1+(p_d-p_\parallel)^2}}, v_\phi, -\sin(\theta) \right) \right]_{-\sinh^{-1}\left(\frac{p_\perp}{\sqrt{1+(p_d-p_\parallel)^2}}\right)}^{\sinh^{-1}\left(\frac{p_\perp}{\sqrt{1+(p_d-p_\parallel)^2}}\right)}$$
$$- \frac{(p_d + p_\parallel)^2}{4p_\parallel p_\perp \sqrt{1+(p_d+p_\parallel)^2}} \left[\mathcal{F}_0 \left(x, -\cos(\theta)\frac{p_d+p_\parallel}{\sqrt{1+(p_d+p_\parallel)^2}}, v_\phi, -\sin(\theta) \right) \right]_{-\sinh^{-1}\left(\frac{p_\perp}{\sqrt{1+(p_d+p_\parallel)^2}}\right)}^{\sinh^{-1}\left(\frac{p_\perp}{\sqrt{1+(p_d+p_\parallel)^2}}\right)} , \tag{1.92}$$

$$\mathcal{C}_{xy} = \frac{p - p_\parallel}{4p_\parallel p_\perp} \left[\mathcal{F}_1 \left(x, -\cos(\theta)\frac{p_d-p_\parallel}{\sqrt{1+(p-p_\parallel)^2}}, v_\phi, -\sin(\theta) \right) \right]_{-\sinh^{-1}\left(\frac{p_\perp}{\sqrt{1+(p-p_\parallel)^2}}\right)}^{\sinh^{-1}\left(\frac{p_\perp}{\sqrt{1+(p-p_\parallel)^2}}\right)}$$
$$- \frac{p + p_\parallel}{4p_\parallel p_\perp} \left[\mathcal{F}_1 \left(x, -\cos(\theta)\frac{p+p_\parallel}{\sqrt{1+(p_d+p_\parallel)^2}}, v_\phi, -\sin(\theta) \right) \right]_{-\sinh^{-1}\left(\frac{p_\perp}{\sqrt{1+(p_d+p_\parallel)^2}}\right)}^{\sinh^{-1}\left(\frac{p_\perp}{\sqrt{1+(p_d+p_\parallel)^2}}\right)} . \tag{1.93}$$

The function $\mathcal{F}_n$ are defined as

$$\mathcal{F}_n(\cdot, a, b, c) = \int \frac{\sinh^n}{a + b\cosh^n + c\sinh^n} \tag{1.94}$$

For $n = (0, 1, 2)$, we get

$$\mathcal{F}_0(x, a, b, c) = \frac{2}{\sqrt{b^2 - a^2 - c^2}} \tan^{-1}\left[\frac{(b-a)\tanh\frac{x}{2} + c}{\sqrt{b^2 - a^2 - c^2}} \right] , \tag{1.95}$$

$$\mathcal{F}_1(x, a, b, c) = \frac{2ac}{(c^2 - b^2)\sqrt{b^2 - a^2 - c^2}} \tan^{-1}\left[\frac{(a-b)\tanh\frac{x}{2} - c}{\sqrt{b^2 - a^2 - c^2}} \right]$$
$$+ \frac{cx}{c^2 - b^2} - \frac{b}{c^2 - b^2} \ln\left(a + b\cosh(x) + c\sinh(x)\right) , \tag{1.96}$$

$$\mathcal{F}_2(x, a, b, c) = -2\frac{a^2(b^2 + c^2) - b^2(b^2 - c^2)}{(c^2 - b^2)^2\sqrt{b^2 - a^2 - c^2}} \tan^{-1}\left[\frac{(a-b)\tanh\frac{x}{2} - c}{\sqrt{b^2 - a^2 - c^2}} \right]$$
$$- \frac{a(b^2 + c^2)x}{(c^2 - b^2)^2} + \frac{b\sinh(x) - c\cosh(x)}{c^2 - b^2} + \frac{2abc}{(c^2 - b^2)^2} \ln\left(a + b\cosh(x) + c\sinh(x)\right) . \tag{1.97}$$

These formulae being fully analytical, the numerical computations of the corresponding susceptibility tensors can be very fast. Hence, this allows the use of a large number of waterbags for an accurate fit of any distribution functions. This is the basis of the multi-waterbag model presented in Sec. 1.4.3.

1.4.2 Branch cuts

The functions $\mathcal{F}_0(x,a,b,c)$, $\mathcal{F}_1(x,a,b,c)$ and $\mathcal{F}_2(x,a,b,c)$ of Eqs. (1.95), (1.96) and (1.97) are multivaluated for the complex phase speed $v_\phi = b$. The logarithmic term can be recast as

$$\ln(a + v_\phi \cosh(x) \pm c \sinh(x)) = \ln(|a + v_\phi \cosh(x) \pm c \sinh(x)|) + i\theta_{a+v_\phi \cosh(x) \pm c \sinh(x)} \,. \quad (1.98)$$

We will set the complex phase of $v_\phi \pm \sqrt{a^2 + c^2}$ and $a + v_\phi \cosh(x) \pm c \sinh(x)$ in the interval $[-\pi, \pi]$.

1.4.3 Multi-waterbag decomposition

Principle

The computation of Eqs. (1.16), (1.17) and (1.18) can be performed with over 10000 waterbags (Eqs. (1.84)-(1.93)) in only a few seconds by means of a standard mathematical software (Matlab). This enables to solve the dispersion relation of any relativistic distribution function approximated to a good accuracy as a sum of waterbags.

We have employed a very simple fitting technique which proceeds along two steps. The first step consists in determining the locus of the distribution function in the momentum space of interest. We introduce the maximum value of the distribution function, $f_{\max}$, and the number of decades, N_d, of the given distribution function $f^{(0)}$ we want to capture. Hence, we will only consider the part of $f^{(0)}$ verifying $f^{(0)} \in [10^{-N_d} f_{\max}, f_{\max}]$. We will decompose this interval in N_f mesh-points, resulting in N_f loci of $f^{(0)}$. These loci thus verify $f^{(0)}(p_x, p_y) = f_{\max} 10^{-kN_d/N_f}$ for a natural number $1 \leq k \leq N_f$. They are easily determined via a contour plot in a finely discretized portion of the momentum plane as illustrated in Fig. 1.6(a,b).

In a second step, we discretize these loci in N_x different waterbags. For that purpose we introduced $\Delta p_{x,k}$, the x-momentum width of the kth locus on the x-axis and l, a natural number verifying $0 \leq l < N_x$. For each locus $p_{y,k}(p_x)$, we obtain N_x different waterbags with mean momentum $p_{d,k,l} = (l + 0.5)\Delta p_{x,k}/N_x$, momentum spreads $p_{\parallel,k,l} = \Delta p_{x,k}/2N_x$ and $p_\perp = 2p_{y,k}(p_{d,k,l})$, and statistical weight $f_k = f_{\max} 10^{-kN_d/N_f}(1 - 10^{-N_d/N_f})$. This step is depicted in Fig. 1.6(c) where the waterbags have been colored for the sake of clarity. This scheme finally results in the superposition of $N_x N_f$ different waterbags characterized by their mean momentum, momentum spreads and statistical weight as illustrated by Fig. 1.6(d). The final normalized and approximated distribution function, f_{MW}, is given by:

$$f_{\mathrm{MW}} = \sum_{l=1}^{N_x} \sum_{k=1}^{N_f} \frac{f_k - f_{k-1}}{p_{\perp,k,l} p_{\parallel,k,l}} H(p_{\parallel,k,l} - |p_x - p_{d,k,l}|) H(p_{\perp,k,l} - |p_y|) \,, \quad (1.99)$$

with $f_{k=0} = 0$.

The distribution f_{MW} depends on three natural numbers N_x, N_f and N_d. The two first parameters determine the resolution of, respectively, the p_x-axis and the distribution function level. The third one is the number of distribution decades we want to approximate.

Applicability of the scheme

Because of its simplicity, our fitting scheme is robust and can be applied to a large variety of distributions, provided they are even function of p_y as imposed by the model-Waterbag function [Eq. (1.81)]. Moreover, this algorithm is based on the assumption that the loci of the distribution function are close to ellipses centered on the x-axis. Yet the distribution functions taken from PIC simulations usually show elliptic loci only over the finely resolved part of the momentum space. The resolution of the thermal tail of the particle distribution function is usually noisy and highly

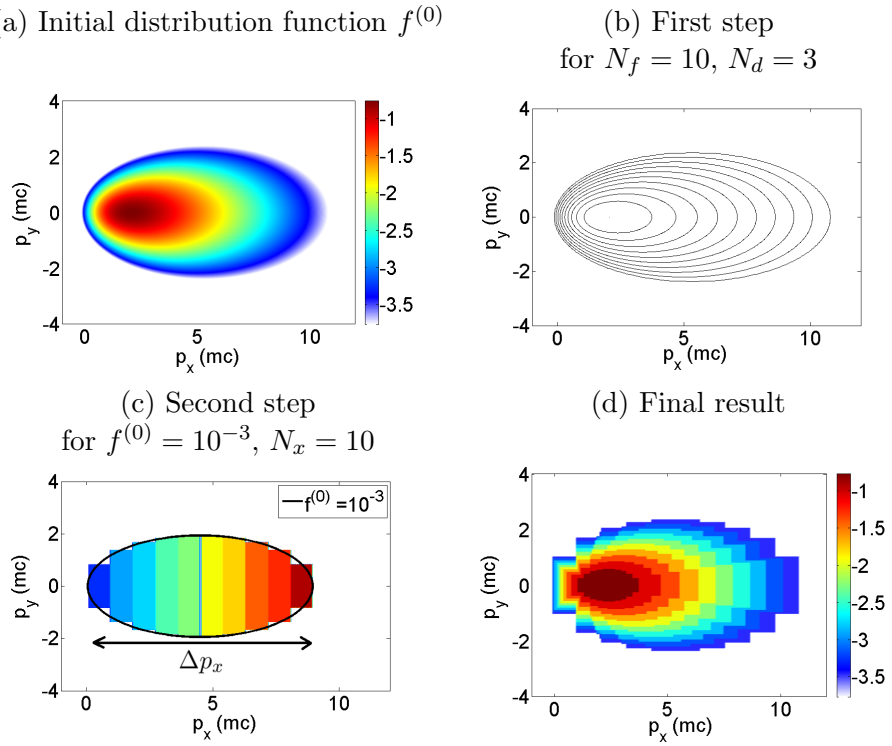

Figure 1.6. (a) Logarithmic-scale colormap of a 3D Maxwell-Jüttner distribution function of Eq. (1.22) with $\mu = 10$ and $\beta_d = 0.9$ at $p_z = 0$. (b) Result of the first step of the multi-waterbag decomposition of $f^{(0)}$ with $N_f = 10$, $N_d = 3$. (c) Taking the locus $f^{(0)}(\mathbf{p}) = 10^{-3}$ of (b), the second step of the multi-waterbag decomposition for $N_x = 10$ gives the colored waterbags. (d) Logarithmic-scale colormap of the multi-waterbag decomposition of (a) with $N_x = 10$, $N_f = 10$ and $N_d = 3$.

sensitive to the number of macroparticles in the simulation. This observation has motivated us to introduce the number of decades N_d, over which the fitting scheme is applied. One has to make sure that the N_d first decades of the distribution are well resolved by the macroparticles. In this thesis, we have typically used $N_d = 2 - 3$ for a distribution function calculated over $\sim 10^5$ macroparticles.

Multi-waterbag decomposition applied to the filamentation instability

We will now apply the multi-waterbag decomposition to the numerical resolution of the growth rate of the Weibel-filamentation instability. The dispersion relation of the latter is given by Eq. (1.21) with $\theta = \pi/2$.

Let us first consider the case of two symmetric electron beams described by 2D bi-Maxwellians [Eq. (1.65)] with $\beta_d = \pm 0.2$ and $T_x = T_y = 5.11$ keV. The solid red curve of Fig. 1.7(a) plots the exact growth rate obtained by the generalized Fried & Gould method (Sec. 1.1.2). This growth rate is compared with that obtained from the decomposition of the bi-Maxwellian distribution into 100, 400, 900 and 2500 waterbags (in blue lines). The 100-waterbag curve captures the low-k part of the curve but not its peak value nor its decreasing high-k side. As expected, the exact growth rate is reproduced to within an accuracy increasing with the waterbag resolution. Figure 1.7(a) shows that a resolution of ~ 1000 waterbags is enough to reproduce satisfactorily both the maximum and the high-k tail of the growth rate. This evidences the validity of the multi-waterbag decomposition scheme.

As a second example, let us address the case of two 3D Maxwell-Jüttner distributed electron beams with $\beta_d = \pm 0.9$ and $T = m_e c^2/100$. The exact growth rate is displayed in Fig. 1.7(b)

(a) $\beta_d = 0.2$, $T = m_e c^2/100$ (b)$\beta_d = 0.9$, $T = m_e c^2/100$

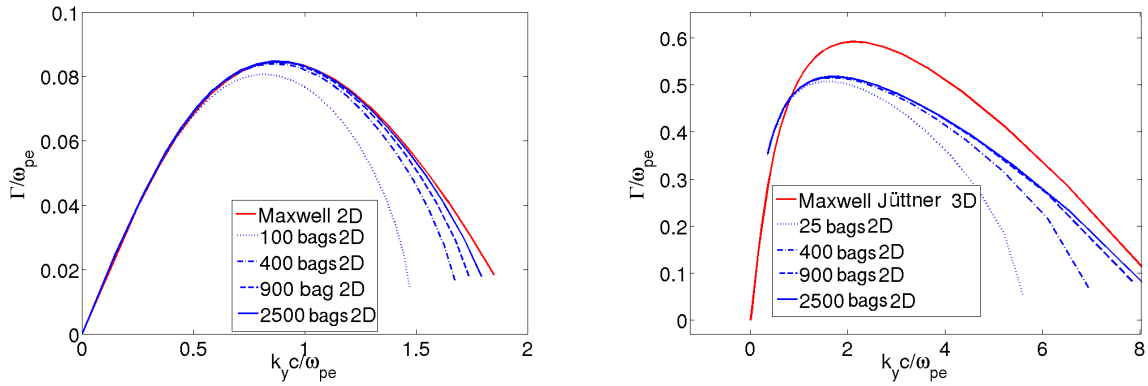

Figure 1.7. Filamentation growth rate solved using the scheme of Sec. 1.1.2. (a) Non-relativistic 2D counter-streaming bi-Maxwellian filamentation plasma with $\beta_d = \pm 0.2$ and $T = m_e c^2/100$ (red line) compared to 2D (normalized) multi-waterbag decomposition. (b) Comparison between 3D Maxwell-Jüttner for $\beta_d = 0.9$, $T = m_e c^2/10$ and 2D (normalized) multi-waterbag decomposition.

as a solid red line. The blue lines plot the growth rates computed from multi-Waterbag fit of $f^{(0)}(p_x, p_y, p_z = 0)$ with varying accuracy. While these curves show convergence for $N_f > 1000$, a 15% discrepancy with the exact curve remains, owing to the reduced dimensionality of the fitting waterbags.

1.5 Summary

The resolution scheme of a non-relativistic electrostatic Maxwellian dispersion relation introduced by Fried and Gould in 1961 has been generalized. It can be applied to the fully electromagnetic dispersion relation in the entire k-space. Moreover, it can be applied to any gyrotropic distribution function, provided the system has a symmetry axis. We have gathered in this chapter, the dielectric tensors associated with the Maxwell-Jüttner, the bi-Maxwellian and Waterbag distribution functions. Also, we have proposed a multi-waterbag fitting technique for handling arbitrary-shaped distributions. These schemes represent powerful tools for solving the linear dispersion relation of any field free equilibrium system as will be shown in the next chapters.

Chapter 2

Electromagnetic fluctuations and normal modes of a drifting relativistic plasma

(a) Theoretical spectrum (b) Simulated spectrum

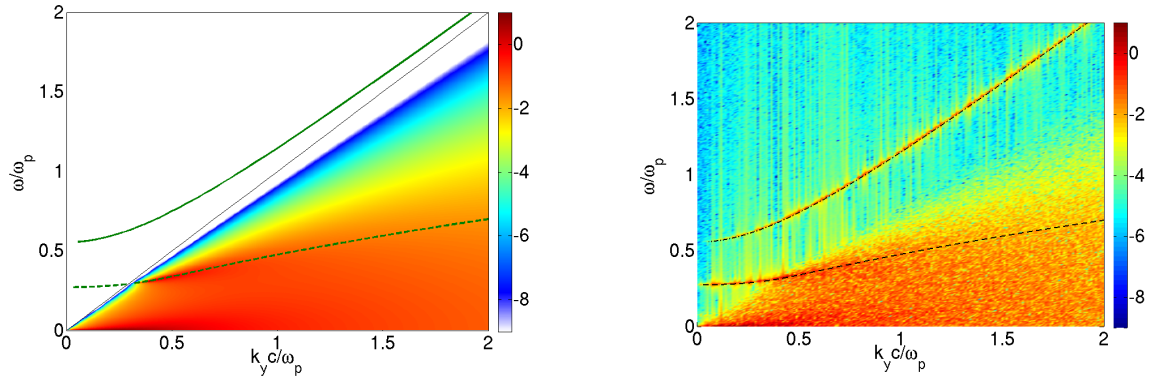

Figure 2.1. (a) Theoretical and (b) simulated (k_y, ω) thermal magnetic fluctuation spectrum in $\log_{10}$ scale for a Maxwell-Jüttner- distributed electron beam ($T = 51.1$keV and $\beta_d = 0.9$) with $\mathbf{k} \perp \boldsymbol{\beta}_d$.

This chapter addresses the relativistic equilibrium of a plasma. A neutral plasma slab of infinite size (or a lot bigger than its skin-depth) has a field-free equilibrium. This means that the locally averaged values of $\mathbf{E}$ et $\mathbf{B}$ are equal to zero. However, the locally averaged electromagnetic energy ($\mathbf{E}^2$ and $\mathbf{B}^2$) is not equal to zero due to the field fluctuations induced by the finite number of particles. In this chapter, we will study the spectrum of this energy for a relativistic equilibrium plasma and will then focus on its influence on the development of the Weibel instability.

2.1 Introduction

An equilibrium, or near-equilibrium, plasma sustains a finite level of electromagnetic energy due to the random motion of particles combined with the collective behavior of the plasma. These spontaneous electromagnetic fluctuations play a major role in plasma physics since they act as seeds for the instabilities driven by an input of free energy. Since Rostoker and Rosenbluth's pioneering dressed-particle theory (Rostoker & Rosenbluth 1960), the fluctuation spectrum of a thermal plasma has been analyzed within several frameworks in many papers and textbooks (Akhiezer *et al.* 1975; Sitenko 1982; Klimontovich 1982; Ichimaru 1992; Tajima & Cable 1992; Lund *et al.* 1995; Opher & Opher 1996; Yoon 2007; Tautz & Schlickeiser 2007). However, except for a few works restricted to isotropic particle distributions or electrostatic modes (Lerche 1968a; Stewart 1973; Klimontovich 1982), all these studies were carried out in the nonrelativistic regime, and thus did not address the spectrum induced by a plasma beam of relativistic temperature and mean drift velocity. Such a configuration is of particular interest for the modeling of relativistic beam-plasma instabilities (Bret *et al.* 2010b; Cottrill *et al.* 2008) and the related generation of collisionless shocks (Lyubarsky & Eichler 2006; Spitkovsky 2008a; Lemoine & Pelletier 2011; Bret *et al.* 2013). Schlikeiser, Lazar, Yoon and Felten (Schlickeiser & Yoon 2012; Lazar *et al.* 2012; Felten *et al.* 2013) recently worked out a general fluctuation theory valid for unstable relativistic plasmas; yet they performed applied calculations in the nonrelativistic limit only.

The objective of this chapter is to present exact analytical and numerical calculations of the fluctuation spectra associated to drifting relativistic plasmas described by a Maxwell-Jüttner distribution function (Wright & Hadley 1975; Bret *et al.* 2010a). We will consider electromagnetic fluctuations propagating along or normal to the mean plasma velocity with different polarizations. In each case, we will compute both the (ω, k)- and k-resolved spectra. To this goal, we will distinguish between the contributions of the damped subluminal and undamped supraluminal normal modes. The latter will be computed from the electromagnetic dispersion relation by generalizing the numerical scheme originally proposed by Fried and Gould (Fried & Gould 1961) in the nonrelativistic electrostatic regime (Sec. 1.1.2). With a view on the Weibel-like filamentation instability of a relativistic plasma (Yoon 2005; Achterberg & Wiersma 2007), we will evaluate the spectrum of magnetic modes with wave vectors normal to the plasma drift velocity. The obtained formulae will be used to estimate the saturation time of the relativistic Weibel-filamentation instability triggered by two symmetric overlapping electron-positron beams.

This chapter is organized as follows. In Sec. 2.2, we recall the formalism of the standard fluctuation theory and adapt it to Maxwell-Jüttner distributions. The spectrum of longitudinal and transverse electric fluctuations propagating along the plasma drift velocity is treated in Sec. 2.3, whereas the spectrum of magnetic fluctuations propagating normal to the plasma drift velocity is computed in Sec. 2.4. Section 2.5 confronts our theoretical results to particle-in-cell (PIC CALDER) simulations. We will then use our analytical formulae to evaluate the saturation time of the Weibel filamentation instability in counter-streaming pair plasmas. Good agreement will be obtained between our estimates and PIC simulation results (Bret *et al.* 2013). Finally, our results are summarized in Sec. 2.7.

2.2 Electromagnetic fluctuation theory

2.2.1 General formalism

Let us consider a uniform relativistic plasma composed of a number of charged particle species of mass m_s, charge q_s and density n_s. According to Refs. (Sitenko 1982; Ichimaru 1992), assuming an adiabatic switch-on of the electromagnetic interactions, the spectral density tensor of the plasma

electric fluctuations writes

$$\langle \mathbf{E}\mathbf{E}^\dagger \rangle_{\mathbf{k},\omega} = \mathbf{Z}_{\mathbf{k},\omega} \cdot \langle \mathbf{j}\mathbf{j}^\dagger \rangle_{\mathbf{k},\omega} \cdot \mathbf{Z}^\dagger_{\mathbf{k},\omega} \,, \tag{2.1}$$

where the fluctuation source $\langle \mathbf{j}\mathbf{j}^\dagger \rangle_{\mathbf{k},\omega}$ is the spectral density tensor of the ballistic plasma current density

$$\langle j_\alpha j^*_\beta \rangle_{\mathbf{k},\omega} = 2\pi\epsilon_0 \sum_s m_s \omega_{ps}^2 \int_{\mathbb{R}^3} d^3p \, v_\alpha v_\beta f_s^{(0)}(\mathbf{p}) \delta(\omega - \mathbf{k}\cdot\mathbf{v}) \,, \tag{2.2}$$

with $f_s^{(0)}(\mathbf{p})$ the equilibrium distribution function and $\omega_{ps}^2 = n_s q_s^2 / m_s \epsilon_0$ the plasma frequency of the sth species. The tensor $\mathbf{Z}_{\mathbf{k},\omega}$ is defined from the linear relation

$$\mathbf{E}_{\mathbf{k},\omega} = \mathbf{Z}_{\mathbf{k},\omega} \cdot \mathbf{j}_{\mathbf{k},\omega} \,. \tag{2.3}$$

The derivation of the above formulae is detailed in Appendix 6.2.

For a plasma described by gyrotropic equilibrium distribution functions, $f_s^{(0)}(p_\perp^2, p_x)$, the wave vector of the fluctuations can be chosen in the (k_x, k_y) plane without loss of generality. The tensor $\mathbf{Z}_{\mathbf{k},\omega}$ then reads

$$\mathbf{Z}_{\mathbf{k},\omega} = -i\frac{\omega}{\epsilon_0} \begin{pmatrix} \dfrac{1}{\omega^2\epsilon_{zz} - k^2c^2} & 0 & 0 \\ \dfrac{\omega^2\epsilon_{xx} - k_y^2c^2}{D} & -\dfrac{\omega^2\epsilon_{xy} + k_yk_xc^2}{D} & 0 \\ -\dfrac{\omega^2\epsilon_{xy} + k_yk_xc^2}{D} & \dfrac{\omega^2\epsilon_{yy} - k_x^2c^2}{D} & 0 \\ 0 & 0 & \dfrac{1}{\omega^2\epsilon_{zz} - k^2c^2} \end{pmatrix} . \tag{2.4}$$

We have introduced D and the dielectric tensor elements (Ichimaru 1973) detailed in Sec. 1.1.1:

$$\boldsymbol{\epsilon}_{\alpha\beta}(\mathbf{k},\omega) = \delta_{\alpha\beta} + \sum_s \frac{\omega_{ps}^2}{\omega^2} \iiint d^3p \, \frac{p_\alpha}{\gamma} \frac{\partial f_s^{(0)}}{\partial p_\beta} + \sum_s \frac{\omega_{ps}^2}{\omega^2} \iiint d^3p \, v_\alpha \frac{p_\beta}{\gamma} \frac{\mathbf{k}\cdot\partial f_s^{(0)}/\partial \mathbf{p}}{\omega - \mathbf{k}\cdot\mathbf{v}} \,. \tag{2.5}$$

The equation $|\mathbf{Z}_{\mathbf{k},\omega}| = 0$ defines the dispersion relation of the discrete normal modes of the system $\omega_l(\mathbf{k})$:

$$\omega^2\epsilon_{zz} - k^2c^2 = 0 \,, \tag{2.6}$$

$$D = (\omega^2\epsilon_{xx} - k_y^2c^2)(\omega^2\epsilon_{yy} - k_x^2c^2) - (\omega^2\epsilon_{xy} + k_yk_xc^2)^2 = 0 \,. \tag{2.7}$$

2.2.2 Maxwell-Jüttner distribution functions

From now on, the particle species are assumed to obey drifting Maxwell-Jüttner distribution functions (Wright & Hadley 1975) (1.22):

$$f_s^{(0)}(\mathbf{p}) = F_s \exp\left[-\mu_s(\gamma - \beta_{ds}p_x)\right] , \tag{2.8}$$

where $\gamma = \sqrt{1 + p^2/(m_sc)^2}$ is the relativistic factor, $\mu_s = m_sc^2/T_s$ the normalized inverse temperature and $\beta_{ds} = \langle v_x/c \rangle$ the x-aligned mean velocity. We have introduced the normalization factor $F_s = \mu_s / 4\pi(m_sc)^3\gamma_{ds}^2 K_2(\mu_s/\gamma_{ds})$, with $\gamma_{ds} = (1-\beta_{ds}^2)^{-1/2}$ and K_2 the modified Bessel function of the second kind. The distribution functions are normalized to unity: $\int f_s^{(0)}(\mathbf{p}) d^3p = 1$. Charge and current neutralization is assumed so as to ensure a field-free equilibrium.

Let us introduce θ, the angle between the wave vector $\mathbf{k}$ and the x-axis, and $\beta_\phi = \omega/kc$, the normalized wave phase velocity. By changing to velocity variables in cylindrical coordinates along

$\mathbf{k}$, the triple integrals involved in the dielectric tensor gathered in the Chapter 1 can be reduced to the following one-dimensional quadratures (Bret *et al.* 2010b)

Making use of the above definitions, the source tensor (2.2) simplifies to

$$\langle \mathbf{jj}^\dagger_{zz} \rangle_{\mathbf{k},\omega} = (2\pi)^2 \epsilon_0 H(1-|\beta_\phi|) \sum_s \frac{F_s m_s \omega_{ps}^2}{k} \left[f_{D_s} \right]_{\beta=\beta_\phi} , \tag{2.9}$$

$$\langle \mathbf{jj}^\dagger_{yy} \rangle_{\mathbf{k},\omega} = (2\pi)^2 \epsilon_0 H(1-|\beta_\phi|) \sum_s \frac{F_s m_s \omega_{ps}^2}{k} \left[f_{A_s} \cos^2\theta + f_{B_s} \sin^2\theta + 2 f_{C_s} \cos\theta \sin\theta \right]_{\beta=\beta_\phi} , \tag{2.10}$$

$$\langle \mathbf{jj}^\dagger_{xx} \rangle_{\mathbf{k},\omega} = (2\pi)^2 \epsilon_0 H(1-|\beta_\phi|) \sum_s \frac{m_s F_s \omega_{ps}^2}{k} \left[f_{A_s} \sin^2\theta + f_{B_s} \cos^2\theta - 2 f_{C_s} \cos\theta \sin\theta \right]_{\beta=\beta_\phi} , \tag{2.11}$$

$$\langle \mathbf{jj}^\dagger_{yx} \rangle_{\mathbf{k},\omega} = (2\pi)^2 \epsilon_0 H(1-|\beta_\phi|) \sum_s \frac{m_s F_s \omega_{ps}^2}{k} \left[(f_{B_s} - f_{A_s}) \cos\theta \sin\theta + f_{C_s} (\cos^2\theta - \sin^2\theta) \right]_{\beta=\beta_\phi} , \tag{2.12}$$

where $H(x)$ denotes the step function. The derivation of Eqs. (2.9), (2.10), (2.11) and (2.12) uses the three calculation steps detailed in Chapter 1.

In the following, we will compute the (ω, k)-resolved spectra of the longitudinal and transverse fluctuations propagating along the beam direction ($\theta = 0$), and of the magnetic fluctuations propagating normal to the beam direction ($\theta = \pi/2$).

2.3 Fluctuations with wave vectors parallel to the plasma drift velocity

2.3.1 Longitudinal fluctuations

Basic formulae

Here, we consider electrostatic fluctuations with $\mathbf{E} \parallel \mathbf{k}$ and $\mathbf{k} \parallel \mathbf{x}$. Combining Eqs. (2.1) and (2.4) yields

$$\langle E_x E_x^* \rangle_{k_x,\omega} = \frac{\langle j_x j_x^* \rangle_{k_x,\omega}}{\epsilon_0^2 \omega^2 |\epsilon_{xx}|^2} , \tag{2.13}$$

For $\theta = 0$, the xx component of Eq. (2.5) can then be recast as

$$\begin{aligned} \epsilon_{xx} = 1 &+ \sum_s \frac{\omega_{ps}^2}{\omega^2} v_\phi \iiint d^3p \frac{\beta_x - \beta_\phi}{\beta_\phi - \beta_x} \partial_{p_\tau} f_s^{(0)} \\ &+ \sum_s \frac{\omega_{ps}^2}{\omega^2} \beta_\phi^2 \iiint d^3p \frac{1}{\beta_\phi - \beta_x} \partial_x f_s^{(0)} . \end{aligned} \tag{2.14}$$

The first integral in Eq. (2.14) being odd and of the Cauchy type, its contribution vanishes. Moreover, Eq. (1.22) leads to

$$\partial_{p_\tau} f_s^{(0)} = -\mu_s (\beta_\tau - \beta_{ds\tau}) f_s^{(0)} . \tag{2.15}$$

Combining the above equations yields

$$\epsilon_{xx} = 1 + \sum_s \frac{\omega_{ps}^2 \mu_s}{k_x^2 c^2} - \sum_s \frac{\omega_{ps}^2 \mu_s}{k_x^2 c^2} (\beta_\phi - \beta_{ds}) \iiint d^3p \frac{f_s^{(0)}}{\beta_\phi - \beta_x} . \tag{2.16}$$

This triple integral can be reduced to a much more tractable one-dimensional quadrature by changing to velocity variables in cylindrical coordinates along the wave vector $\mathbf{v} = (v_\perp \cos(\theta), v_\perp \sin(\theta), v_\parallel)$:

$$\epsilon_{xx} = 1 - \sum_s \frac{\omega_{ps}^2 \mu_s}{k_x^2 c^2} (\beta_\phi - \beta_{ds}) \tilde{B}(\beta_\phi) \,, \tag{2.17}$$

with

$$\tilde{B}(\beta_\phi) = \int d\beta \frac{f_{\tilde{B}}}{v_\phi - v_x} \,, \tag{2.18}$$

$$f_{\tilde{B}} = \frac{\gamma^3 e^{-h_s}}{h_s^5} \left[(h_s + 1)(2\rho_s^2 + \nu_s^2) + \rho_s^2 h_s^2 \right] , \tag{2.19}$$

$$h_s(\theta = 0) = \mu_s \gamma (1 - \beta_{ds} \beta) \,. \tag{2.20}$$

Upon defining the susceptibilities χ_s from the standard relation $\epsilon_{xx} = 1 + \sum_s \chi_s$, and noting that $\langle j_z j_z^* \rangle_s$ is proportional to the singularity of the quadrature B_s, the electric fluctuation spectrum can be further simplified as

$$\langle E_x E_x^* \rangle_{k_x,\omega} = \frac{1}{\epsilon_0 |\epsilon_{xx}|^2} \sum_s \frac{T_s \Im(\chi_s)}{\omega - k_x v_{ds}} \,, \tag{2.21}$$

This expression generalizes the fluctuation-dissipation theorem (Akhiezer *et al.* 1975) to the case of multiple Maxwell-Jüttner-distributed particle species of various drift velocities and temperatures. Note that it is formally identical to the formula derived for nonrelativistic drifting Maxwellians by Lund *et al.* (1995).

Dispersion relation

The fluctuation spectrum [Eq. (2.21)] is strongly peaked around the weakly-damped and undamped solutions of $\epsilon_{xx}(\omega, k_x) = 0$. Because it implicitly assumes unbounded particle velocities, the standard nonrelativistic kinetic description of a stable plasma wrongly predicts that all of its eigenmodes are Landau-damped, whatever their phase velocity. Now, it can be proved from a more rigorous relativistic description that only the subluminal modes (with $\omega/k_x < c$) are damped (Lerche 1969; Schlickeiser 2004). For the sake of numerical convenience, we recast the dispersion relation in the form

$$k_x^2 c^2 = \sum_s 2\pi F_s \mu_s \omega_{ps}^2 (\beta_\phi - \beta_{ds}) \tilde{B}_s(\beta_\phi) - \sum_s \mu_s \omega_{ps}^2 = \mathcal{G}(\beta_\phi) \,. \tag{2.22}$$

This formulation, in which $k_x^2 (> 0)$ is a function of β_ϕ only, lends itself to the efficient numerical scheme introduced by Fried and Gould (Fried & Gould 1961) in a nonrelativistic framework. This scheme is detailed in Chapter 1 and consists, first, in determining the locus of the zeroes of $\Im\mathcal{G}(\beta_\phi)$. This can be readily performed by means of a contour plot in a finely discretized portion of the complex β_ϕ plane. Then, we retain these zeroes fulfilling $\Re\mathcal{G}(\beta_\phi) > 0$ and identify $k_x = \sqrt{\Re\mathcal{G}(\beta_\phi)}$. Depending on the β_ϕ domain considered, this method allows us to simultaneously solve for a set of discrete electrostatic solutions $\omega_L(k_x)$.

As shown in Refs. (Lerche 1969; Laing & Diver 2006) for an isotropic plasma ($\beta_{ds} = 0$), the supraluminal electrostatic modes exist only over a finite interval $0 \leq k_x \leq k_{c\pm}$ (for a positive wavenumber), where the critical value $k_{c\pm}$ depends on the sign of the phase velocity. In the general case, $k_{c\pm}$ can be obtained by setting $\beta_\phi = \pm 1$ in Eq. (2.22), yielding (McKee 1971; Laing & Diver

2006)

$$k_{c\pm}^2 = \sum_s (1 \pm \beta_{ds})^2 \gamma_{ds} \omega_{ps}^2 \frac{K_1(\frac{\mu_s}{\gamma_{ds}}) + 2\frac{\gamma_{ds}}{\mu_s} K_0(\frac{\mu_s}{\gamma_{ds}})}{K_2(\frac{\mu_s}{\gamma_{ds}})} \,. \tag{2.23}$$

Consequently, for a fixed sign of the phase velocity, there is a maximum of one supraluminal longitudinal eigenmode (ω_{LS+} or ω_{LS-}).

(ω, k)-resolved spectrum

Figures 2.2(a-f) display the longitudinal fluctuation spectra of a pair plasma (or, equivalently, of an electron plasma with a neutralizing background) of various drift velocities and temperatures (assumed equal for all species). The main difference between these results and previously published nonrelativistic calculations Lund *et al.* (1995); Tautz & Schlickeiser (2007); Yoon (2007); Schlickeiser & Yoon (2012) is the cutoff occurring for supraluminal modes. Since the quadratures defined by Eq. (1.56) have no pole for $|\beta_\phi| > 1$, the dielectric tensor is purely real; hence, supraluminal modes cannot be excited by an inverse-Landau (Cerenkov) type mechanism. For a pair plasma, Eq. (2.21) is proportional to $\Im(\epsilon_{xx})/|\epsilon_{xx}|^2$. As shown in Ref. (Klimontovich 1982) this implies that $\langle E_x E_x^* \rangle_{k_x,\omega} \propto \delta(\epsilon_{xx})$ in the supraluminal region ($|\beta_\phi| > 1$). Consequently, the supraluminal part of the fluctuation spectra only results from the delta-like singularities (in the absence of collisions) associated to supraluminal eigenmodes, solution of Eq. (2.22).

As expected, the subluminal fluctuation spectra exhibit strong maxima along the weakly-damped part of the eigenmode curves. The latter (plotted as black dashed curves) intersect the $\beta_\phi = \pm 1$ lines at $k_x = k_{c\pm}$. The fluctuation maxima are all the sharper when the plasma temperature drops, being increasingly hard to capture numerically. In the isotropic, low-temperature case ($\mu = 100$) of Fig. 2.2(e), the well-known nonrelativistic Bohm-Gross mode $\omega = \omega_p(1 + 3k_x^2c^2/2\omega_p^2\mu)$ is found to closely match the exact eigenmode. In the isotropic, relativistically-hot case ($\mu = 1$), the fluctuation spectrum broadens away from the eigenmode curves, attaining comparable values over most of the subluminal cone for $k_x c/\omega_p < 1.6$.

The influence of a relativistic drift velocity ($\beta_d = 0.9$) is illustrated in Figs. 2.2(b,d,f). Both the spectra and the dominant eigenmodes turn asymmetric with respect to $\omega = 0$. The fluctuations peak close to the eigenmode, although only the slowest is visible on Figs. 2.2(b,d,f). In the low-temperature case ($\mu = 100$), one can approximate the real frequency of the exact eigenmodes by Lorentz transformation of the Bohm-Gross modes [Fig. 2.2(f)]. Consistently with Eq. (2.23), the supraluminal eigenmodes are found only for a limited range of wave vectors $k_x \in [-k_{c-}, k_{c+}]$ with $k_{c-} \neq k_{c+}$.

k-resolved spectrum

The spatial fluctuation spectrum is of interest both experimentally and theoretically. The integration of Eq. (2.21) over ω gives

$$\langle E_x E_x^* \rangle_{k_x} = -\frac{T}{\epsilon_0} \int_{-\infty}^{+\infty} \frac{d\omega}{2\pi} \frac{1}{(\omega - k_x v_d)} \Im\left(\frac{1}{\epsilon_{xx}}\right) \tag{2.24}$$

This integration can be carried out by the method introduced in Ref. (Langdon 1979) in the non-relativistic case. To this effect, let us rewrite Eq. (2.24) as

$$\langle E_x E_x^* \rangle_{k_x} = -\frac{1}{\epsilon_0} \int_{-\infty}^{+\infty} \frac{d\omega}{2\pi} \Im\left[\frac{T}{(\omega - k_x v_d)} \left(\frac{1}{\epsilon_{xx}} - 1\right)\right] = \Im \int_{-\infty}^{+\infty} \frac{d\omega}{2\pi} I(\omega, k_x) \,, \tag{2.25}$$

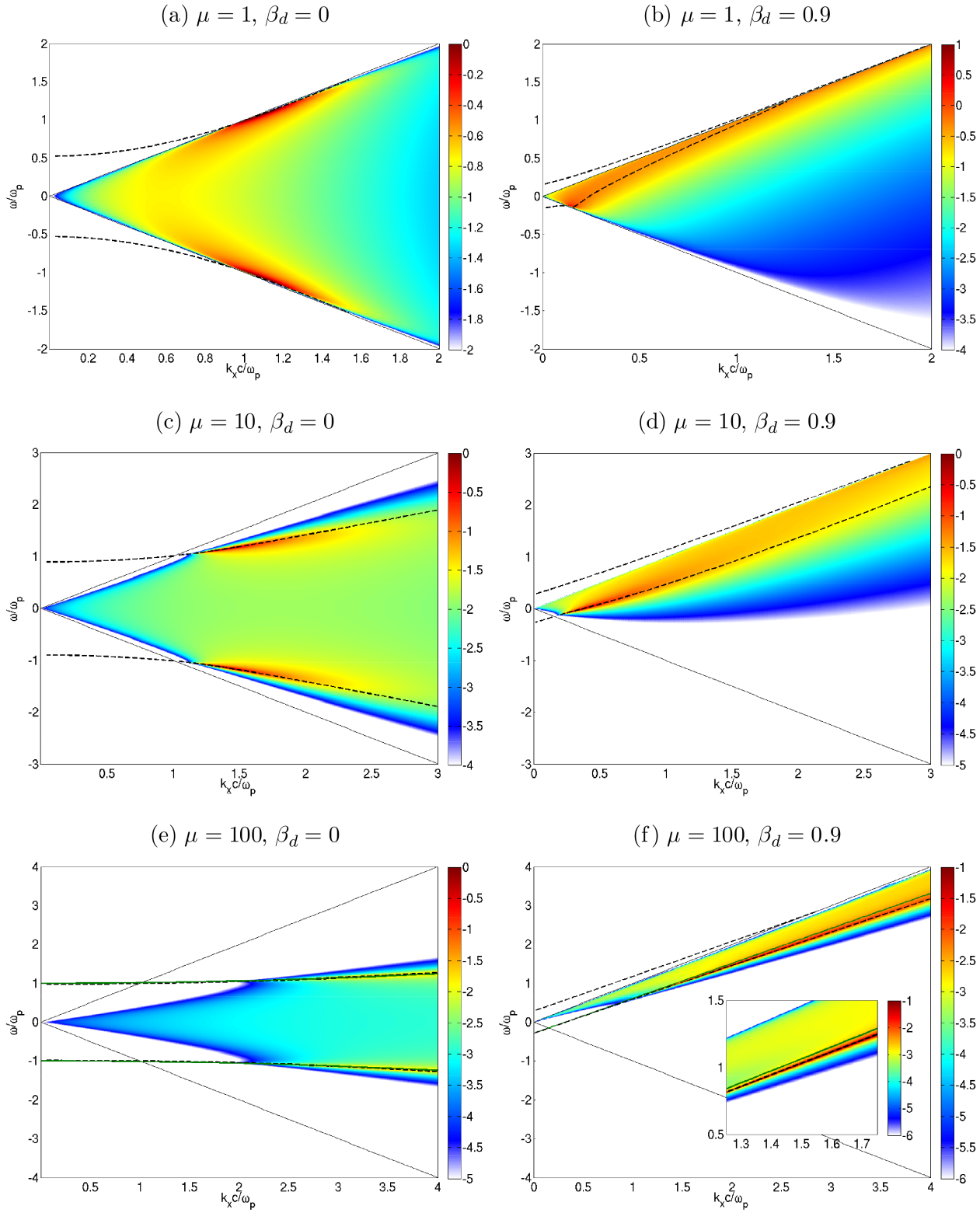

Figure 2.2. Power spectrum $\langle E_x E_x^* \rangle_{k_x,\omega}$ (normalized to $m_e^2 c^3/e^2$) in $\log_{10}$ scale for an $e^- e^+$ pair plasma and various μ and β_d values. The two black solid lines delimit the subluminal region ($|\beta_\phi| \leq 1$). The black dashed curves plot the exact eigenmodes computed from Eq. (2.22). In the low-temperature case ($\mu = 100$), the green solid line plots the Bohm-Gross mode in panel (e) and the Lorentz-transformed Bohm-Gross mode in panel (f).

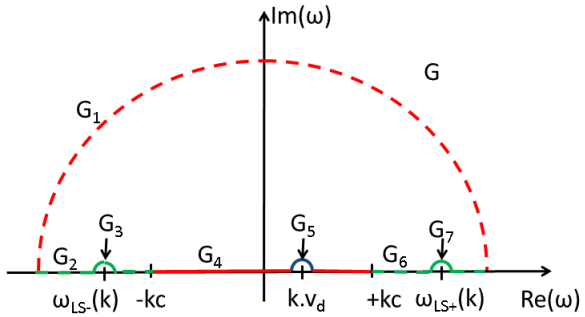

Figure 2.3. Closed contour $G = \cup_{i=1}^{7} G_i$ in the complex ω-plane used in Eq. (2.27). The arrows indicate the ballistic singularity $k\beta_d$ and the supraluminal eigenmodes $\omega_{LS\pm}(k)$.

where we have defined

$$I(\omega, k_x) = -\frac{T}{\epsilon_0(\omega - k_x v_d)}\left(\frac{1}{\epsilon_{xx}} - 1\right). \tag{2.26}$$

This function is analytic in the upper half ω-plane but has several singularities on the real ω-axis. The first one is due to the ballistic term $(\omega - k_x v_d)^{-1}$ and is located in the subluminal region $|\omega/k_x c| < 1$. The others correspond to the supraluminal (undamped) eigenmodes $\omega_{LS\pm}(k_x)$. There follows

$$\sum_{i=1}^{7} \Im \int_{G_i} d\omega I(\omega, k_x) = 0\,, \tag{2.27}$$

where the closed integration contour $G = \cup_{i=1}^{7} G_i$ is drawn in Fig. 2.3. Since $\lim_{|\omega|\to+\infty}\left(\epsilon_{xx}^{-1} - 1\right) = 0$ and $I \in \mathbb{R}$ for $|\omega/k_x c| > 1$, the integrals over the G_1, G_2 and G_6 contours vanish, yielding

$$\langle E_x E_x^* \rangle_{k_x}^{|\beta_\phi|<1} - \pi \sum_{\omega=\omega_{LS\pm}} \mathrm{Res}(I)_\omega = -\pi \mathrm{Res}(I)_{k_x v_d}\,. \tag{2.28}$$

To obtain Eq. (2.28), the G_4 term has been identified with the subluminal part of fluctuation spectrum, $\langle E_x E_x^* \rangle_{k_x}^{|\beta_\phi|<1}$, and the integrals over the semi-circle contours G_3, G_5 and G_7 have been evaluated using the residue theorem. The second term on the left hand side corresponds to the supraluminal fluctuation spectrum:

$$\langle E_x E_x^* \rangle_{k_x}^{|\beta_\phi|>1} = -\pi \sum_{\omega=\omega_{LS\pm}} \mathrm{Res}(I)_\omega = \sum_{\omega=\omega_{LS\pm}} \frac{T}{2\epsilon_0(\omega - k_x v_d)} \frac{1}{\partial\epsilon_{xx}/\partial\omega|_\omega}\,. \tag{2.29}$$

The total (subluminal and supraluminal) spatial fluctuation spectrum is therefore given by the ballistic singularities

$$\langle E_x E_x^* \rangle_{k_x} = \frac{T}{2\epsilon_0} \frac{\omega_p^2 \mu}{\omega_p^2 \mu + k_x^2 c^2}\,, \tag{2.30}$$

which generalizes the nonrelativistic result of Ref. (Langdon 1979).

As a test, we have numerically integrated Eq. (2.24) over the subluminal region $\omega \in [-k_{c-}c, k_{c+}c]$ and compared the results to the formula

$$\langle E_x E_x^* \rangle_{k_x}^{|\beta_\phi|<1} = \frac{T}{2\epsilon_0} \frac{\omega_p^2 \mu}{\omega_p^2 \mu + k_x^2 c^2} - \sum_{\omega=\omega_{LS\pm}} \frac{T}{2\epsilon_0(\omega - k_x v_d)} \frac{1}{\partial\epsilon_{xx}/\partial\omega|_\omega}\,. \tag{2.31}$$

where the supraluminal eigenmodes ω_{LS} are obtained from solving Eq. (2.22). Figure 2.4 shows

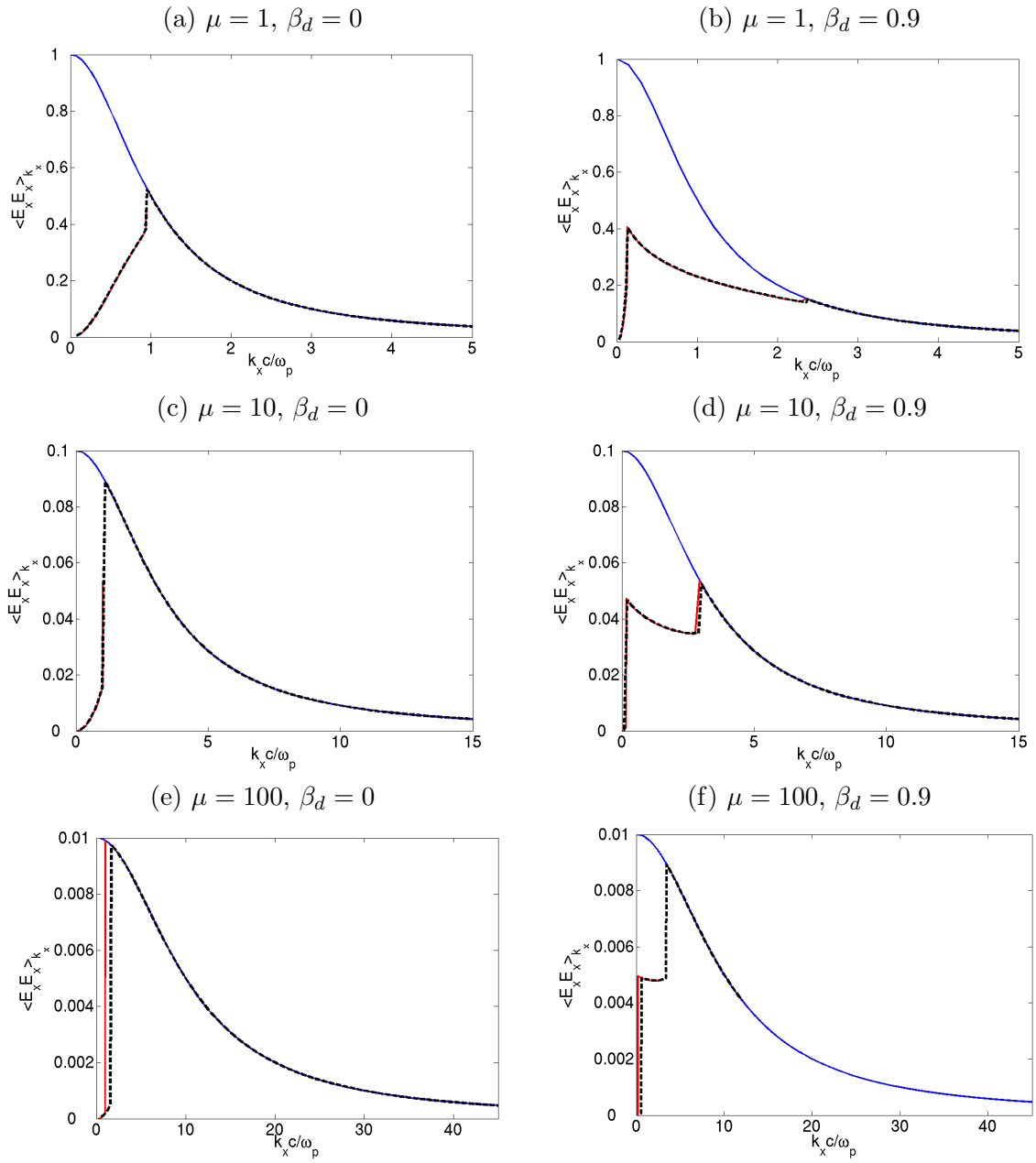

Figure 2.4. Spatial fluctuation spectra $\langle E_x E_x^* \rangle_{k_x}$ (normalized to $\frac{m_e^2 c^3}{e^2}(\sum_s \omega_{ps}^2)^{1/2}$) for an electron/pair plasma and various μ and β_d values (identical for all species). The blue and red lines correspond to the total and subluminal spectra computed from Eqs. (2.30) and (2.31), respectively. The black-dotted lines correspond to the numerical integration of Eq. (2.21) over the subluminal domain.

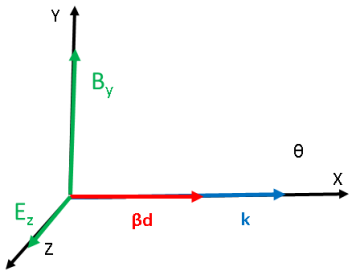

Figure 2.5. Frame of the system studied in Sec. 2.3.2.

excellent agreement between the numerical and theoretical spectra for $\mu = (1, 10, 100)$ and $\beta_d = (0, 0.9)$. The discontinuities seen in the subluminal spectra correspond to the supraluminal eigenmode cutoffs at $k_x = k_{c\pm}$. Both negative and positive-phase velocity supraluminal eigenmodes exist for $k_x < k_{c-} < k_{c+}$, whereas only the positive-phase velocity supraluminal eigenmode exists for $k_{c-} < k_x < k_{c+}$ and all eigenmodes are subluminal for $k_x > k_{c+}$. As a result, the total and subluminal spectra exactly coincide for $k_x > k_{c+}$. Note that these discontinuities are hard to capture numerically in the low-temperature regime ($\mu = 100$) due to the delta-like trace of the subluminal eigenmode for $|\beta_\phi| \sim 1$ [see Figs. 2.2(e,f)].

2.3.2 Transverse fluctuations

Basic formulae

Let us now consider the electromagnetic fluctuations propagating parallel to the plasma drift velocity, as illustrated in Fig. 2.5. Plugging $\theta = 0$ into Eq. (1.52) and (1.53) first yields

$$\epsilon_{yy} = \epsilon_{zz} = 1 - \sum_s \frac{2\pi F_s \mu_s \omega_{ps}^2}{\omega^2}(\beta_\phi - \beta_{ds}) A_s(\beta_\phi). \tag{2.32}$$

The electromagnetic spectra then write

$$\langle E_z E_z^* \rangle_{k_x,\omega} = \frac{\langle j_z j_z^* \rangle_{k_x,\omega}}{\omega^2 \epsilon_0^2 |\epsilon_{zz} - \frac{k_x^2 c^2}{\omega^2}|^2} \tag{2.33}$$

$$= \frac{1}{\epsilon_0 |\epsilon_{xx} - \frac{k_x^2 c^2}{\omega^2}|^2} \sum_s \frac{T_s \Im(\chi_{zz}^{(s)})}{\omega - k_x v_{ds}}, \tag{2.34}$$

$$\langle B_y B_y^* \rangle_{k_x,\omega} = \frac{k_x^2}{\omega^2} \langle E_z E_z^* \rangle_{k_x,\omega}. \tag{2.35}$$

This is the generalized fluctuation-dissipation theorem for a multispecies plasma with arbitrary drift velocities and temperatures. For equal temperatures and drift velocities, it reduces to

$$\langle E_z E_z^* \rangle_{k_x,\omega} = \frac{-T}{2\epsilon_0(\omega - k_x v_d)} \Im\left(\frac{1}{\epsilon_{zz} - \frac{k_x^2 c^2}{\omega^2}} \right), \tag{2.36}$$

$$\langle B_y B_y^* \rangle_{k_x,\omega} = \frac{-T/v_\phi^2}{2\epsilon_0(\omega - k_x v_d)} \Im\left(\frac{1}{\epsilon_{zz} - \frac{k_x^2 c^2}{\omega^2}} \right). \tag{2.37}$$

Dispersion relation

Combining Eqs. (1.11) and (2.32), the dispersion relation of the transverse fluctuations can be recast as

$$k_x^2 c^2 = \frac{1}{\beta_\phi^2 - 1} \sum_s 2\pi F_s \mu_s \omega_{ps}^2 (\beta_\phi - \beta_{ds}) A_s(\beta_\phi) = \mathcal{H}(\beta_\phi)\,. \tag{2.38}$$

The transverse normal modes $\omega_T(k_x)$ can then be numerically computed using the method detailed in Sec. 2.3.1. An analytical expression of the supraluminal transverse modes ω_{TS} can be obtained in the $k_x \to 0$ limit, which reads

$$\omega_{TS}^2(0) = \sum_s \omega_{ps}^2 \mu_s \langle \beta_x^2 \rangle_s\,, \tag{2.39}$$

where $\langle \beta_x^2 \rangle_s$ denotes the average of β_x^2 for species s. This limiting value is independent of the phase velocity (see the eigenmode curves in Figs. 2.6(a-f)).

Taking $\lim_{\beta_\phi \to \pm 1}$ in Eq. (2.38), and given $\lim_{\beta_\phi \to \pm 1} A(\beta_\phi)$ is finite and non-zero, yields $\lim_{\beta_\phi \to \pm 1} k_x^2 = \infty$ so that there are only exactly two transverse supraluminal modes (one per sign of β_ϕ) as shown in Figs. 2.6(a-f).

(ω, k)-resolved spectrum

Figures 2.6(a-f) and 2.7(a-f) represent the spectra of the transverse electric and magnetic fluctuations, respectively, for various values of μ and β_d. As for the longitudinal spectra, the supraluminal fluctuations are proportional to the delta function of the dispersion relation. Consequently, Eqs. (2.36) and (2.37) vanish for $|\beta_\phi| > 1$ except along the supraluminal solutions of the dispersion relation Eq. (2.38). In the $\beta_d = 0$ case, the subluminal spectra are symmetric with respect to $\omega = 0$ and do no exhibit localized maxima due to the absence of weakly-damped subluminal eigenmodes. By contrast, the subluminal spectra associated to $\beta_d = 0.9$ are peaked close to a weakly-damped acoustic-like branch $\omega_T \sim k_x v_d$. The damping rate of this so-called beam mode can be estimated by inserting $\omega_T = k_x v_d + i\Gamma(k)$ into Eq. (2.6) with $|\Gamma| \ll k_x v_d$. A first-order Taylor expansion of $\epsilon_{zz}(k_x v_d + i\Gamma, k_x)$ then yields

$$\epsilon_{zz}(k_x \beta_d, k_x) + i\Gamma \frac{\partial \epsilon_{zz}}{\partial \omega}(k_x \beta_d, k_x) - \frac{k_x^2 c^2}{(k_x v_d + i\Gamma)^2} = 0. \tag{2.40}$$

Taking the imaginary part of the above equation gives the damping rate

$$\Gamma(k_x) = -\beta_d^2 \frac{k_x^3 c^3}{\sum_s (2\pi)^2 F_s \omega_{ps}^2 \mu_s f_A(\beta_d)}. \tag{2.41}$$

Figure 2.8(b) shows that, for $\mu = 100$ and $\beta_d = 0.9$, this expression closely matches the numerical solution up to $k_x c/\omega_p \sim 0.4$.

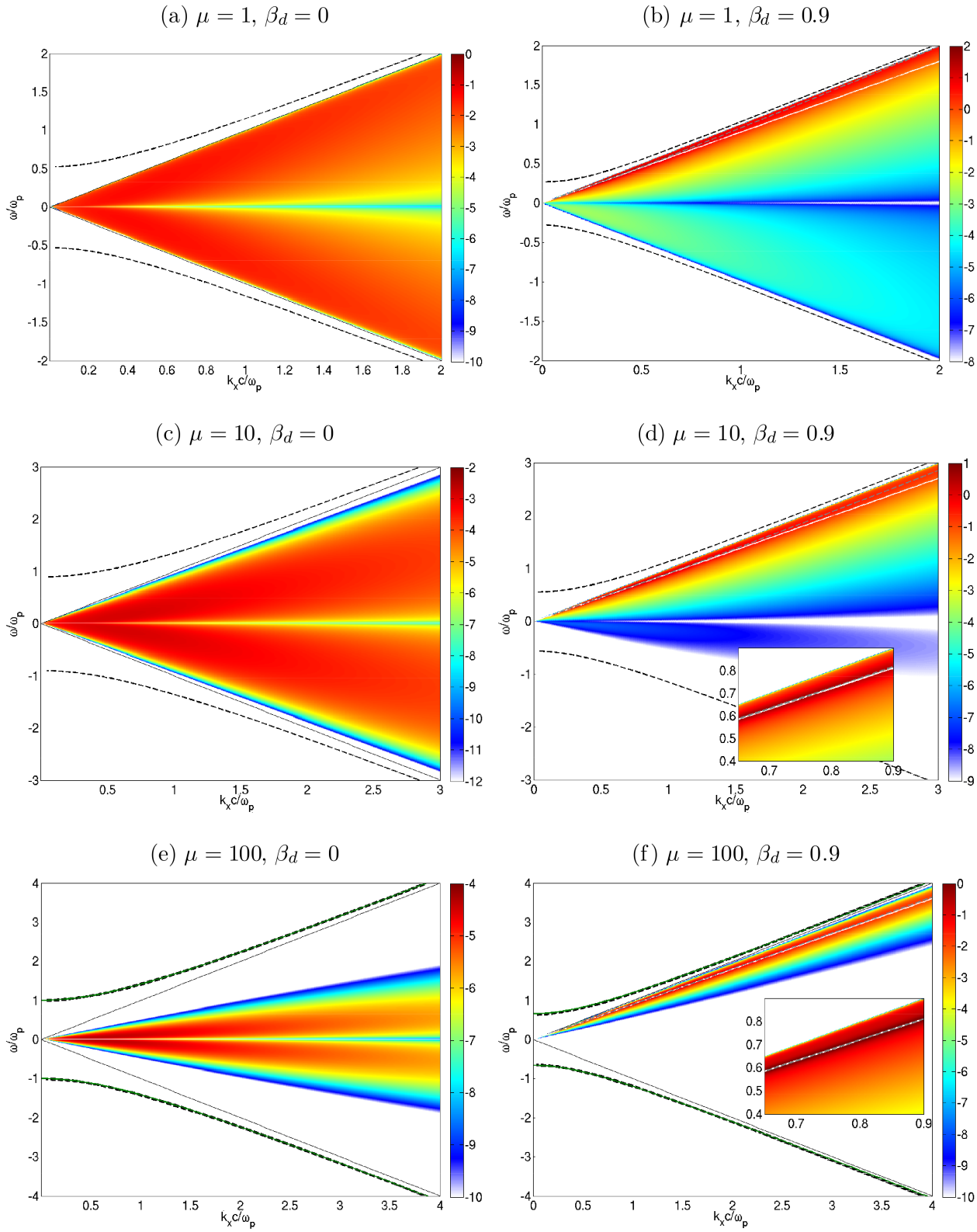

Figure 2.6. Power spectrum $\langle E_z E_z^* \rangle_{k_x,\omega}$ (normalized to $m_e^2 c^3/e^2$) in $\log_{10}$ scale for an electron/pair plasma and various μ and β_d values. The two black solid lines correspond to $\beta_\phi = \pm 1$. The dashed curves plot the exact eigenmodes computed from Eq. (2.38). In the low-temperature case ($\mu = 100$), the solid line plots the nonrelativistic transverse mode in panel (e) and its Lorentz transformation in panel (f). The subpanels in (d) and (f) show the exact eigenmode (grey dashed line) and the approximate beam mode $\omega = k\beta_d$ (white solid line).

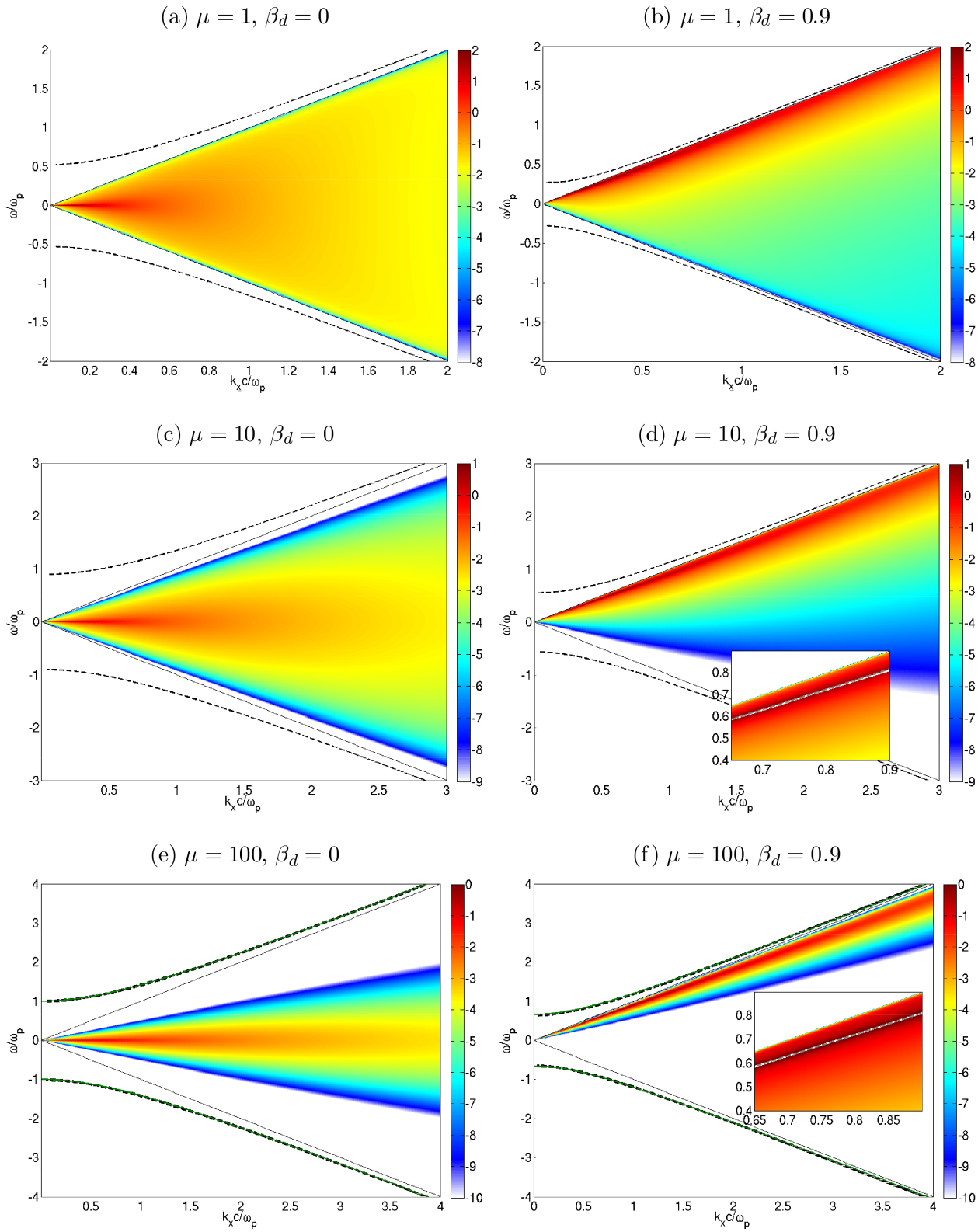

Figure 2.7. Power spectrum $\langle B_y B_y^* \rangle_{k_x,\omega}$ (normalized to $m_e^2 c/e^2$) in $\log_{10}$ scale for an electron/pair plasma and various μ and β_d values. The two black solid lines correspond to $\beta_\phi = \pm 1$. The dashed curves plot the exact eigenmodes computed from Eq. (2.38). In the low-temperature case ($\mu = 100$), the solid line plots the nonrelativistic transverse mode in panel (e) and its Lorentz transformation in panel (f). The subpanels in (d) and (f) show the exact eigenmode (grey dashed) and the approximate beam mode $\omega = k\beta_d$ (white).

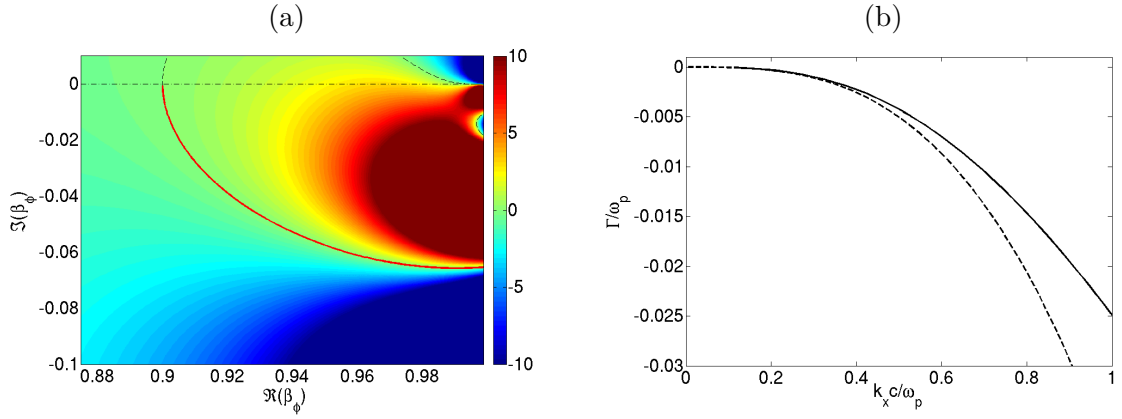

Figure 2.8. (a) Map of the complex function $\mathcal{H}(\beta_\phi)$ defined by Eq. (2.38) for $\mu = 100$ and $\beta_d = 0.9$: the dashed line plots the isocontour $\Im\mathcal{H} = 0$ and the solid line plots the $\Re\mathcal{H} > 0$ part of this isocontour, which corresponds to the acoustic-like eigenmode shown in Fig. 2.6(f). (b) Damping rate of this eigenmode *vs* k_z: comparison between the numerical solution (solid line) and the approximate solution (2.41) (dashed curve).

k-resolved spectrum

The ω-integration of the transverse fluctuation spectra proceeds as in the electrostatic case. Let us therefore introduce the functions

$$I_E(k_x,\omega) = \frac{-T}{\epsilon_0(\omega - k_x v_d)}\left(\frac{1}{\epsilon_{zz} - \frac{k_x^2c^2}{\omega^2}} - 1\right), \tag{2.42}$$

$$I_B(k_x,\omega) = \frac{-T}{\epsilon_0(\omega - k_x v_d)}\frac{1}{v_\phi^2(\epsilon_{zz} - \frac{k_x^2c^2}{\omega^2})}, \tag{2.43}$$

such that

$$\langle E_z E_z^*\rangle_{k_x} = \Im\int_{-\infty}^{+\infty}\frac{d\omega}{2\pi} I_E(\omega,k_x), \tag{2.44}$$

$$\langle B_y B_y^*\rangle_{k_x} = \Im\int_{-\infty}^{+\infty}\frac{d\omega}{2\pi} I_B(\omega,k_x). \tag{2.45}$$

Making use of the closed contour G (Fig. 2.3) and of the following limits

$$\lim_{|\omega|\to 0}\frac{1}{\epsilon_{zz} - \frac{k_x^2c^2}{\omega^2}} - 1 = 0, \tag{2.46}$$

$$\lim_{|\omega|\to 0}\frac{1}{\epsilon_{zz} - \frac{k_x^2c^2}{\omega^2}}\frac{1}{v_\phi^2} = 0, \tag{2.47}$$

we find that the supraluminal part of the transverse fluctuation spectrum is again given by the imaginary singularities related to the transverse supraluminal eigenmodes $\omega_{TS}(k_x)$:

$$\langle E_z E_z^*\rangle_{k_x}^{|\beta_\phi|>1} = -\sum_{\omega=\omega_{TS}}\frac{T}{2\epsilon_0(\omega - k_x v_d)}\frac{1}{\frac{\partial\epsilon_{zz}}{\partial\omega} + 2\frac{k_x^2c^2}{\omega^3}}, \tag{2.48}$$

$$\langle B_y B_y^*\rangle_{k_x}^{|\beta_\phi|>1} = -\frac{k_x^2}{\omega^2}\sum_{\omega=\omega_{TS}}\frac{T}{2\epsilon_0(\omega - k_x v_d)}\frac{1}{\frac{\partial\epsilon_{zz}}{\partial\omega} + 2\frac{k_x^2c^2}{\omega^3}}. \tag{2.49}$$

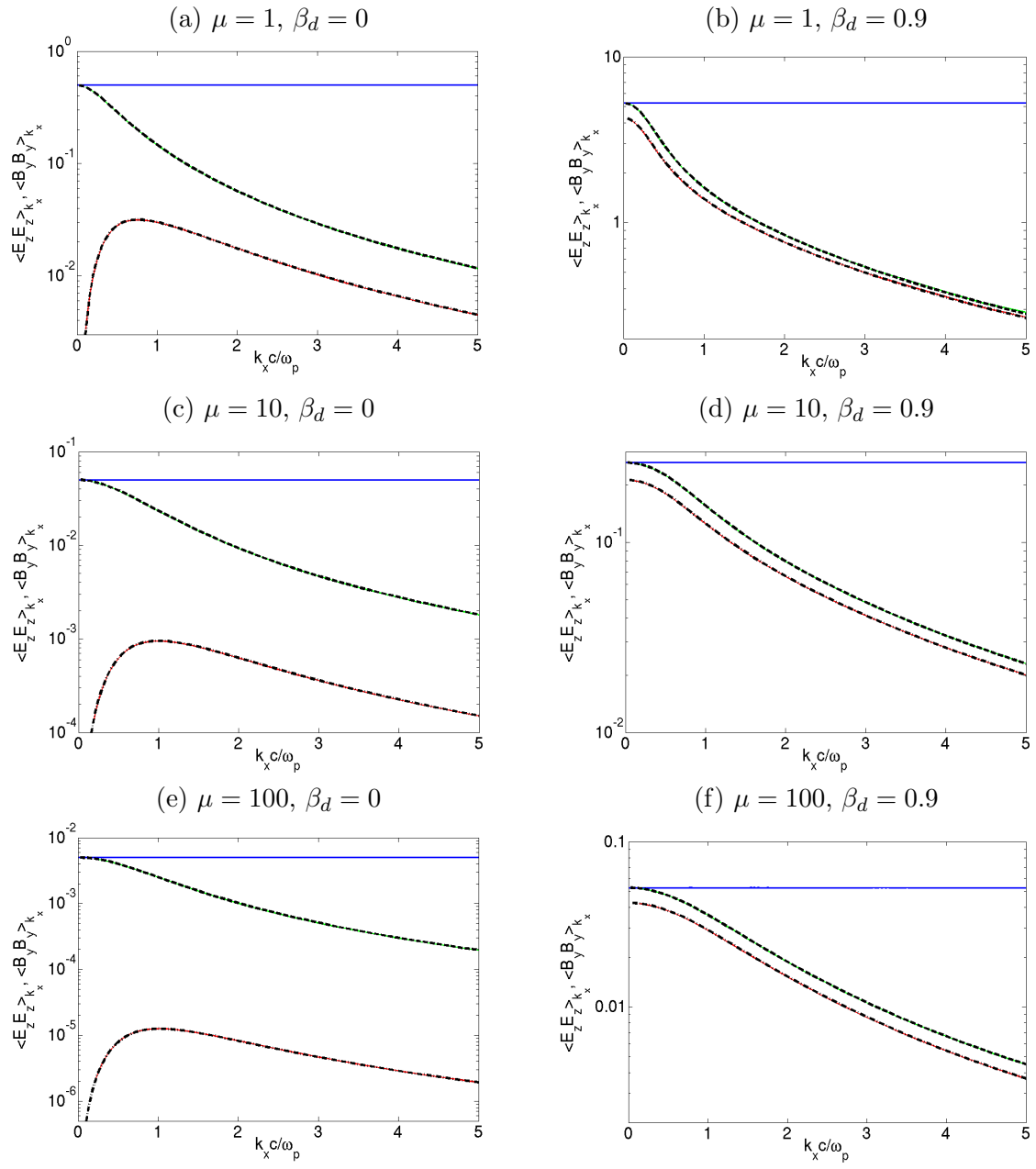

Figure 2.9. Spatial power spectra of the electromagnetic fluctuations in an electron/pair plasma for $\theta = 0$ and various values of μ and β_d. The electric and magnetic spectra are normalized to $\frac{m_e^2 c^3}{e^2}(\sum_s \omega_{ps}^2)^{1/2}$ and $\frac{m_e^3 c^3 \epsilon_0}{ne^4}(\sum_s \omega_{ps}^2)^{1/2}$, respectively. Comparison of the total fluctuation spectra (blue solid line), subluminal $\langle E_z E_z^* \rangle_{k_x}^{|\beta_\phi|<1}$ spectra (red solid line), the subluminal $\langle B_y B_y^* \rangle_{k_x}^{|\beta_\phi|<1}$ spectra (green solid line). Also plotted are the numerical integration of Eq. (2.44) (dashed line) and of Eq. (2.45) (dashed-dotted line).

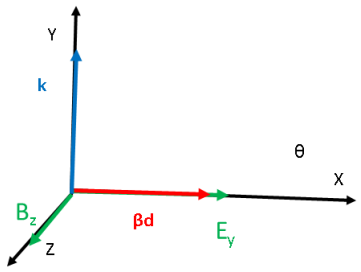

Figure 2.10. Frame of the system studied in Sec. 2.4.

Similarly, the total spatial fluctuations are determined by the ballistic singularities, and turn out to be independent of the wavenumber:

$$\epsilon_0 \langle E_z E_z^* \rangle_{k_x} = \frac{1}{\mu_0} \langle B_y B_y^* \rangle_{k_x} = \gamma_d^2 \frac{T}{2} \,. \tag{2.50}$$

In the case of a vanishing drift velocity, this formula is identical to the nonrelativistic expression (Sitenko 1982), as pointed out in Ref. (Klimontovich 1982). The subluminal electric and magnetic spectra, $\langle E_z E_z^* \rangle_{k_x}^{|\beta_\phi|<1}$ and $\langle B_y B_y^* \rangle_{k_x}^{|\beta_\phi|<1}$, readily follow from subtracting Eq. (2.48) and (2.49) to Eq. (2.50). Simple analytical expressions can be obtained at $k_x = 0$:

$$\langle E_z E_z^* \rangle_{k_x=0}^{|\beta_\phi|<1} = \frac{\gamma_d^2 \beta_d^2}{\epsilon_0} \frac{T}{2} \,, \tag{2.51}$$

$$\langle B_y B_y^* \rangle_{k_x=0}^{|\beta_\phi|<1} = \mu_0 \gamma_d^2 \frac{T}{2} \,. \tag{2.52}$$

Whereas the $k_x = 0$ magnetic spectra is always purely subluminal, its electric counterpart generally involves both supraluminal and subluminal contributions. The latter vanishes for $\beta_d = 0$ and prevails in the ultra-relativistic limit $\gamma_d \gg 1$. The full k_x-dependence of the subluminal, supramuminal and total spectra of the transverse fluctuations is shown in Figs. 2.9(a-f) for various values of μ and β_d.

2.4 Magnetic fluctuations with wave vectors normal to the plasma drift velocity

2.4.1 Basic formulae

We now consider the spectrum of magnetic fluctuations propagating normally to the mean plasma velocity ($\theta = \pi/2$) as illustrated by Fig. 2.10. . Without loss of generality, the wave vector is taken along the y-axis. Since we are interested in estimating the seed of growing filamentation modes in counterpropagating plasma flows (Bret *et al.* 2013), the magnetic field is chosen along the z-axis, so that the electric field lies in the xy-plane. In contrast to the previous cases, the tensorial quantities $\boldsymbol{\epsilon}$, $\mathbf{Z}$, $\langle \mathbf{j}\mathbf{j}^\dagger \rangle$ and $\langle \mathbf{B}\mathbf{B}^\dagger \rangle$ are now no longer diagonal. For an electron or pair plasma with

equal temperatures and velocities, one gets

$$\langle j_z j_z^* \rangle_{k_y,\omega} = \frac{T\omega \Im(\epsilon_{zz})}{\epsilon_0}\,, \tag{2.53}$$

$$\langle j_y j_y^* \rangle_{k_y,\omega} = \frac{T\omega \Im(\epsilon_{yy})}{\epsilon_0}\,, \tag{2.54}$$

$$\langle j_x j_x^* \rangle_{k_y,\omega} = \frac{T\omega \Im(\epsilon_{xx})}{\epsilon_0} = \frac{T\Im(\omega^2\epsilon_{zz} - k_y^2 c^2)}{\epsilon_0 \omega}\,, \tag{2.55}$$

$$\langle j_y j_x^* \rangle_{k_y,\omega} = -\frac{T\omega \Im(\epsilon_{yx})}{\epsilon_0}\,. \tag{2.56}$$

Substituting $\langle E_x E_x^* \rangle_{k_y,\omega} = (\omega/k_y c)^2 \langle B_z B_z^* \rangle_{k_y,\omega}$ into Eq. (2.1) leads to

$$\langle B_z B_z^* \rangle_{k_y,\omega} = k_y^2 \frac{|\epsilon_{yy}|^2 \langle j_x j_x^* \rangle_{k_y,\omega} + |\epsilon_{yx}|^2 \langle j_y j_y^* \rangle_{k_y,\omega} + 2\Re(\epsilon_{yy}\epsilon_{yx}^*) \langle j_y j_x^* \rangle_{k_y,\omega}}{|(\omega^2\epsilon_{xx} - k_y^2)\epsilon_{yy} - \omega^2\epsilon_{yx}^2|^2}\,. \tag{2.57}$$

The susceptibility tensor is given by Eqs. (1.52)-(1.55) with $\theta = \pi/2$:

$$\epsilon_{zz} = 1 - \sum_s \frac{2\pi F_s \mu_s \omega_{ps}^2}{\omega k_y} D_s \tag{2.58}$$

$$\epsilon_{yy} = 1 - \sum_s \frac{2\pi F_s \mu_s \omega_{ps}^2}{\omega k_y} B_s \tag{2.59}$$

$$\epsilon_{xx} = 1 - \sum_s \frac{2\pi F_s \mu_s \omega_{ps}^2}{\omega k_y} A_s + \sum_s \frac{\mu_s \omega_{ps}^2}{\omega^2} \beta_{ds}^2 \tag{2.60}$$

$$\epsilon_{yx} = \sum_s \frac{2\pi F_s \mu_s \omega_{ps}^2}{\omega k_y} C_s. \tag{2.61}$$

The corresponding sources are

$$\langle j_z j_z^* \rangle_{k_y,\omega} = H(1 - |\beta_\phi|) \sum_s \frac{(2\pi)^2 F_s \mu_s n_s q_s^2}{\omega k_y} f_D\,, \tag{2.62}$$

$$\langle j_y j_y^* \rangle_{k_y,\omega} = H(1 - |\beta_\phi|) \sum_s \frac{(2\pi)^2 F_s \mu_s n_s q_s^2}{\omega k_y} f_B\,, \tag{2.63}$$

$$\langle j_x j_x^* \rangle_{k_y,\omega} = H(1 - |\beta_\phi|) \sum_s \frac{(2\pi)^2 F_s \mu_s n_s q_s^2}{\omega k_y} f_A\,, \tag{2.64}$$

$$\langle j_y j_x^* \rangle_{k_y,\omega} = H(1 - |\beta_\phi|) \sum_s \frac{(2\pi)^2 F_s \mu_s n_s q_s^2}{\omega k_y} f_C\,. \tag{2.65}$$

Inserting Eq. (2.54)-(2.56) into Eq. (2.57) gives the magnetic spectrum

$$\langle B_z B_z^* \rangle_{k_y,\omega} = -\frac{k_y^2 T}{\epsilon_0 \omega} \Im \left[\frac{\epsilon_{yy}}{(\omega^2\epsilon_{xx} - k_y^2 c^2)\epsilon_{yy} - \omega^2 \epsilon_{yx}^2} \right]\,. \tag{2.66}$$

2.4.2 Dispersion relation

The denominator of Eq. (2.66) corresponds to the electromagnetic dispersion (2.6) with $k_x = 0$. Its explicit form is obtained by plugging Eqs. (2.58) and (2.61). There follows a second-order

polynomial equation in k_y^2:

$$k_y^4 c^4(\beta_\phi^2-1) - k_y^2 c^2\left[(\beta_\phi^2-1)\sum_s 2\pi F_s\mu_s\omega_{ps}^2\frac{B_s(\beta_\phi)}{v_\phi} - \sum_s \mu_s\omega_{ps}^2\beta_{ds}^2 + \sum_s 2\pi F_s\mu_s\omega_{ps}^2 v_\phi A_s(\beta_\phi)\right]$$
$$+\sum_s 2\pi F_s\mu_s\omega_{ps}^2\frac{B_s(\beta_\phi)}{v_\phi}\left[\sum_s 2\pi F_s\mu_s\omega_{ps}^2 v_\phi A_s(\beta_\phi) - \sum_s \mu_s\omega_{ps}^2\beta_{ds}^2\right] - \left[\sum_s 2\pi F_s\mu_s\omega_{ps}^2 C_s(\beta_\phi)\right]^2 = 0\,. \tag{2.67}$$

The solutions of the above equation then pertain to two distinct branches, $\beta_{\phi,1} = \omega_1/k_y c$ and $\beta_{\phi,2} = \omega_2/k_y c$, defined, respectively, by

$$k_y^2 c^2 = \frac{-a_1(\beta_{\phi,1}) + \sqrt{\Delta(\beta_{\phi,1})}}{2(\beta_{\phi,1}^2-1)}\,, \tag{2.68}$$

$$k_y^2 c^2 = \frac{-a_1(\beta_{\phi,2}) - \sqrt{\Delta(\beta_{\phi,2})}}{2(\beta_{\phi,2}^2-1)}\,. \tag{2.69}$$

We have introduced $\Delta = a_1^2 - 4(v_\phi^2-1)a_0$, where a_n is the nth order coefficient of the polynomial in k_y^2 defined by Eq. (2.67). Again, we employ the Fried and Gould scheme to compute the entire set of eigenmodes associated to each branch.

We find that there exist a maximum number of four undamped, or weakly-damped, eigenmodes (two symmetric modes of opposite phase velocities per branch). As displayed by the coloured dashed curves in Figs. 2.11(a-c), these solutions correspond to the Lorentz-transformed dominant electromagnetic (branch 1) and electrostatic (branch 2) modes in the plasma rest frame. This is demonstrated in the low-temperature regime ($\mu = 100$) by the precise coincidence between the exact curves and the Lorentz transforms of the modes $\omega = \omega_p(1 + k^2c^2/\omega_p^2)^{1/2}$ and $\omega = \omega_p(1 + 3k^2c^2/\omega_p^2\mu)^{1/2}$. Note that the eigenmodes associated to branch 1 are purely supraluminal for all k_y's.

Owing to the non-vanishing ϵ_{yx} term in Eq. (2.6), the electric field associated to eigenmodes with wave vectors normal to the plasma drift velocity has both longitudinal (E_y) and transverse (E_x) components. This property has been analyzed in detail in Refs. (Tzoufras *et al.* 2006; Bret *et al.* 2007) in the context of the filamentation instability. The orientation of the electric field is determined by the following formula (Bret *et al.* 2004):

$$\frac{E_y}{E_x} = -\frac{\omega^2\epsilon_{zz} - k_y^2c^2}{\omega^2\epsilon_{yx}} = -\frac{\omega^2\epsilon_{yx}}{\omega^2\epsilon_{yy}}\,. \tag{2.70}$$

Making use of Eqs. (2.58)-(2.61), this can be recast as

$$\frac{E_y}{E_x} = -\frac{\sum_s \pi F_s\omega_{ps}^2\mu_s\beta_\phi C(\beta_\phi)}{\omega^2 - \sum_s 2\pi F_s\omega_{ps}^2\mu_s\beta_\phi B(\beta_\phi)} = \frac{k_y^2c^2 - \omega^2 + \sum_s \omega_{ps}^2\mu_s[2\pi F_s\beta_\phi A(\beta_\phi) - \beta_d^2]}{\sum_s 2\pi F_s\omega_{ps}^2\mu_s\beta_\phi C(\beta_\phi)} \tag{2.71}$$

The above equation can be analytically evaluated in the $k_y \to 0$ and $k_y \to \infty$ limits. It is easy to

demonstrate that

$$\lim_{k_y\to\infty}\omega_{1\pm}^2=\lim_{k_y\to\infty}\omega_{2\pm}^2=k_y^2c^2\,, \tag{2.72}$$

$$\lim_{k_y\to 0}\omega_{1\pm}^2=\sum_s 2\pi F_s\omega_{ps}^2\mu_s\int_{-1}^{+1}f_B\,d\beta\,, \tag{2.73}$$

$$\lim_{k_y\to 0}\omega_{2\pm}^2=\sum_s 2\pi F_s\omega_{ps}^2\mu_s\int_{-1}^{+1}f_A\,d\beta-\sum_s\omega_{ps}^2\mu_s\beta_{ds}^2\,. \tag{2.74}$$

where use has been made of $\lim_{\beta_\phi\to\infty}\beta_\phi B(\beta_\phi)=\int_{-1}^{+1}d\beta f_B$. It follows that the eigenmode $\omega_{1,\pm}$ is purely longitudinal for $k_y=0$ ($E=E_y$) and becomes purely transverse for $k_y\to\infty$ ($E=E_x$). By contrast, the eigenmode $\omega_{2,\pm}$ is purely longitudinal for $k_y\to\infty$ and purely transverse for $k_y=0$. The k_y-dependence of the angle $\phi=\arctan(E_y/E_x)$ is plotted for both branches in Fig. 2.12(d) in a relativistically hot case ($\mu=1$, $\beta_d=0.9$).

2.4.3 (ω,k)-resolved spectrum

Figures 2.11(a,b,c) display Eq. (2.66) for $\beta_d=0.9$ and $\mu=(1,10,100)$. Only half the spectrum is shown due to its parity in ω. As expected, the trace of the eigenmode $\omega_{2,+}$ increasingly stands out in the subluminal region as the plasma temperature drops.

Similarly to Figs. 2.7(a,c,e), these spectra exhibit a peaked structure around $\omega=0$. As pointed out in Refs. (Yoon 2007; Tautz & Schlickeiser 2007; Bret *et al.* 2013), these zero-frequency fluctuations are associated to the unstable magnetic filamentation (Weibel) mode. Combining Eqs. (2.58)-(2.57) gives the closed-form expression

$$\langle B_zB_z^*\rangle_{k_y,\omega=0}=\frac{\gamma_d^3}{k_y^3}\frac{\mathcal{J}}{\left(k_y^2+\frac{\omega_p^2\mu}{\gamma_d^2}\right)^2}\frac{\omega_p^2e^{-\frac{\mu}{\gamma_d}}}{2\mu^2K_2(\frac{\mu}{\gamma_d})}\,, \tag{2.75}$$

with

$$\begin{aligned}\mathcal{J}=&(k_y^2+\omega_p^2\mu)^2\left[\left(\frac{\mu}{\gamma_d}+1\right)\left(1+2\beta_d^2\right)+\beta_d^2\frac{\mu^2}{\gamma_d^2}\right]+\omega_p^4\mu^2\beta_d^2\left[\left(\frac{\mu}{\gamma_d}+1\right)\left(2+\beta_d^2\right)+\frac{\mu^2}{\gamma_d^2}\right]\\&-2\left(k_y^2+\omega_p^2\mu\right)\omega_p^2\mu\beta_d^2\left(3\frac{\mu}{\gamma_d}+3+\frac{\mu^2}{\gamma_d^2}\right)\,.\end{aligned} \tag{2.76}$$

We have thus generalized to arbitrary temperatures and drift velocities the formula obtained by Yoon (2007) for a nondrifting, nonrelativistic Maxwellian plasma. As in the nonrelativistic limit, we find that $\langle B_zB_z^*\rangle_{k_y,\omega=0}$ scales as k_y^{-3} for $k_y^2\ll\omega_p^2\mu/\gamma_d^2$.

2.4.4 k-resolved spectrum

In order to carry out the integration of $\langle B_zB_z^*\rangle_{k_y,\omega}$ over $\omega\in\mathbb{R}$, we define the function

$$L_B=-\frac{T}{\epsilon_0\omega}\frac{k_y^2\epsilon_{yy}}{(\omega^2\epsilon_{xx}-k_y^2c^2)\epsilon_{yy}-\omega^2\epsilon_{yx}^2}\,, \tag{2.77}$$

so that

$$\langle B_zB_z^*\rangle_{k_y}=\Im\int_{-\infty}^{+\infty}\frac{d\omega}{2\pi}L_B\,. \tag{2.78}$$

(a) $\mu = 1,\ \beta_d = 0.9$

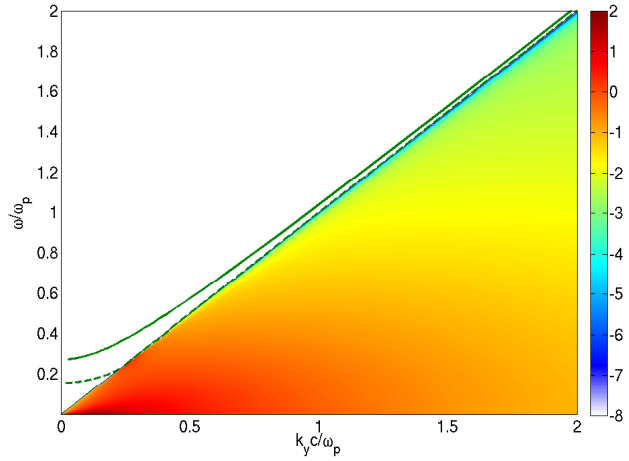

(b) $\mu = 10,\ \beta_d = 0.9$

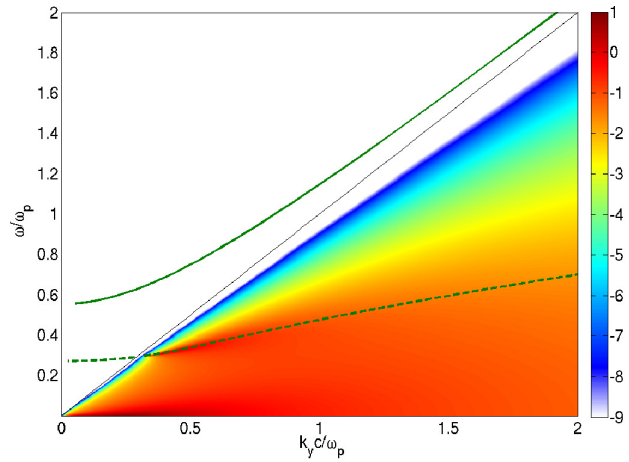

(c) $\mu = 100,\ \beta_d = 0.9$

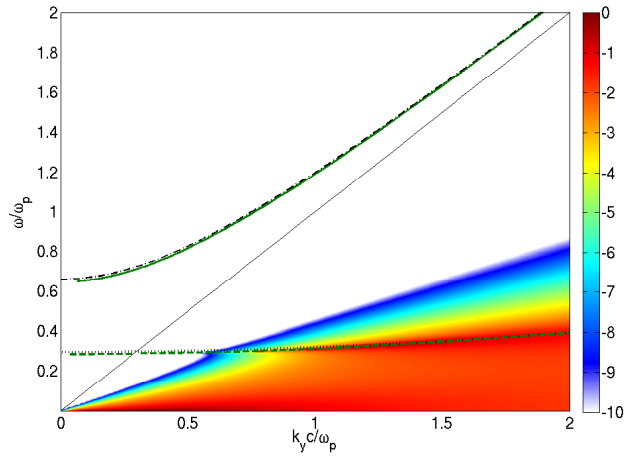

Figure 2.11. Power spectrum $\langle B_z B_z^* \rangle_{k_y,\omega}$ (normalized to $m_e^2 c/e^2$ and in $\log_{10}$ scale) of an electron or pair plasma for $\alpha = \pi/2$, $\beta_d = 0.9$ and various values of μ. The white solid lines delimit the subluminal region $|\beta_\phi| \leq 1$. The exact eigenmodes are plotted in green solid lines (branch 1) and dashed curves (branch 2). In panel (c) are also plotted the Lorentz transforms of the classical transverse eigenmode (black blue dotted-dashed line) and of the longitudinal eigenmode (dotted black line).

Proceeding as in Secs. 2.3.1 and 2.3.2, we find that the total k-resolved magnetic spectrum is determined by the ω^{-1} term of Eq. (2.77). The calculation of the corresponding residue requires to evaluate the $\omega \to 0$ limits of ϵ_{yy}, $\omega\epsilon_{yx}$ and $\omega^2\epsilon_{xx}$. Equation (2.5) with $\alpha = \pi/2$ yields

$$\epsilon_{yy} = 1 - \sum_s \frac{\omega_{ps}^2\mu_s}{\omega} \int_{\mathbb{R}} d^3p \frac{v_y v_y}{\omega - k_y v_y} f_s^{(0)} \,, \tag{2.79}$$

$$\omega\epsilon_{yx} = -\sum_s \omega_{ps}^2\mu_s \int_{\mathbb{R}} d^3p \frac{v_y v_x}{\omega - k_y v_y} f_s^{(0)} \,, \tag{2.80}$$

$$\omega^2\epsilon_{xx} = \omega^2 - \sum_s \omega_{ps}^2\mu_s\omega \int_{\mathbb{R}} d^3p \frac{v_x v_x}{\omega - k_y v_y} f_s^{(0)} \,. \\ + \sum_s \omega_{ps}^2\mu_s\beta_{ds}^2 \tag{2.81}$$

Taking $\omega \to 0$ in Eqs. (2.79)-(2.81) and using

$$\lim_{v_\phi \to 0} \frac{1}{v_\phi} \int d^3p \frac{v_y^2 f_s^{(0)}}{v_\phi - v_y} = \int d^3p f_s^{(0)} = 1 \,, \tag{2.82}$$

gives

$$\lim_{\omega\to 0} \epsilon_{yy} = 1 + \sum_s \frac{\omega_{ps}^2\mu_s}{k_y^2} \,, \tag{2.83}$$

$$\lim_{\omega\to 0} \omega\epsilon_{yz} = -\sum_s \frac{\omega_{ps}^2\mu_s}{k_y}\beta_{ds} \,, \tag{2.84}$$

$$\lim_{\omega\to 0} \omega^2\epsilon_{zz} = \sum_s \omega_{ps}^2\mu_s\beta_{ds}^2 \,. \tag{2.85}$$

Using Eqs. (2.83)-(2.85), the total spectrum reads

$$\langle B_z B_z^* \rangle_{k_y} = \frac{\mu_0 T}{2} \frac{k_y^2c^2 + \omega_p^2\mu}{k_y^2c^2 + \omega_p^2\mu/\gamma_d^2} \,. \tag{2.86}$$

As usual, the supraluminal spectrum results from the supraluminal singularities $\omega_{1,2S}$ of Eq. (2.77).

$$\langle B_z B_z^* \rangle_{k_y}^{|\beta_\phi|>1} = \sum_{\omega=\omega_{1,2S}} \frac{\mu_0 T}{2} \frac{k_y^2\epsilon_{yy}}{\omega\partial D/\partial\omega|_\omega} \,, \tag{2.87}$$

with $D = (\omega^2\epsilon_{xx} - k_y^2c^2)\epsilon_{yy} - \omega^2\epsilon_{yx}^2$. For $k_y^2c^2 > k_{2S}^2$ (Eq. (2.88)), only the pair of solutions $\omega_{1S\pm}$ contribute to the above equation, yielding $\langle B_z B_z^* \rangle_{k_y}^{|\beta_\phi|>1} \sim \mu_0 T/2$. For the sake of completeness, the $\langle \mathbf{E}\mathbf{E}^\dagger \rangle_{k_y}$ and $\langle B_x B_x^* \rangle_{k_y}$ spectra are summarized in Sec. 2.4.5.

Figures 2.12(a,b,c) plot the k_y-dependence of the total, supraluminal and subluminal magnetic spectra for $\beta_d = 0.9$ and various values of μ. Note that the magnetic fluctuations are purely subluminal at $k_y = 0$, with $\langle B_z B_z^* \rangle_{k_y=0} = \mu_0\gamma_d^2 T/2$. As expected in the infinite-wavelength limit, we retrieve the value (2.52) obtained for $\alpha = 0$. Again, the numerical integration of Eq. (2.66) over the subluminal ω-domain accurately reproduces the analytical formula deduced from subtracting Eq. (2.87) to Eq. (2.86). The jumps seen in the supraluminal and subluminal spectra stem from

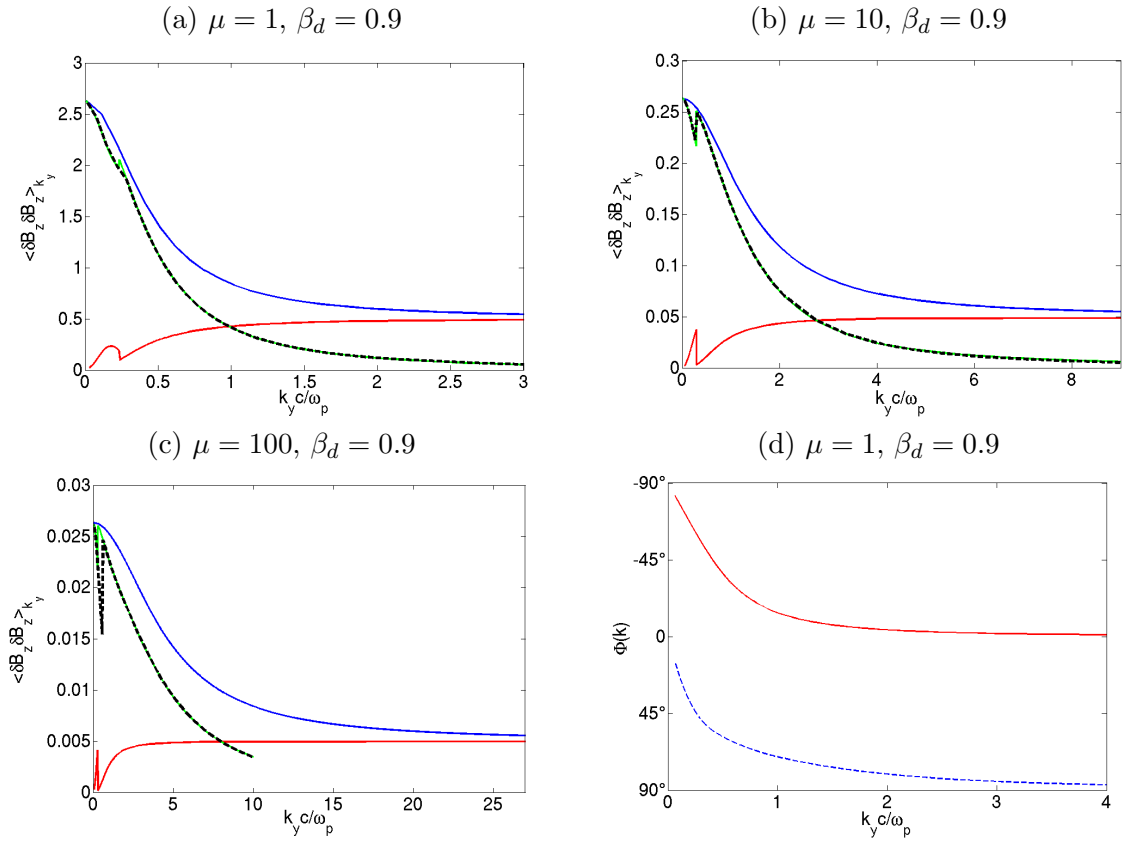

Figure 2.12. (a,b,c) $< B_z B_z^* >_{k_y}$ spectra [in $\frac{m_e^2 c^3}{e^2}(\sum_s \omega_{ps}^2)^{1/2}$ units] of a single-temperature electron/pair plasma for $\beta_d = 0.9$ and various values of μ. Comparison of the total (blue), supraluminal (red) and subluminal (green) spectra. The dashed black curve plots the numerical integration of Eq. (2.66) over the subluminal domain $|\omega| < k_y c$. (d) Variation of the angle $\phi(k_y) = \arctan(E_y/E_x)$ for the eigenmodes belonging to branch 1 (solid red) and branch 2 (dashed blue).

the pair of solutions $\omega_{2S\pm}$ turning subluminal above a critical wave vector

$$k_{2S}^2 = \sum_s \frac{\omega_{ps}^2}{\gamma_d^3} \frac{K_1(\frac{\mu_s}{\gamma_{ds}}) + 2\frac{\gamma_{ds}}{\mu_s} K_0(\frac{\mu_s}{\gamma_{ds}})}{K_2(\frac{\mu_s}{\gamma_{ds}})}\,, \tag{2.88}$$

obtained from a Lorentz transform of Eq. (2.23) taken at $\beta_d = 0$. As in Sec. 2.3.1, this discontinuity is difficult to resolve in the cold case $\mu = 100$.

2.4.5 Calculation of the $\langle \mathbf{E}\mathbf{E}^\dagger \rangle_{k_y}$ and $\langle B_z B_x^* \rangle_{k_y}$ spectra for $\theta = \pi/2$

In the case of an electron or pair plasma with equal temperatures and velocities, Eq. (2.1) yields

$$\langle E_x E_x^* \rangle_{k_y,\omega} = -\frac{T}{\epsilon_0 \omega} \Im\left(\frac{\omega^2 \epsilon_{yy}}{(\omega^2 \epsilon_{xx} - k_y^2 c^2)\epsilon_{yy} - \omega^2 \epsilon_{yx}^2} \right). \tag{2.89}$$

$$\langle E_z E_z^* \rangle_{k_y,\omega} = -\frac{T}{2\pi \epsilon_0 (\omega - k_y v_d)} \Im\left(\frac{1}{\epsilon_{zz} - \frac{k_y^2 c^2}{\omega^2}} \right). \tag{2.90}$$

Proceeding as in Sec.2.3.1, we obtain the total and supraluminal spatial $\langle E_x E_x^* \rangle_{k_y}$ spectra:

$$\langle E_x E_x^* \rangle_{k_y} = \frac{T}{2\epsilon_0}\,, \tag{2.91}$$

$$\langle E_x E_x^* \rangle_{k_y}^{|\beta_\phi|>1} = \frac{T}{2\epsilon_0} \sum_{\omega=\omega_{1,2S}} \frac{\omega \epsilon_{yy}}{\partial D/\partial \omega}. \tag{2.92}$$

Likewise, one can readily derive the total and supraluminal spatial $\langle E_z E_z^* \rangle_{k_y}$ and $\langle B_x B_x^* \rangle_{k_y}$ spectra

$$\epsilon_0 \langle E_z E_z^* \rangle_{k_y} = \frac{1}{\mu_0} \langle B_x B_x^* \rangle_{k_y} = \frac{T}{2}\,, \tag{2.93}$$

$$\langle E_z E_z^* \rangle_{k_y}^{|\beta_\phi|>1} = -\sum_{\omega=\omega_{XS}} \frac{T}{2\epsilon_0(\omega - k_y v_d)} \frac{1}{\partial G/\partial \omega}\,, \tag{2.94}$$

$$\langle B_x B_x^* \rangle_{k_y}^{|\beta_\phi|>1} = -\sum_{\omega=\omega_{XS}} \frac{T}{2\epsilon_0(\omega - k_y v_d)} \frac{1}{v_\phi^2 \partial G/\partial \omega}\,. \tag{2.95}$$

Here $\omega_{XS}(k_y)$ denotes the supraluminal solution of the dispersion relation Eq. (2.6). The latter is recast in the form

$$k_y^2 c^2 = \frac{1}{\beta_\phi^2 - 1} \sum_s 2\pi F_s \mu_s \omega_{ps}^2 (\beta_\phi - \beta_{ds}) D_s(\beta_\phi)\,. \tag{2.96}$$

Finally, combining Eqs. (2.1) and (2.58)-(2.65) yields

$$\begin{aligned} \langle E_y E_y^* \rangle_{k_y,\omega} = \frac{\omega^2}{|D|^2} \Big[& |\epsilon_{yx}|^2 \langle j_x j_x^* \rangle_{k_y,\omega} \\ & + |\omega^2 \epsilon_{xx} - k_y^2|^2 \langle j_y j_y^* \rangle_{k_y,\omega} \\ & + 2\Re\big((\omega^2 \epsilon_{xx} - k_y^2 c^2)\epsilon_{yx}^*\big) \langle j_y j_x^* \rangle_{k_y,\omega} \Big]\,. \end{aligned} \tag{2.97}$$

For an electron or pair plasma with equal temperatures and velocities, this equation reduces to

$$\langle E_y E_y^* \rangle_{k_y,\omega} = -\frac{T}{\epsilon_0 \omega} \Im \left(\frac{\omega^2 \epsilon_{xx} - k_y^2 c^2}{(\omega^2 \epsilon_{xx} - k_y^2 c^2)\epsilon_{yy} - \omega^2 \epsilon_{yx}^2} \right). \tag{2.98}$$

There follow the spatial spectra

$$\langle E_y E_y^* \rangle_{k_y} = \frac{T}{2\epsilon_0} \frac{\omega_p^2}{k_y^2 c^2 + \omega_p^2 \mu/\gamma_d^2}\,, \tag{2.99}$$

$$\langle E_y E_y^* \rangle_{k_y}^{|\beta_\phi|>1} = \frac{T}{2\epsilon_0} \sum_{\omega=\omega_{1,2S}} \frac{\omega^2 \epsilon_{xx} - k_y^2 c^2}{\omega \partial D/\partial \omega}\,. \tag{2.100}$$

2.5 Comparison with PIC simulations

We now confront our analytical formulae to the electromagnetic fluctuations induced in a numerical PIC-modeled plasma. The purpose is to analyze the numerical noise seeding amplified modes in PIC simulations of relativistic plasma instabilities (see Sec. 2.6). Note that the ability of PIC simulations to correctly render electrostatic fluctuations has already been checked (Dieckmann *et al.* 2004). Our code CALDER (Lefebvre *et al.* 2003; Drouin 2009) employs the standard Yee solver for the Maxwell equations (Yee 1966) and a charge-conserving current deposition scheme (Esirkepov 2001) with a

third-order weight factor for the macro-particles. The simulation geometry is one-dimensional in space (along or normal to the plasma velocity) and three-dimensional in momentum. The spatial and temporal step sizes are $\Delta z = 0.1c/\omega_p$ and $\Delta t = 0.095/\omega_p$, respectively. The plasma length is $560c/\omega_p$ with periodic boundary conditions for both the fields and macro-particles. The fields are initially zero. We consider an e^+e^- pair plasma initialized according to Eq. (1.22), with $\mu = 10$ and $\beta_d = 0.9$. The macro-particles have a charge and a mass equal, respectively, to $Q_p = \pm W_p q_e$ and $M_p = W_p m_e$, where W_p is the statistical weight. For the numerical plasma to behave collectively as its physical counterpart, the plasma frequencies of the two systems must be equal, which implies

$$W_p = n_e \frac{\Delta z}{N_p}\,, \tag{2.101}$$

where N_p is the number of macro-particles per mesh and species ($N_p = 2000$ here). In the 1-D geometry under consideration, W_p thus corresponds to an areal density. Since the normalized inverse temperature μ is an invariant, the susceptibility tensor is unchanged in the simulation. By contrast, the source term is modified according to

$$\langle \mathbf{j}\mathbf{j}^\dagger \rangle^{\rm PIC}_{\mathbf{k},\omega} = W_p \langle \mathbf{j}\mathbf{j}^\dagger \rangle_{\mathbf{k},\omega}\,. \tag{2.102}$$

Note that in the above equation, the left and right hand-side involves respectively a 1D and 3D Fourier transform. Its homogeneity is ensured by W_p, which is a surface density n 1D. The effect of the finite spatial width of the macro-particles is here neglected (Birdsall & Langdon 1985). The relevant simulated quantity to be compared to the theoretical spectrum is therefore $W_p \langle \mathbf{E}\mathbf{E}^\dagger \rangle^{\rm PIC}_{\mathbf{k},\omega}$. In practice, the fluctuation power spectrum is computed from the absolute square of the fast Fourier transform in space and time $|{\rm FFT}_{x,t}(E_\alpha)|^2$. Care is taken to select a temporal domain over which the system has reached a quasi-stationary state. The total simulation time is a few $1000\omega_{pe}^{-1}$. Taking into account the relation between a continuous and a discrete Fourier transform, $\langle \mathbf{E}\mathbf{E}^\dagger \rangle_{\mathbf{k},\omega}$ has to be compared with

$$\langle \mathbf{E}\mathbf{E}^\dagger \rangle_{\mathbf{k},\omega} \equiv W_p |{\rm DFT}_{x,t}(E_\alpha)|^2 \left(\frac{L_x}{2\pi}\right)^2 \tag{2.103}$$

Figures 2.13(a,b,c) display the (k,ω)-resolved power spectra of the simulated electric and magnetic fluctuations for $\theta = 0$ (a,b) and $\theta = \pi/2$ (c). In the latter case, the simulation resolves the beam-normal y-axis. These results satisfactorily agree (over ~ 4 decades) with the theoretical predictions depicted in Figs. 2.2(d), 2.7(d) and 2.11(b). A noticeable difference, however, is that the supraluminal eigenmodes appear as finite-width structures in the simulations instead of delta-like singularities. This can be attributed to a number of reasons: the finite temporal window, the numerical collisions between the finite-width macro-particles and the non-adiabatic switch-on of the fields. Regarding the latter, the level of the supraluminal fluctuations was theoretically shown to be highly sensitive to the details of the plasma initialization in Refs. (Lerche 1968b, 1969a,b). A PIC study of the impact of the plasma initialization upon the asymptotic field fluctuations is outside the scope of this work.

Let us now consider the spatial fluctuation spectra. From the same reasoning as above, one has to compare the theoretical formulae (obtained in Secs. 2.3.1, 2.3.2 and 2.4.4) to the simulated quantity $2\pi W_p \langle |{\rm FFT}_x(E_\alpha)|^2 \rangle_t (L_x/2\pi)^2$, where $\langle\rangle_t$ denotes a temporal average. The PIC spatial spectra shown in Figs. 2.14(a,b,c) turn out to better match the subluminal spectra than the total spectra. This behavior, which is particularly pronounced for the transverse fluctuations with $\theta = 0$ [Fig. 2.14(b)], confirms the observed discrepancy between the simulated and theoretical supraluminal spectra. We have checked that the energy stored in the supraluminal structures of Figs. 2.13(a,b,c) significantly underestimates the theoretical expectations.

(a) $\theta = 0$: $\frac{n_0 \Delta_z}{N_p} \frac{m_e^2 c^3}{e^2} |\mathrm{FFT}_{x,t}(E_x)|^2$

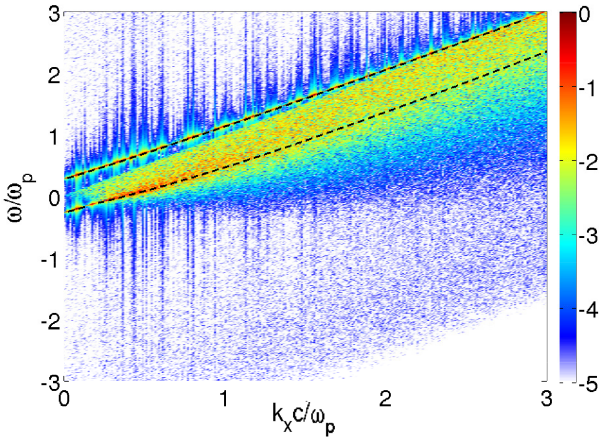

(b) $\theta = 0$: $\frac{n_0 \Delta_z}{N_p} \frac{m_e^2 c}{e^2} |\mathrm{FFT}_{x,t}(B_y)|^2$

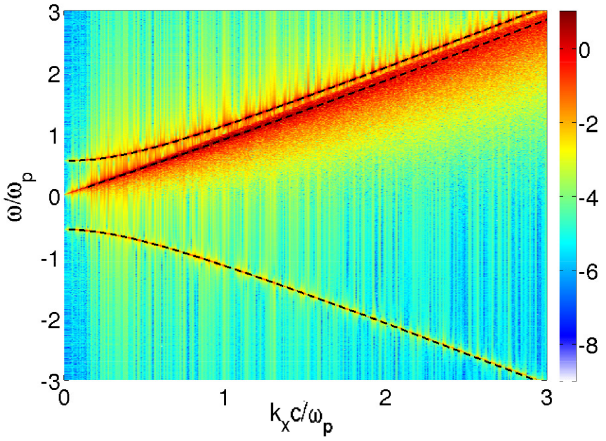

(c) $\theta = \pi/2$: $\frac{n_0 \Delta_y}{N_p} \frac{m_e^2 c}{e^2} |\mathrm{FFT}_{y,t}(B_z)|^2$

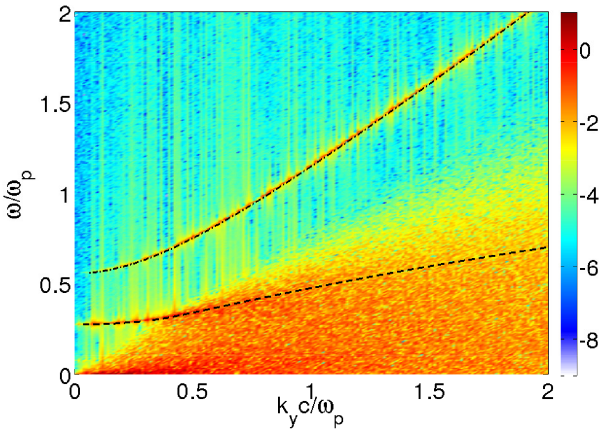

Figure 2.13. Simulated (k, ω) spectra in $\log_{10}$ scale for $\mu = 10$ and $\beta_d = 0.9$ (see text for details). Panels (a) and (b) correspond to wave vectors parallel to the beam ($\theta = 0$), whereas panel (c) corresponds to wave vectors normal to the beam ($\theta = \pi/2$). The dashed and dotted-dashed curves plot the eigenmodes solving Eq. (2.22) (a), Eq. (2.38) (b) and Eq. (2.67) (c). The system size is $L = 560c/\omega_p$ in all cases.

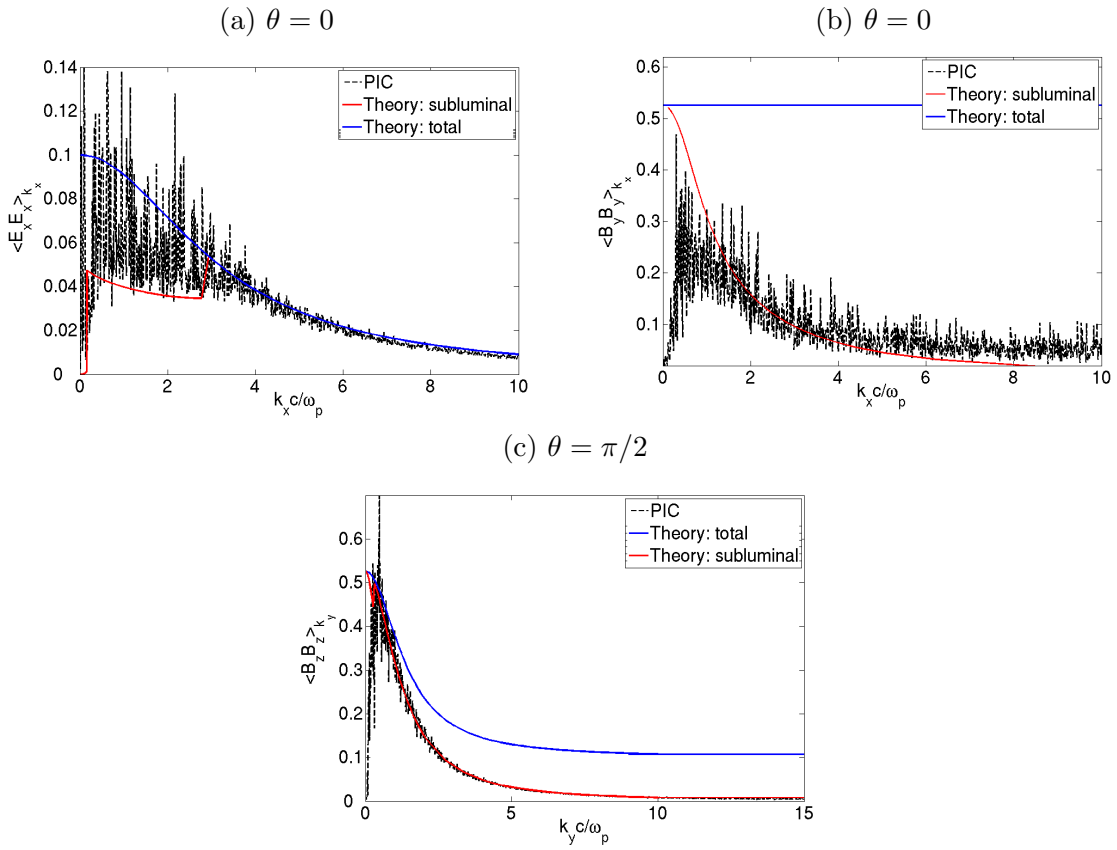

Figure 2.14. Simulated spatial spectra (dashed lines) for $\theta = 0$ (a,b) and $\pi/2$ (c) compared to the theoretical subluminal (red solid lines) and total (blue solid lines) spectra (in $\frac{m_e^2 c^3}{e^2}(\sum_s \omega_{ps}^2)^{1/2}$ units).

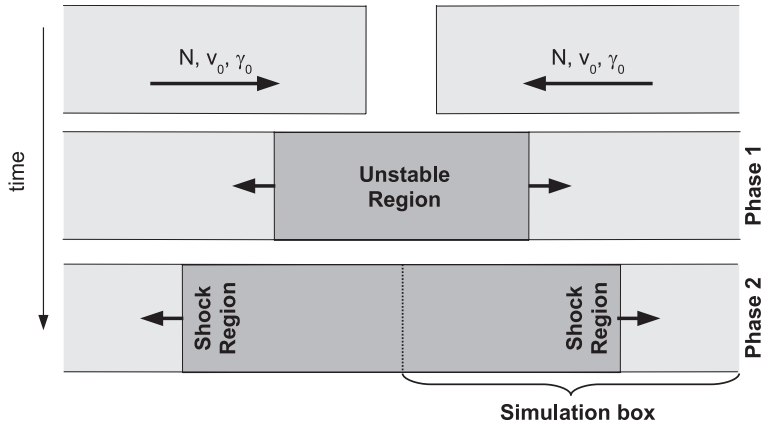

Figure 2.15. Phases of the shock formation. Two identical pair plasmas interpenetrate. The overlap region turns unstable, and two shocks form near the border of each shell. The simulation box contains half of the system.

2.6 Application of the saturation time of the Weibel instability in pair plasma (Bret *et al.* 2013)

Colliding plasma shells are present in a variety of physical settings. Astrophysical jets produced by black holes are expected to generate a shock when interacting with the interstellar medium (Begelman *et al.* 1984; Harris & Krawczynski 2006). Still in astrophysics, the Fireball scenario for Gamma-Rays-Bursts (Piran 2004; Nakar 2007) relies on shock particle acceleration (Bell 1978a,b), where the shock arises from the encounter of two ultra-relativistic plasma blobs ejected from a central engine. Non-relativistic supernova remnant Shocks are also instrumental in accelerating high energy cosmic rays (Koyama *et al.* 1995; Dieckmann *et al.* 2000).

For the collisionless environments considered, PIC simulations are an efficient tool to study these processes. The formation of a shock following the Weibel-unstable collision of two plasmas was first explored in Ref. (Silva *et al.* 2003). Subsequent particle acceleration has been observed in numerous simulations (Hededal *et al.* 2004; Nishikawa *et al.* 2005; Chang *et al.* 2008; Spitkovsky 2008a,b; Martins *et al.* 2009).

Although the full shock formation process has thus been now repeatedly observed in simulations, a first principle understanding of the very birth of the shock is still lacking. Such a theoretical understanding could provide an accurate timing of the shock formation time, and constraints the conditions required to form a shock in the first place. Whether they are in the lab, in a computer simulation or in the vicinity of a supernova, it should be possible to separate the scenario leading to the shock into two phases represented schematically in Fig. 2.15. In the first phase, plasma shells make contact and overlap, triggering an electromagnetic Weibel-filamentation instability An instability grows and saturates. At this junction, the total density in the overlapping region is roughly the sum of each plasma density. A second phase is therefore needed during which nonlinear processes pick-up the system from the end of the linear phase, and build-up the expected Rankine-Hugoniot density jump near the borders of the inter-penetrating shells.

The present section is concerned with the first of these two phases. The collision of two identical cold relativistic pair plasmas has been simulated in 2D with the PIC code OSIRIS (Fonseca *et al.* 2002, 2008) in a collaboration with A. Stockem, F. Fiuza , with L. Narayan and L. O. Silva on an original idea of A. Bret. The details of the simulations are given in Section 2.6.4. This setup has been chosen for its simplicity, allowing for a direct comparison with theory as the only free parameter is the initial Lorentz factor of the shells γ_d. In the simulation, a neutral e^-/e^+ plasma

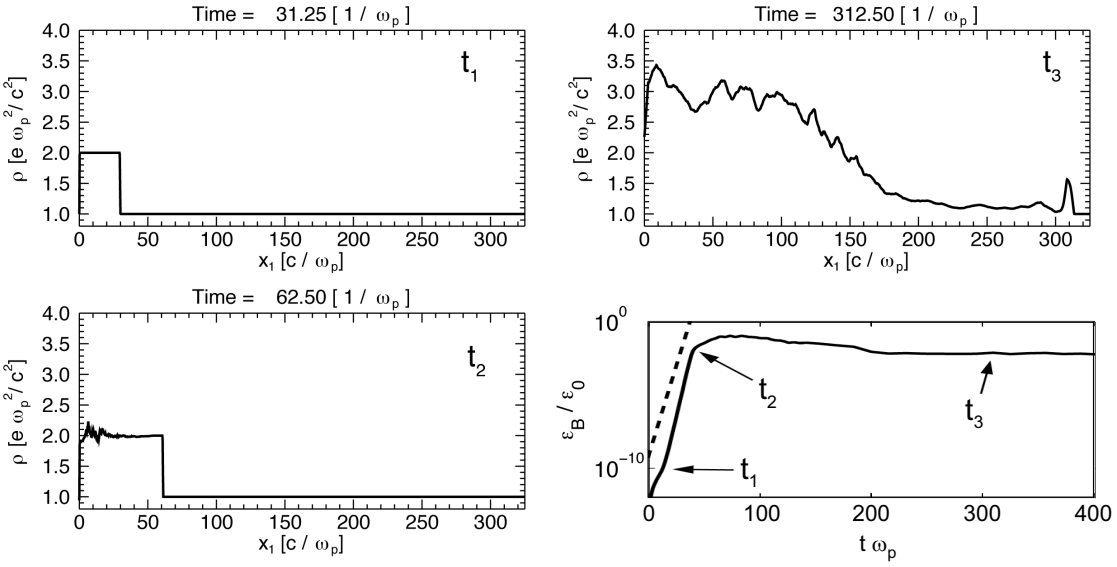

Figure 2.16. Integrated density in the direction normal to the flow at three different times during a typical shock formation simulation. The lower right plot shows the growth of the magnetic energy integrated over the transverse direction, and $x \in [0, 7\sqrt{\gamma_d}c/\omega_p]$. The dashed line is the theoretical growth rate. The initial Lorentz factor is $\gamma_d = 25$. All the field growth plots look qualitatively the same until $\gamma_d = 10^4$. The times associated to the density plots are indicated: t_1 corresponds to the start of the linear phase; t_2 to the end of the linear phase (*i.e.* the saturation phase); t_3 to the strongly non-linear phase, just after shock formation. 8 macroparticles per cell are used.

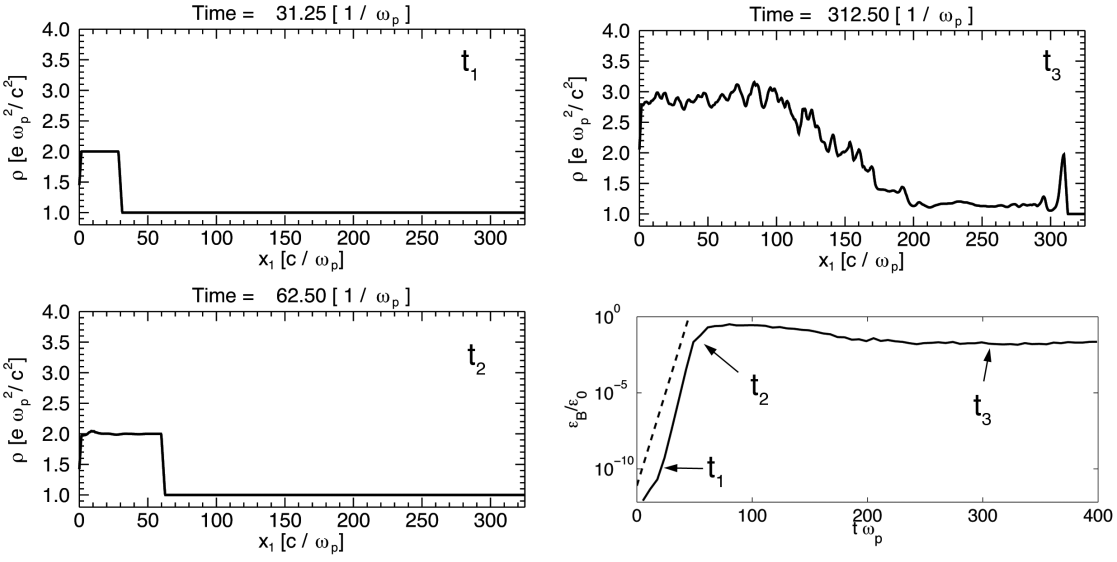

Figure 2.17. Same as Fig. 2.16, but using 800 particles per cell.

is made to bounce back against a wall and to interact with itself (Fig. 2.15), which enables to describe only half of the symmetric physical system. Periodic boundary conditions are applied in the transverse direction. A series of snapshots from a simulation with $\gamma_d = 25$ is displayed in Fig. 2.16. Only the right part of the system pictured on Fig. 2.15 is showed. These successive plots of the integrated density along the direction normal to the flow show the instability development in the overlap region at twice the upstream density, before the shock density jump builds up. The three snapshots illustrate three distinct phases of the instability: t_1 corresponds to the start of the linear phase; t_2 to the end of the linear phase (*i.e.* the saturation phase); t_3 to the strongly non-linear phase, just after shock formation. The peak density in the overlap region has increased from a ballistic value of two to expected value of ~ 3 in a 2D relativistic shock. We observe in the simulations that in phase 1 the fields grow in a well defined spatial region that extends up to $\sim 7\sqrt{\gamma_d}c/\omega_p$ from the wall. The saturation time τ_s (t_2 in Figure 2.16) is defined as the end of the exponential growth of the field energy integrated over the region $x \in [0, 7\sqrt{\gamma_d}c/\omega_p]$.

As discussed in Sec. 2.6.4, simulations have been run with 8 particles per cell. Figure 2.17 displays the same data as Fig. 2.16, but running the simulations with 800 particles per cell. Except for a somewhat smoother density profile in the shocked (downstream) region, no significant difference can be found between the two simulations.

As will be checked, the instability at play can be interpreted within a purely temporal formalism, although the geometry is not periodic. As it amplifies a seed field from its initial fluctuation value to saturation, the instability governs this first phase of the shock formation process for a time τ_s that we labeled "saturation time". A theoretical determination of this time, in good agreement with the simulations, is the main result of this section. Not only does τ_s give a lower bound for the shock formation time, it also sheds light on the amplitude of the amplified initial thermal fluctuations.

2.6.1 Instability analysis

Here we deal with the first phase of the shock formation, namely the instability in the overlap region, where we focus on relativistic shocks. Let us start ignoring the finite geometry at stake here, and analyze the system as if it were homogeneous. The full unstable $\mathbf{k}$ spectrum has been analyzed long ago in the cold regime, where a shell is much denser than the other (Faĭnberg *et al.* 1970; Watson *et al.* 1960b; Bludman *et al.* 1960). These early results were recently generalized to the hot symmetric case (Bret & Deutsch 2005; Bret *et al.* 2010b). For wave-vectors aligned with the flow, we find two-stream unstable modes. For wave-vectors normal to the flow, we find the current filamentation, or Weibel, instability. Finally, modes propagating at arbitrary angle with the flow are also unstable. As the two plasmas penetrate each other, all the modes are excited. But the fastest growing one quickly overcomes the others, and shapes the linear phase. For the case we consider, a calculation of the growth rate for every possible wave number is pictured in Fig. 2.18 for two Lorentz factors, $\gamma_d = 1.1$ and 10, in terms of the reduced wave-vector,

$$\mathbf{Z} = \frac{\mathbf{k}v_d}{\omega_p}, \tag{2.104}$$

where v_d is the initial velocity of the plasmas, and ω_p the electronic plasma frequency of one of them. The calculation, like the simulation, is conducted in the center of mass reference frame, where the two plasmas come from opposite directions at the same speed. For $\gamma_d = 1.1$, the dominant mode is oblique while for $\gamma_d = 10$, current filamentation dominates. An in-depth study of the problem found indeed that only these two types of modes can dominate (Bret & Deutsch 2005; Bret *et al.* 2010b). The transition from oblique to filamentation occurs for $\gamma_d = \sqrt{3/2}$, as explained in Appendix 6.3. Note that although the analysis of Refs. (Bret & Deutsch 2005; Bret *et al.* 2010b) was conducted for counter-streaming *electron* beams, counter-streaming *pair* beams are linearly equivalent because

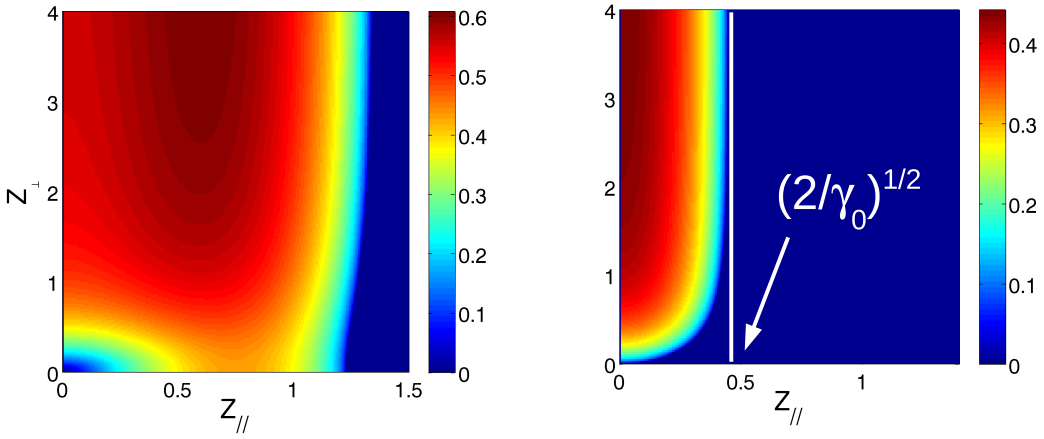

Figure 2.18. (Color Online) Growth-rate in ω_p units, in terms of $\mathbf{Z} = \mathbf{k}v_d/\omega_p$ for $\gamma_d = 1.1$ (*left*) and $\gamma_d = 10$ (*right*).

the linear regime scales like the square of the charge.

We thus find that, for $\gamma_d < \sqrt{3/2}$, current filamentation should govern the interaction with a growth rate,

$$\frac{\Gamma}{\omega_p} = \frac{v_d}{c}\sqrt{\frac{2}{\gamma_d}} \sim \sqrt{\frac{2}{\gamma_d}}. \tag{2.105}$$

Comparing this value to the growth of the field observed in the overlap region results in a very satisfactory agreement, as evidenced in Fig. 2.16. We have also checked that the Weibel/oblique transition does occur around $\gamma_d \simeq \sqrt{3/2}$. Note that a shock *also* forms for $\gamma_d < \sqrt{3/2}$ (not shown).

This oblique/filamentation transition may seem at odds with previous works on instability hierarchy (Bret & Deutsch 2005; Bret 2009; Bret *et al.* 2010b), suggesting filamentation always governs the spectrum for symmetric systems. Electrostatic instabilities with parallel wave vectors have equally been found slower than filamentation for relativistic flows (Michno & Schlickeiser 2010; Shaisultanov *et al.* 2012). However, the relevant hierarchy maps, like Fig. 5 of Ref. (Bret 2009) for example, already showed filamentation does not govern symmetric systems all the way down to $\gamma_d = 1$. Instead, a very narrow γ-region was found in which oblique electrostatic modes to dominate, between $\gamma_d = 1$ and a unspecified value of $\gamma_d > 1$. Until now, this little gap has not attracted much interest, and it is still overall fair to say that in the relativistic regime, filamentation is the important instability for symmetric systems.

How can a theory developed for an homogeneous system, apply to the present inhomogeneous system? The instability time scale varies like $\Gamma^{-1} \propto \sqrt{\gamma_d}/\omega_p$. Now, by a time $\sim \sqrt{\gamma_d}/\omega_p$ after contact, the overlap region is already $d \sim \sqrt{\gamma_d}c/\omega_p$ wide. But the parallel scale length relative to instabilities is precisely $\lambda = \sqrt{\gamma_d}c/\omega_p$ [Fig 2.18 (right)]. Even if at the very beginning of the instability process, $d \gg \lambda$ is not fulfilled, the strong inequality is quickly realized with time passing, so that most of the instability process develops in a setting fulfilling the homogeneous approximation. A rigorous demonstration of this growth behavior would require a space-time (instead of purely temporal) perturbative analysis over the overlap region, which has not been carried in this Manuscript.

The knowledge of the growth-rate (2.105) allows for an approximate timing of the linear phase. Assuming the instability amplifies a seed field of amplitude B_i up to a saturation level B_s, we can

write for the saturation time τ_s,

$$B_f = B_i e^{\delta \tau_s} \quad \Rightarrow \quad \tau_s = \frac{1}{2\delta} \ln\left(\frac{B_f^2}{B_i^2}\right), \tag{2.106}$$

where, for convenience, we consider the field energy B^2 ratio, instead of the field itself. Determining the saturation time amounts then to determine the initial and final fields. We will first discuss the saturation field.

2.6.2 Field at saturation

One way to derive the value of the saturation field $B_f = B(\tau_s)$, consists in stating that the field grows exponentially as long as it is small enough for the system to fit the linear approximation. Since a field B_f affects particles on a time scale given by the cyclotron frequency, this implies (Achterberg *et al.* 2007)

$$\frac{qB_{f1}}{\gamma_d m_e c} = \delta \quad \Rightarrow \quad B_{f1} = \frac{\gamma_d m_e}{q_e} \Gamma c. \tag{2.107}$$

Another way of evaluating the field at saturation is to write that as it grows, particles start oscillating transversely in the field of the fastest growing k_m at the bounce frequency (Davidson *et al.* 1972; Achterberg & Wiersma 2007),

$$\omega_B^2 = \frac{q_e v_d k B}{\gamma_d m_e c} \sim \frac{q_e k_m B}{\gamma_d m_e}. \tag{2.108}$$

Here again, linear theory yielding to an exponential growth breaks down when $\omega_B \sim \Gamma$, which gives a second value for the field at saturation,

$$B_{f2} = \frac{\gamma_d m_e}{q_e} \frac{\gamma^2}{k_m}. \tag{2.109}$$

Finally, one can write the linear approximation breaks down when the Larmor radius of the particles in the growing field equates k_m^{-1}Califano *et al.* (1998). This third criterion thus gives,

$$B_{f3} = \frac{\gamma_d m_e}{q_e} c^2 k_m, \tag{2.110}$$

where $v_d \sim c$ has been used. The dominant wavevector at saturation k_m has been numerically measured with

$$k_m \sim \frac{\omega_p}{c\sqrt{\gamma_d}}. \tag{2.111}$$

Making use of the growth rate expression (2.105) gives

$$B_{f1}^2 = 2\gamma_d b^2, \tag{2.112}$$
$$B_{f2}^2 = 4\gamma_d b^2, \tag{2.113}$$
$$B_{f3}^2 = \gamma_d b^2, \tag{2.114}$$

where

$$b = \frac{m_e c \omega_p}{q_e}, \tag{2.115}$$

is the magnetic field unit of the simulations.

The magnetic field for the filamentation instability grows like $\sin(ky)e^{\Gamma t}$. As a result, particles in the vicinity of $y = 0$ $[\pi]$ are the ones involved in the second saturation mechanism, described by Eq. (2.109). Particles near $y = \pi$ $[\pi]$ experience the kind of trapping involved with Eqs. (2.107,2.110).

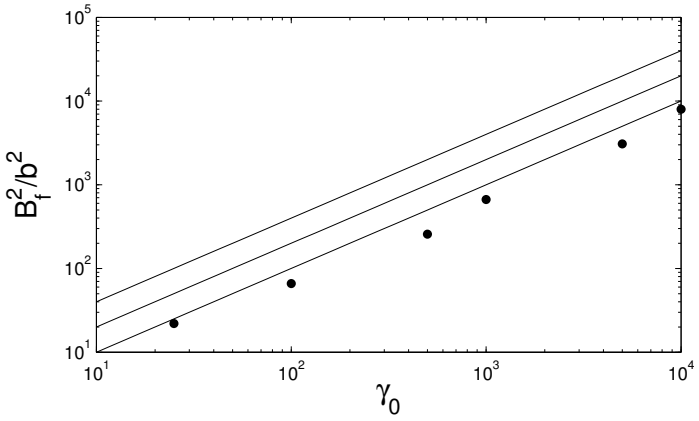

Figure 2.19. Field at saturation from the simulations (*circles*), compared with Eqs. (2.112-2.114).

The linear hypothesis is first broken when the field reaches $\min(B_{f1}, B_{f2}, B_{f3}) = B_{f3}$. Figure 2.19 compares the field observed in the simulation at the end of the linear phase with Eqs. (2.112-2.114). The agreement with Eq. (2.114) is good and the correct scaling is recovered. At any rate, a numerical pre-factor cannot play a major role once inserted into the logarithm of Eq. (2.106) for the saturation time.

A consequence of the observed γ_d scaling is that the field energy relative to the beam one reads,

$$\frac{B_f^2/2\mu_0}{\gamma_d n m_e c^2} \sim 1, \tag{2.116}$$

displaying the near-equipartition already noted by various authors (Medvedev & Loeb 1999; Silva *et al.* 2003).

2.6.3 The initial field amplitude

We now turn to the evaluation of the initial field amplitude. The idea is that the instability mechanism picks up a seed field from the spontaneous fluctuations of the system, and amplifies it. A first question to ask could be the following: should we consider the instability starts from the fluctuations of one single plasma, or from the fluctuations of the system formed by the two overlapping plasmas? In other words, should we consider the fluctuations of the system *before* it turns unstable, or *after*? We will now argue that we consider the fluctuations of the stable, isolated plasma shells, *before* they inter-penetrate. Before they overlap, each plasma shell comes with its own fluctuations. As they start to overlap, the fluctuation fields for each plasma will adapt to each other. But on the very same time scale, the instability process begins. We thus consider that the seeds for the instability are those present in the system *before* the plasmas started to overlap. Filamentation for example, needs unbalanced counter-streaming currents to start growing. As they approach each other, both plasma shells already display spontaneous fluctuations normal to the drift. When they start to inter-penetrate, these fluctuations instantaneously provide the needed unbalanced currents to destabilize the whole system. Hence, their amplitude will be the amplitude they had *before* they go unstable.

Fluctuation power spectrum

We are interested in the magnetic fluctuation spectra of a relativistically drifting, equilibrium plasma. One could assume the instability process is indeed a initial condition problem, so that it can discriminate the unstable $\mathbf{k}$'s, but not their frequency. In such case, the ω-integrated spectra Eqs. (2.75) and (2.86) should be used to derive the initial field amplitude. We here argue instead that the instability process can discriminate the fluctuation frequency, but up to a precision $\pm\delta$. In other words, $\omega = 0$ is selected for growth, but this selection should be inaccurate to an order $\pm\delta$ because during the first growth period, the plasma cannot discriminate waves varying at $\omega = 0 \pm \delta$ from the ones at $\omega = 0$. The two approaches will be later compared, and the "$\omega = 0$ selection" will be found in slightly better agreement with the simulations.

The k-integration domain

Whether we use Eqs. (2.75) and (2.86) for the available energy for growth, we thus need to integrate over a $\mathbf{k}$ domain. As indicated in Fig. 2.18, wave-vectors selected for growth form a narrow band around the normal axis, extending to infinity and of width

$$Z_\parallel \sim \sqrt{\frac{2}{\gamma_d}} \Longrightarrow k_{\parallel,max} \sim \sqrt{\frac{2}{\gamma_d}}\frac{\omega_p}{c}, \tag{2.117}$$

in the parallel direction (we set here $v_d \sim c$).

Regarding the integration domain in the normal direction, it has already been mentioned that the fastest growing mode has been numerically found for $k_\perp \sim \omega_p/c\sqrt{\gamma_d}$. We shall thus integrate Eqs. (2.75) and (2.86) from $k_{\perp,min}$ to $k_{\perp,max}$ with,

$$\begin{aligned} k_{\perp,min} &= \frac{1}{2}\frac{\omega_p}{c\sqrt{\gamma_d}}, \\ k_{\perp,max} &= 2\frac{\omega_p}{c\sqrt{\gamma_d}}, \end{aligned} \tag{2.118}$$

where the factors 1/2 and 2 have been arbitrarily chosen to bracket $k_m = \omega_p/c\sqrt{\gamma_d}$. Note that the end result is almost independent of these constants because of the logarithm function in Eq. (2.106).

Saturation time from ω-integrated fluctuations

The ω-integrated energy density, Eq. (2.86) is now integrated in the following way. Clearly, it is an *averaged* initial amplitude over the modes likely to grow the most. The result reads,

$$\frac{B_i^2}{2\mu_0} = \pi\sqrt{\frac{2}{\gamma_d}}\left(\frac{15}{4\gamma_d} + \mu\ln\left[\frac{1+4\gamma_d/\mu}{1+\gamma_d/4\mu}\right]\right)\left(\frac{\omega_p}{c}\right)^3 T. \tag{2.119}$$

Inserting this result in Eq. (2.106) for the saturation time, we find

$$\begin{aligned} \tau_s\omega_p &= \frac{\sqrt{\gamma_d}d}{2\sqrt{2}}\ln\left[\frac{n(c/\omega_p)^3}{\sqrt{2}\pi}\frac{\mu\gamma_d^{3/2}}{\frac{15}{4\gamma_d}+\mu\ln\left[\frac{1+4\gamma_d/\mu}{1+\gamma_d/4\mu}\right]}\right] \\ &\sim \frac{\sqrt{\gamma_d}}{2\sqrt{2}}\ln\left[\frac{2\sqrt{2}}{15\pi}n\left(\frac{c}{\omega_p}\right)^3\sqrt{\gamma_d}\mu\right], \quad \text{for} \quad \gamma_d \ll \mu, \end{aligned} \tag{2.120}$$

where n is the plasma density.

Saturation time from fluctuations near $\omega = 0$

While the **k**-integration domain remains unchanged, an ω-integration domain is now needed. As stated earlier, physical reasoning would suggest an integration over $[-\delta, \delta]$, because the instability mechanism cannot discriminate fluctuations with $\omega = 0$ from the ones with $-\delta < \omega < \delta$ during the first growth period or so. Once a given fluctuations has been significantly amplified, i.e, has grown during $\sim \delta^{-1}$, it will keep on growing.

But the integration domain is eventually much smaller than $[-\delta, \delta]$ because the spectral density $B_{k_\perp,\omega}$ is extremely peaked around $\omega = 0$ with,

$$B_{k_\perp,\omega} = B_{k_\perp,0}\left(1 - \frac{\omega^2}{\delta\omega^2} + o(\omega^2)\right). \tag{2.121}$$

At $k_\perp = \omega_p/c\sqrt{\gamma_d}$, the spectral width $\delta\omega$ is given by a Taylor expantion of Eq. (2.75) around $\omega = 0$

$$\delta\omega \sim \frac{\omega_p}{\gamma_d\sqrt{6\mu}}, \tag{2.122}$$

which turns out thinner than the growth rate $\delta = \omega_p\sqrt{2/\gamma_d}$, especially for $\mu \gg 1$. The energy density Eq. (2.75) is therefore integrated over $[-\delta\omega, \delta\omega]$, yielding the magnetic seed energy

$$\frac{B_i^2}{2\mu_0} = \int_{k_{\perp,min}}^{k_{\perp,max}} 2\pi k_\perp dk_\perp \int_{-k_{\parallel,max}}^{k_{\parallel,max}} dk_\parallel \int_{-\delta\omega}^{\delta\omega} d\omega \frac{B_{k_\perp,0}^2}{2\mu_0}. \tag{2.123}$$

Given the narrowness of the $(\mathbf{k}, \omega)$ integration domain, we set $B_{k,\omega} \sim B_{k_\perp,0}$ as given by Eq. (2.75) in the integrand. A little algebra gives

$$\frac{B_i^2}{2\mu_0} = \frac{15\sqrt{\pi/6}}{4}\frac{\sqrt{\gamma_d}}{\mu}\left(\frac{\omega_p}{c}\right)^3 mc^2, \tag{2.124}$$

and the saturation time can be cast in the form

$$\tau_s\omega_p = \frac{\sqrt{\gamma_d}}{2\sqrt{2}}\ln\left[\frac{4}{15}\sqrt{\frac{6}{\pi}}n\left(\frac{c}{\omega_p}\right)^3\sqrt{\gamma_d}\mu\right]. \tag{2.125}$$

Finally, it is to be reminded that our theory has been implemented for a 3D geometry, whereas simulations are 2D. The corresponding 2D saturation time is derived in Appendix 6.4 and reads

$$\tau_s\omega_p = \frac{\sqrt{\gamma_d}}{2\sqrt{2}}\ln\left[4\times 10^2\sqrt{\frac{\pi}{3}}\frac{\mu}{\gamma_d}N_p\right], \tag{2.126}$$

where N_p is the number of macro-particles per cell.

2.6.4 Comparison with simulations

In order to test the theory in the early stage of shock formation, ab-initio particle-in-cell simulations have been performed using the code OSIRIS (Fonseca *et al.* 2002, 2008). The shock is launched with the piston-wall method, where two counter-propagating symmetric plasma beams are produced by injecting one beam by a cathode from one side of the simulation box, and being reflected at the opposite wall. Here we simulate a low temperature pair plasmas $\mu = mc^2/T = 10^6\gamma_d$, and Lorentz factor $\gamma_d \in [25, 10^4]$, so that $1 \ll \gamma_d \ll \mu$ is fulfilled. The particles are injected along the x axis with a temporal resolution $\Delta t = 0.025\sqrt{\gamma_d}/\omega_p$ and the size of a cell being $\Delta x = 0.05\sqrt{\gamma_d}c/\omega_p$, using quadratic interpolation and 8 particles per cell. The two-dimensional box with $L_x = 125\sqrt{\gamma_d}c/\omega_p$

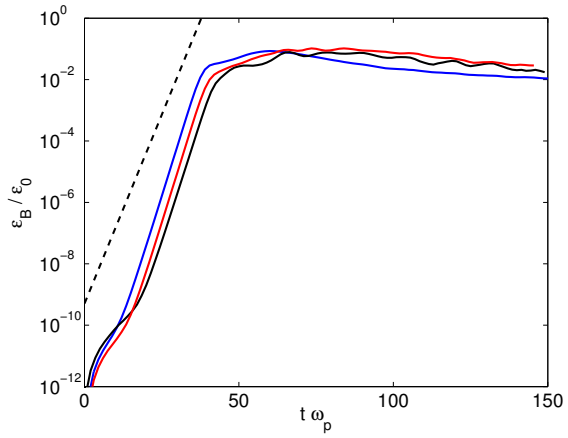

Figure 2.20. Magnetic field energy evolution for different simulation setups and $\gamma_d = 25$. *Black*: piston-wall method, *Red*: full shock picture, *Blue*: periodic system of counter-streaming beams, *Black dashed*: theoretical growth rate. A detailed description of the models is given in the text.

and $L_y = 5\sqrt{\gamma_d}c/\omega_p$ has absorbing boundaries for the particles on the right x side and is periodic along y. For the fields, conducting boundaries are used at the perfectly reflecting left wall and open boundary conditions on the right side. Note that this results in a grid size much larger than the Debye length, which could trigger the grid instability. However, for the combination of grid sizes and number of particles per cell we have used, this instability has a much longer time scale than the typical times analyzed in our simulations. Moreover, in our simulations we use higher order particle shapes and current smoothing (a 5 pass binomial smooth is used). This improves significantly the energy conservation properties of the algorithm and slows down even further numerical heating Fonseca *et al.* (2008). Simulations performed with smaller cell sizes and larger number of macroparticles (up to 800) were performed. No significant deviations was found (see Fig. 2.17).

Since we are interested in the early stage of shock formation, the question arises as to whether the piston-wall method is appropriate. We first simulate the periodic system of counter-streaming beams, corresponding to the model of unstable fluctuations that is the basis of our theoretical approach. In this case, no shock is formed and we are able to identify the growth rate and saturation time of the magnetic field energy. We compare the periodic system with the piston-wall setup and, furthermore, with the full shock formation process, where in x direction absorbing boundaries are used for the particles and conducting boundaries for the fields. In the latter case, two symmetric shocks are propagating outwards and this allows us to identify non-physical fields at the reflecting wall in the piston-wall setup.

Figure 2.20 shows the evolution of the magnetic field energy W_B normalized to the kinetic energy in the box at time zero K_0 for the three different setups for $\gamma_d = 25$. The comparison shows that the growth rate and saturation level of the field is independent of the setup. The theory of the periodic system applies to the non-periodic system as well, where the overlapping beams go unstable, and the fields at the reflecting wall do not seem to affect this process. There is only a small deviation in the initial fluctuation level, which for $\gamma_d = 25$ leads to a shift of the saturation time $\sim \omega_p^{-1}$ between the different setups. On the relevant time scales for the saturation time (see Fig. 2.21) this deviation is negligible, so that we conduct the simulations with the piston-wall setup in order to save simulation time.

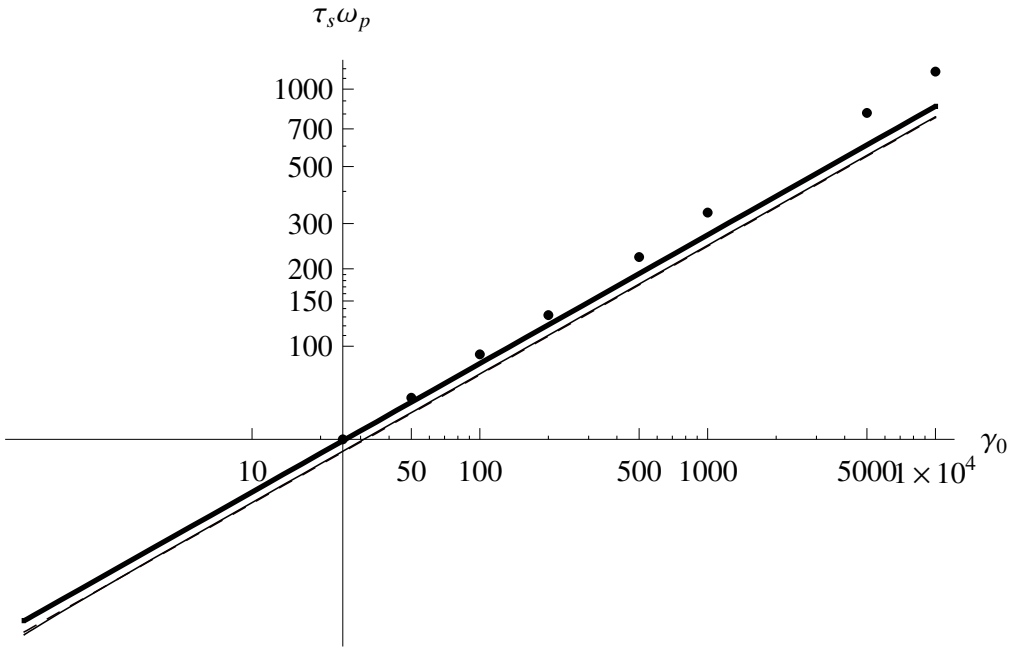

Figure 2.21. Saturation time $\tau_s\omega_p$ from the PIC simulations, *circles*, from the fluctuations near $\omega = 0$ Eq. (2.125), *bold line*, from the ω-integrated fluctuations Eq. (2.120), *thin line*, and from the 2D $\omega = 0$ formula (2.126), *thin dashed line*. The 3D ω-integrated and the 2D $\omega = 0$ theories give almost the same result.

Theoretical results are now bridged setting

$$n\left(\frac{c}{\omega_p}\right)^3 = \frac{8}{0.05^3\,\gamma_d^{3/2}}. \tag{2.127}$$

Figure 2.21 compares the saturation time measured in the simulations with the ω-integrated or $\omega = 0$ (2D or 3D) formulae. As expected, considering only the fluctuations around $\omega = 0$ yields a larger saturation time, arising from a lower initial noise amplitude. The slight underestimation of the simulation results can be attributed to at least two factors. On the one hand, Eq. (2.120) necessarily remains a lower limit, as the integration domain only brackets the mode selected for growth. On the other hand, it is difficult to model the level of fluctuations in the simulations realistically, since it is dependent and sensitive on the choice of numerical parameters of the simulations.

2.7 Summary and conclusions

The power spectra of the electric and magnetic fluctuations spontaneously induced in unmagnetized, collisionless plasmas described by relativistic Maxwell-Jüttner distribution functions have been explicitly evaluated for wave vectors parallel or normal to the plasma mean velocity. Closed-form analytical formulae of the ω-integrated spectra have been worked out in all cases, distinguishing between the contributions of the subluminal and supraluminal electromagnetic fluctuations. We have found that the well-known nonrelativistic results (Akhiezer *et al.* 1975) still hold for nondrifting relativistic plasmas. Use has been made of the generalized Fried and Gould method (Fried & Gould 1961) to solve for the full set of eigenmodes of the system. This scheme, evidently, could also handle unstable systems and oblique wave vectors.

The particular case of magnetic fluctuations with wave vectors normal to the beam velocity has

been treated in details. We have found that the long-wavelength ($k_y \ll \omega_p\sqrt{\mu}/c$) spatial magnetic fluctuations exceed the short-wavelength fluctuations by a factor γ_d^2. An explicit expression of the $\omega = 0$ magnetic fluctuations is also provided. We have confronted our theoretical results to 1-D PIC simulations of drifting thermal plasmas. Overall, the theoretical spectra are well reproduced in the subluminal region. The eigenmode dispersion relations are accurately captured, yet with somewhat underestimated energy in the supraluminal domain.

Finally, our formula has served to estimate the seed and saturation time of the relativistic filamentation instability of counterpropagating plasmas. Fair agreement with PIC simulations has been found provided both plasmas are in thermal equilibrium before overlapping (Bret *et al.* 2013).

Part II

Saturation of the ion Weibel instablity and collisionless shocks

s

Chapter 3

Non-relativistic ion Weibel instability and saturation regime

This chapter aims to study the ion-Weibel instability triggered by two symmetric and counter-propagating ion-electron beams in a simple academic framework. The plasma drift velocities considered corresponds to a high velocity, although non-relativistic: $0.01c \lesssim v \lesssim 0.5c$. We will address a fully predictive model of the plasma parameter evolution in its saturation regime.

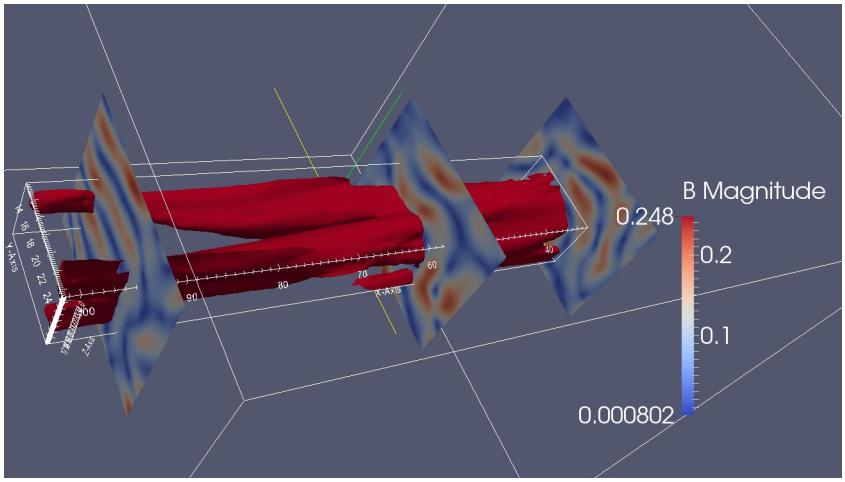

Figure 3.1. Coalescence of two ion current filaments (red current isosurface) in a three dimensional periodic simulation. The system consists of two counter-propagating, neutral plasmas drifting at $v = 0.2c$ with a reduced ion mass of $m_i = 100m_e$. Slices of the magnetic field (normalized to $m_e\omega_{pe}/e$) amplitude are superposed.

3.1 Introduction

Section 2.6 has dealt with the unstable interaction of two relativistic electron/positron beams. In this case, the Weibel instability prevails over the other kinetic instabilities as shown in Refs. (Bret & Deutsch 2005; Bret *et al.* 2010b). The instabilities triggered by the superposition of two beams are more numerous when we consider collisionless ions/electrons plasmas ($m_i > m_e$) in the non-relativistic regime ($\beta_d \lesssim 0.5$). Determining which instability prevails over the others is then trickier. In this chapter, we will focus on non-relativistic electron-ion colliding plasmas whose late-time dynamics is ruled by the ion Weibel instability which, in turns, may trigger a collisionless shock. Although Stockem *et al.* (2014) recently performed a parametric location of the collisionless shocks driven by electrostatic or Weibel-filamentation instability, the growth, the saturation of the fields and the evolution of the plasma parameters remain poorly understood. In the following, our goal will be to shed light on the various microscopic kinetic processes likely to occur in colliding-beam systems up to a stage of strong isotropisation, and therefore close to shock formation. Special emphasis will be put on modelling the nonlinear phase of the ion Weibel instability. For that purpose, a set of hydrodynamic equations will be derived from quasilinear kinetic theory and combined to a model of magnetic filament coalescence. We will consider a simplified configuration where the beams are assumed homogeneous and infinite.

This chapter is organized as follows. The two first sections mainly present the results of a reference simulation, describing the unstable interaction of two symmetric counter-propagating electron-ion beams. In Sec. 3.2.1, we study the first instability appearing in this system shown to be mainly electronic and longitudinal. We will then show that for a vast part of the parametric space $\beta_d < 0.5$, $T_{ex} < 10 m_e c^2$, the longitudinal instability called the electron acoustic instability (Bohm & Gross 1949) rules the early times of the field growth. We will then demonstrate that the electron Weibel instability rapidly dominate the system and eventually lead to an ion-Weibel instability. The saturation regime of the ion-ion Weibel instability will then be studied in Sec. 3.3. A quasilinear model (Davidson *et al.* 1972) will be presented and approximate relations between the magnetic field spectrum and the plasma parameters will be obtained. The comparison with various PIC simulations in Sec. 3.3.4 will evidence the robustness of these simple relations. In order to work out a self-consistent nonlinear model, we will introduce a simple description of the filaments' coalescence. The resulting set of equations, of which we will derive an approximate analytical solution, will be shown in fair agreement with PIC predictions of the evolution of the ion beam's parameters.

3.2 Main instabilities triggered by counter-streaming, non-relativistic electron-ion beams

The PIC simulations presented in this chapter are 3D in the momentum space. The temporal and spatial steps are respectively $\Delta t = 0.069\omega_{pe}^{-1}$ and $\Delta x = \Delta y = 0.1c/\omega_{pe}$. The simulation box has periodic boundary conditions and its size is $L_x = 102.4c/\omega_p$ and $L_y = 96c/\omega_p$. The Esirkepov current deposition scheme is used with a third interpolation order weight factor (see 6). We employ 50 macroparticles per mesh. The ions (of mass m_i subsequently defined) and electrons are initialized as counter-propagating Maxwell-Jüttner distributed beams (Eq. (1.22)) of temperature $T_{e,i} = m_e c^2/100$ and drift velocity $v_{de} = v_{di} = \pm v_d$. The density of each beam is normalized to the total electron density ($n_{i,e} = 0.5$).

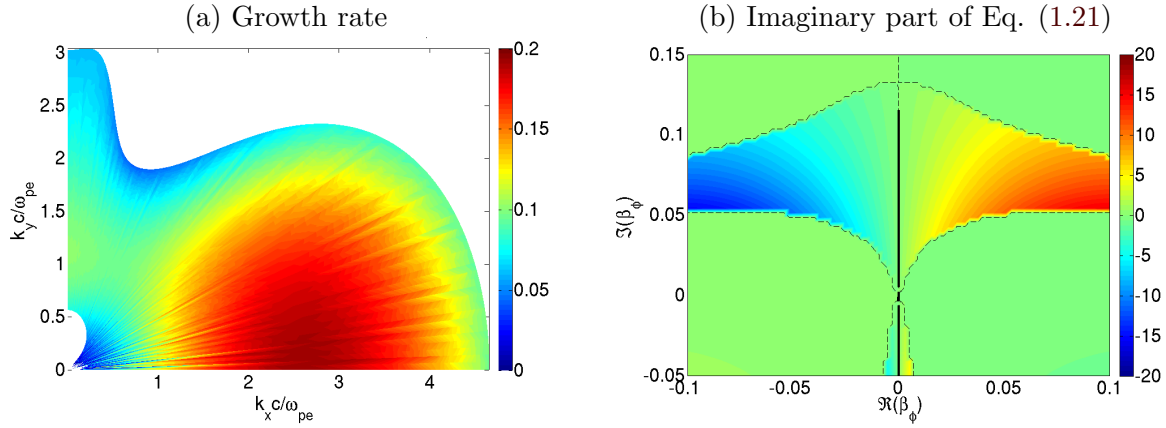

Figure 3.2. Eigenmodes in a system made of two symmetric electron-ion beams ($m_i = 100m_e$) with drift velocity $v_d = 0.2c$. (a) Growth rate $\Gamma(k_x, k_y)/\omega_{pe}$ in the $(k_x c/\omega_{pe},\ k_y c/\omega_{pe})$ plane, as computed from Eq. (1.21). The eigenmode's real frequency equal to zero for all the resolved growth rate. (b) $\Im[\mathcal{G}_2(\beta_\phi)]$ [Eq. (1.21)] as a colored map in the complex phase speed plane for $\theta = 0$. All the locus verifying $\Im(\mathcal{G}_2) = 0$ are superposed as thin black dashed lines and the eigenmode ($\Im(\mathcal{G}_2) = 0$ and $\Re(\mathcal{G}_2) > 0$) is in plain black line.

3.2.1 The two-stream instability triggered by overlapping symmetric ions/electrons plasma beams

We will now focus on the system of drift velocity $v_d = \pm 0.2c$ with an ion mass of $m_i = 100m_e$. Making use of the dispersion relation solver of Sec. 1.1.2, we can compute the growth rate map $\Gamma(k_x, k_y)$. Figure 3.2(a) shows a broad continuum of unstable modes and, in particular, a continuous transition from the longitudinal electron electrostatic instability (*i.e.* the well-known electron two-stream instability with $k_y = 0$) to the transverse electron Weibel-filamentation (with $k_x = 0$). The Weibel-filamentation instability has a maximum growth rate of $\Gamma \simeq 0.1\omega_{pe}/c$ around $k_y \simeq 1.\omega_{pe}/c$, $k_x = 0$ close to the non-relativistic cold fluid limit, $\Gamma_W/\omega_{pe} \simeq \beta_d = 0.2$ and $k_y c/\omega_{pe} \simeq 1$ (Achterberg & Wiersma 2007). Using an infinite ion mass (fixed ions) yields no significant difference on the Weibel growth rate. Because the electron mainly contribute to this instability, it will be termed electron Weibel-filamentation. The dominant longitudinal model ($k_y = 0$) is located at $k_x \simeq 3\omega_{pe}/c$ and has a growth rate $\Gamma \simeq 0.2\omega_{pe}$. With fixed ions, it is shifted to $k_x \simeq 3.8\omega_{pe}/c$ and $\Gamma \simeq 0.14\omega_{pe}$. It thus corresponds to an electron two-stream instability (Bohm & Gross 1949), resulting in the growth of the E_x field component, shown in Fig. 3.3(a) for $t\omega_{pe} < 40$. We can compute the effective growth rate in the simulation of $\Gamma/\omega_{pe} \simeq 0.14$, which is consistent with the theoretical value. Note that, as the Weibel-filamentation instability, the electron two-stream does not propagate ($\omega_r = 0$) due to the symmetry of the ion and electron beams in our system (Bret 2009).

Consequently, the electron two-stream instability is expected to dominate the Weibel-filamentation instability at early times as supported by the simulation results of Fig. 3.3(a-d). The electrostatic instability heats the electrons in the x direction. Figure 3.3(b) shows that the axial electron temperature (T_{ex}) rises by a factor ~ 2 over $\simeq 30\omega_{pe}^{-1}$ while the transverse temperature (T_{ey}) stays unchanged. In order to understand the influence of the longitudinal electron heating on the system evolution, we will compare the Weibel-filamentation and the two-stream growth rates for a rising axial temperature. We need to increase T_{ex} while keeping T_{ey} fixed, which requires a two-temperature model distribution. Thus, a bi-Maxwellian (1.65) distribution will be used instead of the input 3D Maxwell-Jüttner distribution (1.22). The neglect of the z-momentum is valid in the non-relativistic regime ($v_d \ll c$ and $T_{x,y} \ll m_e c^2$). Figure 3.3(c) shows that the electron energy (black dashed line in Fig. 3.3(a)) decreases by only 20% for $t\omega_{pe} \lesssim 50$. Neglecting this variation, we can relate approximately the evolution of the electron average speed v_e to the axial temperature variation

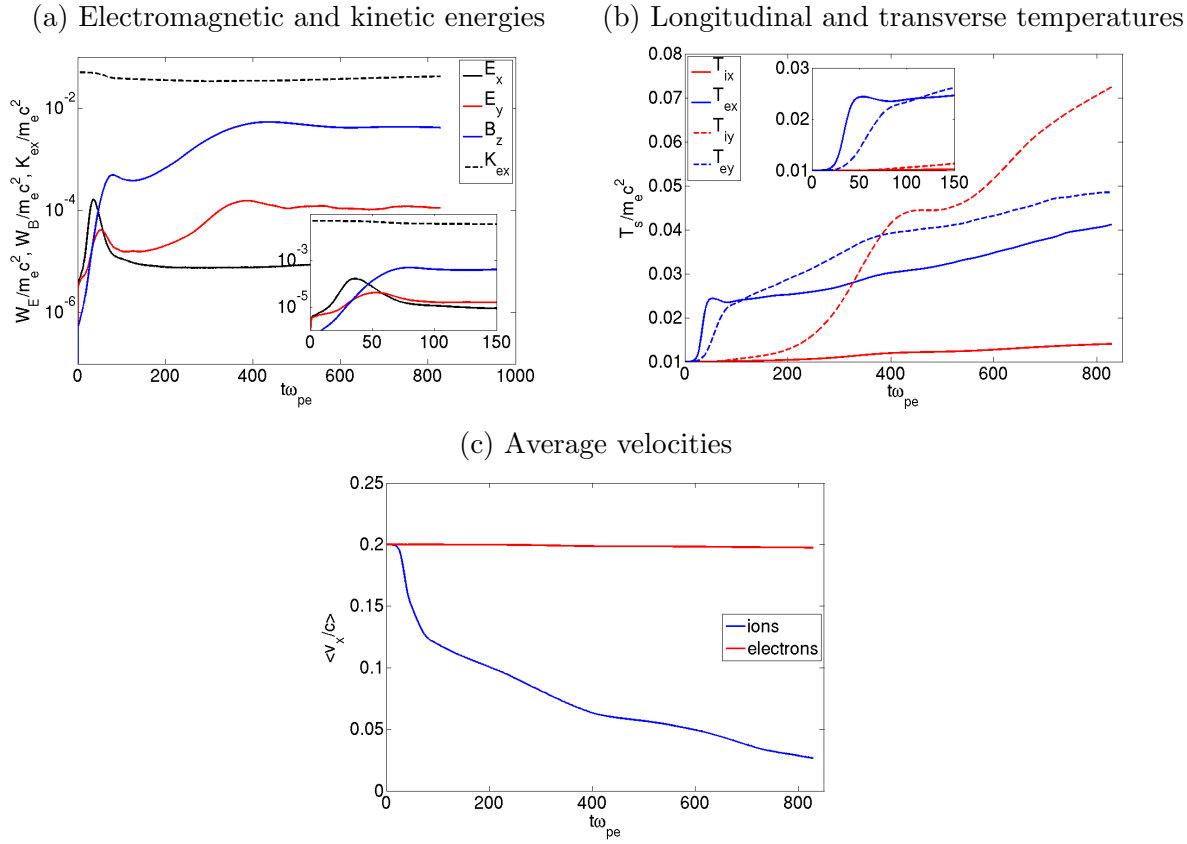

Figure 3.3. (a) Temporal evolution of the total E_x (black), E_y (red) and B_z (blue) electromagnetic energies. The electron longitudinal kinetic energy, K_{ex}, is superposed as a black dashed line. The time is normalized to ω_{pe}^{-1}. (b) Temporal evolution of the average T_x/m_ec^2 (dashed line) and T_y/m_ec^2 (plain line) for ions (red) and electrons (blue). The inset zooms in on the early-time phase. (c) Temporal evolution of the electron (blue) and ion (red) average speed $v_{de,i} = \langle v_x \rangle$

$\Delta T_{ex}(t) = T_{ex}^{(1)}(t) - T_{ex}^{(0)}(t)$:

$$v_{de}^{(1)}(t) = \sqrt{v_d^{(0)2} - \frac{\Delta T_{ex}}{m_e}}\,, \tag{3.1}$$

for unchanged T_{ey}. We then calculate the maximum growth rate of Weibel-filamentation and of the longitudinal two-stream instability for various T_{ex}, and v_{de} fulfilling Eq. (3.1), keeping fixed $T_{ey} = T_{ey}^{(0)} = 10^{-2}m_ec^2$. As is well known, the maximum two-steam growth rate decreases when T_{ex} increases. By contrast, the Weibel growth rate hardly varies due to its weak dependence on T_{ex} and to the weak evolution of the averaged electron speed [inset of Fig. 3.3(c)]. Figure 3.4 evidences that the Weibel-filamentation takes over the two-stream instability for $T_{ex} \geq 1.35 \times 10^{-2}m_ec^2$, so that a small axial heating is enough to ease significantly the initial two-stream instability. These results can be generalized so as to obtain the (T_{ex}, v_{de}) parameter region governed by the two-stream instability for fixed T_{ey} in the symmetric regime only. Following the isocontour of $K_{ex} = m_ev_{de}^2 + T_{ex}$ [black thin lines in Fig. 3.4(b)] starting from a given initial condition, gives the approximate evolution of T_{ex} and v_{de} over the course of the electron two-stream instability. Along this trajectory, v_{de} decreases and T_{ex} increases, hence weakening the two-stream growth rate. The Weibel-filamentation becomes equal to the two-stream growth rate, on the plain red curve in Fig. 3.4(b). Consequently, the electron two-stream domain of preponderance is located under the red curve of Fig. 3.4(a). As discussed in the next section, above the red curve the system can experience not only Weibel-filamentation but also an oblique instability. The electron two-steam saturates at $t\omega_{pe} \simeq 40$ as evidenced by the

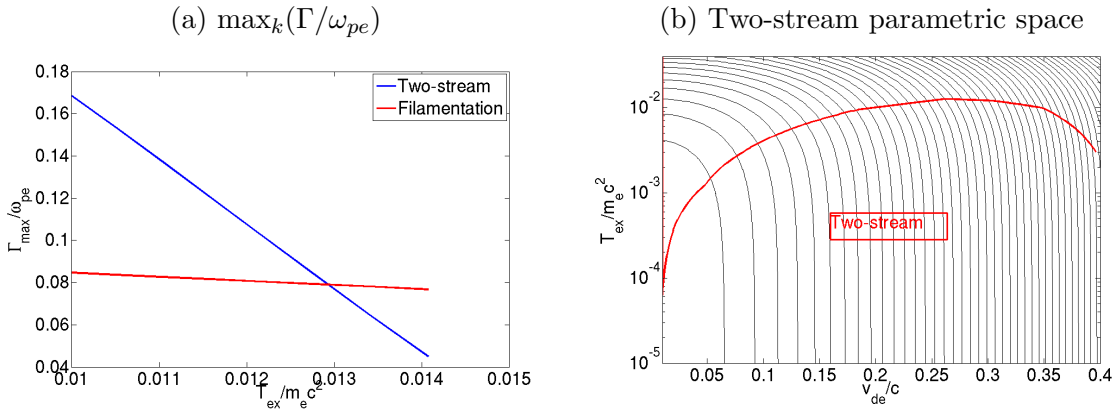

Figure 3.4. (a) Maximum growth rate $\Gamma_{\max}/\omega_{pe}$ for the two-stream instability (blue) and the Weibel-filamentation (red). Symmetric bi-Maxwellian electrons are considered with $T_{ex}(t)$ and $v_{de}(t)$ related through Eq. (3.1) and $T_{ey}^{(0)} = T_{ex}^{(0)} = m_e c^2/100$ and $v_{de}^{(0)} = 0.2c$ (fixed ions). (b) Locus of equal Weibel-filamentation and two-stream growth rate in the (T_{ex},v_{de}). The isocontours of $T_{ex} + m_e v_{de}^2$ are added as thin black lines.

maximum of the E_x-energy [Fig. 3.4(b)]. At this time, the longitudinal temperature has increased to $T_{ex} \simeq 0.017$, in fair agreement with the above estimate.

3.2.2 Transition to the ion-ion Weibel-filamentation instability

Just after saturation of the electron two-stream instability, the electromagnetic spectra of Figs. 3.5(a,b,c) at $t\omega_{pe} = 52$, show that a significant part of the electromagnetic fields are oblique ($k_x \neq 0$ and $k_y \neq 0$). The spectrum of the growing Ey fluctuations shows a maximum located around $(k_x\omega_{pe}/c, k_y\omega_{pe}/c) = (\pm 1, 1)$. The spectrum of E_x [Fig. 3.5(a)] is not purely longitudinal anymore and the E_x energy decreases at $t\omega_{pe} = 52$ while the E_y energy increases. Moreover the spectrum of E_y is mainly oblique which may be due to a transition from an electron two-stream to an oblique ion instability. Between $t\omega_{pe} = 40$ and 50, the inset of Fig. 3.3(b) evidences both a longitudinal and a transverse electron heating. This could correspond to an ion oblique instability (Forslund & Shonk 1970), although a clear identification is made difficult by its short duration.

Simultaneously, the magnetic energy overtakes the electric one for $t\omega_{pe} > 50$ and the corresponding spectrum is mainly transverse [Fig. 3.3(c)]. It exponentially increases over $10 < t\omega_{pe} < 70$ with an effective growth rate of $\Gamma/\omega_{pe} \simeq 0.06$, close the theoretical value of the electron-Weibel instability, $\Gamma_W/\omega_{pe} = 0.08$ [Fig. 3.4(a)]. Hence, while the system is experiencing a two-stream electron instability and associated saturation, a transverse magnetic modulation is growing at comparable rate and finely overcomes the electrostatic instabilities (electron two-stream or oblique). A first magnetic saturation occurs at around $t\omega_{pe} = 75$. At this time, the magnetic field energy dominates the other field components and its spectrum is even more transverse than at $t\omega_{pe} = 50$ [Fig. 3.3(c,d)]. Moreover, the electron drift velocity has then dropped by a factor ~ 2, which indicates that they start to be isotropized by the longitudinal and electromagnetic instabilities. Measuring the plasma parameters at $t\omega_{pe} = 75$ from Fig. 3.3(a,b,c) ($T_{ix} = T_{iy} = 0.01 m_e c^2$, $T_{ex} = 0.02 m_e c^2$, $T_{ey} = 0.025 m_e c^2$, $v_{di} = \pm 0.2c$, and $v_{de} = \pm 0.125c$), the theoretical maximum growth rate of the Weibel instability is $\Gamma_W/\omega_{pe} \simeq 0.03$ around $k_y c/\omega_{pe} \simeq 0.7$. For fixed ions, it drops down to $\Gamma_W/\omega_{pe} \simeq 0.018$ around $k_y c/\omega_{pe} \simeq 0.5$, which indicates that the ions start to play a role in destabilizing the system. This is also consistent with the transverse ion heating evidenced in the inset of Fig. 3.3(b) for $t\omega_{pe} \gtrsim 75$. The magnetic growth observed in Fig. 3.3(a), for $t\omega_{pe} \gtrsim 75$, is therefore mainly due to the ion Weibel instability, although the electrons do play a role, at least at the beginning. The exponential increase of W_{B_z} for $200 < t\omega_{pe} < 400$, is characterized by an effective growth rate of $\Gamma_W/\omega_{pe} \simeq 8 \times 10^{-3}$

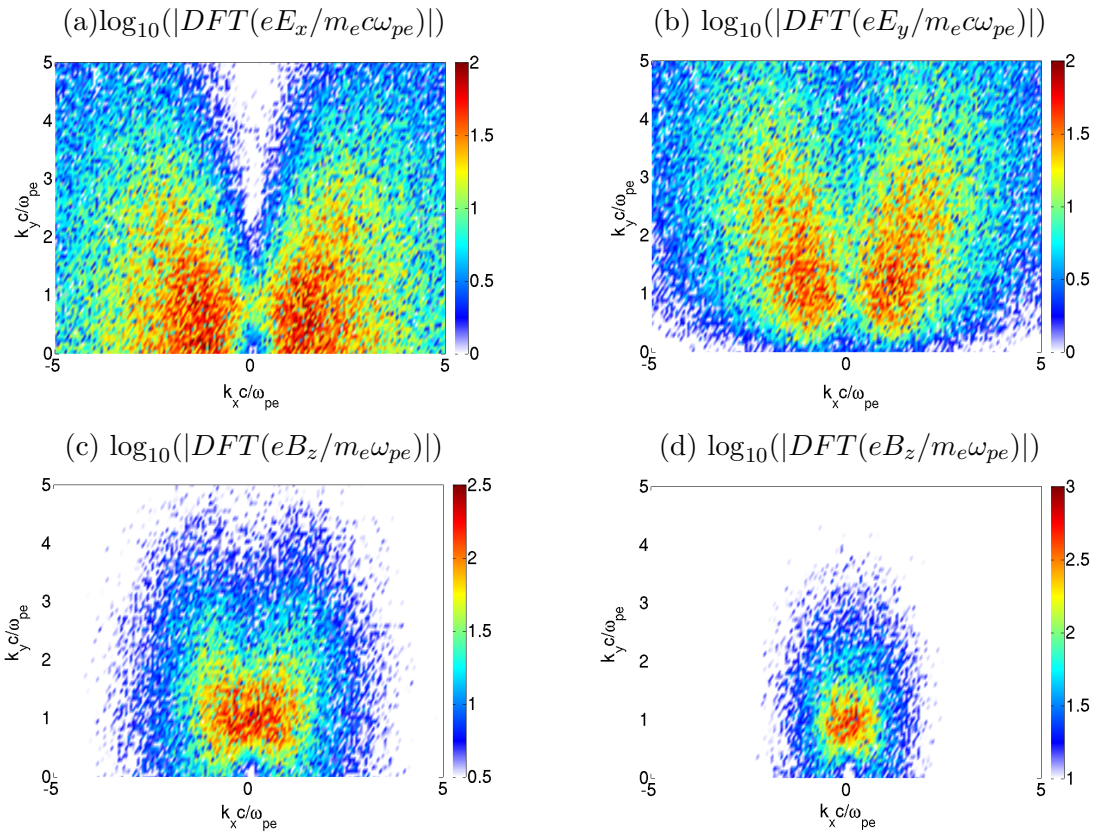

Figure 3.5. Fourier transform of E_x (a) and E_y (b) and B_z at $t\omega_{pe} = 52$ (c) and at $t\omega_{pe} = 70$.

close to the theoretical value of 1.2×10^{-2} (for $T_{ix} = 0.011 m_e c^2$, $T_{iy} = 0.023 m_e c^2$, $T_{ex} = 0.028 m_e c^2$, $T_{ey} = 0.035 m_e c^2$, $v_{di} = \pm 0.2c$, and $v_{de} = \pm 0.08c$). Note that the magnetic saturation happening at $t\omega_{pe} \simeq 75$ seems to invalidate the linear approximation made in deriving the dispersion relations of Chapter 1. However, the second magnetic growth [Fig. 3.3(a)] is exponential and is consistent with the linear dispersion relations.

An increase of the E_y energy is visible around $t\omega_{pe} \simeq 300$ [Fig. 3.3(a)], with an effective growth rate $\Gamma/\omega_{pe} \simeq 8 \times 10^{-3}$ equal to the ion-Weibel value. Measuring the plasma parameters in the simulation at $t\omega_{pe} = 210$, 360 and 570, the growth rates are solved in the (k_x, k_y) plane and displayed in Figs. 3.6(a,b,c). At $t\omega_{pe} = 210$, an oblique unstable mode dominates the Weibel mode but rapidly declines until $t\omega_{pe} = 570$ at which the Weibel filamentation takes over. The most unstable oblique modes are essentially electrostatic ($\mathbf{E} \parallel \mathbf{k}$) with an angle very close to $\pi/2$. It can thus contribute to the growth of the E_y energy over $180 < t\omega_{pe} < 380$. While in our case they are largely dominated by the ion Weibel modes (by ~ 2 orders of magnitudes), these electrostatic ion oblique modes (Forslund & Shonk 1970) can be critical in low velocity ($v_{de} \lesssim 5 \times 10^{-3}$) configurations. In such cases, they have been shown to disrupt the propagation of laminar electrostatic shocks (Kato & Takabe 2010a; Dieckmann *et al.* 2013).

3.3 Ion-ion Weibel-filamentation instability

In the cold relativistic electron-positron systems considered in Sec. 2.6, the filamentation instability was found to prevail from early on. This contrasts with the present non-relativistic warm electron-ion system, which experiences a progressive transition from dominant electrostatic electron-driven

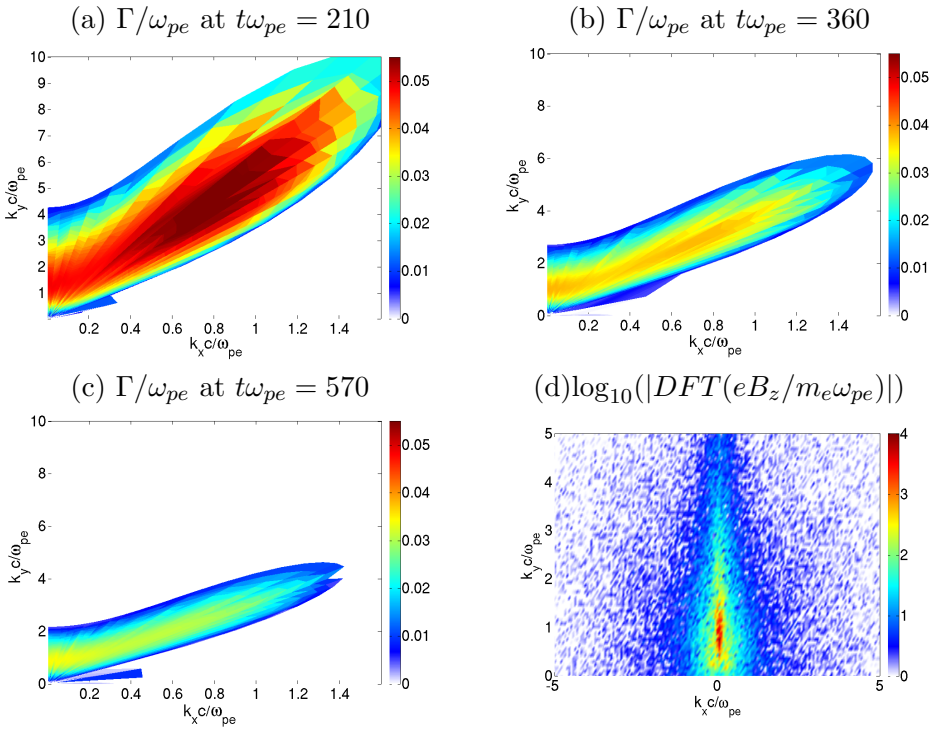

Figure 3.6. Growth rate Γ/ω_{pe} in the $(k_x\omega_{pe}/c, k_y\omega_{pe}/c)$ plane for the plasma parameters extracted from the simulation at times $t\omega_{pe} = 210$ (a), $t\omega_{pe} = 360$ (b) and $t\omega_{pe} = 570$ (c). (d) $\log_{10}(|DFT_{x,y}(eB_z/m_e\omega_{pe})|)$ at $t\omega_{pe} = 360$ (d) Fourier transform of B_z at $t\omega_{pe} = 360$ (d).

modes to a regime ruled by the ion Weibel instability. The exponential phase of the latter takes place over the time interval $200 < t\omega_{pe} < 400$. The magnetic growth ends at $t\omega_{pe} = 400$, when the spectrum is mainly transverse as illustrated in Fig. 3.6(c).

From this time on, the nonlinear saturation phase of the Weibel instability takes place. Figure 3.7(a) shows that the ion current modulations are stronger than the electron current modulations. The magnetic field modulations are thus mainly induced by the ions so that the observed transverse instability is the ion-ion Weibel-filamentation instability. As a result of the instabilities developing at early times (electron two-stream, electron Weibel and ion-ion acoustic), the electron distribution function shown in Fig. 3.7(a) turns out to be nearly isotropized. The averaged speed of each electron beam has dropped down to $v_e = 0.06c$ at the beginning of the ion-Weibel saturation phase ($t\omega_{pe} > 400$). Figure 3.3(a) shows that E_x-energy does not evolve much during the Weibel-filamentation development. However, the E_y and B_z energies increase in a correlated fashion (Bret *et al.* 2010b). Moreover, the green plain line of Fig. 3.7(a) shows that the spatial period of E_y ($\sim 5/\omega_{pe}$) is twice smaller than the spatial period of B_z ($\sim 10c/\omega_{pe}$). The ion density inside a filament is roughly 1.4 time larger than its initial value [Fig. 3.7(b)]. The factor of 2 between the B_z and E_y wavelengths suggests that, in the Weibel nonlinear phase, an approximate balance between the electric and magnetic forces is established on the electron fluid: $E_y \propto \partial_y(B^2)/2q_e\mu_0 n_e$. From this estimate, we predict a typical amplitude $q_e E_y/m_e c\omega_{pe} \sim 10^{-2}$ (with $q_e B_z/m_e\omega_{pe} \sim 0.2$ and $k_y c/\omega_{pe} \sim 0.63$) in fair agreement with Fig. 3.7(a) (Dieckmann *et al.* 2009).

The density map of Fig. 3.7(b) illustrates that the ion filaments are not purely transverse. At this stage, the filaments present both kink-like (Milosavljević & Nakar 2006) and coalescence (Medvedev *et al.* 2005; Achterberg *et al.* 2007) features. In Sec. 3.4.2, the latter secondary instability will be shown to govern the nonlinear evolution of the magnetic turbulence.

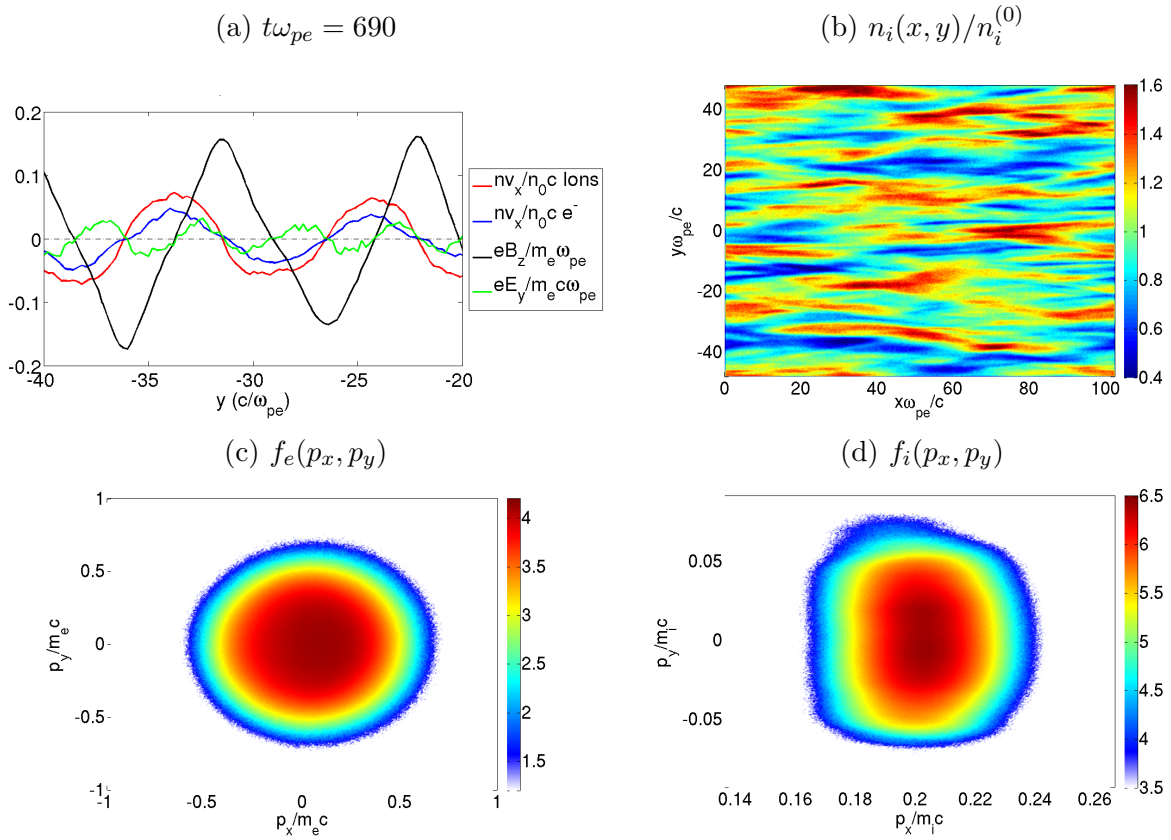

Figure 3.7. (a) Transverse lineouts of the particles'mean x-velocity and of E_y and B_z profiles. (b) Total ion density (normalized to the total initial density $n_i^{(0)}$). (c) Electron and (d) ion (p_x, p_y) distributions. For all the figures is $\omega_{pe}t = 690$ and the simulation parameters are: $v_e = v_i = \pm 0.2c$ and $T_e = T_i = m_e c^2/100$.

3.3.1 Temporal evolution of the magnetic spectrum

Ion Weibel-filamentation dispersion relation in a non-relativistic and symmetric colliding-beam system

The temporal evolution of the magnetic spectrum can be related to the plasma parameters in the linear approximation. For a system made of two symmetric bi-Maxwellian beams, the dispersion relation of Eq. (1.21) for transverse wavevectors ($k = k_y$, $\theta = \pi/2$) can be simplified to $\omega^2\epsilon_{xx} - k_y^2 = 0$, where the dielectric tensor component ϵ_{xx} reads

$$\epsilon_{xx} = 1 - \sum_{e,i} \frac{\omega_{ps}^2}{\omega^2} \left[1 + (1 + a_s)(1 + \xi_s \mathcal{Z}(\xi_s))\right] , \tag{3.2}$$

$$a_s = \frac{m_s v_{ds}^2 + T_{sx}}{T_{sy}} - 1 , \tag{3.3}$$

as demonstrated in Sec. 1.3.2. We have introduced the anisotropy factor of the sth specie a_s. The Weibel-filamentation instability being non-propagating ($\Re(\omega) = 0$) and transverse ($\mathbf{k} \perp \mathbf{v}_d$) (Weibel 1959), the argument of the plasma dispersion function is $\xi_s = i\sqrt{m_s/2T_{ys}}\Gamma/k_y$. The resulting

dispersion relation follows from $\omega = 0 + i\Gamma_{k_y}$ into the real part of Eq. (3.2) (Davidson *et al.* 1972):

$$k_y^2c^2 + \Gamma_{k_y}^2 + \sum_s \omega_{ps}^2 - \sum_s \omega_{ps}^2(a_s+1)\Re\left[1 + i\sqrt{\frac{m_s}{2T_{sy}}}\frac{\Gamma}{k_y}\mathcal{Z}\left(i\sqrt{\frac{m_s}{2T_{sy}}}\frac{\Gamma}{k_y}\right)\right] = 0 \tag{3.4}$$

We will now neglect the influence of the electrons. This approximation is valid when the electron population is initially isotropic. In the case of initially anisotropic electrons, the simulation $v_i^{(0)} = v_e^{(0)} = 0.2c$, $m_i = 100m_e$ shows that the electron instabilities (two-stream, Weibel...) which have grown and saturated first leaves the electrons hot and mostly isotropized. This will be subsequently verified for other initial plasma parameters, in 1D or 2D simulations. Taking an electron temperature of $T_{ey} \simeq 0.04m_ec^2$ (Fig. 3.3(b) $t\omega_{pe} = 300$) yields $|\xi_e| \simeq 0.1$ and $|\Re(\xi_e\mathcal{Z}(\xi_e))| \simeq 0.15$. We will thus neglect this term in front of unity [bracketed term of Eq. (3.4)]. Consequently, even for initially anisotropic electrons, when the ion Weibel-filamentation saturates, the electrons are mostly isotropic and the corresponding dispersion function can be neglected within 15% error.

As for the ions, we will assume (and subsequently justify) that $|\xi_i|$ is smaller than unity at the beginning of the saturation stage of the ion Weibel-filamentation instability. We can therefore make use of the Taylor expansion of $\xi_i\mathcal{Z}(\xi_i)$ for $|\xi| \ll 1$, giving

$$\mathcal{Z}(\xi) = -2\xi + \frac{4}{3}\xi^3 + i\sqrt{\pi}\frac{k}{|k|}\exp -\xi^2 + O(\xi^4)\,. \tag{3.5}$$

To leading order, we obtain $\xi_i\mathcal{Z}(\xi_i) \simeq i\sqrt{\pi}\xi_i$. Equation (3.4) can thus be recast using Eq. (3.5) and neglecting $\xi_e\mathcal{Z}(\xi_e)$:

$$\omega_{pi}^2(a_i+1)\sqrt{\frac{\pi m_i}{2T_{iy}}}\Gamma_{k_y} + k_y^2\left(k_y^2 - \frac{\omega_{pe}^2a_e}{c^2} - \frac{\omega_{pi}^2a_i}{c^2}\right) = 0\,. \tag{3.6}$$

Equation (3.6) gives

$$\Gamma_{k_y} \simeq \sqrt{\frac{2T_{iy}}{\pi m_i}}|k_y|\frac{k_{\max}^2c^2 - k_y^2c^2}{\omega_{pi}^2(a_i+1)}\,, \tag{3.7}$$

where we have introduced the upper bound of the Weibel-unstable domain $k_{\max}$

$$k_{\max}^2c^2 = \omega_{pe}^2a_e + \omega_{pi}^2a_i\,. \tag{3.8}$$

This approximated growth rate was first derived in the electron-electron filamentation in Davidson *et al.* (1972). The only difference lies here in $k_{\max}$, which involves both the ion and the electron anisotropies.

The accuracy of the estimate, Eq. (3.7), is illustrated in Fig. 3.8(a) for the plasma parameters $v_{di} = \pm 0.2c$, $v_{de} = 0$, $T_{ix} = 0.05m_ec^2$, $T_{iy} = 0.05m_ec^2$, $T_{ex} = 0.05m_ec^2$ and $T_{ey} = 0.05m_ec^2$. Correct agreement is found between the exact and approximated growth rate curves, with respect to both their general shapes and the location/amplitude of the dominant mode.

Simplified wavevector and growth rate

In order to capture the dominant wavevector of the Weibel instability as a function of the plasma parameters, we will assume that most of the magnetic energy is contained in the spectral region surrounding the growth rate maximum. Making use of Eq. (3.7), we obtain

$$\partial_{k_y}\Gamma_{k_y} = 0 \Rightarrow k_{\text{sat}} = \frac{\omega_{pe}^2a_e + \omega_{pi}^2a_i}{c^2\sqrt{3}} \simeq 0.5k_{\max}\,. \tag{3.9}$$

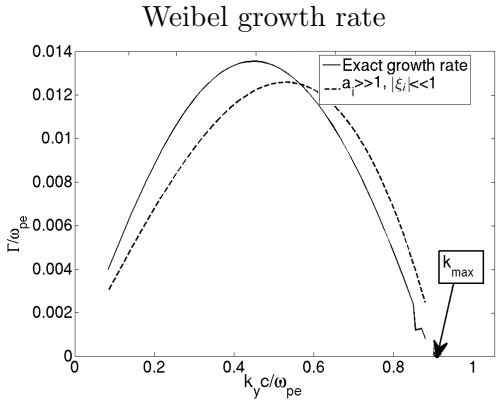

Figure 3.8. Exact calculation as plain lines through the generalized Fried and Gould scheme (dispersion Eq. (3.4)) of the growth rate, normalized to ω_{pe}. The approximations using Eq. (3.7) are superposed as dashed lines. The plasma parameters are $v_d = 0.2c$ and $m_i = 25m_e$.

To further simplify our analysis, we will take the large-ion-anisotropy limit ($a_i \gg 1$) in our equations. This approximation is justified in all our simulations. For instance, we have $a_i = 400$ in our reference simulation ($v_d = 0.2c$, $m_i = 100m_e$ and $T_i = 5$keV). By contrast, the electrons will be assumed sufficiently isotropized for their anisotropy ratio to be neglected. There follow the simplified formulae:

$$\frac{k_{\rm sat}}{k_{\rm max}} = \eta_i \simeq 0.5\,, \tag{3.10}$$

with

$$k_{\rm max} \simeq \frac{\omega_{pi}}{c}\sqrt{a_i}\,, \tag{3.11}$$

and

$$\Gamma_{k_y} \simeq \sqrt{\frac{2T_{iy}}{\pi m_i}}\left(1 - \frac{k_y^2}{k_{\rm max}^2}\right) k_y\,. \tag{3.12}$$

For $k_y = k_{\rm sat}$, it reads:

$$\Gamma_{\rm sat} = \Gamma_{k_{\rm sat}} \simeq 0.3\omega_{pi}\sqrt{\frac{T_{ix}}{m_i c^2} + \beta_i^2}\,. \tag{3.13}$$

This equation confirms the well-known scaling of the Weibel-filamentation growth rate in the cold limit ($T_{ix} \ll m_i c^2$) which reads $\Gamma \propto \omega_{pi} v_i/c$ (Achterberg & Wiersma 2007).

Furthermore, the argument of the plasma dispersion function involved in the ion term of Eq. (3.4) simplifies to

$$\xi_i \simeq i\frac{1}{\sqrt{\pi}}\left(1 - \frac{k_y^2}{k_{\rm max}^2}\right)\,. \tag{3.14}$$

This expression shows that, for $a_i \gg 1$, ξ_i depends only on the ratio $k_y^2/k_{\rm max}^2$ and takes its maximum value $|\xi_i| = 1/\sqrt{\pi}$ for $k_y = 0$. At $k = k_{\rm sat}$, we have $|\xi_i^{\rm sat}| \simeq 0.4$. The small-argument expansion of $\mathcal{Z}$ in Eq. (3.4) is then marginally justified.

3.3.2 Temporal evolution of the plasma parameters

Quasilinear equations of the plasma parameters

The main assumption made in Sec. 3.3.1 consists in using the linear dispersion relation computed on the spatially averaged distribution functions to relate the ion anisotropy ratio to the main wavevector

$k_{\rm sat}$.

This approach is equivalent to the quasilinear kinetic theory of the Weibel instability as first exploited by Davidson *et al.* (1972), or more recently Sadovskiĭ & Galeev (2001); Pokhotelov & Amariutei (2011); Hellinger *et al.* (2013). The quasilinear kinetic theory for the Weibel-filamentation instability is valid provided $|\xi_{i,e}| \ll 1$, a regime also assumed in Sec. 3.3.1. Within these two approximations, Davidson *et al.* (1972) derived the Weibel-filamentation quasilinear theory for a bi-Maxwellian (1.65) distribution function. This yields a relation between the temporal derivatives of the distribution function moments and the time derivatives of $|B_{k_y}|^2$. It reads

$$\partial_t f^{(0)} = \sum_{k_y} \frac{-i\omega_{pi}^2 |B_{k_y}|^2}{\mu_0 n_i m_i c^2 k_y^2} \left[-k_y v_x \partial_{v_y} + (i\Gamma_{-k} + k_y v_y)\partial_{v_x}\right] \times \left[\frac{k_y v_x \partial_{v_y} + (i\Gamma_k - k_y v_y)\partial_{v_x}}{i\Gamma_k - k_y v_y}\right] f^{(0)} . \tag{3.15}$$

The quasilinear theory usually assumes:

$$\partial_t |B_{ky}|^2 \equiv 2\Gamma_{k_y} |B_{ky}|^2 . \tag{3.16}$$

If the distribution functions stay bi-Maxwellian and making use of Eq. (3.16), the three first moments of Eq. (3.15) give a set of differential equations on the temperatures and drift velocities of the distribution functions.

The s subscript refers now either to one of the ion beams or to the whole electron population (assumed isotropized):

$$n_s \partial_t v_{ds} = -\sum_{k_y} \frac{\omega_{ps}^2}{k_y^2 c^2} \frac{v_{ds}}{T_{sy}} \Re\left[1 + \xi_s \mathcal{Z}(\xi_s)\right] \frac{\partial_t |B_{k_y}|^2}{\mu_0} , \tag{3.17}$$

$$n_s \partial_t T_{sy} = +\sum_{k_y} \frac{\omega_{ps}^2}{k_y^2 c^2} (a_s + 1) \Re\left[1 + \xi_s \mathcal{Z}(\xi_s)\right] \frac{\partial_t |B_{k_y}|^2}{\mu_0} , \tag{3.18}$$

$$n_s \partial_t K_{sx} = -\sum_{k_y} \frac{\omega_{ps}^2}{k_y^2 c^2} \Re\left[2(a_s + 1)(1 + \xi_s \mathcal{Z}(\xi_s)) - 1\right] \frac{\partial_t |B_{k_y}|^2}{\mu_0} , \tag{3.19}$$

where $|B_{k_y}|^2$ has the dimension of an energy density unit and $K_{sx} = T_{sx} + m_s v_{ds}^2$. Proceeding as in Sec. 3.3.1 for the electrons, we neglect $\xi_e \mathcal{Z}(\xi_e)$ (valid for $|\xi_e| \lesssim 0.01$) and obtain

$$n_e \partial_t v_{de} = -\frac{\omega_{pe}^2}{\mu_0 c^2} \frac{v_{de}}{T_{ey}} \partial_t S_p , \tag{3.20}$$

$$n_e \partial_t T_{ey} = +\frac{\omega_{pe}^2}{\mu_0 c^2} (a_e + 1) \partial_t S_p , \tag{3.21}$$

$$n_e \partial_t K_{ex} = -\frac{\omega_{pe}^2}{\mu_0 c^2} (2a_e + 1) \partial_t S_p , \tag{3.22}$$

where we have introduced

$$S_p = q_e^2 \sum_{k_y} \frac{|B_{k_y}|^2}{k_y^2} = q_e^2 \sum_{k_y} |A_{k_y}|^2 , \tag{3.23}$$

homogeneous to the square of a momentum. Note that Eq. (3.20) implies that if $v_{de} = 0$ initially, it remains so at $t > 0$.

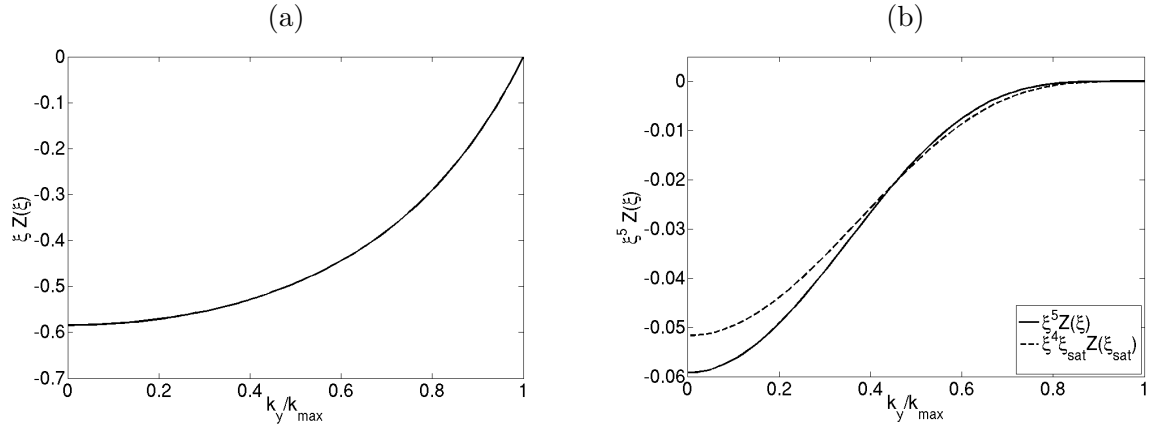

Figure 3.9. (a) $\xi_i \mathcal{Z}(\xi_i)$ *vs.* the ratio $k_y/k_{\max}$ from Eq. (3.14) (independent from any plasma parameter). (b) $\xi_i^5 \mathcal{Z}(\xi_i)$ *vs.* the ratio $k_y/k_{\max}$ from Eq. (3.14) (solid line) and with $\xi_i^4 \xi_i^{\rm sat} \mathcal{Z}(\xi_i^{\rm sat}) = -0.5\xi_i^4$ (dashed line).

In order to make analytical progress, we will make use of the approximation

$$\sum_{k_y} \Re\left(1 + \xi_{k_y} \mathcal{Z}(\xi_{k_y})\right) \partial_t |B_{k_y}|^2/k_y^2 \simeq \Re\left(1 + \xi_{\rm sat} \mathcal{Z}(\xi_{\rm sat})\right) S_p \tag{3.24}$$

From Eq. (3.14), and using the small-argument expansion of $\mathcal{Z}$, $\xi_{\rm sat}\mathcal{Z}(\xi_{\rm sat}) \simeq -0.5$, independent, to first approximation, of the plasma parameters under the physical conditions considered.

The error made in replacing $\xi_i \mathcal{Z}(\xi_i)$ by a constant factor of -0.5 can be estimated at the saturation stage of the Weibel-filamentation instability. The amplitude of the magnetic field at saturation can be inferred by a magnetic trapping argument (Davidson *et al.* 1972). In a current filament, ions oscillate transversely at the so-called bouncing frequency:

$$\omega_B = \sqrt{Z_i k_y B/m_i v_d}\,. \tag{3.25}$$

Since the linear theory assumes a ballistic motion of particles during a field growth time, Γ^{-1}, the saturated field amplitude (*i.e.* at the beginning of the non-linear stage) may be estimated from equating Γ and ω_B, yielding (Davidson *et al.* 1972)

$$B_{k_y}^{\rm sat} \simeq \frac{m_i \Gamma_{k_y}^2}{v_d Z_i k_y}\,. \tag{3.26}$$

This estimate can also be viewed as the limit above which the spectral component B_{k_y} can modify the ion motion. Hence, making use of the above expression, and assuming that the unstable modes saturates independently from each other, one can obtain that the magnetic spectrum and thus $|B_{k_y}|^2/k_y^2$ scales as ξ_i^4. Consequently, the $\xi_i \mathcal{Z}(\xi_i)|B_{k_y}|^2/k_y^2$ term in Eqs. (3.17), (3.18) and (3.19) should vary as $\xi_i^4 \xi_i \mathcal{Z}(\xi_i)$ at saturation. Figure 3.9(b) compares the exact value of $\xi_i^5 \mathcal{Z}(\xi_i) \propto \xi_i \mathcal{Z}(\xi_i)|B_{ky}|^2/k_y^2$ to the approximated formula $-0.5\xi_i^4 \propto \xi_i^{\rm sat} \mathcal{Z}(\xi_i^{\rm sat})|B_{ky}|^2/k_y^2$. The relative error is found to be smaller than 20% in the $k_y \to 0$ limit and vanishes for $k_y = k_{\rm sat}$. We insist on the fact that $\xi(k_{\rm sat}) = \xi_i^{\rm sat}$ tends to be a constant in the large-ion-anisotropy limit. Hence the approximation of Eq. (3.24) does not depend on the ion parameters and can be made whenever the ions are non-relativistic in the Weibel quasilinear theory. Moreover, the trapping criterion of Davidson's formula (Eq. (3.26)) has not been injected in the quasilinear equations but has only served to support the $|\xi_i| \ll 1$ and Eq. (3.24) approximations.

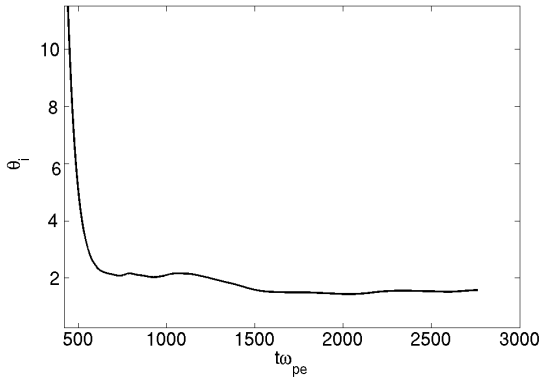

Figure 3.10. Temporal evolution of the ratio θ_i of [Eq. (3.31)] in the reference simulation ($v_d = 0.2c$ and $m_i = 100m_e$) by $-(K_{ix} - K_{ix}^{(0)})/(T_{iy} - T_{iy}^{(0)})$.

Since $\xi_{\rm sat}\mathcal{Z}(\xi_{\rm sat})$ may be considered as a constant, we define

$$\alpha_i = 1 + \xi_i^{\rm sat}\mathcal{Z}(\xi_i^{\rm sat}) \simeq 0.5\,. \tag{3.27}$$

Equations (3.17), (3.18) and (3.19) can now be recast as

$$n_i\partial_t v_i = -\frac{\omega_{pi}^2}{\mu_0 c^2}\alpha_i\frac{v_i}{T_{iy}}\partial_t S_p\,, \tag{3.28}$$

$$n_i\partial_t T_{iy} = +\frac{\omega_{pi}^2}{\mu_0 c^2}\alpha_i(a_i+1)\partial_t S_p\,, \tag{3.29}$$

$$n_i\partial_t K_{ix} = -\frac{\omega_{pi}^2}{\mu_0 c^2}\left(2\alpha_i a_i + 2\alpha_i - 1\right)\partial_t S_p\,. \tag{3.30}$$

Resolution of the quasilinear evolution

An additional simplification can be made upon realizing that the ratio of Eqs. (3.29) and (3.30) is essentially constant in the $a_i \gg 1$ limit:

$$\frac{\partial_t K_{ix}}{\partial_t T_{iy}} \equiv -\theta_i = -\frac{2\alpha_i a_i + 2\alpha_i - 1}{\alpha_i(a_i+1)}\,, \tag{3.31}$$

$$\simeq -2\left[1 + \frac{1}{a_i}\left(1 - \frac{1}{\alpha_i}\right)\right]\,. \tag{3.32}$$

The validity of this approximation is supported by Fig. 3.10 which plots the time history of the quantity θ_i in the reference simulation. As predicted, θ_i saturates at a value ~ 2 once the ion Weibel instability reaches saturation ($\omega_{pe}t > 450$). At later times, θ_i slowly decreases (reaching $\simeq 1.8$ at $\omega_{pe}t = 2700$) as a result of decreasing ion anisotropy [see Fig. 3.11(e)]. We will then make the assumption that θ_i is a quasi-constant and neglect all its time derivatives. Equation (3.31) can then readily integrated, giving

$$K_{ix} = K_{ix}^{(0)} - \theta_i(T_{iy} - T_{iy}^{(0)})\,, \tag{3.33}$$

where $X^{(0)}$ stands for $X(t=0)$. Plugging Eq. (3.33) into (3.29) gives

$$\frac{n_i T_{iy}}{K_{ix}^{(0)} - \theta_i(T_{iy} - T_{iy}^{(0)})}\partial_t T_{iy} = \frac{\omega_{pi}^2}{\mu_0 c^2}\alpha_i\partial_t S_p\,. \tag{3.34}$$

For practical reasons, we will introduce the parameter

$$K_{\theta_i} = \theta_i T_{iy}^{(0)} + T_{ix}^{(0)} + m_i v_i^{(0)2} \,, \tag{3.35}$$

which has the dimension of an energy. For $\theta_i = 2$, we have $K_2 = 2T_{iy}^{(0)} + T_{ix}^{(0)} + m_i v_i^{(0)2}$, which is larger than the initial ion energy. The integration of Eq. (3.34) is straightforward and yields

$$T_{iy} - T_{iy}^{(0)} + \frac{K_2}{\theta_i} \ln\left(\frac{K_2 - \theta_i T_{iy}}{K_2 - \theta_i T_{iy}^{(0)}}\right) = -\theta_i \frac{Z_i^2}{m_i} \alpha_i (S_p - S_p^{(0)}) \,. \tag{3.36}$$

The Taylor expansion of the logarithmic term for $T_{iy}/K_2 \ll 1$ (high anisotropy limit) gives

$$T_{iy} = \sqrt{T_{iy}^{(0)2} + 2\frac{Z_i^2}{m_i} \alpha_i K_2 (S_p - S_p^{(0)})} \tag{3.37}$$

Inserting Eq. (3.37) into (3.28) yields

$$\partial_t v_{di} = -\frac{Z_i^2}{m_i} \alpha_i \frac{v_{di} \partial_t S_p}{\sqrt{T_{iy}^{(0)2} + 2\frac{\omega_{pi}^2}{n_i c^2} \alpha_i K_2 (S_p - S_p^{(0)})}} \,, \tag{3.38}$$

which may be readily integrated:

$$v_i = v_i^{(0)} \exp\left(-2\frac{T_{iy} - T_{iy}^{(0)}}{K_2}\right) = v_i^{(0)} \exp\left[-\frac{2}{K_2}\left(\sqrt{T_{iy}^{(0)2} + 2\frac{Z_i^2}{m_i} \alpha_i K_2 (S_p - S_p^{(0)})} - T_{iy}^{(0)}\right)\right] . \tag{3.39}$$

Combining Eqs. (3.33) and (3.37) allows us to solve for K_{ix}:

$$K_{ix} = K_2 - \theta_i \sqrt{T_{iy}^{(0)2} + 2\frac{Z_i^2}{m_i} \alpha_i K_2 (S_p - S_p^{(0)})} \,. \tag{3.40}$$

There follows the anisotropy ratio

$$a_i = \frac{K_2}{\sqrt{T_{iy}^{(0)2} + 2\frac{Z_i^2}{m_i} \alpha_i K_2 (S_p - S_p^{(0)})}} - 2 \,, \tag{3.41}$$

and the effective spectrum

$$S_p - S_p^{(0)} = \frac{m_i}{2Z_i^2 \alpha_i K_2} \left[\left(\frac{K_2}{2 + a_i}\right)^2 - T_{iy}^{(0)2}\right] . \tag{3.42}$$

The non-resonant quasilinear theory relates the instantaneous temperatures and drift velocities to the effective magnetic energy S_p, independently of the time history of the system (Sadovskiĭ & Galeev 2001; Pokhotelov & Amariutei 2011). Of course, this property holds insofar as the Weibel instability rules the evolution of the system. We also remind that the obtained equations are valid within the assumption of $a_i \gg 1$. The limiting values of the above quantities may be assessed by

inserting $a_i = 2 > 1$ in their corresponding expressions:

$$S_p^f = \frac{m_i}{2Z_i^2 \alpha_i K_2} \left[\frac{K_2^2}{16} - T_{iy}^{(0)2} \right] , \tag{3.43}$$

$$T_{iy}^f = \frac{K_2}{4} , \tag{3.44}$$

$$v_i^f = v_i^{(0)} \exp\left(-2 \frac{K_2/4 - T_{iy}^{(0)}}{K_2} \right) , \tag{3.45}$$

$$K_{ix}^f = \frac{K_2}{2} . \tag{3.46}$$

3.3.3 Summary of the model's assumptions

Before confronting our formulae to PIC simulation results, let us gather the assumptions underlying our quasilinear model. Firstly, we consider that the spatially averaged distribution functions will remain bi-Maxwellian. We then obtain simple relations between the moments of the distributions. Note that a quasilinear model taking into account the distribution deformation is presented in Pokhotelov & Amariutei (2011).

Secondly, constant ion and electron densities are assumed. This assumption is valid in the periodic simulations of Sec. 3.3.4. However, in a system with open boundaries, the nonlinear late-time evolution of the Weibel-instability will result in a significant decrease in the ion drift velocity which, in turn, may entail a density increase. We will assess this assumption in the next chapter, where our quasilinear model will be applied to shock formation.

Thirdly, the electrons are assumed sufficiently hot ($|\xi_e| \ll 1$) and isotropic ($a_e \ll a_i/m_i$). The validity of this approximation will be checked in 1D, 2D and 3D simulations for various plasma parameters. In all cases, it will prove valid by the time the ion-Weibel instability has saturated. Moreover, the hot ion approximation $|\xi_i| < 1$ is also assessed at ion-Weibel saturation for various plasma parameters. This assumption, being the validity condition of the ion-quasilinear equations, is also used to simplify the growth rate and estimate the dominant wavevector $k_{\rm sat}$. However, in a few nearly-relativistic cases ($v_i \geq 0.4c$), $\xi_i \sim 1$ at Weibel saturation time even though the quasilinear relations works well.

Finally, the ion anisotropy ratio a_i is assumed large in order to derive a simple expression of the dominant wavevector $k_{\rm sat}$. In this limit, ξ_i only depends on $k_y/k_{\rm max}$ and is independent of the plasma parameters. This also enables to simplify the quasilinear equations, leading us to $\xi_{\rm sat}\mathcal{Z}(\xi_{\rm sat}) \simeq -0.5$ and to $\partial_t K_{ix}/\partial_t T_{iy} \simeq -2$ (Figs. 3.9 and 3.10). We will assess the validity of this approximation in the simulation of Sec. 3.3.4 and by estimating the plasma parameters until the marginal limit of $a_i = 2$ on Eqs. (3.43)-(3.46).

3.3.4 Comparison with PIC simulation results

This section gathers the simulation results obtained using a variety of periodic geometries and plasma parameters, and confronts them to the above analytical expressions. The unknown effective magnetic spectrum, S_p, will be measured as a function of time in the simulations. The evolution of S_p and $k_{\rm sat}$ computed from Eqs. (3.23) and (3.10), respectively, will also be compared to the values obtained making use of the plasma parameters measured in the simulations.

1D periodic simulations

Since our model considers a 1D magnetic spectrum, we will first present 1D simulations where the drift velocities are taken perpendicular to the resolved spatial axis. The size of the simulation domain

is $L_x = 102.4c/\omega_{pe}$ and periodic boundary conditions are applied for the fields and particles. The temporal and spatial steps are $\Delta t = 0.095\omega_{pe}^{-1}$ and $\Delta x = 0.1c/\omega_{pe}$ respectively. The ions (of mass m_i to be defined) and electrons are initialized in the forms of two counter-propagating Maxwell-Jüttner-type beams (1.22). The only unstable modes able to arise in this configuration are the electron or ion-driven Weibel modes. A total number of 50000 macroparticles per mesh and per species is used. The spectral quantity S_p is calculated as

$$S_p^{1D} = q_e^2 \sum_{k_y} \frac{|DFT_y(B_z)|^2}{k_y^2}\,, \tag{3.47}$$

where the sum runs over the negative and positive discrete wavevectors.

The case of $v_{de} = v_{di} = 0.2c$, $T_{e,i} = 0.01 m_e c^2$ and $m_i = 100 m_e$ is first considered in Fig. 3.11. During the first $100\omega_{pe}^{-1}$, the electron drift velocity of the initially $v_d > 0$ beam drops by a factor ~ 2 and the transverse temperature T_{ey} rises from $0.01 m_e c^2$ to $0.035 m_e c^2$ [Fig. 3.11(d,f)]. Consequently, the electrons anisotropy ratio drops from $\simeq 5$ to $\simeq 0.3$ showing that they are rapidly isotropized, in fair agreement with our hot and isotropic electron approximation. The analytical estimate of the dominant wavevector, Eq. (3.10), underestimates the PIC wavevector by 40% [Fig. 3.11(b)].

At saturation ($t\omega_{pe} \simeq 400$), the plasma parameters are $T_{e,ix} \simeq 0.01 m_e c^2$, $T_{ex} \simeq 0.04 m e_c^2$, $T_{ey} \simeq 0.05 m_e c^2$, $v_i \simeq \pm 0.2c$, $v_e \simeq \pm 0.04$. The exact Weibel dispersion relation, Eq. (3.4), is then solved exactly so as to yield an estimate of $\xi_{\rm sat} = i\Gamma_{k_y}/k_y\sqrt{2T_{i,ey}/m_{i,e}}$ where k_y maximizes the growth rate. For the electrons, $|\xi_e| \simeq 0.07 \ll 1$, which approximately fulfills the assumption of hot isotropic electrons. For the ions, $|\xi_i| \simeq 0.6 < 1$ matches the theoretical prediction $|\xi_{\rm sat}| \simeq 0.5$. Consequently, the assumptions underlying the quasilinear equations may be considered valid. The PIC curves of v_{di}, a_i and T_{iy} are satisfactorily reproduced (to within a 20% error) by Eqs. (3.39), (3.41) and (3.37) making use of the PIC S_p curve.

A second periodic 1D simulation illustrated in Figs. 3.12, has been run, with isotropic electrons ($v_e = 0$) and ion parameters $v_i = \pm 0.5c$, $m_i = 100 m_e$. All temperatures are initialized at $T_{i,e}^{(0)} = 0.01 m_e c^2$. Since the electrons are initially isotropic, the only instability developing is the ion Weibel-filamentation instability. The validity of the hot electrons approximation [leading to the neglect of $\xi_e \mathcal{Z}(\xi_e)$ in Eq. (3.4)] can also be assessed in this case. Solving the exact dispersion relation Eq. (3.4) for the system at saturation ($t\omega_{pe} = 300$, $T_{e,ix} = 0.01 m_e c^2$, $T_{ey} = 0.04 m e_c^2$, $T_{ex} = 0.12 m_e c^2$, $v_i = 0.5c$, $v_e = 0$) and maximizing the growth rate gives an estimate of $|\xi_e| \simeq 0.056 \ll 1$. Consequently, even though the electrons do not trigger any instability before the ion-Weibel filamentation, the hot electron approximation is valid. Moreover, we have $|\xi_i| \simeq 0.36 < 1$ at saturation, close to the theoretical value of $|\xi_{\rm sat}| = 0.45$ whereas $|\xi_i| \simeq 1.6$ at $t = 0$. Hence, the Weibel-induced ion heating is sufficient to validate the assumption $|\xi_i| < 1$. We notice that the quasilinear relations seem to give fairly good results as early as $t = 0$, even though the condition $|\xi_i| < 1$ is not initially fulfilled.

In addition, S_p and $k_{\rm sat}$ correctly reproduce the PIC results. As in the previous 1D simulation, the system reaches a quasi-stationary state shortly after the saturation of the Weibel instability, the plasma and turbulence properties remaining essentially frozen after $\omega_{pe}t \simeq 500$.

2D periodic simulations

For the 2D PIC simulations, S_p can be calculated using a Fourier transform in the transverse y direction, averaged over the x direction:

$$S_p^{2D} = q_e^2 \sum_{k_y} \frac{\langle |DFT_y(B_z)|^2 \rangle_x}{k_y^2}\,. \tag{3.48}$$

in all cases, the simulation boxes have dimensions of $L_x = 102.4c/\omega_{pe}$ and $L_y = 102.4c/\omega_{pe}$

Periodic 1D simulation with initial conditions:

$$v_{di} = \pm 0.2c\,, v_{de} = \pm 0.2c\,, m_i = 100 m_e \text{ and } T_{i,e}^{(0)} = 0.01 m_e c^2\,.$$

(a) S_p normalized to $m_e^2 c^2$ (b) Dominant wavevector

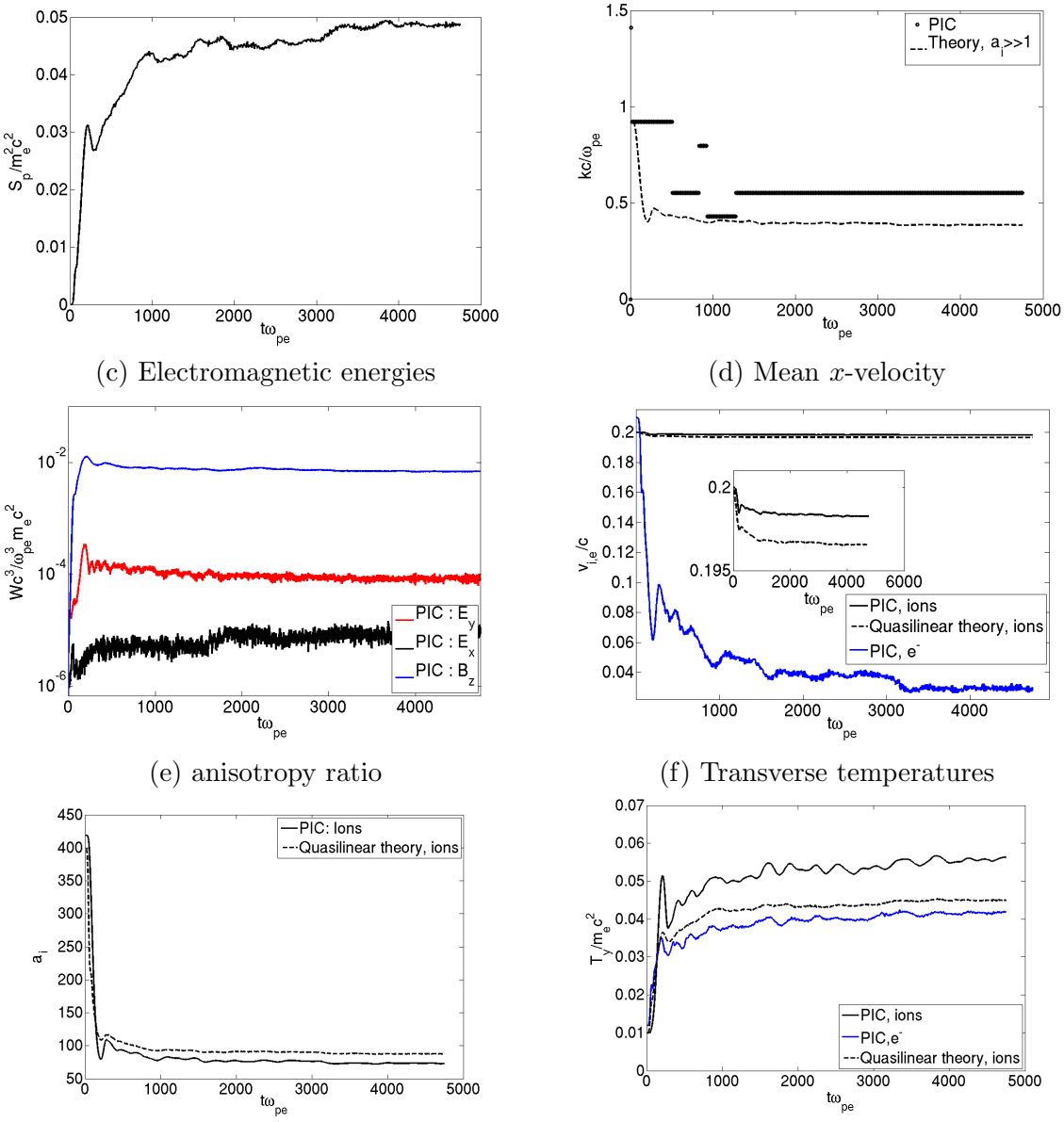

(c) Electromagnetic energies (d) Mean x-velocity

(e) anisotropy ratio (f) Transverse temperatures

Figure 3.11. (a) Temporal evolution of S_p, defined by Eq. (3.23) (normalized to $m_e^2 c^2$) from the simulation (plain line). (b) Temporal evolution of k_{sat}, maximizing the B_z-spectrum, (normalized to ω_{pe}/c) from the simulation (dots) and from Eq. (3.10) (dashed line). (c) Temporal evolution of the mean electromagnetic energies (normalized to $m_e c^2 \omega_{pe}^2/c^2$). Temporal evolutions of v_i/c (d), a_i (e) and $T_{i,ey}/m_e c^2$ (f) from the simulation (plain lines) and from Eqs. (3.39), (3.41) and (3.37) (dashed lines), measuring S_p in the simulation (black line of (a)). Time is normalized to ω_{pe}^{-1}.

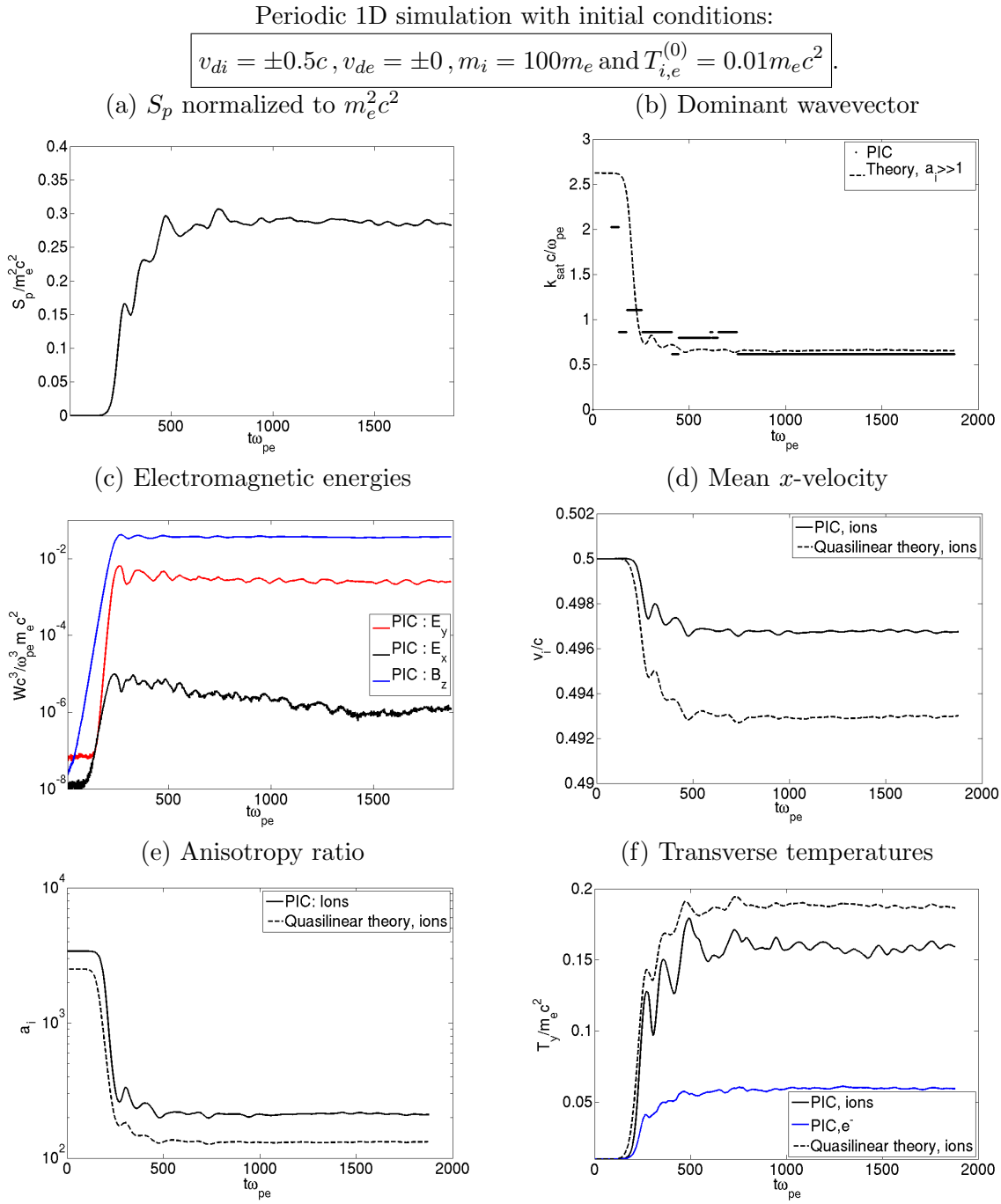

Figure 3.12. (a) Temporal evolution of S_p, defined by Eq. (3.23) (normalized to $m_e^2 c^2$) from the simulation (plain line). (b) Temporal evolution of $k_{\rm sat}$ maximizing the B_z-spectrum (normalized to ω_{pe}/c) from the simulation (plain line) and from Eq. (3.10) (dashed line). (c) Temporal evolution of the mean electromagnetic energies normalized to $m_e c^2 \omega_{pe}^2/c^2$. Temporal evolutions of v_i/c (d), a_i (e) and $T_{i,ey}/m_e c^2$ (f) from the simulation (plain lines) and from Eqs. (3.39), (3.41) and (3.37) in dashed lines, taking S_p in the simulation (black solid line of (a)). Time is normalized to ω_{pe}^{-1}.

with periodic boundary conditions. The temporal and spatial steps are respectively $\Delta t = 0.069\omega_{pe}^{-1}$ and $\Delta x = 0.1c/\omega_{pe}$. All the simulations consider Maxwell-Jüttner-distributed plasma species with $T_{i,e}^{(0)} = 0.01 m_e c^2$. Each cell initially contains 50 macroparticles per species.

Since we neglect the electron anisotropy in our quasilinear model, we will first consider the case of isotropic electrons ($v_{de} = 0$). The results of a simulation with $v_{di} = \pm 0.2c$, $v_{de} = 0$ and $m_i = 100 m_e$ are gathered in Fig. 3.13. From the beginning of the simulation onwards, the growth of transverse magnetic fluctuations rules the system. They increase essentially during the interval $200 \leq \omega_{pe} \leq 600$ at an effective rate $\Gamma/\omega_{pe} \sim 10^{-2}$ close to the maximum theoretical growth rate of $\Gamma_{\rm sat}/\omega_{pe} \simeq 1.3 \times 10^{-2}$. Moreover, the resolution of the dispersion relation shows no unstable longitudinal mode ($k = k_x$). This confirms that the system is dominated by the Weibel filamentation instability from the beginning. The saturation of the instability starts at $t\omega_{pe} = 600$ as evidenced by Fig. 3.13(c). From this time, our quasilinear model, Eqs. (3.39), (3.41) and (3.37), correctly captures (to within a factor ~ 2) the variations of the S_p curve. It should be emphasized that, in contrast to the previous simulations, the plasma parameters keep on evolving during the instability saturation stage. Within our quasilinear model, these variations stem from the steady increase in S_p, which should be contrasted to the essentially constant magnetic energy for $\omega_{pe} t \gtrsim 600$. These distinct behaviors point to a time-changing magnetic spectrum, as confirmed by the decreasing $k_{\rm sat}$ curve of Fig. 3.13(b). At saturation, the B_z-energy is about 40 times larger than the E_y-energy.

The ξ_i factor at the beginning of the simulation (using the initial conditions) can be estimated by maximizing the growth rate, computed from the exact dispersion relation. At $t\omega_{pe} = 0$, $|\xi_i| \simeq \Gamma_{\rm max}/k_{\rm sat}\sqrt{2T_{iy}^{(0)}/m_i} \simeq 1.2 > 1$: this violates the $|\xi_i| < 1$ quasilinear validity condition. However, taking the plasma parameters after saturation gives at $t\omega_{pe} = 600$, $|\xi_i| \simeq \Gamma_{\rm max}/k_{\rm sat}\sqrt{2T_{iy}^{(0)}/m_i} \simeq 0.5 < 1$ and in good agreement with the approximated value of 0.5. Figure 3.13(d) show that the evolution of the ion drift velocity is well reproduced by the quasilinear equation over all the simulated time range. The evolution of T_{iy} [Fig. 3.13(e)] and a_i [Fig. 3.13(f)] are well reproduced by the quasilinear theory until $t\omega_{pe} = 1400$. Later on, our model underestimates by a factor ~ 2 the increase in the ion transverse temperature, and consequently, overestimates by the same factor the ion anisotropy ratio.

The case $v_{de} = v_{di} = 0.2c$ is considered in Fig. 3.14, the other parameters being identical to the previous simulation. The two-stream and oblique instabilities triggered during the first $500\omega_{pe}^{-1}$ of this simulation have already been discussed in Sec. 3.2. By the time the Weibel instability saturates, the electron drift velocity has decreased by more than a factor two and the electron anisotropy ratio has dropped to $a_e \simeq -0.2 \ll a_i$. Moreover, using the plasma parameters at $t\omega_{pe} = 500$ ($T_{i,ex} \simeq 0.01 m_e c^2$, $T_{i,ey} \simeq 0.03 m_e c^2$, $v_{di} \simeq \pm 0.2c$ and $v_{de} \simeq \pm 0.08c$) yields $|\xi_e| \simeq 0.04 \ll 1$ and $|\xi_i| \simeq 0.41 < 1$. Since the assumptions of hot and isotropic electrons and strongly anisotropic ions are well verified, the analytical estimate of $|\xi_{\rm sat}| \simeq 0.45$ matches the numerical value. Plugging the simulated value of S_p [Eq. (3.48)] in Eqs. (3.39), (3.41), (3.37) (3.10) and (3.23) gives an estimate of the quasilinear evolution of the plasma and spectrum parameters. As in previous cases, the $k_{\rm sat}$ estimate, Eq. (3.10), underestimates the simulation value by 40% for $t\omega_{pe} > 500$ [Fig. 3.14(b)]. Although the ion drift velocity evolution v_i is very well reproduced by the quasilinear theory [Fig. 3.14(d)], the transverse temperature T_{iy} is underestimated by a factor ~ 2 (Fig. 3.14(d)). This implies that the theory overestimates by a factor ~ 2 the simulated value of the ion anisotropy ratio [Fig. 3.14(c)].

The periodic simulation of 3.15 has been run with a realistic proton mass ($m_i = 1836 m_e$) with $v_{di} = \pm 0.4c$ and $v_{de} = 0$. The fully periodic simulation domain has dimensions $L_x = 102.4c/\omega_{pe}$, $L_y = 102.4c/\omega_{pe}$, and the numerical discretization is $\Delta t = 0.14\omega_{pe}^{-1}$ and $\Delta x = 0.2c/\omega_{pe}$. The theoretical growth rate map shown in Fig. 3.16(a) predicts that the system is initially dominated by a longitudinal instability. This instability propagates at $\sim 0.4c$ with dominant growth rate of

Periodic 2D simulation with initial conditions:

$$\boxed{T_{i,e}^{(0)} = 0.01 m_e c^2 \, , m_i = 100 m_e \, , v_i = \pm 0.2c \, \text{and} \, v_e = 0} \, .$$

(a) S_p normalized to $m_e^2 c^2$

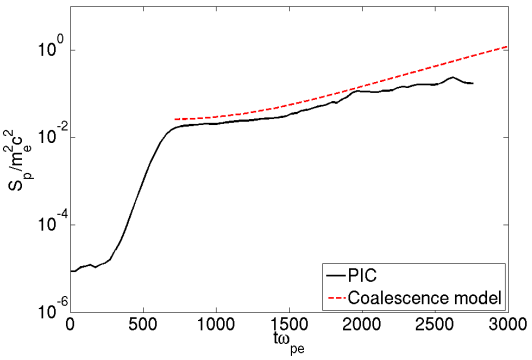

(b) Dominant wavevector

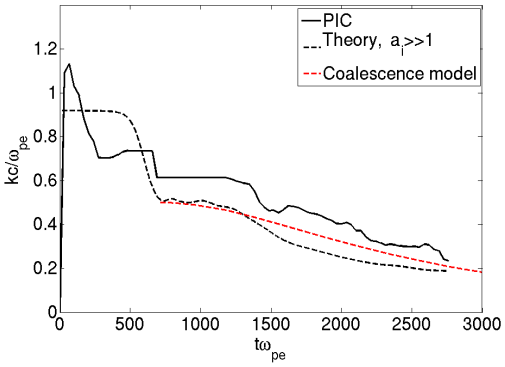

(c) Electromagnetic energies

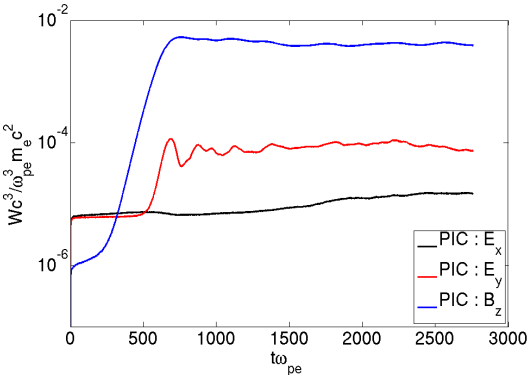

(d) Mean x-velocity

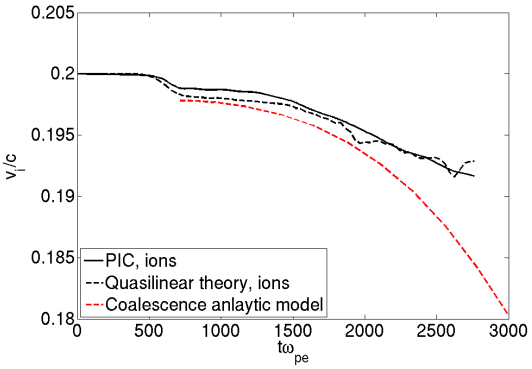

(e) Anisotropy ratio

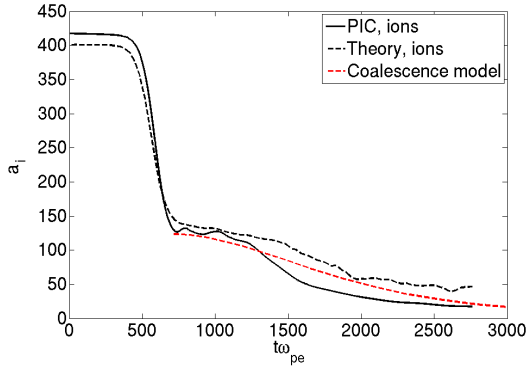

(f) Transverse temperatures

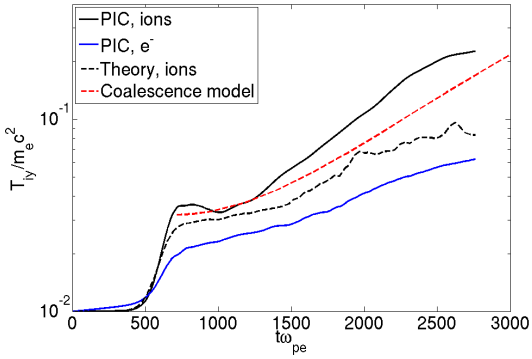

Figure 3.13. (a) Temporal evolution of S_p, defined by Eq. (3.23), (normalized to $m_e^2 c^2$) from the simulation (plain line). (b) Temporal evolution of k_{sat}, maximizing the B_z-spectrum, (normalized to ω_{pe}/c) from the simulation (plain line) and from Eq. (3.10) (dashed line). (c) Temporal evolution of the mean electromagnetic energies (normalized to $m_e c^2 \omega_{pe}^2/c^2$). Temporal evolutions of v_i/c (d), a_i (e) and $T_{i,ey}/m_e c^2$ (f) from the simulation (red solid lines) and from Eqs. (3.39), (3.41) and (3.37) (red dashed lines), taking S_p from the simulation (solid line of (a)). The analytical predictions, Eqs. (3.80)-(3.85), are superposed as dashed red lines (details in Sec. 3.4.5). Time is normalized to ω_{pe}^{-1}.

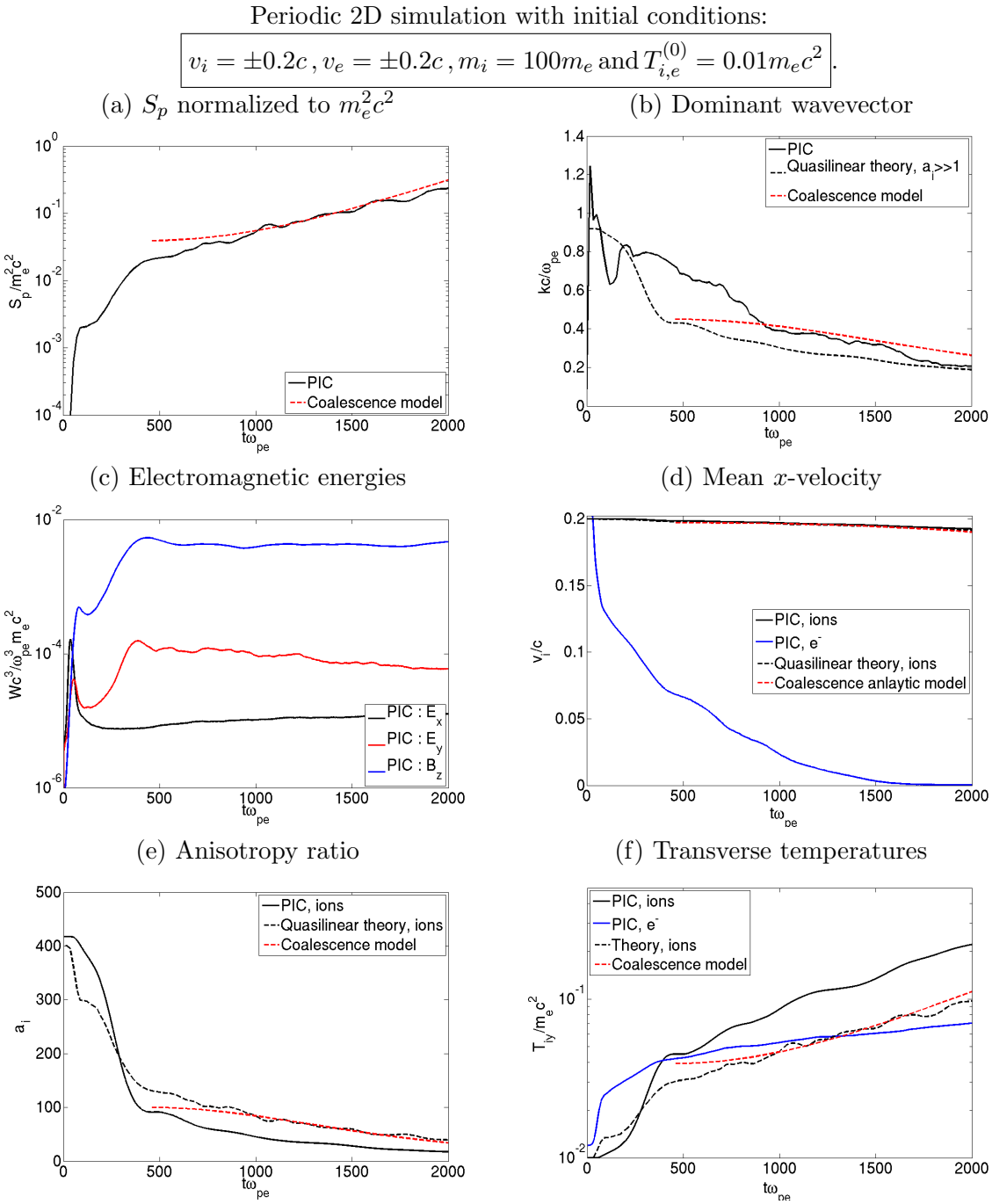

Figure 3.14. (a) Temporal evolution of S_p, defined by Eq. (3.23), (normalized to $m_e^2 c^2$) from the simulation (plain line). (b) Temporal evolution of $k_{\rm sat}$, maximizing the B_z-spectrum, (normalized to ω_{pe}/c) in the simulation (plain line) and using estimate of Eq. (3.10) (dashed line). (c) Temporal evolution of the mean electromagnetic energies (normalized to $m_e c^2 \omega_{pe}^2/c^2$). Temporal evolutions of $v_{i,e}/c$ (d), a_i (e) and $T_{i,ey}/m_e c^2$ (f) from the simulation (plain lines) and from Eqs. (3.39), (3.41) and (3.37) in dashed lines, taking S_p from the simulation (solid line of (a)). The analytical predictions of Eqs. (3.80)-(3.85) are superposed as dashed red lines (details in Sec. 3.4.5). Time is normalized to ω_{pe}^{-1}.

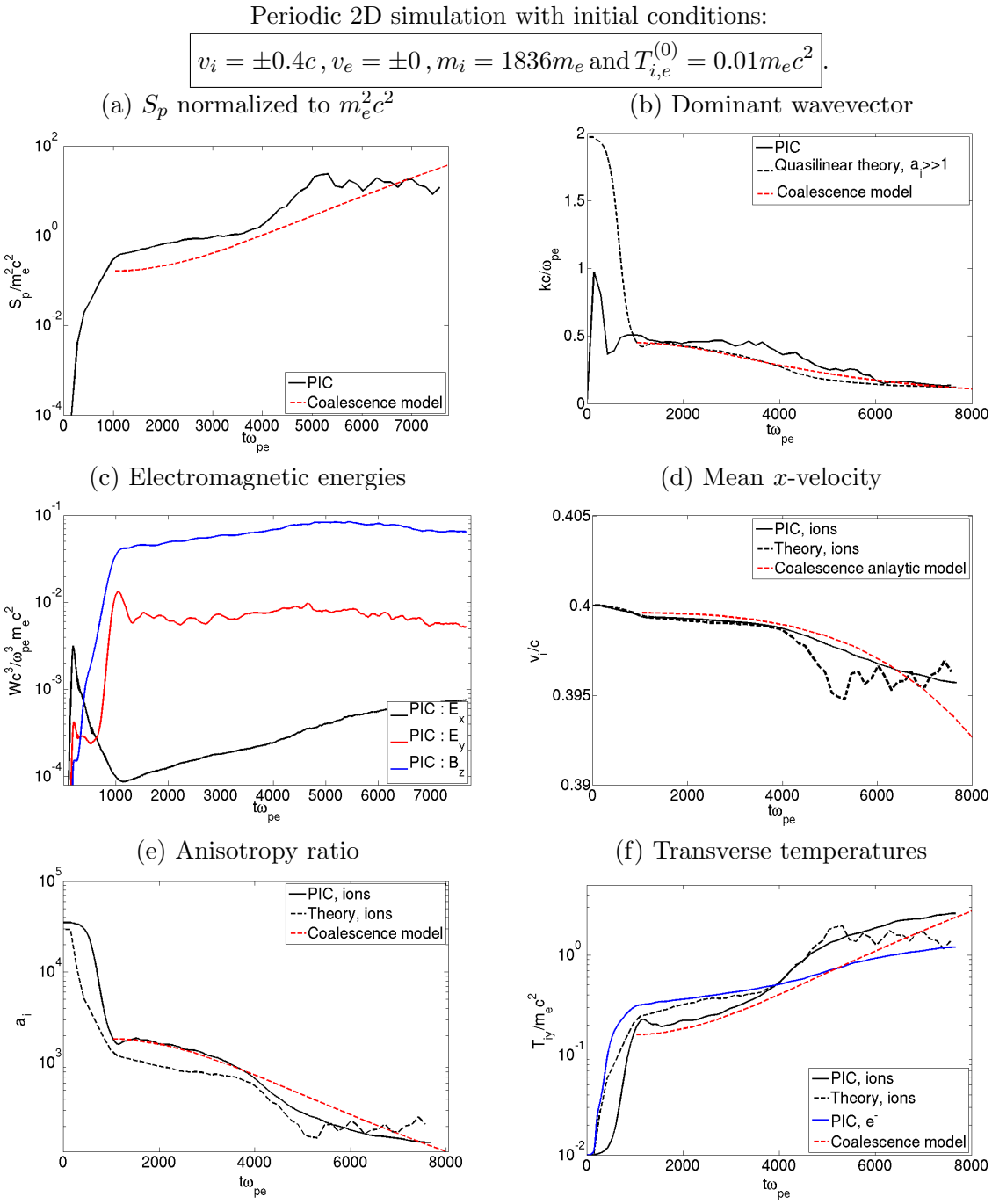

Figure 3.15. (a) Temporal evolution of S_p, defined by Eq. (3.23), (normalized to $m_e^2c^2$) from the simulation (plain line). (b) Temporal evolution of $k_{\rm sat}$, maximizing the B_z-spectrum, (normalized to ω_{pe}/c)from the simulation (plain line) and from Eq. (3.10) (dashed line). (c) Temporal evolution of the mean electromagnetic energies (normalized to $m_e c^2 \omega_{pe}^2/c^2$). Temporal evolutions of $v_{i,e}/c$ (d), a_i (e) and $T_{i,ey}/m_e c^2$ (f) from the simulation (plain lines) and from Eqs. (3.39), (3.41) and (3.37) (dashed lines), taking S_p in the simulation (solid line of (a)). The analytical predictions of Eqs. (3.80)-(3.85) are superposed as dashed red lines (details in Sec. 3.4.5). Time is normalized to ω_{pe}^{-1}..

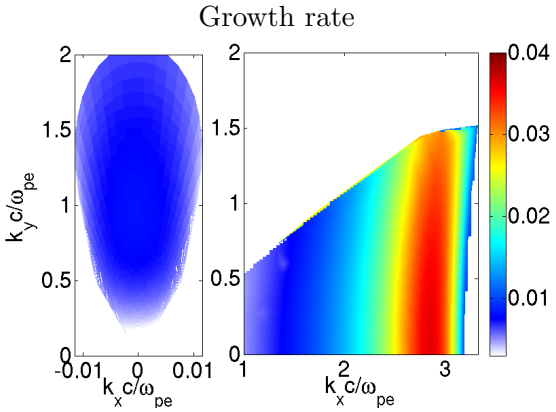

Figure 3.16. Growth rate $\Gamma(k_x, k_y)$ normalized to ω_{pe} in the (k_x, k_y) plane. The associated real frequency vanishes for the transverse wavevectors (left panel), while the dominant longitudinal eigenmodes (right panel at $k_x c/\omega_{pe} \simeq 0.3$) propagates at real phase speed of $0.4c$. The system is made of two symmetric beams with drift velocities $v_{di} = \pm 0.4c$, isotropic electrons, $v_{de} = 0$, and temperature $T^{(0)}_{x,yi,e} = 0.01 m_e c^2$. The ion mass is $m_i = 1836 m_e$.

$\Gamma/\omega_{pe} \simeq 0.04$ comparable to the effective E_x-growth giving $\Gamma/\omega_{pe} \simeq 0.03$ in the simulation. This corresponds to the Buneman instability, driven by the ion drift velocities which exceed the electron thermal velocity (Buneman 1959). This explains the exponential growth of the electric field energy, W_{E_x} [Fig. 3.15(c)], which saturates around $t\omega_{pe} \simeq 200$. Figure 3.15(c) further shows that the magnetic field energy overcomes the electric field for $t\omega_{pe} > 400$, as a result of a then dominant ion Weibel instability, and saturates at $t\omega_{pe} \simeq 1000$. As in the previous cases, the magnetic energy remains approximately constant after saturation. The evolution of $k_{\rm sat}$ is well reproduced by Eq. (3.10) for $t\omega_{pe} > 1000$ [Fig. 3.15(b)] while the theoretical evolution of S_p [Fig. 3.15(a)] overestimates the PIC curve by a factor ~ 4. The temporal evolutions of v_i, T_{iy} and a_i in the simulation are very well reproduced by the quasilinear theory (even at large time for $t\omega_{pe} > 5000$) [Figs. 3.15(d,e,f)]. This confirms that the accuracy of the model increases with the ion anisotropy. Note that the agreement is very good, at the beginning of the Weibel-saturation stage, when $|\xi_i| \simeq 1.2 > 1$ (with $T_{iy} = 0.2 m_e c^2$, $T_{ey} = 0.3 m_e c^2$, $T_{i,ex} = 0.2 m_e c^2$, $v_i = \pm 0.4c$, $v_e = 0$). Later on, however, $|\xi_i|$ decreases progressively down to $|\xi_i| \simeq 0.78 < 1$ at $t\omega_{pe} = 4000$.

3D periodic simulations

All the quasilinear equations developed here can easily be generalized to the 3D geometry using symmetry of rotation around the x axis. It is not surprising since many numerical studies (Fonseca *et al.* 2003; Romanov *et al.* 2004; **?**; Bret *et al.* 2008) evidence very similar plasma evolution between 3D simulations and 2D simulations, when the latter resolve the drift direction. In the simulations, S_p^{3D} can be calculated using a Fourier transform in the yz plane of the transverse (B_y and B_z) magnetic field components. Moreover the dispersion relation (3.4) and the non-relativistic bi-Maxwellian dielectric tensors remain unchanged from 2D to 3D distribution functions. The quasilinear equations, as presented previously, can be generalized to the 3D case, given the following definition of S_p

$$S_p^{3D} = q_e^2 \sum_{k_y,k_z} \frac{\langle |DFT_{y,z}(B_y)|^2 + |DFT_{y,z}(B_z)|^2 \rangle_x}{k_y^2 + k_z^2} . \tag{3.49}$$

In the following, the periodic simulation domain has dimensions $L_x = 102.4c/\omega_{pe}$, $L_y = L_z = 96c/\omega_{pe}$, with space and time steps $\Delta x = 0.2c/\omega_{pe}$ and $\Delta t = 0.114\omega_{pe}^{-1}$. The ions, of mass

$m_i = 100m_e$, and electrons are initialized by counter-propagating Maxwell-Jüttner type (1.22) distribution functions of temperature $T_{e,i} = m_e c^2/100$ and drift velocity $v_{e,i} = \pm 0.2c$. We use $N_p = 30$ macroparticles per mesh and per species. The 2D and 3D simulations [Figs. 3.14 and 3.17] show very similar results, although the S_p evolution is slightly faster in the 2D case. The predictions from quasilinear theory matches fairly well the simulation results during the Weibel-saturation stage ($t\omega_{pe} > 300$).

3.4 Spectral dynamics: from the growth rate evolution to the collective filament dynamics

The above model leads to simple analytical formulae relating the ion temperatures and drift velocity to the evolution of the spectral quantity $S_p = q_e^2 \sum_k |A_k|$. These equations have been shown to match the PIC simulation results for various plasma parameters, provided the ion anisotropy remains large enough in the nonlinear stage. However, an additional relation must be provided in order to have a fully predictive model of the ion-Weibel saturation. Two strategies have been tried for that purpose, which we will now present.

3.4.1 Growth rate evolution

A simple approach to predict the evolution of the spectrum uses the exponential growth of the unstable electromagnetic modes. During the linear phase of the Weibel instability, before saturation, the magnetic field can be linked to the growth rate through $B_{k_y}(t)^2 = B_{i,k_y}^2 \exp(2\Gamma_{k_y} t)$, use being made of the initial seed-field B_i^2 as in Sec. 2.6. However, during the magnetic field growth, Γ_{k_y} varies with time so that a more rigorous quasilinear formulation is

$$B_{k_y}^2(t) = B_i^2 \exp\left[2\int_0^{t'} dt' \Gamma_{k_y}(t')\right] . \tag{3.50}$$

In the nonlinear stage, a significant part of the spectrum obeys (at least qualitatively) the saturation scaling of Eq. (3.26) (Davidson *et al.* 1972). Drawing upon the model of Gedalin *et al.* (2010, 2012), we will assume that, at a gven time, only the modes of wavevector $k > k_c(t)$ (where k_c is the time-dependent critical wavevector) have saturated and obey Eq. (3.26), while the modes with $k < k_c(t)$ keep on growing according to Eq. (3.50). Gedalin *et al.* (2010, 2012) identify the critical wavevector $k_c(t)$ to the wavevector maximizing the magnetic spectrum, $k_{\rm sat}(t)$. Hence, for $k = k_c(t) = k_{\rm sat}(t)$, the Davidson criterion is applied for each exponentially-growing mode of magnetic spectrum:

$$\frac{m_i \Gamma_{\rm sat}^2}{Z_i v_i k_{\rm sat}^2} = B_i^2 \exp\left(2\int_0^{t} dt' \Gamma_{k_{\rm sat}}(t')\right) . \tag{3.51}$$

Taking the time derivative of the logarithm of the above equation yields:

$$2\Gamma_{k_{\rm sat}} = \partial_t \ln\left[\left(\frac{m_i^2 \Gamma_{k_{\rm sat}}^4}{Z_i^2 v_i^2 k_{\rm sat}^2}\right)\frac{1}{B_i^2}\right] . \tag{3.52}$$

For a system in initially thermal equilibrium as described in Chapter 2, B_i^2 is given by Eq. (2.75), so that $B_i^2 \propto k^{-3}$. However, the simulations of this chapter have been run without ensuring that the field spectra have converged to their thermal equilibrium shape before turning unstable. Therefore, we will take $B_i^2 \propto k^{-n_k}$ where $n_k > 0$ is an undetermined spectral coefficient. There follows

$$2\Gamma_{k_{\rm sat}} = 4\partial_t \ln(\Gamma_{k_{\rm sat}}) - (2 - n_k)\partial_t \ln(k_{\rm sat}) - 2\partial_t \ln(v_i) , \tag{3.53}$$

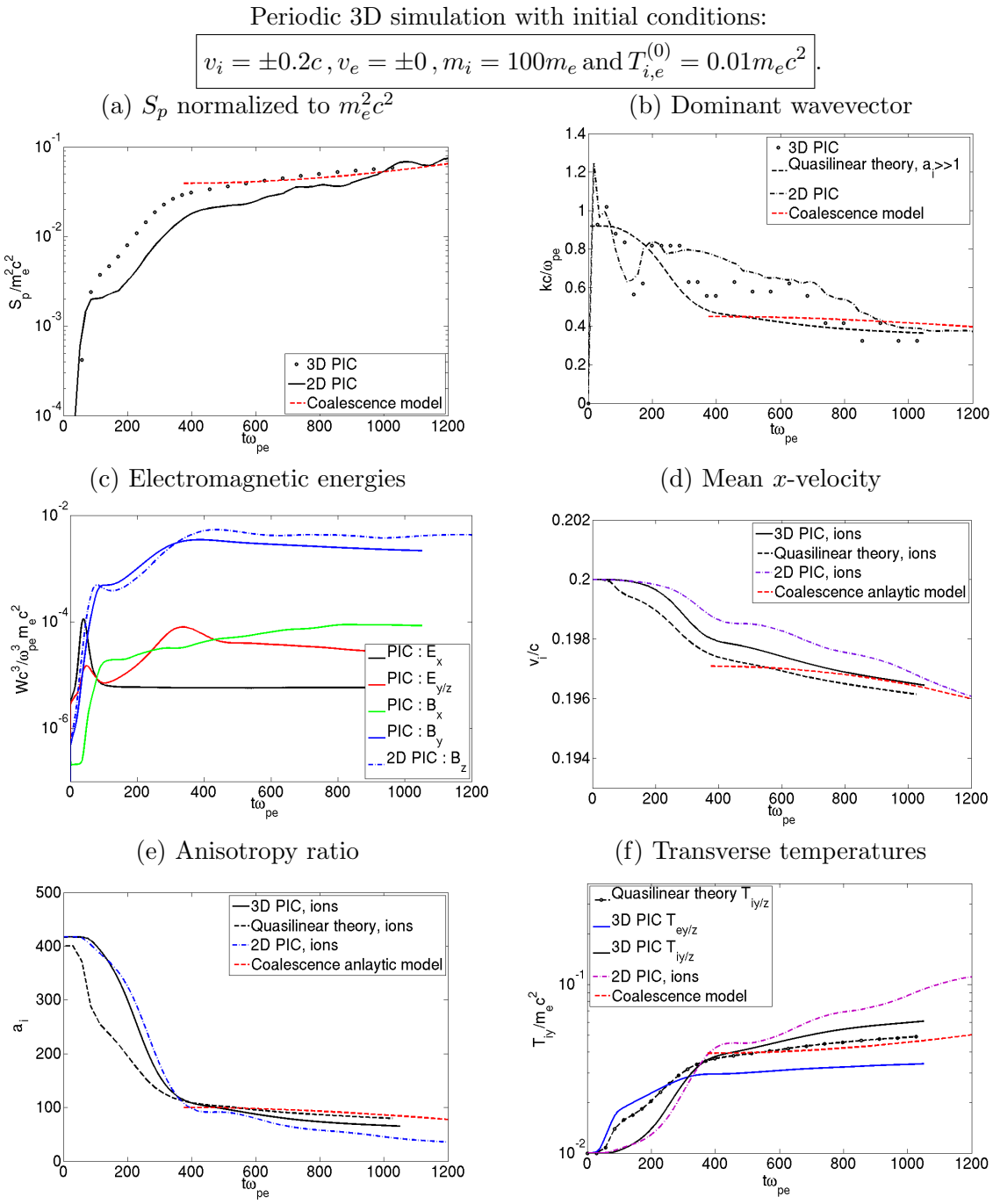

Figure 3.17. (a) Temporal evolution of S_p, defined by Eq. (3.23), (normalized to $m_e^2c^2$) from the 3D simulation (circles). (b) Temporal evolution of $k_{\rm sat}$ (maximizing the B_z-spectrum) normalized to ω_{pe}/c from the simulation (circles) and from Eq. (3.10) (red dashed line). (c) Temporal evolution of the mean electromagnetic energies (normalized to $m_e c^2 \omega_{pe}^2/c^2$). Care has been taken to verify that B_y and B_z has the exact same energy evolution. The corresponding 2D plots is superposed dotted-dashed line. Temporal evolutions of v_i/c (d), a_i (e) and $T_{i,ey}/m_e c^2$ (f) from the simulation in plain lines and of Eqs. (3.39), (3.41) and (3.37) in dashed lines, measuring S_p from the simulation (circles of (a)). All the 2D PIC simulation results from (same plasma parameters) of The corresponding results from a 2D simulation using the same parameters [Fig. 3.14] are superposed as black dotted-dashed lines. The analytical predictions of Eqs. (3.80)-(3.85) are superposed as dashed red lines (details in Sec. 3.4.5). Time is normalized to ω_{pe}^{-1}.

where in the limit $a_i \gg 1$, Eqs. (3.7) (3.10) leads to $\Gamma_k \simeq 0.3\omega_{pi}\sqrt{K_{ix}/m_i}$ and $k_{\rm sat}c/\omega_{pi} \simeq \eta_i\sqrt{a_i}$. Hence, $\partial_t \ln(\Gamma_{k_{\rm sat}}) \simeq \partial_t \ln(K_{ix})/2$. Making use of $\partial_t K_{ix} \simeq -2\partial_t T_{iy}$ and Eq. (3.29) gives

$$\partial_t \ln(\Gamma_{k_{\rm sat}}) \simeq -\frac{\partial_t T_{iy}}{K_{ix}} \simeq -\alpha_i \frac{\omega_{pi}^2}{n_i c^2}\frac{\partial_t S_p}{T_{iy}} \,. \tag{3.54}$$

Plugging (3.10), (3.41) and (3.42) into $\partial_t S_p = \partial_{a_i} S_p \cdot \partial_{k_{\rm sat}} a_i \cdot \partial_t k_{\rm sat}$ gives

$$\partial_t \ln(\Gamma_{k_{\rm sat}}) \simeq \frac{2K_2}{T_{iy}} \frac{1}{(2+a_i)^3}\frac{k_{\rm sat}c^2}{\omega_{pi}^2 x^2} \,. \tag{3.55}$$

Moreover, $\partial_t \ln(v_i)$ can be related to $\partial_t T_{iy}$:

$$\partial_t \ln(v_i) = \frac{-2}{K_2}\partial_t T_{iy} \simeq \frac{4K_2}{T_{iy}}\frac{k_{\rm sat}c^2}{\omega_{pi}^2 x^2}\partial_t k_{\rm sat} \,. \tag{3.56}$$

We then obtain

$$\Gamma_{k_{\rm sat}} k_{\rm sat} = \left[\frac{4K_2}{T_{iy}}\frac{k_{\rm sat}^2 c^2}{\omega_{pi}^2 x^2}\left(2+\frac{k_{\rm sat}^2 c^2}{\omega_{pi}^2 x^2}\right)^{-3} - 2\frac{4K_2}{T_{iy}}\frac{k_{\rm sat}^2 c^2}{\omega_{pi}^2 x^2} - 1 + \frac{n_k}{2}\right]\partial_t k_{\rm sat} \,, \tag{3.57}$$

with T_{iy} given by (3.37) and (3.42). This first order differential equation is expected to be valid as soon as the instability enters its saturation regime. While it can be solved numerically, analytical progress can be made by taking advantage of $a_i \simeq k_{\rm sat}c/\omega_{pi}x \gg 1$. To leading order, the above equation can be recast as

$$dt \simeq -\frac{1}{\Gamma_{k_{\rm sat}}}\frac{8K_2}{T_{iy}}\frac{k_{\rm sat}c^2}{\omega_{pi}^2 x^2} dk_{\rm sat} \,, \tag{3.58}$$

which does not depend anymore on the spectral coefficient n_k. The filamentation wavelength $\lambda_{\rm sat} = 2\pi/k_{\rm sat}$ then verifies

$$\frac{1}{c}\partial_t \lambda_{\rm sat} \simeq \frac{0.28x^2\pi}{4}\sqrt{\frac{K_{ix}}{m_i c^2}}\left(\frac{m_e}{m_i}\right)^2 \frac{T_{iy}}{E2} a_i^{-\frac{3}{2}} \,. \tag{3.59}$$

Hence, at the beginning of the saturation phase, making use of $K_2/T_{iy} \sim a_i$, $\partial_t \lambda_{\rm sat}$ is expected to scale as $a_i^{-5/2}/m_i^2$. In the 1D simulations associated to $m_i = 100m_e$ and $v_i = 0.2c$ (respectively $v_i = 0.5c$) [Figs. 3.11 and 3.12], we measure $a_i \simeq 100$ at $t\omega_{pe} = 500$ (respectively $a_i \simeq 200$ at $t\omega_{pe} = 500$) and thus obtain $\partial_t \lambda_{\rm sat} \sim 10^{-10}c$ (respectively $a_i \simeq 4\times 10^{-11}c$) from Eq. (3.59). Consequently, these two systems would need at least $10^{10}\omega_{pe}^{-1}$ to undergo an increase of only $0.1c/\omega_{pe}$ of the Weibel wavelength. This is confirmed by the 1D simulations of Figs. 3.11 and 3.12, which show weakly varying spectral and plasma parameters during the saturation stage. This stationary state contrasts with the continuously evolving system predicted by 2D and 3D simulations. Even though the magnetic turbulence remains essentially transverse ($k_{y,z} \gg k_x$), the existence of longitudinal gradients has a dramatic influence on the long-time evolution of the system in enabling the coalescence of ion-current filaments. This process, forbidden in 1D simulations, will be shown to quantitatively explain the long-time evolution of the multidimensional Weibel-unstable systems.

3.4.2 The coalescence of two filaments

The 2D and 3D simulations presented in Sec. 3.3.4 show similar spectral evolutions. After Weibel saturation, the B_z-energy [blue lines in Figs. 3.11-3.17(c)] remains constant while S_p goes on increasing [black lines in Fig. 3.11-3.17(c)]. This suggests that the instability is ruled by the

evolution of the dominant wavevector $k_{\rm sat}$. As the ions are heated, $k_{\rm sat}$ decreases accordingly to Eq. (3.10). Since $\langle B_z^2\rangle$ remains constant, there follows a steady increase in $S_p \sim \langle B_z^2\rangle/k_{\rm sat}^2$. Hence, if $\langle B_z^2\rangle_y$ stays constant and $k_{\rm sat}$ is decreasing, $S_p \sim \langle B_z^2\rangle_y/k_{\rm sat}^2$ is increasing.

Previous studies have found that the filament dynamics is subject to secondary instabilities, such as filament coalescence (or merging) which, in terms of magnetic turbulence generates increasingly low-k_y modes (Honda *et al.* 2000; Gremillet 2001; Medvedev *et al.* 2005) or kink instabilities (Milosavljević & Nakar 2006), which generates $k_x \neq 0$ modes. In our reference simulation, the magnetic spectrum stays mainly localized on the axis $k_x = 0$, although it shows a small spread in the k_x direction [Fig. 3.3(c)]. This suggests that the nonlinear Weibel evolution is dominated by filament coalescence in our simulations. Some simple models of filament merging already exist (Medvedev *et al.* 2005; Achterberg *et al.* 2007). Its underlying mechanism is as follows. In the nonlinear stage, strong ion current filaments are formed, which are partially screened by the essentially isotropized electrons. Typical profiles of the ion and electron current densities are plotted in Fig. 3.7(a). Each filament creates a magnetic loop, which attracts the neighboring filaments of same current sign. The merging of two filaments generates a larger filament, of roughly twice the size of the primary filaments. As analyzed in Polomarov *et al.* (2008), this process goes along with a decrease or increase of the magnetic energy if the initial filaments are respectively super-Alvfénic or under-Alfvénic.

Figure 3.18 is a focus on two merging filaments in a 3D periodic simulation with parameters $v_{di} = v_{de} = 0.2c$, $mi = 100m_e$ (Sec. 3.3.4). The ion current isosurface (red) shows two separated filaments at $t\omega_{pe} = 400$ as confirmed by the slice of the magnetic field modulus at $x\omega_{pe}/c = 60$. After a delay of $170\omega_{pe}^{-1}$, the two filaments have merged in the region $30 < x\omega_{pe}/c < 60$. Moreover, we notice that the filament dynamics also includes kink modes since at $t\omega_{pe} = 400$, the filaments are slightly winding. The coalescence process in 1D and 2D geometry will be discussed in Sec. 3.4.5.

A critical parameter ruling the coalescence time is the total current carried by a filament. This current includes an ion contribution, j_i, which can be estimated assuming spatial separation of the (initially superposed) counter-streaming ion beams: $j_i \simeq 0.5q_eZ_in_iv_i$, where n_i is the total density of the ion population (including the two beams). This estimate fairly agrees with the value $j_i = 0.1q_en_ec$ measured in the 2D simulation with $v_i = 0.2c$, $m_i = 100m_e$ [red line in Fig. 3.7(a)]. The electrons tend to screen the ion current and their response depends on the size of the filament. This can be understood qualitatively for an isotropic electron distribution: its screening contribution will be more efficient if the size of the filament exceed the electron skin depth ($\lambda_{\rm sat}/2 \gg c/\omega_{pe}$). On the contrary, if the size of the filament verifies $\lambda_{\rm sat}/2 \sim c/\omega_{pe}$, the electron screening will be less efficient. Assuming a linear response of the electrons, the general form of the screening factor, $\kappa = j/j_i$, has been derived by Achterberg *et al.* (2007) in a 3D geometry. It reads

$$\kappa = \frac{j}{j_i} = 2I_1\left(\frac{\pi\omega_{pe}}{2ck_{\rm sat}}\right)K_1\left(\frac{\pi\omega_{pe}}{2ck_{\rm sat}}\right), \tag{3.60}$$

where I_1 and K_1 are the modified Bessel functions of respectively the first and second kind. Making use of a large-argument expansion, the above equation can be approximated by $j \simeq j_i 2ck_{\rm sat}/\pi\omega_{pe}$. Equation (3.60) is plotted in Fig. 3.19(b) as a solid line. Applying the above expression to the simulation $v_{di,e} = 0.2c$, $m_i = 100m_e$, we measure a wavelength of $\lambda_{\rm sat}\omega_{pe}/c \simeq 10$ and thus predict a screening electron current of $|j_e| \simeq 0.5j_i$, matching the blue solid curve [Fig. 3.7(a)]. The estimate $j/j_i \simeq 2ck_{\rm sat}/\pi\omega_{pe}$, superposed in 3.19(b) as a dashed black line, matches fairly well the exact expression of $k_{\rm sat}c/\omega_{pe} \gtrsim 0.8$. Moreover, it can be shown that $j/j_i = 2ck_{\rm sat}/\pi\omega_{pe}$ is the exact 2D screening factor. Consequently, we deduce an approximated total current

$$j \simeq q_eZ_in_iv_ick_{\rm sat}/\pi\omega_{pe}\,. \tag{3.61}$$

(a) $t\omega_{pe} = 400$

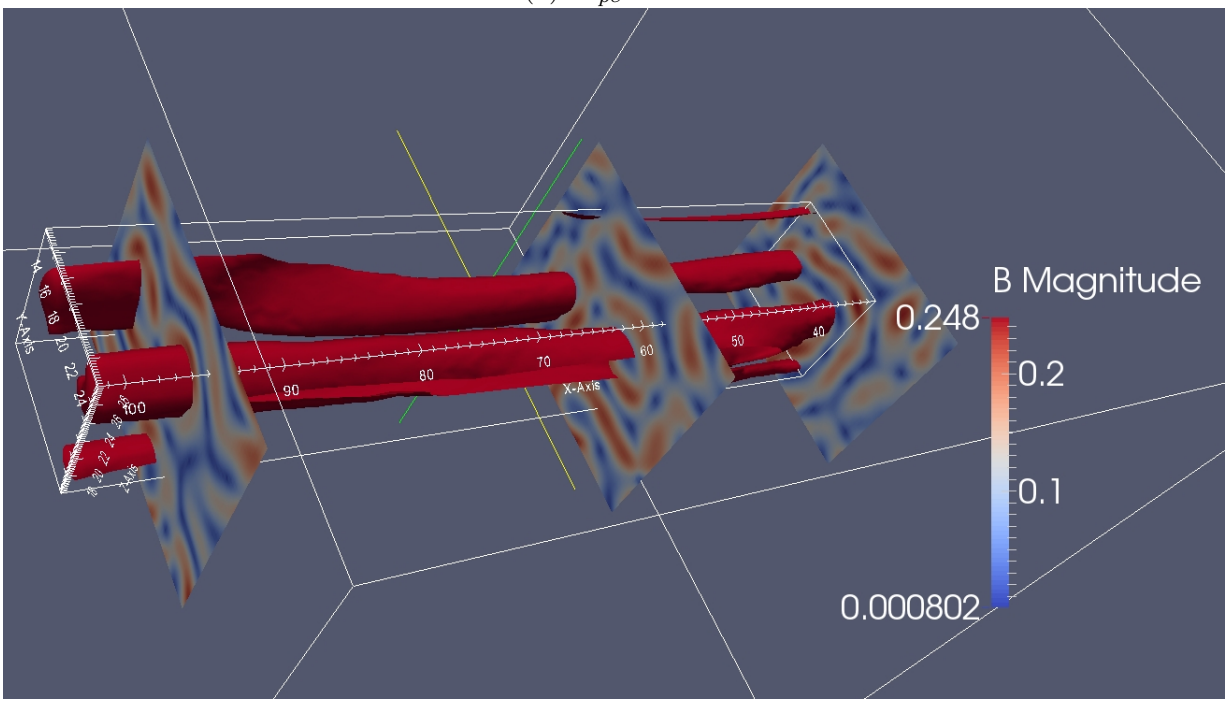

(b) $t\omega_{pe} = 570$

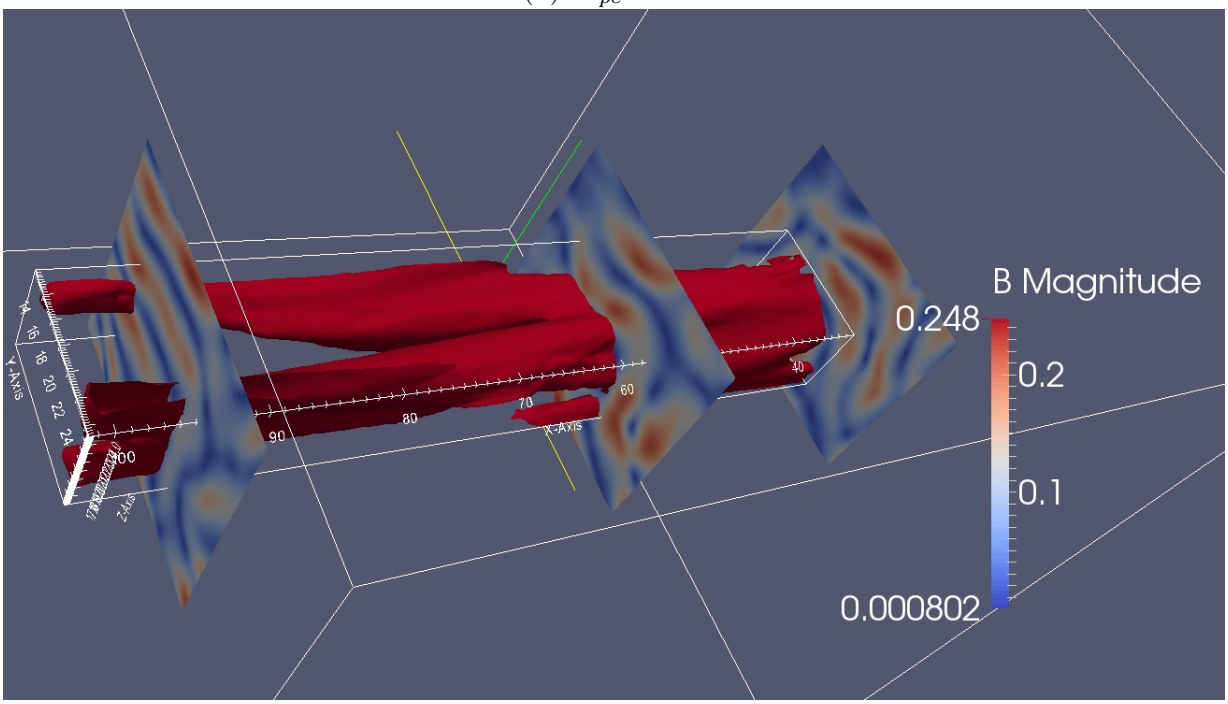

Figure 3.18. Merging of two ion filaments in a 3D a simulation with initial parameters $v_{di} = 0.2c, v_{de} = 0.2c$, $m_i = 100m_e$ and $T_{i,e}^{(0)} = 0.01m_e c^2$. Ion current isosurface (in red) at $j_i = 0.085q_e n_i c$ at $t\omega_{pe} = 400$ (a) and $t\omega_{pe} = 570$ (b).The ions in the filaments are streaming from right to left. Three slices of the magnitude of B ($|\mathbf{B}|$ normalized to $m_e\omega_{pe}/c$) are superposed. Space is normalized to c/ω_{pe}.

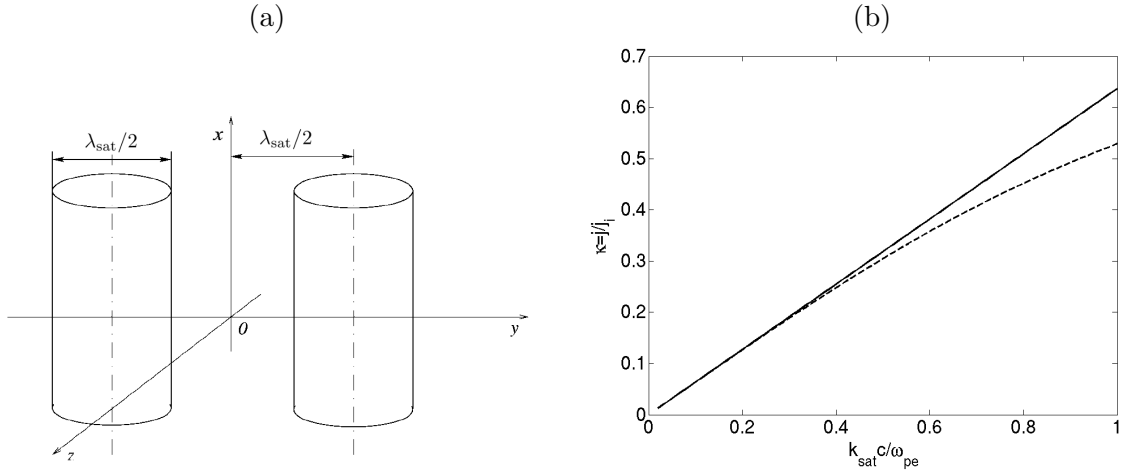

Figure 3.19. (a) Schematic representation of the initial state taken from Ref. Medvedev *et al.* (2005) for two attracting filaments. Here the distance D_0 can be linked to the magnetic field period: $D_0 = \lambda_{\rm sat}/2$. (b) Screening factor Eq. (3.60) as a function of $k_{\rm sat}c/\omega_{pe}$ in black solid line. The estimate $j/j_i = 2ck_{\rm sat}/\pi\omega_{pe}$ is superposed as black dashed line.

As a result, in the limit $k_{\rm sat}c/\omega_{pe} \ll \pi/2$, the total current carried by a filament verifies $I_0 \simeq n_i v_i c k_{\rm sat}\lambda_{sat}^2/16\omega_{pe}$.

We will now present a simple model of the influence of collective filaments coalescence on the evolution of $k_{\rm sat}$.

3.4.3 Collective coalescence dynamics

Following the general idea of Medvedev *et al.* (2005); Achterberg *et al.* (2007), we start by the equation of motion applied to the distance between two filaments, $\lambda_{\rm sat}$, as illustrated in Fig. 3.19. We also assume that the filaments' diameter is $\lambda_{\rm sat}/2$. Their mass per length unit is $\rho_l \simeq m_i n_i S$ where $S \propto (\lambda_{\rm sat}/2)^2$ (respectively $S \propto \lambda_{\rm sat}/2$) is the section of the filament in 3D (respectively 2D):

$$\rho_l d_{tt}^2(\lambda_{\rm sat}) = SBj\,. \tag{3.62}$$

Here j and B are the magnetic field and current, averaged on a filament. As the filament get closer, we assume that ρ_L and j stay essentially constant. Making use of Eq. (3.61), the above equation can be recast as

$$m_i d_{tt}^2 \lambda_{\rm sat} = \frac{j}{n_i} B\,, \tag{3.63}$$

where κ is the screening electron factor. We emphasize that no assumption is made on the exact value of the filament section S. Equation (3.63) stays approximately valid as long as two attracting filaments have the same typical width $\sim \lambda_{\rm sat}/2$. Moreover, the above equation is valid in both 2D and 3D geometries. The average effective force Bj/n_i applied to the filament derives from a potential energy Aj/n_i where A and j are also averaged over a filament's width. Hence, the sum of the potential energy with the effective kinetic energy $0.5m_i[d_t(\lambda_{\rm sat})]^2$ is conserved, which yields

$$m_i d\left[(d_t\lambda_{\rm sat})^2\right] = -\frac{j}{n_i} dA\,. \tag{3.64}$$

Our goal is not to solve the exact dynamics of merging filaments but, rather, to estimate the temporal evolution of the average separation length of a large number of filaments during their collective dynamics. Consequently, we will average Eq. (3.64) on the y direction, over a large

number of filaments. We thus obtain

$$d\left[m_i(d_t\lambda_{\rm sat})^2\right] = \frac{j}{n_i} d\langle A\rangle_y \,. \tag{3.65}$$

We now introduce the total current estimate of Eq. (3.61). Because A and j are always of the same sign for two attracting filaments, the variations of $\langle A\rangle_y$ can be related to the variations of $\sqrt{S_p}$. Since $\langle A\rangle_y$ is averaged over a filament width, the estimate $\langle |A|\rangle_y \simeq q_e^{-1}\sqrt{S_p}$ neglects the long-wavelength component of the spectrum ($\lambda \gtrsim 2\lambda_{\rm sat}$). There follows

$$d\left[m_i(d_t\lambda_{\rm sat})^2\right] \simeq Z_i \kappa v_i d\sqrt{S_p}\,, \tag{3.66}$$

which can be readily integrated:

$$m_i(d_t\lambda_{\rm sat})^2 - m_i(d_t\lambda_{\rm sat})^2_{t_0} = Z_i \int_{S_p(t_0)}^{S_p(t)} \frac{\kappa v_i}{2\sqrt{S_p}} dS_p \,. \tag{3.67}$$

Since this equation only involves quantities spatially averaged over a large number of filaments, it can be combined to the quasilinear equations of Sec. 3.3.2. We notice that, in principle, the quasilinear theory assumes that the coherence time of the particles though the magnetic fluctuations ($\sim \omega/kv_{th}$) is negligible compared to the growth time (Γ^{-1}) of the fluctuations in contrast with a field evolution ruled by magnetic trapping. However, as previously observed by Davidson *et al.* (1972), the simulations presented in Sec. 3.3.4 support the validity of the quasilinear model up to the nonlinear, magnetic-trapping regime.

The initial state of the collective coalescence dynamics of Eq. (3.66) is taken at the end of the linear phase ($t = t_*$), where the plasma has been proven to verify $|\xi_i| \leq 1$. At the beginning of the saturation phase, a quasi-equilibrium filamented state sets in (Suzuki 2008; Suzuki & Shigeyama 2009; Gedalin *et al.* 2010; Abraham-Shrauner 2010). Assuming $\partial_t\lambda_{\rm sat} = 0$ at the beginning of the saturation phase ($t = t_*$).

Taking the temporal derivative of Eq. (3.67) and making use of Eqs. (3.42) and (3.10), one obtains

$$d_{tt}^2\lambda_{\rm sat} = \frac{\kappa v_0^2}{(2\alpha_i)^{1/2}\lambda_{\rm sat}} \frac{a_i}{(a_i+2)^2} \,. \tag{3.68}$$

The above equation can be solved numerically with v_{di}, S_p, a_i and κ verifying Eqs. (3.39), (3.42), (3.10) and (3.60). This exact resolution is plotted in Figs. 3.20(a,b) as black solid lines. The dashed red lines correspond to the numerical resolution of Eq. (3.68), neglecting the initial temperature ($T_{ix}^{(0)} = T_{iy}^{(0)} = 0$), the drift velocity variations ($v_{di} = v_0$) and using the simplified screening factor $\kappa \simeq 2ck_{\rm sat}/\pi\omega_{pe}$. No significant difference is found between the approximate and exact curves. Consequently, we will now simplify further Eqs. (3.28), (3.37), (3.41), (3.42) and (3.60). With

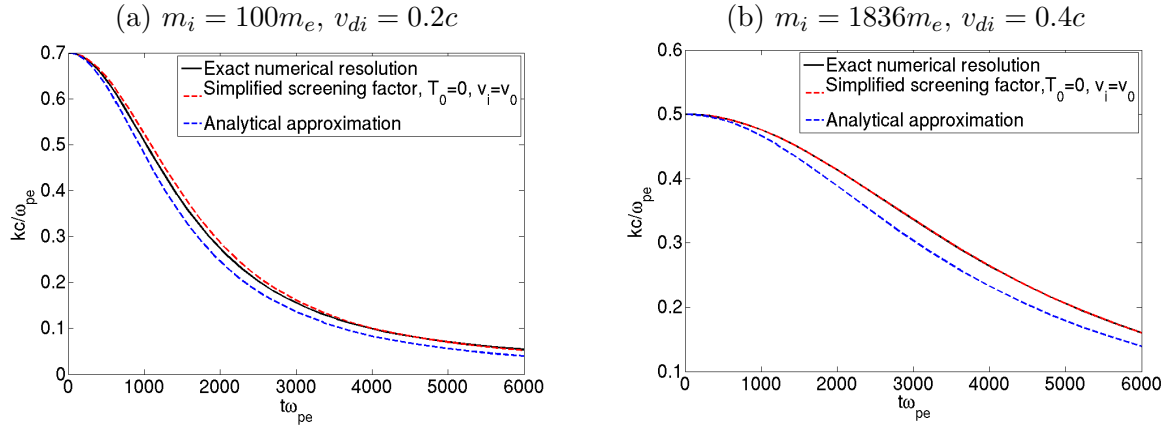

Figure 3.20. Temporal evolution of the dominant wavevector, $k_{\rm sat}$, from the exact numerical resolution of Eq. (3.68) (black solid line) for $m_i = 100m_e$, $v_{id} = 0.2c$ (a) and $m_i = 1836m_e$, $v_{di} = 0.4c$ (b). The ion temperature is taken to be $T^{(0)}_{ix,y} = 0.01m_ec^2$ in both cases. The wavevector at the beginning of the saturation phase are $k_*c/\omega_{pe} = 0.7$ (a) and $k_*c/\omega_{pe} = 0.45$ (b) (see Figs. 3.15(b) and 3.13(b)). The numerical solutions of (3.68), with $T^{(0)}_{ix,y} = 0$, with constant drift velocity $v_i = v_0$, and a implified screening factor $\kappa \simeq 2ck_{\rm sat}/\pi\omega_{pe}$ are superposed in red dashed lines. The analytical approximations in the large-ion anisotropy limit, Eq. (3.80), are superposed as dashed blue lines.

$K_2 = m_iv_0^2 + 3T_0 \simeq m_iv_0^2$, $\eta_i = k_{\rm sat}/k_{\rm max} \simeq 0.5$ and $\alpha_i = 0.5$:

$$S_p \simeq \frac{1}{2\alpha_i Z_i^2}\left(\frac{m_iv_0}{2+a_i}\right)^2, \tag{3.69}$$

$$k_{\rm sat} \simeq \frac{\eta_i\omega_{pi}}{c}\sqrt{\frac{m_iv_0}{\sqrt{2\alpha_iZ_i^2S_p}} - 2}\,, \tag{3.70}$$

$$a_i \simeq \frac{m_iv_0}{\sqrt{2\alpha_iZ_i^2S_p}} - 2\,, \tag{3.71}$$

$$T_{iy} \simeq \sqrt{2\alpha_iZ_i^2v_0^2S_p}\,, \tag{3.72}$$

$$v_i \simeq v_i^{(0)}\exp\left[2\frac{T_0}{K_2} - \frac{2\sqrt{2\alpha_iZ_i^2S_p}}{m_iv_0}\right], \tag{3.73}$$

$$\kappa \simeq \frac{2ck_{\rm sat}}{\pi\omega_{pe}}\,. \tag{3.74}$$

Plugging Eqs. (3.69)-(3.74) into Eq. (3.66) with $v_i = v_0$ yields

$$(d_t\lambda_{\rm sat})^2 \simeq \frac{2\omega_{pi}v_0\eta_i}{m_i\pi\omega_{pe}}\int_{S_0}^{S_p}\frac{dS_p}{2\sqrt{S_p}}\sqrt{\frac{m_iv_0}{\sqrt{2\alpha_iZ_i^2S_p}} - 2}\,. \tag{3.75}$$

By making the change of variable $S_p = (p_0/2)^2 \sin(t)^4$ where $p_0 = m_i v_0/\sqrt{2\alpha_i Z_i^2}$, one obtains

$$(d_t \lambda_{\rm sat})^2 = \frac{2\omega_{pi} v_0 \eta_i}{m_i \pi \omega_{pe}} \frac{p_0}{\sqrt{2}} \times \left[\arcsin\left(\sqrt{\frac{2}{p_0}} S_p^{\frac{1}{4}}\right) - \arcsin\left(\sqrt{\frac{2}{p_0}} S_0^{\frac{1}{4}}\right) + \sqrt{\frac{2}{p_0}} S_p^{\frac{1}{4}} \sqrt{1 - \frac{2}{p_0} S_p^{\frac{1}{2}}} - \sqrt{\frac{2}{p_0}} S_0^{\frac{1}{4}} \sqrt{1 - \frac{2}{p_0} S_0^{\frac{1}{2}}} \right] . \tag{3.76}$$

Using Eqs. (3.69) and (3.70), the argument of the arcsin function can be recast as

$$\sqrt{\frac{2}{p_0}} S_p^{\frac{1}{4}} = \frac{\lambda_{\rm sat}}{\sqrt{\lambda_{\rm sat}^2 + \lambda_c^2}} , \tag{3.77}$$

where the critical wavelength $\lambda_c = \sqrt{2\pi^2/\eta_i^2} c/\omega_{pi}$ is of the order of an ion skin-depth. We have shown that in the high-anisotropy limit ($a_i \gg 2$), the wavelength at saturation is smaller than the ion skin-depth, $\lambda_{\rm sat} \ll 2\pi c/\omega_{pi}$. The regime $\lambda_{\rm sat} \sim \lambda_c \sim 2\pi c/\omega_{pi}$ is found only close to ion isotropization ($a_i < 2$). Consequently, in the high ion anisotropy limit and until quasi-isotropization of the ions ($a_i \sim 2$), the following condition is fulfilled

$$\sqrt{\frac{2}{p_0}} S_p^{\frac{1}{4}} \simeq \frac{\lambda_{\rm sat}}{\lambda_c} \ll 1 . \tag{3.78}$$

Hence, Eq. (3.76) can be solved in the high anisotropy limit, yielding

$$\lambda_{\rm sat} \simeq \lambda_* \left(1 + \frac{(t - t_*)^2}{\tau_0^2}\right) , \tag{3.79}$$

$$k_{\rm sat} \simeq \frac{k_*}{1 + \frac{(t-t_*)^2}{\tau_0^2}} , \tag{3.80}$$

where t_* is the start time of the nonlinear Weibel phase, $\lambda_* = \lambda_{\rm sat}(t_*)$ and

$$\tau_0 = \sqrt{\frac{\lambda_* c}{\omega_{pi}}} \frac{\pi (2\alpha_i)^{\frac{1}{4}}}{v_0 \eta_i} \sqrt{\frac{2\omega_{pe}}{\omega_{pi}}} , \tag{3.81}$$

is the typical coalescence time, that is, the time over which $k_{\rm sat}$ decreases by a factor two. It can also be viewed as the lifetime of the slowly-evolving filamentary state established at magnetic saturation. As expected, it increases with the typical distance between filaments after saturation λ_* Note that the dependence of τ_0 upon the unknown parameters λ_* cancels out in the long-time limit of $\lambda_{\rm sat}(t)$. Also, the influence of the electron screening transpires through the ω_{pe} term in Eq. (3.81). Figures 3.20(a,b) show good agreement between the approximated formula, Eq. (3.79) , and the numerical resolution of Eq. (3.68). The initial wavevectors are measured in the PIC simulations summarized in Figs. 3.13(b) and 3.15(b).

The last step consists in plugging Eq. (3.80) into (3.69)-(3.73) to obtain a fully predictive analytical formulation of the plasma parameters as a function of $\Delta t = t - t_*$, the plasma initial

conditions (at $t = 0$) and the wavevector at the end of the linear phase k_* at ($t = t_*$):

$$a_i \simeq \frac{k_*^2 c^2}{\omega_{pi}^2 \eta_i^2} \frac{1}{(1 + \Delta t^2/\tau_0^2)^2}\,, \tag{3.82}$$

$$S_p \simeq \frac{m_i^2 v_0^2}{2\alpha_i Z_i^2} \frac{(1 + \Delta t^2/\tau_0^2)^4}{\left(k_*^2 c^2/\omega_{pi}^2 \eta_i^2 + 2(1 + \Delta t^2/\tau_0^2)^2\right)^2}\,, \tag{3.83}$$

$$T_{iy} \simeq m_i v_0^2 \frac{(1 + \Delta t^2/\tau_0^2)^2}{k_*^2 c^2/\omega_{pi}^2 \eta_i^2 + 2(1 + \Delta t^2/\tau_0^2)^2}\,, \tag{3.84}$$

$$v_i \simeq v_0 \exp\left[\frac{2T_0}{K_2} - \frac{2(1 + \Delta t^2/\tau_0^2)^2}{k_*^2 c^2/\omega_{pi}^2 \eta_i^2 + 2(1 + \Delta t^2/\tau_0^2)^2}\right]\,, \tag{3.85}$$

$$K_{ix} \simeq \frac{k_*^2 c^2}{\omega_{pi}^2 \eta_i^2} m_i v_0^2 \frac{k_*^2 c^2/\omega_{pi}^2 \eta_i^2}{k_*^2 c^2/\omega_{pi}^2 \eta_i^2 + 2(1 + \Delta t^2/\tau_0^2)^2}\,. \tag{3.86}$$

Taking $\Delta t = 0$ gives the plasma parameters at the beginning of the Weibel saturation phase for a given k_*:

$$a_i(t_*) \simeq \frac{k_*^2 c^2}{\omega_{pi}^2 \eta_i^2}\,, \tag{3.87}$$

$$S_p(t_*) \simeq \frac{m_i^2 v_0^2}{2\alpha_i Z_i^2} \frac{1}{\left(k_*^2 c^2/\omega_{pi}^2 \eta_i^2 + 2\right)^2}\,, \tag{3.88}$$

$$T_{iy}(t_*) \simeq m_i v_0^2 \frac{1}{k_*^2 c^2/\omega_{pi}^2 \eta_i^2 + 2}\,, \tag{3.89}$$

$$v_i(t_*) \simeq v_0 \exp\left[\frac{2T_0}{K_2} - \frac{2}{k_*^2 c^2/\omega_{pi}^2 \eta_i^2 + 2}\right]\,, \tag{3.90}$$

$$K_{ix}(t_*) \simeq \frac{k_*^2 c^2}{\omega_{pi}^2 \eta_i^2} m_i v_0^2 \frac{k_*^2 c^2/\omega_{pi}^2 \eta_i^2}{k_*^2 c^2/\omega_{pi}^2 \eta_i^2 + 2}\,. \tag{3.91}$$

The cold-limit approximation made in deriving Eqs. (3.69)-(3.74) (*i.e.* assuming $T_{i,e}^{(0)} = 0$) is assumed valid provided the initial temperature (at $t = 0$), verifies,

$$T_{i,x/y}^{(0)} \ll T_{iy}(t_*) \simeq m_i v_0^2 \frac{1}{k_*^2 c^2/\omega_{pi}^2 \eta_i^2 + 2}\,. \tag{3.92}$$

According to the simulations presented in Sec. 3.3.4, one has k_* scales as $k_* \sim [0.5 - 0.7]\omega_{pe}/c$, so that $T_{i,x/y}^{(0)} \lesssim 4 m_e v_0^2$. For instance, the case of $v_{di} = 0.2c$, $m_i = 100 m_e$ leads to $T_{i,x/y}^{(0)} = 0.01 m_e c^2 \ll [2 - 4] m_e v_0^2 = [0.08 - 0.16] m_e c^2$.

3.4.4 Influence of the initial filament size

Our model requires the knowledge of the typical filament wavelength at the beginning of the ion-Weibel saturation phase, λ_*. While its precise evaluation is very challenging, we can approximate it by making use of Davidson's magnetic trapping model. Equation (3.26) can be recast in order to

estimate the amplitude of the potential vector, $A_{k_y}^{\rm sat}$, at the end of the ion-Weibel linear phase:

$$A_{k_y}^{\rm sat}(t_*) \simeq \frac{m_i \Gamma_{k_y}^2}{v_d q_e Z_i k_y^2}\,. \tag{3.93}$$

Making use of $\xi_i = \Gamma/k_y\sqrt{2T_{iy}^{(0)}/m_i}$ and $A_{k_y}^{\rm sat} \sim \sqrt{S_p}$, we obtain

$$S_p(t_*) \sim \frac{T_0^2}{v_0^2 Z_i^2}\xi_i^4\,. \tag{3.94}$$

In the above equation, ξ_i can be calculated at $t=0$, by numerically solving the dispersion relation of Eq. (3.4). We can resort to the quasilinear relations of Eqs. (3.41) and (3.10) to obtain an estimate of λ_* and k_*:

$$\lambda_* \sim \frac{c}{\eta_i \omega_{pi}} \frac{2\pi}{\sqrt{\frac{K_2}{T_{iy}^{(0)}\sqrt{1+\frac{2\alpha K_2}{m_i v_0^2}\xi_i^4}} - 2}}\,, \tag{3.95}$$

$$k_* \sim \eta_i \frac{\omega_{pi}}{c} \sqrt{\frac{K_2}{T_{iy}^{(0)}\sqrt{1+\frac{2\eta_i K_2}{m_i v_0^2}\xi_i^4}} - 2}\,, \tag{3.96}$$

where $K_2 = m_i v_0^2 + 2T_{iy}^{(0)} + T_{ix}^{(0)}$, $\eta_i \simeq 0.5$ and $\alpha \simeq 0.5$. If the plasma is initially cold: ($T_{iy}^{(0)} = T_{ix}^{(0)} \ll m_i v_0^2$), we obtain:

$$k_* \sim \eta_i \frac{\omega_{pi}}{c} \frac{\sqrt{a_i(t=0)}}{(1+\xi_i^4)^{\frac{1}{4}}}\,. \tag{3.97}$$

The ξ_i factor can be estimated by maximizing the growth rate obtained from the exact resolution of the initial dispersion relation. For initially cold plasmas, the initial ion anisotropy ratio verifies $a_i(t=0) \propto m_i$, and the initial wavelength λ_* therefore scales as the electron skin-depth. The above formulation, based on the Davidson scaling, depends on ξ_i^4 calculated at $t=0$ and is thus imprecise. Making use of Eq. (3.95), the case of Fig. 3.21(a) gives $\lambda_*\omega_{pe}/c \simeq 9.3$ for $\xi_i \simeq 1.8$ and $\tau_0 \simeq 1500\omega_{pe}$. The case of Fig. 3.21(b) gives $\lambda_*\omega_{pe}/c \simeq 17$ $\lambda_*\omega_{pe}/c \simeq 14$) for $\xi_i \simeq 3.8$ and $\tau_0 \simeq 4300\omega_{pe}$. In these two cases, the estimated λ_* differs from the value used in the PIC comparison. However the growth estimate of Eq. (3.95) does not affect the long term evolution.

As already reminded, the long-time evolution of $\lambda_{\rm sat}(t)$ is independent of λ_*. For $\Delta t \gtrsim 3\tau_0$, we can neglect unity with respect to $\Delta t^2/\tau_0^2$ [see Eq. (3.79)], and thus obtain

$$\lambda_{\rm sat} \simeq \frac{\eta_i^2}{3\pi^2(2\alpha_i)^{\frac{1}{2}}}\left(\frac{v_0}{c}\right)^2 \frac{c}{\omega_{pe}}(\omega_{pi}\Delta t)^2\,. \tag{3.98}$$

$\lambda_{\rm sat}$ is found to depend on the electron mass in contrast to its early time evolution. From Eq. (3.10), we derive the long time evolution of the ion anisotropy ratio:

$$a_i \simeq \frac{4\pi^2 c^2}{\eta_i^2 \omega_{pi}^2}\left(\frac{\pi^2(2Z_i^2\alpha_i)^{\frac{1}{2}}}{\eta_i^2 Z_i}\frac{2\omega_{pe}}{\omega_{pi}}\frac{c}{\omega_{pi}v_0^2}\right)^2 (\Delta t)^{-4}\,, \tag{3.99}$$

$$\simeq \frac{32\pi^6\alpha_i}{\eta_i^6}\frac{m_i}{Z_i m_e}\left(\frac{c}{v_0}\right)^4 (\omega_{pi}\Delta t)^{-4}\,. \tag{3.100}$$

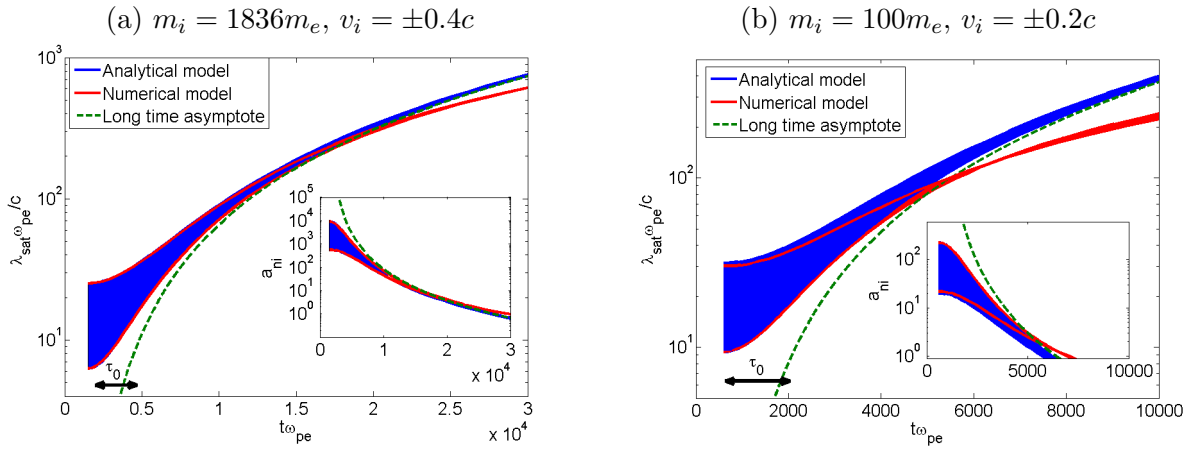

Figure 3.21. Temporal evolution of $\lambda_{\rm sat}\omega_{pe}/c$ from the numerical (red solid line) and analytical approximate (blue solid line) resolution of Eq. (3.68) for two systems. (a) $m_i = 1836m_e$, $v_i = \pm 0.4c$ with the initial conditions $6 < \lambda_*\omega_{pe}/c < 25$ at $t_*\omega_{pe} = 1500$. (b) $m_i = 100m_e$, $v_i = \pm 0.2c$ with the initial conditions $9 < \lambda_*\omega_{pe}/c < 30$ at $t_*\omega_{pe} = 600$. The subpanels plot the temporal evolution of the ion anisotropy ratio, the typical time τ_0 is superposed as a black arrow. The long-time approximations of Eqs. (3.98) and (3.100) are superposed as green dashed lines.

The time required to reach a given $a_i = 2$ can therefore be estimated (assuming the initial condition $a_i^{(0)} \gg 1$) as

$$\Delta t_{\rm form} \simeq 32 \frac{c}{v_0 \omega_{pi}} \sqrt{\frac{\omega_{pe}}{\omega_{pi}}}, \tag{3.101}$$

This time can be viewed as a lower limit of the shock formation time $\tau_{\rm sh}$, since it does not take into account the time required to achieve saturation of the ion-Weibel instability, or to achieve complete ion isotropization ($a_i = 0$). The corresponding limit of the shock formation length is

Figures 3.21(a,b) illustrate for two parameter sets the theoretical evolution of λ_* and a_i. In each case, we have considered a finite range of values for λ_*. As expected, the curves converge to the same limiting curve after a few τ_0's. This behavior holds as long as the ion anisotropy stays large.

3.4.5 Comparison with periodic PIC simulations

The theoretical predictions of the plasma and spectral parameters are displayed in Figs. [3.13, 3.14, 3.15]. In the cases of Fig. 3.13 ($m_i = 100m_e$, $v_i = 0.2c$, $v_e = 0$), Fig. 3.14 ($m_i = 100m_e$, $v_i = 0.2c$, $v_e = 0.2c$) and Fig. 3.15 ($m_i = 1836m_e$, $v_i = 0.4c$, $v_e = 0$), the dominant wavevectors at the end of the linear phase are measured to be $k_*c/\omega_{pe} = 0.5$ (at $t_*\omega_{pe} = 700$), $k_*c/\omega_{pe} = 0.45$ (at $t_*\omega_{pe} = 450$) and $k_*c/\omega_{pe} = 0.45$ (at $t_*\omega_{pe} = 1000$) respectively. For the sake of completeness, we gave an estimate of k_*. Applying Eq. (3.97) for the three case gives $0.3 < k_*c/\omega_{pe} < 0.6$ which is consistent with the simulations.

In the three cases considered, after the ion Weibel saturation is reached, the spectral and plasma parameters present a flat profile reproduced by the coalescence analytical expressions. This correspond to the quasi-equilibrium filamented state discussed previously. A few τ_0's later, a strong increase (respectively decrease) of the transverse temperature (respectively ion anisotropy ratio and drift velocity) is found in agreement with our predictions. The observed weak variations of the ion drift velocities [Figs. 3.13, 3.14, 3.15(a,b,d,e,f)], support the assumption of constant ion drift velocities ($v_{di} = v_0$) made in deriving our analytical estimates.

In a 3D geometry, the coalescence of two filaments does not necessarily involve a third repulsed filament as in 2D. Moreover, the quasi-equilibrium taking place at the beginning of the Weibel-

filamentation seems less pronounced [Fig. 3.17(b)]. Apart from these differences, the 3D plasma parameters match (solid red lines) very well the 2D simulation (dotted-dashed black line).

3.5 Conclusion

The slow dynamics of the saturated Weibel-filamentation instability has been described using a set of quasilinear relations developed in Sec. 3.3.2. Good agreement between the theoretical expectations and simulations has been found for various plasma parameters in the case of highly anisotropic ion beams and homogeneous profiles. The successful comparison in the non-linear regime has motivated us to model the spectrum dynamics. Unlike in 1D geometry, we have found that the process of filament merging mostly drives the plasma and spectrum evolution in 2D and 3D geometries. This process represents the long-time evolution of the magnetic spectrum up to ion isotropisation. A simple model of collective coalescence has been developed and solved in the high-ion anisotropy limit. The typical time required to "quasi-isotropize" the ion population scales as $\omega_{pi}^{-1}(m_i/m_e)^{1/4}$. Hence, due to the electron screening contribution, this time scale as $\omega_{pi}^{-3/4}/m_e^{1/4}$ instead of ω_{pi}^{-1}. Another way to evidence its importance consist in neglecting the variations of the electron screening factor. Starting from Eq. (3.67) and assuming κ constant, one can show that the analytical estimate of the dominant wavelength verifies $\lambda_{\rm sat} \simeq \lambda_* \cosh(\Delta t/\tau_0')$ (where $\tau_0' \propto \lambda_*^{1/2}$ is a typical time). Hence, the short time evolution of the system is similar with or without constant electron screening (since $\cosh(\Delta t/\tau_0) \simeq 1 + \Delta t^2/\tau_0^2$ for small values of $\Delta t/\tau_0' \ll 1$). However, the long-time dynamics for constant screening shows an exponential growth of $\lambda_{\rm sat}$ which greatly contrasts with the result Eq. (3.79) ($\lambda_{\rm sat} \propto \Delta t^2$).

The relevance of our model to a more shock-relevant configuration will be addressed in the next chapter. The electron screening effect will be shown to be critical for understanding recent colliding plasma experiments.

Chapter 4

Weibel-mediated collisionless shock formation and propagation

This chapter addresses the formation and propagation of the ion-electron non-relativistic collisionless shocks in the non-relativistic regime. We demonstrate the validity of the coalescence model previously developed in a shock-relevant configuration until quasi-isotropization of the ions. Successful comparisons with recent experiments will be shown. Finally, the shock propagation will be studied and a model of the shock profile will be worked out.

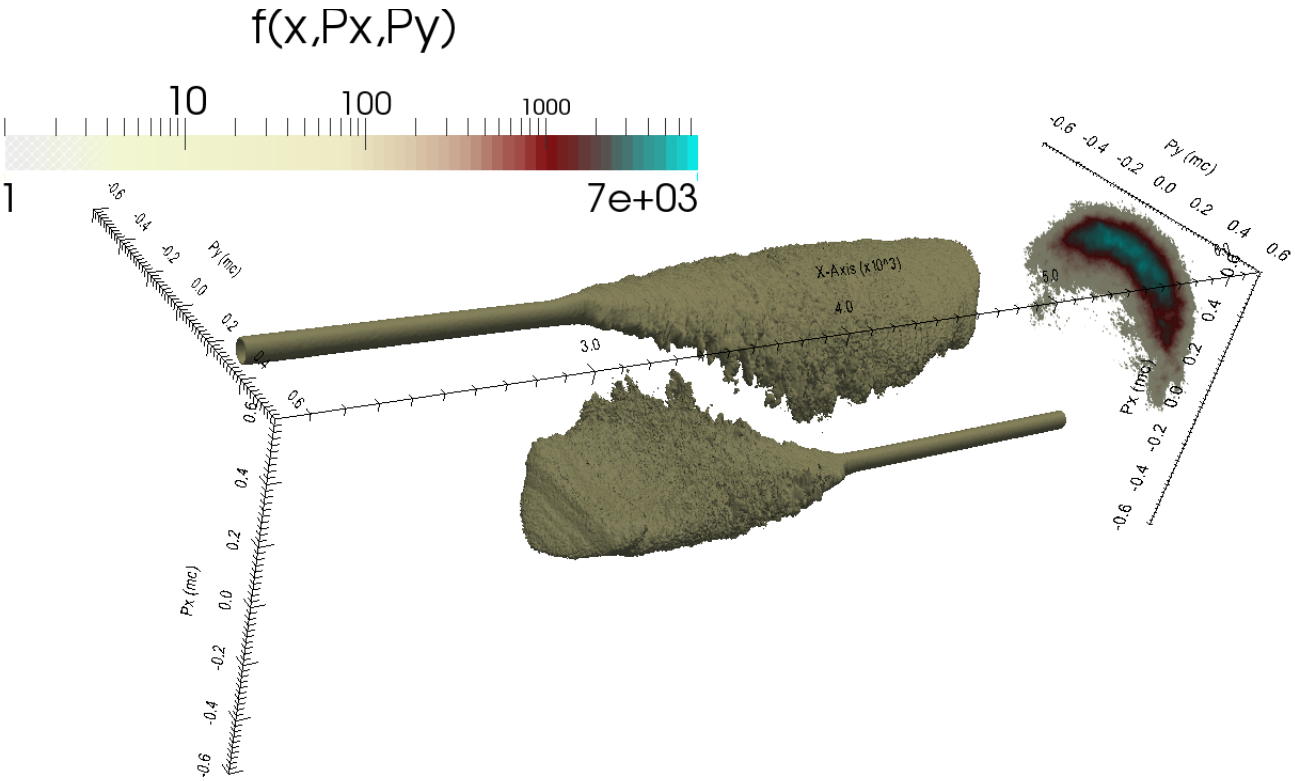

Figure 4.1. Three-dimensional phase space of two colliding bi-Maxwellian plasma slabs. The grey surface is an isosurface of the distribution function of each beams. A cut of the distribution function of one beam at the center $x = 4200c/\omega_{pe}$ is superposed as a colormap.

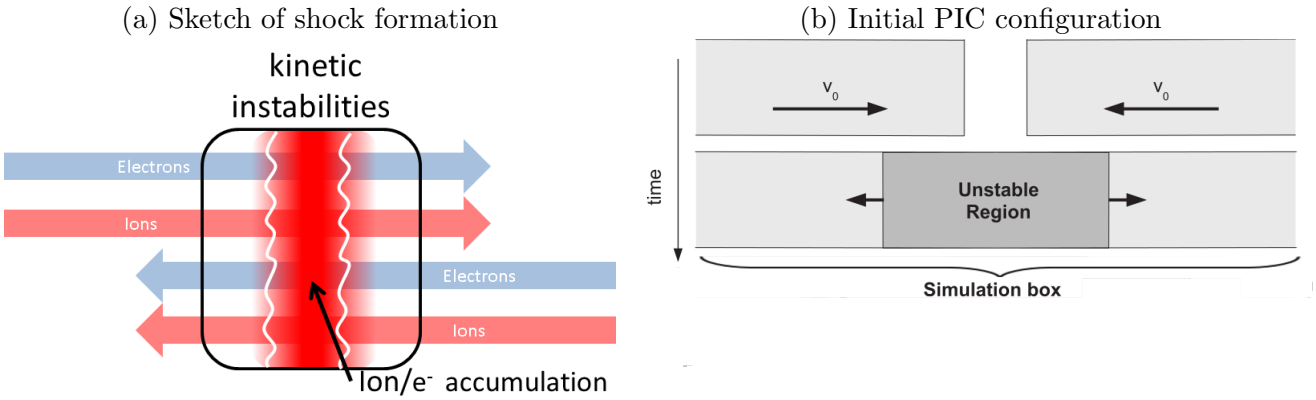

Figure 4.2. (a) Sketch of shock formation. The white wavy lines represent the Weibel transverse modulations (B-field and current density). (b) Initial PIC configuration of the simulations in this chapter

4.1 Introduction

Ab initio kinetic simulations of electron-ion collisionless shocks are now made possible using massively parallel particle-in-cell (PIC) codes, hence paving the way to a better understanding of the high-energy physics of a number of astrophysical scenarios (Kato & Takabe 2008; Spitkovsky 2008b). These numerical advances go along with experimental progress towards the laser-driven generation of collisionless shocks in laboratory (Kuramitsu *et al.* 2011). The most promising route relies upon the interaction of two counterpropagating plasma flows generated from the ablation of foil targets by nanosecond, high-energy kJ-class laser pulses (Drake & Gregori 2012). Such flows are of relatively low density ($n \ll n_c$, where $n_c \sim 10^{21}\,\mathrm{cm}^{-3}$ is the critical density of the laser) and low velocity ($v_i \sim 100 - 1000\,\mathrm{km\,s}^{-1}$). According to an increasing body of experimental and theoretical research, the kinetic ion-ion instabilities thus excited could lead to the formation of a collisionless shock. A few experiments have already been done (Kugland *et al.* 2013; Fox *et al.* 2013; Yuan *et al.* 2013; Huntington *et al.* 2013).

Electron-driven instabilities (Bret *et al.* 2010b) grow and saturate first, leaving the electrons mostly isotropized over the overlap ion beam-plasma region as shown in Chapter 3 in a simplified configuration. Note that electrostatic ion-driven instabilities, as in Dieckmann *et al.* (2007, 2008), can drive shock structures (Kato & Takabe 2010a; Dieckmann *et al.* 2013). However, for fast flow velocities ($v_i \gtrsim 0.01c$), the ion Weibel-filamentation instability subsequently develops, causing ion scattering off magnetic fluctuations [Fig. 4.2(a)]. Isotropized particles then accumulate in the center of the system until the Rankine-Hugoniot (Drury 1983) conditions are satisfied. The Rankine-Hugoniot conditions, based on energy, momentum and particle conservation across the shock front region give explicit formulation of the density jump ratio of a propagating collisionless shock: $n_{\mathrm{down}}/n_{\mathrm{up}} = (\Gamma_{\mathrm{ad}}+1)/(\Gamma_{\mathrm{ad}}-1)$ if $v_i \gg \sqrt{T_e/m_i}$. We introduced the adiabatic index Γ_{ad} which is equal to 2 in a 2D gaz and to 5/3 in a 3D gaz. Thus a 2D system should verify $n_{\mathrm{down}}/n_{\mathrm{up}} = 3$ and a 3D system yields $n_{\mathrm{down}}/n_{\mathrm{up}} = 4$. Hence each beam undergoes a compression ratio across the discontinuity of the shock front of 50% in 2D and 100% in 3D. Moreover, particle conservation yields a shock-front-velocity of $v_0/2$ in 2D and $v_0/3$ in 3D where v_0 is the velocity of the incoming flows.

Since the ion isotropization responsible of the shock formation results from the Weibel magnetic turbulence (Kato & Takabe 2008; Spitkovsky 2008b), we will use the nonlinear model of the ion-Weibel-filamentation instability developed in the previous chapter to predict the shock formation time. The good agreement between our theory and PIC simulation results will motivate us to apply our theoretic predictions to the interpretation of recent experimental measurements.

Then, the propagation of collisionless shocks will be studied by means of simulations results and quantitative estimate of the particle populations in front of the shock. The predictive coalescence model from chapter 3 will be adapted and successfully compared to two different simulations. This will lead us to an analytic formulation of the magnetic turbulence taking place in the upstream region.

4.2 Shock formation

4.2.1 Quasilinear model of shock formation

The quasilinear model of section 3.3 predicts the evolution of the ion parameters (drift velocities and temperatures), as a function of the effective magnetic energy S_p. Let us now consider two symmetric counter-propagating ions beams with open boundaries on the beam axis. While the plasma slabs overlap, the region experiencing a symmetric interaction is in the center of the system. The phase space $(x,\, p_x)$ of the two symmetric ion-electron beams ($m_i = 100m_e$, $v_i = v_e = \pm 0.2c$) on Fig. 4.3 illustrates that the only region with symmetric particle distributions is located at the center of the simulation box ($x\omega_{pe}/c = 4200$). The symmetric region has a thickness of a few ion skin depths c/ω_{pi}. This implies that we can neglect the influence of the axial gradient on the system if the overlapping region is a lot larger than c/ω_{pi}. Hence, the system verifies this assumption after a time of $\sim 10\omega_{pi}^{-1}$ which is smaller than the time needed to achieve Weibel saturation in all the simulations of Sec. 5.2. Consequently, at the center of the overlapping region, the drift velocities and temperatures being symmetric, their temporal evolution should be correctly predicted by the quasilinear model developed in the previous chapter. Close to each beam front, however, the interaction is no longer symmetric: the reflected/transmitted heated beam interacts with unperturbed Maxwellian distribution of the upstream particles.

4.2.2 Comparison with PIC simulations

Four 2D simulations of shock formation have been performed. We will collide two symmetric ion-electron bi-Maxwellian beams in a simulation box with transverse boundary conditions. In Chapter 2, half the system was simulated, colliding the plasma on refleted boundary conditions. However, we want to follow precisely the spectral and plasma parameters in the center of the overlap region, we will thus simulate the entire system made of the two plasma beams. The temporal and spatial steps are respectively $\Delta t = 0.2\omega_{pe}^{-1}$ and $\Delta x = \Delta y = 0.3c/\omega_{pe}$. The simulation box has periodic boundary conditions and its size is $L_x = 8400c/\omega_{pe}$ and $L_y = 537.6c/\omega_{pe}$ in the case $m_i = 25m_e$ and $L_x = 12600c/\omega_{pe}$ and $L_y = 537.6c/\omega_p$ in the case $m_i = 100m_e$. The Esirkepov scheme and a third interpolation order are used (see 6). We also employ 50 macroparticles per mesh. The ions (of mass m_i subsequently defined) and electrons are initialized by counter-propagating Maxwell-Jüttner type (1.22) distribution functions of temperature $T_{e,i} = m_e c^2/100$ and drift velocity $v_{de} = v_{di} = \pm v_d$, as illustrated in Fig. 4.2(b). The density of the beams is normalized to the total density of the particle population in the overlap region. Hence, the density of each beam is $n_{i,e} = 1/2$. The results, gathered in Figs. 4.4, evidence a fairly good agreement with the theoretical predictions at the center of the overlap region. This is verified down to very small values of the anisotropy ratio. In the case of Fig. 4.4(a,b) ($v_d = 0.2c$, $m_i = 100m_e$), a_i decreases from ~ 20 at $t\omega_{pe} = 1000$ to ~ 2 at $t\omega_{pe} \simeq 5000$. This matches the value of Eq. (3.101) which gives $\Delta t_{\rm form} \simeq 3\tau_0 \simeq 4000\omega_{pe}^{-1}$. For ($v_d = 0.4c$, $m_i = 100m_e$) and ($v_d = 0.4c$, $m_i = 25m_e$), the theoretic quasi-shock formation time reads $\Delta t_{\rm form}\omega_{pe} \simeq 2500$ and 900 respectively, in agreement with the PIC values of ~ 2800 and ~ 800 respectively.

The values of $\lambda_* \omega_{pe}/c = [6\pi, 8\pi]$ used in the model scale fairly well with Eq. (3.96). However, the values are smaller than for the periodic simulations of Chapter 3. These different physical conditions

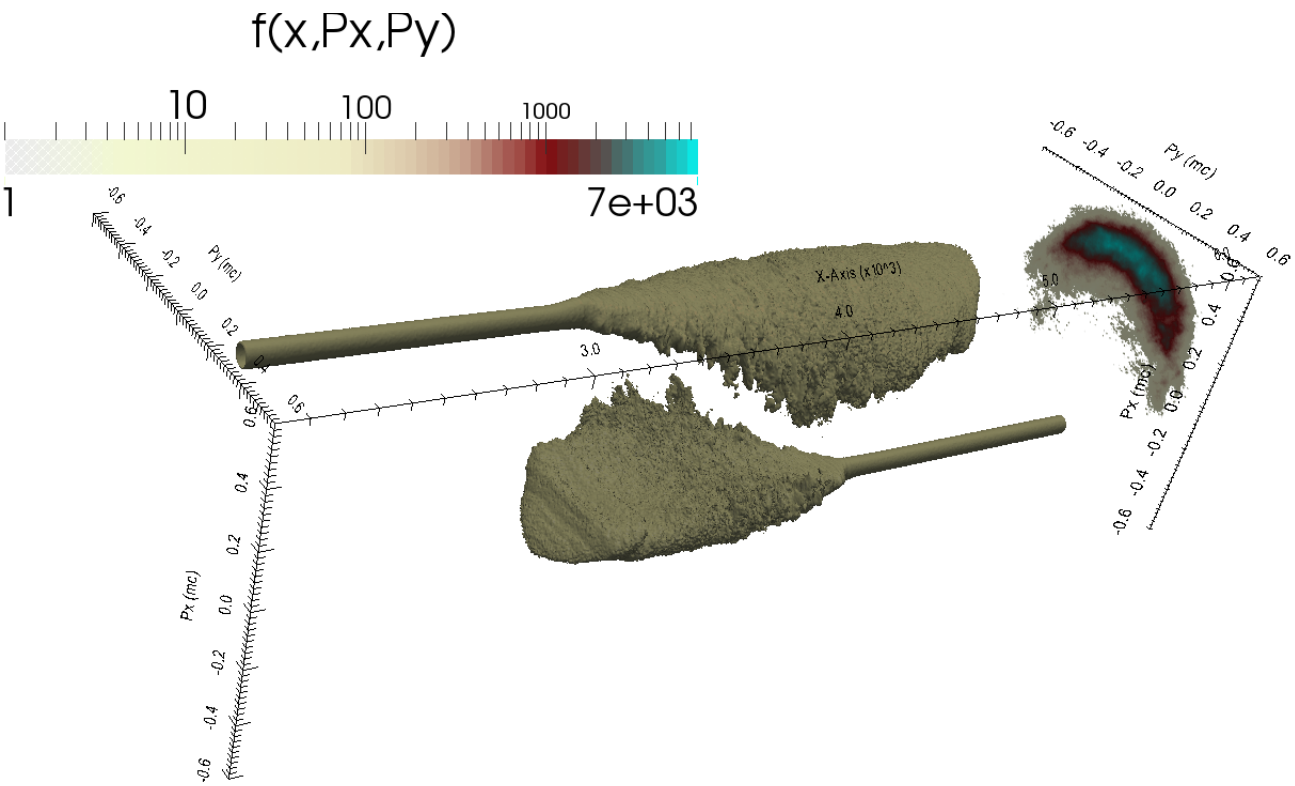

Figure 4.3. Ion phase space $x\omega_{pe}/c$, p_x/m_ic, p_y/m_ic isosurface (grey) before shock formation for two symmetric counter-propagating ions-electron plasma beams for $v_e = v_i = \pm 0.4c$, $m_i = 100m_e$. The colormap corresponds to the ion distribution in logarithmic scale of the beam $v_i = +0.4c$ at the center ($x\omega_{pe}/c = 4200$).

can be qualitatively understood as follows. During the collision, there is a constant influx of energy in contrast to the periodic systems of the previous chapter. Hence, the instabilities preceding the ion-Weibel saturation could result, at $t = t_*$, in a significant increase of the ion temperature, and thus to a larger wavelength. Moreover, the simulated evolutions of the spectral and ion parameters do not show any quasi-equilibrium at the saturation as for the periodic simulations of Chapter 3. This seems to contradict the initial conditions used in our model ($\partial_t \lambda_{\rm sat}(t_*) = 0$). At the time of magnetic saturation ($t = t_*$) in the periodic simulation, the newly formed filaments undergo a quasi-equilibrium, as mentioned in Chapter 3. In the present configuration, the constant influx of energy could destabilize the filaments at saturation and thus explain the difference of initial slope between our model and the simulation results.

The sub-panels of Figs. 4.4(b,d,f) evidence an increase in the ion density at the center of the domain. When the density increase reaches a factor of three, the shock is formed and the central region becomes the downstream region of the shock. From this moment, the model ceases to be valid. Note that when the downstream is formed, the ion anisotropy ratio becomes very small and corresponds to a quasi-isotropic ion distribution function.

4.2.3 Comparison with colliding-plasma experiments

Observation of Weibel-type filamented structures Until recently, no experimental observation of the Weibel-filamentation instability in its fully saturated regime has been done. The first observation of Weibel-filamentation instability has been published in Allen *et al.* (2012). However it is an electron instability and a small number of filaments are observed. Between 2012 and 2013, three experiments have reported detailed measurements of transverse field modulations triggered

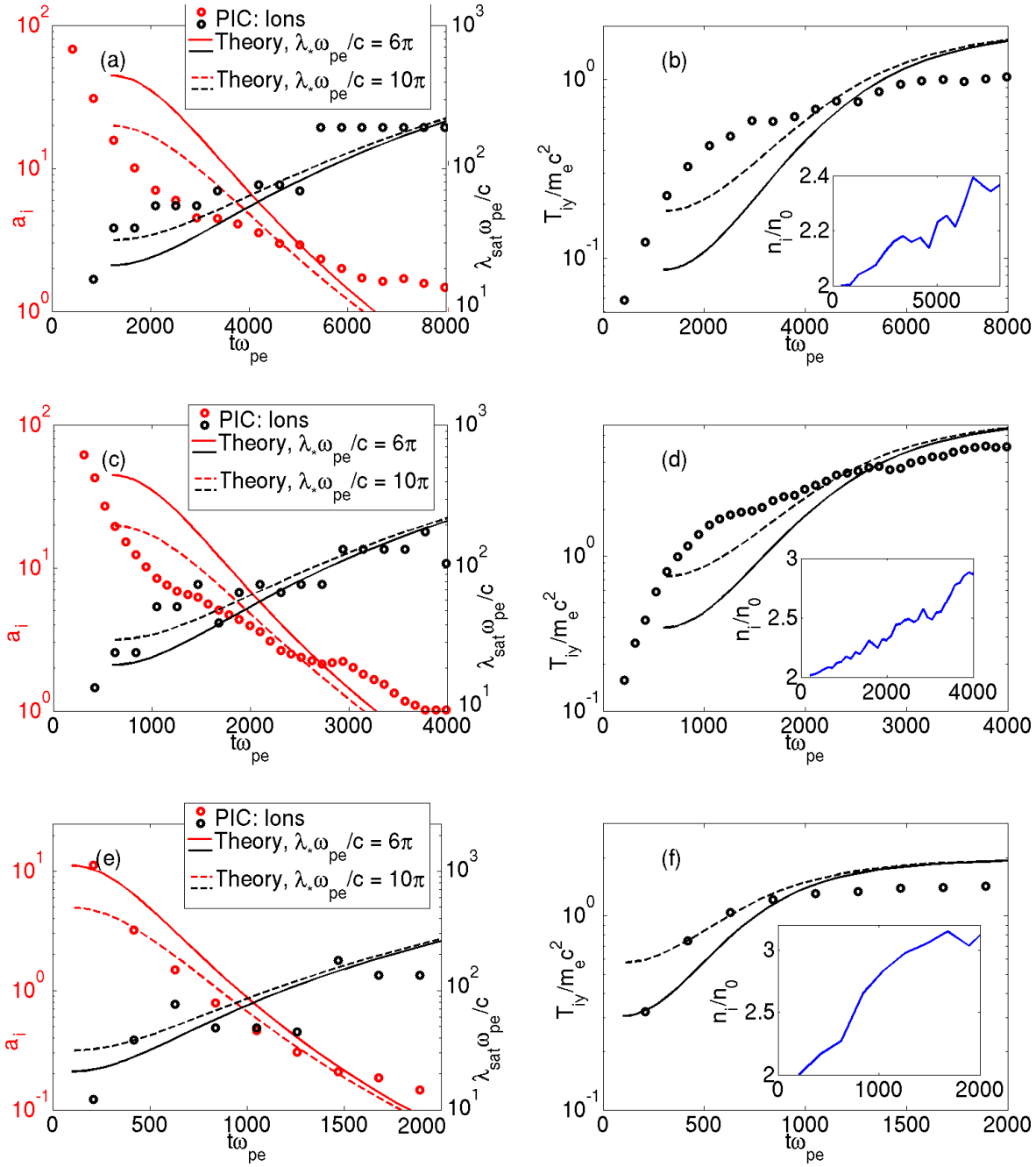

Figure 4.4. Evolution of a_{ni} [red, left axis of (a,c,e)], $\lambda_{\rm sat}\omega_{pe}/c$ [black, right axis of (a,c,e)], T_{iy}/m_ec^2 (b,d,f) and n_i/n_0 [inset of (b,d,f)] as a function of time normalized to ω_{pe}^{-1}. The circles correspond to the 2D PIC simulation values. Equations (3.79), (3.82) and (3.84) are plotted respectively in plain and dashed lines for $\lambda_*\omega_{pe}/c = 6\pi$ and $\lambda_*\omega_{pe}/c = 10\pi$ respectively with (a,b) $v_i = \pm 0.2c$, $m_i = 100m_e$, $t_*\omega_{pe} = 1200$, (c,d) $v_i = \pm 0.4c$, $m_i = 100m_e$, $t_*\omega_{pe} = 600$ and (e,f) $v_i = \pm 0.4c$, $m_i = 25m_e$, $t_*\omega_{pe} = 100$. The values of t_* are extracted from the simulations.

(a) Fox *et al.* (2013)

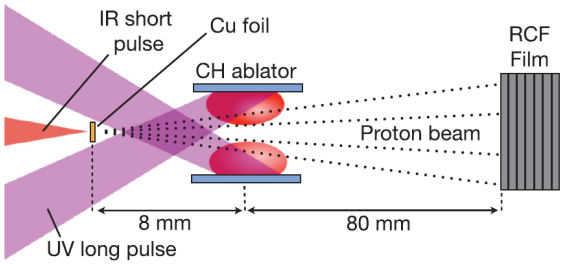

(b) Kugland *et al.* (2012b)

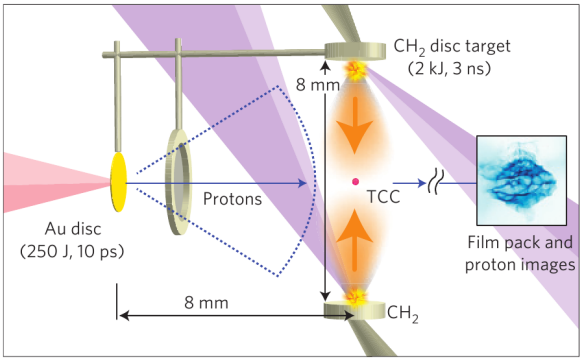

Figure 4.5. Schematic representation of the experimental setup of Fox *et al.* (2013) (a) and Kugland *et al.* (2012b) (b). The two plastic foils are separated by $2L = 4.5$mm in (a).

by the superposition of two plasma beams (Kugland *et al.* 2012b; Yuan *et al.* 2013; Fox *et al.* 2013). Two plastic foils (CH) separated from $2L = 4.5$mm (in the case of Fox *et al.* (2013)) are heated by two long laser pulses. Two plasma plums are then formed, expending in vacuum. The experimental setup is illustrated in Fig. 4.5. It is said that radiation-hydrodynamics simulations show that the plasma velocity and density obey the well-known self-similar solution of an isothermal expanding plasma (Manheimer *et al.* 1982)

$$v \simeq C_s + \frac{L}{t}\,, \tag{4.1}$$

$$n \simeq n_{ab} \exp\left(-\frac{L}{C_s t}\right)\,, \tag{4.2}$$

where the sound speed C_s and the ablation density n_{ab} are estimated to be $C_s \simeq 2\,10^5 \mathrm{m.s}^{-1}$ and $n_{ab} \simeq 7\,10^{20}\mathrm{cm}^{-3}$ respectively (Fox *et al.* 2013). Note that in (Fox *et al.* 2013) the time starts at the beginning of the laser drive whereas in Kugland *et al.* (2012b), it starts when the two plasma collides. The time required for the expending plasmas to collide is of $L/v_d \simeq 2.8$ns and 4ns for Fox *et al.* (2013) and Kugland *et al.* (2012b, 2013) respectively. Hence, the use of Eqs. (4.1) and (4.2) requires time shift (for Kugland *et al.* (2012b, 2013) only) given by $t \equiv t_{xp} + 4$ns, where $0.5\mathrm{ns} \leq t_{xp} \leq 7$ns is the time as defined in the Reference. We then estimate $C_s \simeq 2.3 \times 10^5 \mathrm{m.s}^{-1}$ and $n_{ab} \simeq 9.5\,10^{17}\mathrm{m}^{-3}$ for Kugland *et al.* (2012b, 2013).

The interaction of the plasma plumes has been diagnosed via proton radiography (Mackinnon *et al.* 2004; Kugland *et al.* 2012a). The protons are generated by a secondary, ultra-intense, short-pulse laser shot onto a copper foil. The deflections undergone by the protons though the electromagnetic turbulence induced by the colliding beams are detected by a stack of radiochromic films (RCF). Depending on its depth, a given RCF is mostly sensitive to a specific energy range in the proton spectrum. The radiographs of Fig. 4.6 corresponding to protons of energy $\sim 5-10$MeV, illustrate the evolution of the unstable overlap region over the time interval $3.8\mathrm{ns} \leq t \leq 5.8$ns.

Transverse lines, underlined in red in Fig. 4.6, are visible in (Kugland *et al.* 2012b; Fox *et al.* 2013). They correspond the Biermann battery fields advected by the expanding plasmas and located at the edge of the central interaction region, as explained in Kugland *et al.* (2013). Since this fields revolve around the plasma plumes, the central overlap region should not be affected.

Filamentary structures are also visible on the three radiographs of Fox *et al.* (2013) and also in (Kugland *et al.* 2012b; Yuan *et al.* 2013) (not shown). They demonstrate the existence of electric or magnetic transverse modulations (by the deflection of the protons). We highlight that an electric field pattern could be responsible of such radiographs. Hence, they do not constitute a clear proof

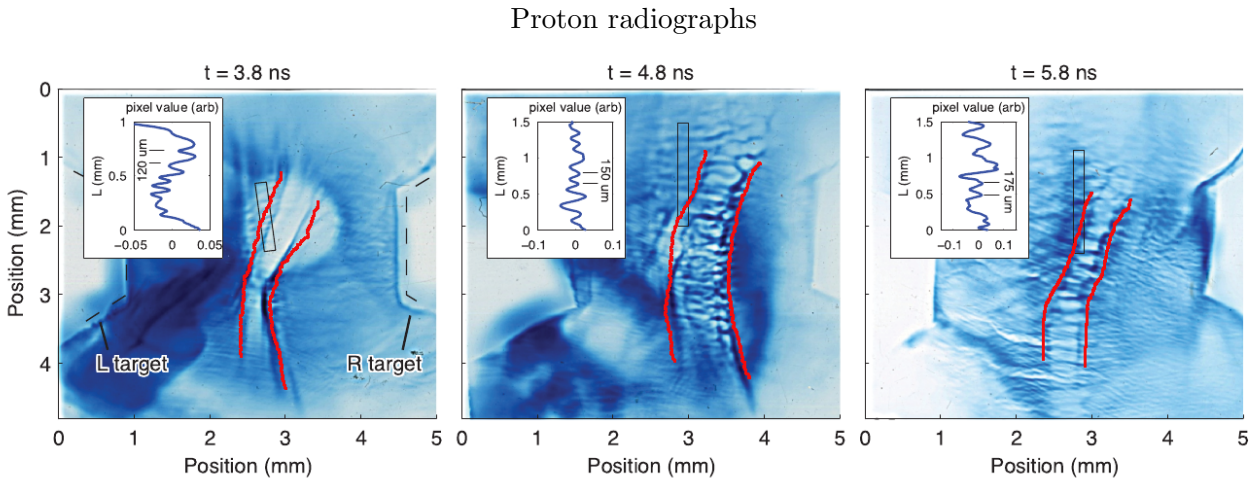

Figure 4.6. Proton radiography diagnostics at $t = 3.8$, 4.8 and 5.8 ns after laser plasma interaction in Fox *et al.* (2013). The probing protons have typical energies of $5 - 10$MeV. The red lines underline the Biermann battery fields advected by the expanding plasmas as explained in Kugland *et al.* (2013). The symmetric Weibel-unstable interaction region is located between these two red lines. Taken from Fox *et al.* (2013). The typical magnetic field seen by the diagnostic protons is of order 60T.

of a Weibel-filamentation instability taking place in the overlap region. However, Fox *et al.* (2013) compare the radiographs with a large-scale 2D PIC simulation with comparable plasma parameters (with ablative velocity and density profiles given by Eqs. (4.1) and (4.2)) but artificially large electron mass (of $\simeq 37m_e$). The simulation evidences transverse magnetic modulations (due to the Weibel-instability) at the center of the overlap region. Although only qualitative comparison is made in the publication, we will proceed to a quantitative comparison between the radiographs, the simulation of Fox *et al.* (2013), and our model.

The case of Kugland *et al.* (2012b) will also be considered, although no comparison with simulations is made. The only differences with Fox *et al.* (2013) are the larger separation of the plastic foils, and the longer laser pulse duration, resulting in a longer interaction time.

Validity of our model assumptions We will now verify the validity of the main assumptions of our model for the experimental parameters Fox *et al.* (2013). the comparison with the quasilinear equations developed in Chapter 3. The model supposes constant plasma density, and velocity and a high ion anisotropy ratio. A CH "mean ion" (10% of C^{6+}, 90% of H^+) drifting at $v > 2\times10^5$m.s^{-1}, initially at $T_i \sim 150$eV (Fox *et al.* 2013) gives an initial anisotropy ratio $a_{CH} \gtrsim 100 \gg 1$ which verifies the large ion anisotropy ratio assumption. However, the density and velocity of the plasma flow in the central region evolve as Eqs. (4.1) and (4.2). This is not handled by the model. We will first assess the influence of the velocity variation of Eq. (4.1) on the quasilinear equations.

In the experiment of Fox *et al.* (2013), the ions are drifting at $v \gtrsim 3\times10^5$m.s^{-1} The velocity variation predicted by our quasilinear relations (Eq. (3.28)) reads $\partial_t v_{di} \simeq \alpha(Z_i^2/m_i)v_{di}\partial_t S_p/T_{iy}$. This can be compared to the ablative velocity variation: $|\partial_t v_{\rm ab}| \simeq x/t^2$ where $x \simeq L = 2.25$mm in the central region. Making use of $S_p \sim q_e^2B^2\lambda_{\rm sat}^2/4\pi^2$, yields $S_p/m_e^2c^2 \sim 0.45$ for $B \simeq 60$T, $\lambda_{\rm sat} \simeq 120\mu$m and for a mean ion of 10% C^{6+} and 90% H^+ (given in Fox *et al.* (2013)). We then estimate $\partial_t S_p$ in the experiment by $S_p/\tau_{\rm xp}$ where we introduced the typical time of the experiment $\tau_{\rm xp} \sim 1$ns. Finally, we have $|\partial_t v_{di}| > |\partial_t v_{\rm ab}|$ for $t \gtrsim \sqrt{L/|\partial_t v_{di}|} \simeq 2$ns. Used has been made of the plasma parameters given in Fox *et al.* (2013): $T_i \simeq 150$eV, $n_i \simeq 1.4\times10^{19}$cm^{-3} (Eq. (4.2) at $t = 2.8$ns with $n_{ab} = 7\times10^{20}$cm^{-3}), and $v_i \simeq 8\times10^5$m.s^{-1}. This evidences that the drift velocity variations due to the ion Weibel-instability dominates the ablative flow velocity variations in the

(a) Predictive model *vs.* Fox *et al.* (2013) (b) Predictive model *vs.* Kugland *et al.* (2012b)

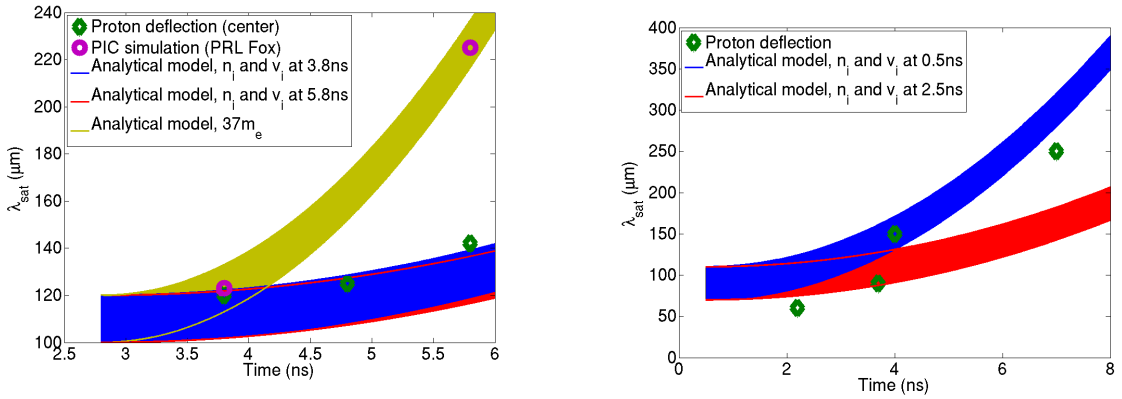

Figure 4.7. Time evolution of the filamentation wavelength as inferred from the experiments of Kugland *et al.* (2012b, 2013) (a) and Fox *et al.* (2013) (b) (green diamonds). The analytical model is illustrated by blue solid lines for the parameters of the experiments. Error bars due to uncertain value of λ_* are provided by the widths of the theoretical curves. (a) Making use of $T_i = 100$eV, $v_d(0.5\text{ns}) \simeq 10^6\text{m.s}^{-1}$ and $n_e(0.5\text{ns}) \simeq 8\times10^{18}\text{cm}^{-3}$ (blue line) and $v_d(2.5\text{ns}) = 8.5\times10^5\text{m.s}^{-1}$ and $n_e(2.5\text{ns}) = 1.3\times10^{19}\text{cm}^{-3}$ (red line) as initial plasma parameters with $70\mu\text{m} < \lambda_* = 110\mu\text{m}$ at $t_* = 0.5$ns. A mean ion made of 33% of C^{6+} and 66% of H^+ has been used (CH_2 target). (b): $T_i = 150eV$ with $v_i = 8\times10^5\text{m.s}^{-1}$, $n_e = 3\times10^{18}\text{cm}^{-3}$ (blue line) and $v_i = 3\times10^5\text{m.s}^{-1}$, $n_e = 8\times10^{18}\text{cm}^{-3}$ (red line) for $100\mu\text{m} < \lambda_* = 120\mu\text{m}$ at $t_* = 2.8$ns. A mean ion made of 10% of C^{6+} and 90% of H^+ has been used (as in the article). The analytical model taking into account the simulated (Fox *et al.* 2013) electron mass of $37m_e$ in the screening factor κ Eq. (3.74) is illustrated as a yellow line.

(Fox *et al.* 2013) experiment for the three diagnostics of Fig. 4.6(b). As for the density variations, their influence on our model will be subsequently estimated, taking as initial plasma condition, the density and velocity at $t = 2.8$ns and $t = 5.8$ns. In the similar experiment of Kugland *et al.* (2012b), velocity variations are dominated by the magnetic turbulence for $t \gtrsim 3$ns for $T_i \simeq 100$eV, $v_d \simeq 1000\text{m.s}^{-1}$ and assuming $B \simeq 60$T (not measured in the experiment). In this case also, the velocity variations are dominated by the magnetic turbulence at long times.

Note that the distance between filaments in Fox *et al.* (2013), is measured in the insets of Fig. 4.6 outside of the central interaction region. It thus corresponds to an asymmetric two-stream configuration which is not supported by our model. We will thus apply our model to the center of the interaction region, located between the Biermann-Battery trace (explained above) for a mean ion of 10% C^{6+} and 90% H^+. The typical length at the *center* of Fig. 4.6 are $\lambda = 120$, 125 and 140μm at respectively $t = 3.8$, 4.8 and 5.8ns (green diamonds of Fig. 4.7(b)). We also superposed the typical length of the simulation results in purple rings. The case of Kugland *et al.* (2012b) in Fig. 4.7(a) gives $\lambda = 70$, 90, 140 and 250μm at, respectively, $t = 2.4$, 3.8, 4 and 7ns.

The predictive model of Sec. 3.4.3 requires that the plasma evolution is dominated by filament coalescence. Moreover, Eqs. (3.80)-(3.86) require $T_i^{(0)} \ll T_{iy}(t_*)$ which is approximately verified since $T_i^{(0)} \sim 2.9\,10^{-4} m_e c^2$ and $T_{iy}(t \geq t_*) > 4\,10^{-4} m_e c^2$. Hence the analytic formulations are approximately valid in the context of the experiments of Kugland *et al.* (2012b); Fox *et al.* (2013).

Comparison with the experiments The initial condition λ_* can be estimated for the two experiments making use of Eq. (3.95). For the Fox *et al.* (2013) experiment, we consider a mean ion of 10%C^{6+}-90%H^+ with the plasma parameters at 2.8ns given in the reference ($T_i \simeq 150$eV, $v_i \simeq 8\times10^5\text{m.s}^{-1}$ and $n_i \simeq 1.4\times10^{19}\text{cm}^{-3}$), and obtain $\lambda_* \simeq 100\mu$m for $|\xi_i| \simeq 0.7$. The theoretical predictions for $100\mu\text{m} < \lambda_* < 120\mu\text{m}$ at $t = 2.8$ns is illustrated by the blue solid line. The width of the colored region provides error for our theoretical estimates as illustrated in Figs. 4.7(a). The weak

influence of the ablative density and velocity variations is assessed using $v_i(5.8ns) \simeq 6 \times 10^5 \mathrm{m.s}^{-1}$ and $n_i(5.8ns) \simeq 2 \times 10^{20} \mathrm{cm}^{-3}$ as initial conditions. Overall, correct agreement is found between the predictions and experimental results.

In order to save computational time, the simulation of Fox *et al.* (2013) makes use of an artificially increase electron mass $m_e^{PIC} \simeq 37 m_e$. This enables to relax the space-time resolution and speed up the early-time electron-driven instability phase. Although realistic ion parameters are used, the overestimated electron mass affects the ion filamentation dynamics due to the weaker electron screening. Hence the PIC simulation overestimate the net current inside a filament and the associated magnetic field, which tends to accelerate the coalescence dynamics. This may explain why, PIC-simulated wavelength increases more rapidly than in the measurements. This discrepancy is well reproduced by our model using the same artificially increased electron mass. As shown by Eq. (3.98), the typical coalescence time is proportional to $m_e^{-1/4}$, so that the filament dynamics is accelerated by a factor $37^{1/4} \simeq 3$ compared to the experiment.

The same analysis can be made for Kugland *et al.* (2012b) experiment (although no PIC simulation results are shown) which gives $70\mu\mathrm{m} < \lambda_* < 110\mu\mathrm{m}$ for $1.2 < |\xi_i| < 2$ (estimated from solving the full H^+-C^{6+}-e^- dispersion relation with $T_0 = 100\mathrm{eV}$, $v_i = 10^6 \mathrm{m.s}^{-1}$). These values of λ_* are taken as initial conditions in our model for $T_i \simeq 100\mathrm{eV}$, $v_d(0.5\mathrm{ns}) \simeq 10^6 \mathrm{m.s}^{-1}$ and $n_e(0.5\mathrm{ns}) \simeq 8 \times 10^{18} \mathrm{cm}^{-3}$ [Eqs. (4.1) (4.2), blue line of Fig. 4.7(a)] which grossly agrees well with the experimental points. The ablative density and flow velocity at $t = 2.5\mathrm{ns}$ (Eqs. (4.1) and (4.2)) ($v_d(2.5\mathrm{ns}) = 8.5 \times 10^5 \mathrm{m.s}^{-1}$ and $n_e(2.5\mathrm{ns}) = 1.3 \times 10^{19} \mathrm{cm}^{-3}$) are used as initial plasma conditions in our model (red solid line) and evidences a discrepancy on the evolution of the wavelength. The density variations due to the ablative regime seems to play a significant role in this case, at least for $t \gtrsim 4\mathrm{ns}$, which is not taken into account in our model. Note that system is followed on a longer time scale in Kugland *et al.* (2012b), $\sim 10^6 \omega_{pe}^{-1}$, than in Fox *et al.* (2013), $\sim 4 \times 10^5 \omega_{pe}^{-1}$.

4.3 Shock propagation

4.3.1 Formation of the downstream

Once the ions are isotropized, particles start to accumulate at the center of the overlap region. This results in a local density increase as illustrated by the enclosed plots of Figs. 4.4(a,b) and s4.4(a,b). The density increases until the Rankine-Hugoniot (Drury 1983) conditions are satisfied. Hence, the shock is formed when the density jump ratio is equal to three in 2D (simulation) and to four in 3D. When the density in the center of the overlapping region has reached its maximum value, the compressed (downstream) region starts expanding outwards behind a front called the shock front. Hence, the downstream of the shock is getting formed. This is illustrated in Fig. 4.8(a) which evidences a density jump ratio of $1.5/0.5 = 3$ and a downstream centered in $x = 4200 c/\omega_{pe}$ of thickness $\sim 1000 c/\omega_{pe}$. The anisotropy ratio profile of Fig. 4.8(d) indeed evidences an isotropic ion population in the downstream. Note that close to the shock front, the ion populations are not exactly isotropic and two distinct beams start to be visible. This is confirmed by the phase space of Fig. 4.9(a,b) detailed later on.

Assuming that the downstream particles are fully isotropized (at least at the center), an estimate of the ion temperature T_i^{ds} can be made from energy conservation. The total energy of downstream population is $3T_i^{\mathrm{ds}}/2$ in 3D $2T_i^{\mathrm{ds}}/2$ in 2D. This can be related to the initial energy of the ion beam

(neglecting the initial temperature): $m_i v_0^2/2$. Hence, we obtain

$$T_i^{\rm ds} \simeq \frac{m_i v_0^2}{2} \qquad \text{(2D)}\,, \tag{4.3}$$

$$T_i^{\rm ds} \simeq \frac{m_i v_0^2}{3} \qquad \text{(3D)}\,. \tag{4.4}$$

The transverse temperature profiles of the two ion beams are illustrated on Fig. 4.8(c) and evidence a downstream ion temperature close to $T_i^{\rm ds} \simeq 2m_e c^2$ as predicted by Eq. (4.3).

The anisotropy ratio, the transverse temperature and the averaged drift velocity profiles of Figs. 4.8(c,d,f) evidence a region composed of two beams for $x\omega_{pe}/c > 5000$ and $x\omega_{pe}/c < 3000$. This region is located close to the shock front and is called the upstream. In this region, the initial drifting plasma ($v_i = 0.4c$) encounters a hot ($T_{iy} \sim m_e c^2$, $-0.5c < v_i < -0.4c$) ion population generated at the shock front. This induces an asymmetric Weibel instability characterized by strong density modulations in the regions $2500 < x\omega_{pe}/c < 3000$ and $5500 < x\omega_{pe}/c < 6000$ [Fig. 4.8(a)]. These ion filaments are induced by magnetic fluctuations illustrated in Fig. 4.8(b). The profile of $S_p = \sum_{k_y} |A_{k_y}|^2$ is [Fig. 4.8(e)] and shows a clear (linear) dependence upon the transverse temperature of the upstream ions. Moreover, a strong magnetic turbulence is found in the downstream, which may be attributed to a finite, albeit weak, ion anisotropy. A thicker downstream may present a region with smaller magnetic energy. This penetration of magnetic energy into the downstream is observed in many numerical studies (Kato & Takabe 2008; Keshet *et al.* 2009), studied in (Stockem *et al.* 2014) and could explain the long time radiative signature of gamma-ray-bursts (Lemoine 2013).

The Rankine-Hugoniot conditions, detailed in the introduction, shows that for a strong shock, the shock front velocity verifies $v_{\rm shock} = v_d/2$ in 2D (and $v_d/3$ in 3D). These simple relations comes from particle conservation across the shock front. They evidence that when an upstream flow, of density and velocity n_i and v_d, accumulates behind the shock front with vanishing drift velocity and density $3n_i$ ($4n_i$), the size of the resulting downstream increases. This results in a displacement of the shock front at the velocity $v_{\rm shock} = v_d/2$ ($v_{\rm shock} = v_d/3$). The temporal evolution of the ion density [Fig. 4.8(g)] for an upstream flow velocity of $v_d = 0.4c$ evidences a shock velocity of $v_{\rm shock} = 0.2c$ which confirms the above relations.

4.3.2 Reflected beam at the shock front

Figures 4.9(a,b) display the ion and electron phase spaces (x, p_x) of the shock at $t\omega_{pe} = 4830$. Two ion beams are clearly visible at $2000 < x\omega_{pe}/c < 3000$. A hot ion population is generated at the shock front ($x\omega_{pe}/c = 3500$) and drifts at $v_i \sim \pm 0.5c$ away from the shock front. The ion velocity profile [Fig. 4.8(f)] shows that, unlike the electrons, part of the incoming ions are transmitted though downstream and leak into the upstream at the opposite side. These counterstreaming ions are usually called "reflected ions" and could be named, in our case "transmitted ions" Hence, this hot and diluted ion populations create a double layer standing close to the shock front. Its density varies from 10% to 25% of the incoming ion density as shown by Fig. 4.8(h). We now introduce R_h, the ratio between the density of the reflected and the incoming ions. Although its local value depends on the distance to the shock front in our simulation, we will use a typical value of $R_h \simeq 0.2$ in the following. The mean velocity of the "transmitted ion population" is close, yet not equal to the opposite of the incoming ion velocity so that the total ion current does not vanish exactly in the upstream. This ion current, however, is efficiently neutralized (on averaged on the y-direction) by the electrons, yielding an essentially null total current [black plain line in Fig. 4.8(f)]. The upstream region then consists of two asymmetric (with respect to the ion density and temperature) ion beams current-neutralized by a hot electron population. This creates a region where two counter-

(a) Ion density n_i/n_0

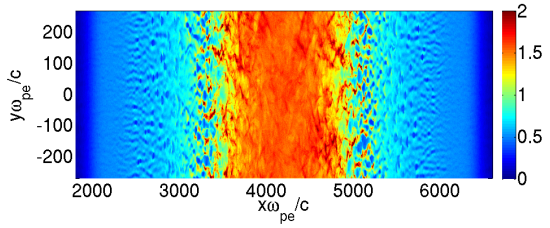

(b) Magnetic field $eB_z/m_e\omega_{pe}$

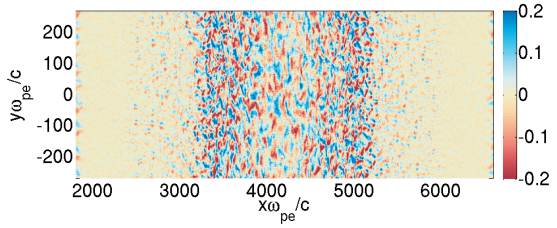

(c) Transverse temperatures

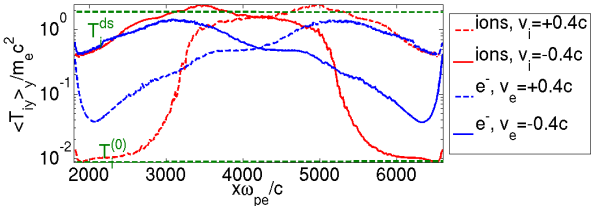

(d) Anisotropy ratio

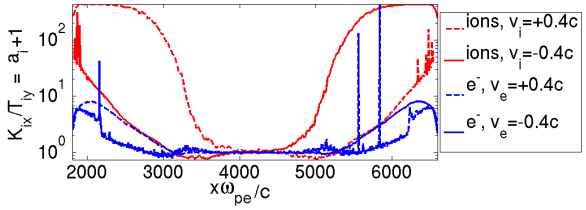

(e) $S_p/m_e^2c^2$

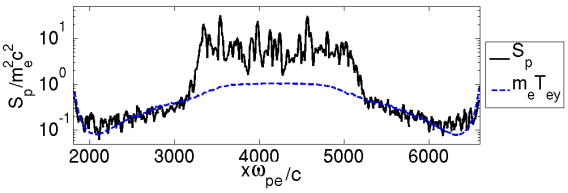

(f) Mean x-velocity

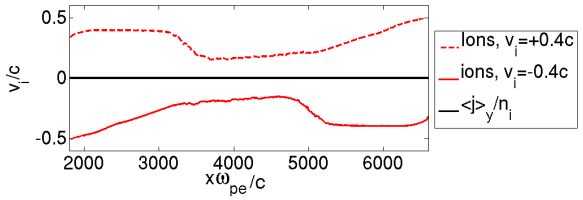

(g) Ion density

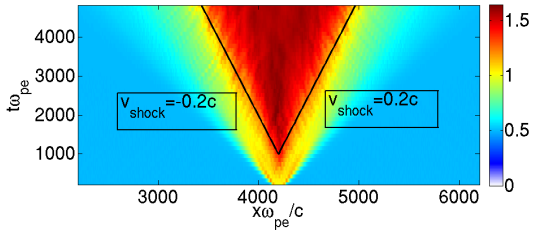

(h) Ion and electron density

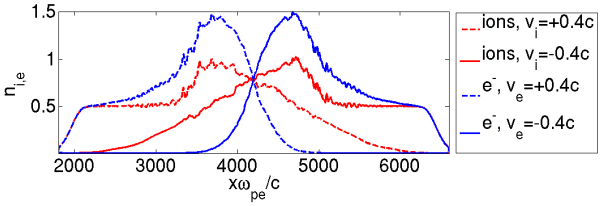

Figure 4.8. Weibel-mediated collisionless shock formed by the collision of two plasma slabs of parameters $m_i = 25m_e$, $v_{e,i} = \pm 0.4c$, $T_{e,i}^{(0)} = 0.01 m_e c^2$ and $n_{e,i} = 0.5$ at $t\omega_{pe} = 4830$. (a) Ion density. (b) Magnetic field $eB_z/m_e\omega_{pe}$. (c) Transverse ion (red) and electron (blue) temperature profiles ($T_{i,ey}/m_e c^2$) averaged in the y direction. The value of $T_i^{\rm ds}$ and $T_i^{(0)}$ are superposed in green. (d) Ion (red) and electron (blue) profiles of $a_i + 1 = K_{ix}/T_{iy}$. (e) Profile of $S_p = q_e^2 \sum_{k_y} |A_{k_y}|^2$ normalized to $m_e^2 c^2$. (f) Ion dirt velocity v_i/c averaged in the y-direction. The total current averaged over the y-direction $\langle j \rangle_y$ normalized to $n_0 c$ has been superposed. (g) Total ion density averaged over the transverse direction as a function of $x\omega_{pe}/c$ and $t\omega_{pe}$. The position of the shock front from Eq. (4.31) is superposed as black solid lines for $t\text{form}\omega_{pe} = 900$. (h) Normalized density of each beam.

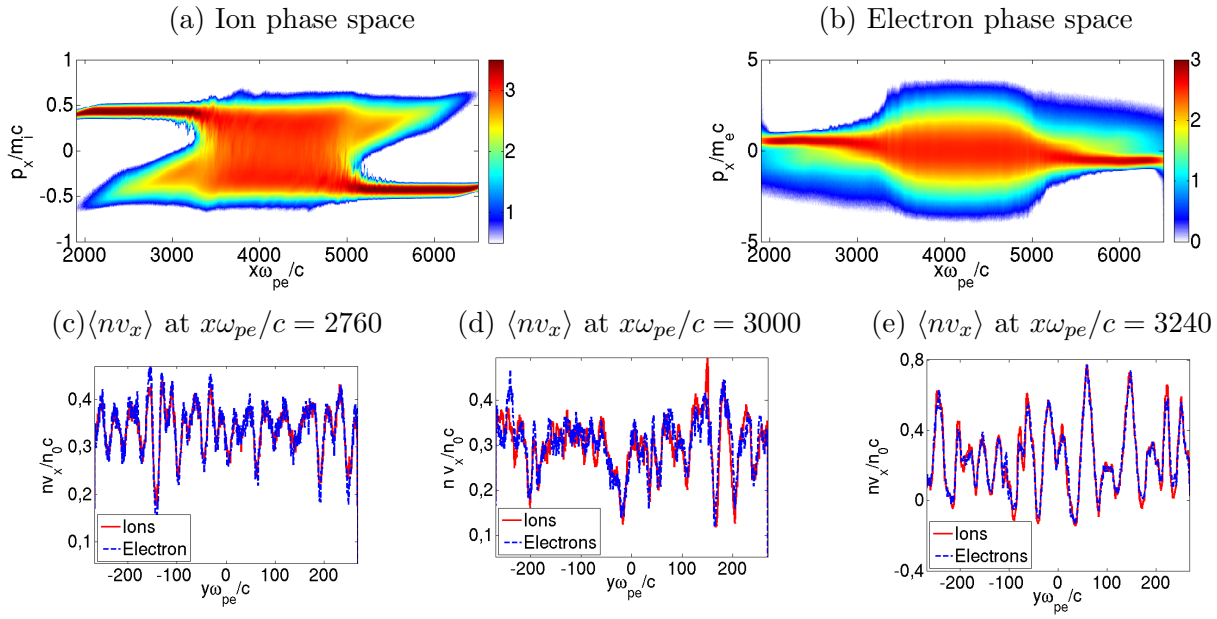

Figure 4.9. Ion (a) and electron (b) x-p_x phase spaces (in logscale). (c,d,e) Ion (solid red line) and electron (dashed blue line) local averaged velocity $\langle nv \rangle$ normalized to $n_0 c$ at $x\omega_{pe}/c = 2760$ (c), $x\omega_{pe}/c = 3000$ (d) and $x\omega_{pe}/c = 3240$ (e) at $t\omega_{pe} = 4830$. The plasma parameters and time are those of Fig 4.8.

propagation plasma beams overlap ($2000 < x\omega_{pe}/c < 3000$ and $5000 < x\omega_{pe}/c < 6000$) which thus trigger the Weibel-filamentation instability. This explains the density and magnetic modulations visible in Fig. 4.8(a,b).

The main difference with the systems studied previously (in Chapter 3 and Sec. 4.2) concerns the asymmetry of the colliding beams in the upstream. In the shock front frame, the incoming flow, initially of low temperature, is increasingly heated as it moves closer to the shock front. On the contrary, the hot counter-streaming ions are hot ($T_h \sim m_e c^2$) cool down when escaping from the turbulent region as illustrated by Fig. 4.8(c). This can drastically affect the dynamics of the instability compared to the symmetric configuration previously studied. The electron and ion contributions to the current modulations can be assessed at different times in Figs. 4.9(c,d,e). The ion current reaches slightly higher amplitudes than the electron current close to the shock front ($x\omega_{pe}/c = 3240$). However, the electron current prevails deeper in the upstream ($x\omega_{pe}/c = 2760$). Therefore, there is no clear evidence for dominant electron or ion contributions in this spatial region.

These observations can be confronted to the predictions of the linear theory. The ion and electron distribution functions at $x\omega_{pe}/c = 2760$, 3000 and 3240 at $t\omega_{pe} = 4830$ [Figs. 4.10(c-h)], can be decomposed as a sum of waterbags using the method exposed in Sec. 1.4.3. We have used the discretization parameters $N_x = 34$, $N_f = 68$ and $N_d = 2.3$, which amounts to a total of ~ 2000 waterbags. The growth rates of the Weibel instability computed with these fitted plasma distributions are plotted in Figs. 4.10(i,j,k). As one moves closer to the shock front, the peak growth rate decreases (from $\sim 4 \times 10^{-3}\omega_{pe}$ to $9 \times 10^{-4}\omega_{pe}$) and shifts to lower wave numbers (from $\sim 0.19\omega_{pe}/c$ to $\sim 0.1\omega_{pe}/c$). This stabilization clearly results from the increasingly hot and isotropic particle distributions. We have checked that the counter-streaming hot ion population is critical in destabilizing the system. Neglecting its contribution in the Weibel dispersion relation suppresses the instability. The space-dependent peak growth rate (black circles) matches the spatial profile of the magnetic spectrum $B_z(x, k_y)$ [Fig. 4.10(a)]. In the following, we will develop an analytic formulation of the Weibel growth rate, which will highlight the respective ion contributions.

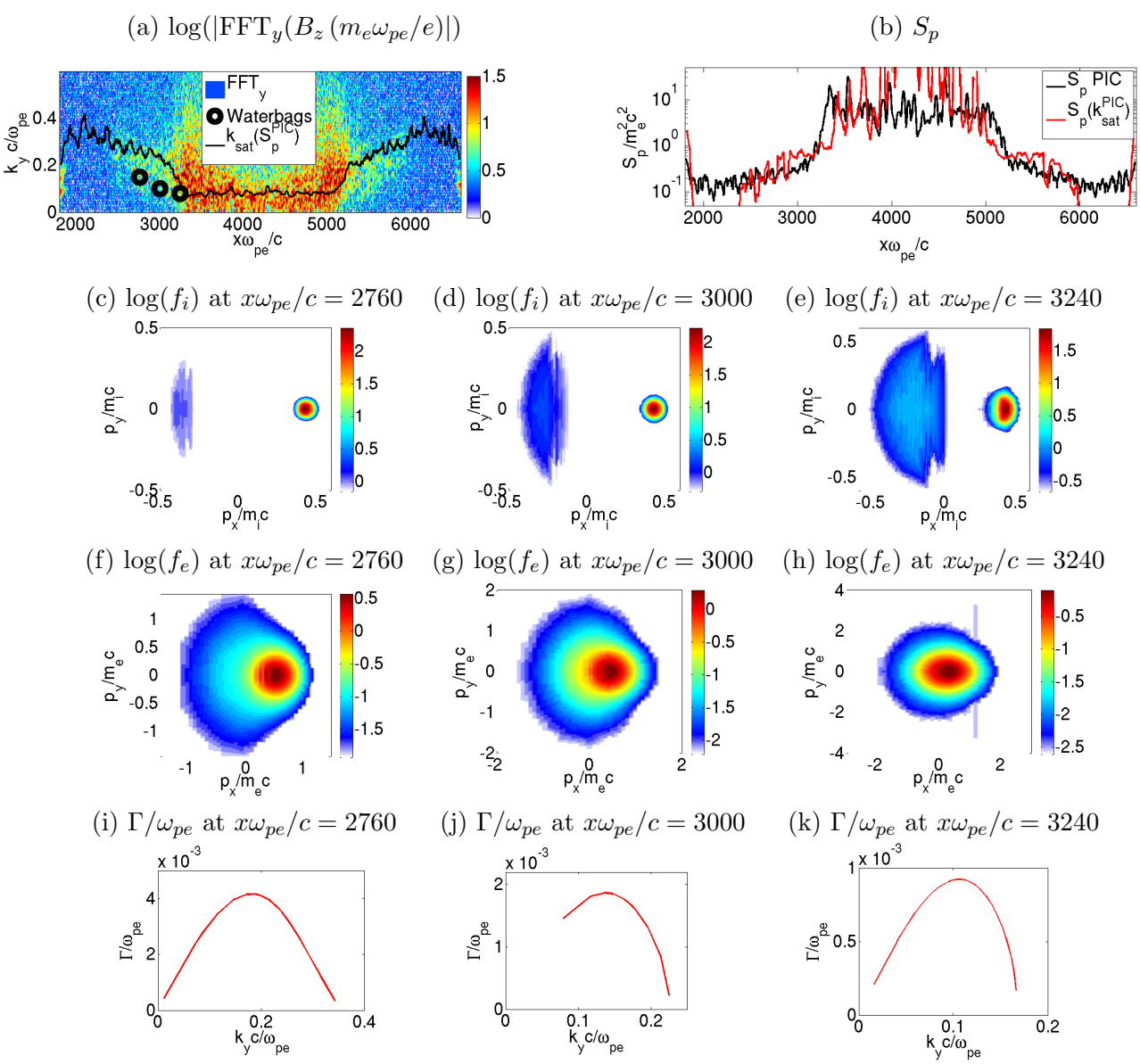

Figure 4.10. Transverse Fourier transform of the magnetic field $B_z e/m_e\omega_{pe}$ (a) and effective magnetic energy S_p (b) in log scale as a function of $x\omega_{pe}/c$ (for a shock formed by two plasma beams with $m_i = 25m_e$, $T_{i,e}^{(0)} = 0.01m_ec^2$ and $v_{i,e} = \pm 0.4c$) at $t\omega_{pe} = 4830$. The profile of $k_{\rm sat}$ (S_p) of Eq. (4.13) is superposed in (a) (in (b)), measuring S_p ($k_{\rm sat}$) in the simulation in black (red) plain line. (c,d,e,f,g,h) Ion and electron Multiwaterbag distribution function at $x\omega_{pe}/c = 2760$, 3000 and 3240 in log scale colormap. (i,j,k) Weibel growth rate calculated at $x\omega_{pe}/c = 2760$ (c), 3000 (d) and 3240 (e) using the multiwaterbag decomposition scheme of Sec. 1.4.3 with $N_x = 34$, $N_f = 68$ and $N_d = 2.3$. The wavevector maximizing the growth rates are superposed in (a) as black circles.

4.3.3 Collective filament dynamics in the upstream region

The Weibel instability taking place upstream of the shock has been shown to be triggered by the superposition of a cold (incoming) and a hot (reflected) ion population, in a hot electron background. Apart from the asymmetric feature of the interaction, the assumptions of the coalescence model extensively used previously appear to be valid. From the growth rate of Fig. 4.10(e), the value of $|\xi|$ reads $|\xi_c| \simeq 0.46 < 1$ and $|\xi_h| \simeq 0.13 < 1$ for the cold and hot ion populations, respectively. For the electrons, we have $|\xi_e| \simeq 2.6 \times 10^{-3} \ll 1$. Moreover, the ion anisotropy ratio is larger than ~ 2 up to the shock front at $x\omega_{pe}/c = 3500$ [Fig. 4.8(d)]. Hence, the turbulent heating of the cold incoming ions could be explained by the model worked out in Chapter 3, provided a few modifications are made to adapt to the present asymmetric configuration.

The quasilinear model of Davidson *et al.* (1972) remains valid in an asymmetric system. Each tensorial formula used in the Davidson calculations concerns a specific ion population. Hence, Eqs. (3.17)-(3.19) should be applied to each particular bi-Maxwellian population (ions or electrons). For two asymmetric ion populations, we have a total of six quasilinear equations, three per ion component. Consequently, the starting equations of the model [Eqs. (3.17)-(3.19)] are valid for an asymmetric system.

The wavevector estimate of Eq. (3.10) is based on a simplified linear growth rate formula. For two (hot and a cold) asymmetric ion populations immersed within a hot isotropic electron background (neutralizing the net ion current), the linear dispersion relation is no longer as simple as Eq. (3.4). One has to solve, in principle, the full electromagnetic dispersion relation (1.11), which is complicated by the non-vanishing ϵ_{xy} term. For bi-Maxwellians distributions and $\theta = \pi/2$ one has

$$\epsilon_{xy} = \sum_s \frac{\omega_{ps}^2}{\omega^2} \frac{2v_{ds}}{v_{th,s}} \left[\xi_s + \xi_s^2 \mathcal{Z}\left(\xi_s\right)\right] , \tag{4.5}$$

where v_s and $v_{th,s} = \sqrt{2T_{sy}/m_s}$ are the mean and thermal velocities of the sth species. We will now consider the case of a cold incoming ion plasma interacting with a more tenuous hot ion beam, originating from either the shock downstream or the shock front, in a neutralizing electron background. From the above equation, we find $\epsilon_{xy} \propto \sum_s \omega_{ps}^2 v_s \alpha_s / v_{th,s}^2$ to leading order in ξ_s. It is therefore convenient to solve the non-relativistic transverse dispersion relation in the frame $\mathcal{R}'$ drifting at

$$v_f = \frac{\frac{n_c v_c}{v_{th,c}^2} - \frac{n_h v_h}{v_{th,h}^2} - \frac{n_e v_e}{v_{th,e}^2}}{\frac{n_c}{v_{th,c}^2} + \frac{n_h}{v_{th,h}^2} + \frac{m_i}{Z_i m_e}\frac{n_c+n_h}{v_{th,e}^2}} , \tag{4.6}$$

where the subscripts c, h and e refer to the cold ions, hot ions and electrons respectively. In $\mathcal{R}'$, $\epsilon_{xy} \simeq 0$ and, to leading order in ξ_s, the Weibel growth rate verifies an equation similar to that derived in the symmetric case [Eq. (3.7)]. The general formula reads, for $s \equiv [c, h, e]$,

$$\Gamma_{k_y} \simeq \frac{k}{\sqrt{\pi}} \frac{\sum_s \omega_{ps}^2 a_s' - k^2}{\sum_s \omega_{ps}^2 \frac{a_s'+1}{v_{th,s}}} , \tag{4.7}$$

where a_s' is the sth species' anisotropy ratio defined in the $\mathcal{R}'$ frame:

$$a_s' = \frac{m_s(v_s - v_f)^2 + T_{sx}}{T_{sy}} - 1 . \tag{4.8}$$

Figures 4.11(a,b,c) compare the exact resolution of the Weibel-filamentation dispersion relation (plain line) to the approximation of Eq. (4.7) (dashed line) for three sets of parameters, made of a hot and a cold ion populations in a neutralizing electron background. Overall, fairly good agreement

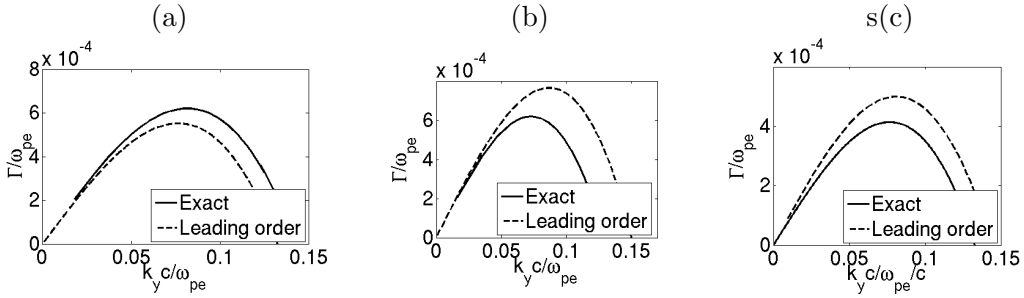

Figure 4.11. Comparison of the exact Weibel growth rate (solid lines) with the approximation of Eq. (4.7) (dashed lines). (a) $m_i = 25m_e$, $v_c = -v_h = 0.4c$, $v_e = 0.36c$, $T_{ih} = 2m_ec^2$. (b) $m_i = 25m_e$, $v_c = -v_h = 0.2c$, $v_e = 0.18c$, $T_{ih} = 0.5m_ec^2$. (c) $m_i = 100m_e$, $v_c = -v_h = 0.4c$, $v_e = 0.36c$, $T_{ih} = 8m_ec^2$. For the three cases, the population densities verify $n_h = 0.05$, $n_c = 0.5$, $n_e = 0.55$, $T_e = 0.5m_ec^2$ and $T_{ic} = 0.05m_ec^2$. The mean electron velocity is chosen to ensure global current neutralization.

is obtained and we thus validates Eq. (4.7). Hence, the wavevector maximizing the growth rate also verifies $k_{\rm sat} \simeq 0.5k'_{\rm max}$ [Eq. (3.10)] with the only difference that $k'_{\rm max}$ now involves all the populations

$$k'_{\rm max} = \sqrt{\frac{\omega_{pc}^2}{c^2}a'_c + \frac{\omega_{ph}^2}{c^2}a'_h + \frac{\omega_{pe}^2}{c^2}a'_e}\,. \tag{4.9}$$

In the upstream region, $k_{\rm sat}$ can be related to a few plasma parameters. Since the incoming ions are dense ($n_c \simeq 10n_h$) and cold ($v_c/v_{th,c}^2 \gg v_h/v_{th,h}^2$), the frame velocity can be approximated to $v_f \simeq v_c$. Hence, if the three populations have comparable (longitudinal and transverse) temperatures, we have $|a'_c| \ll 1$. The hot ion temperature being close to the downstream temperature $T_i^{\rm ds}$ [Eq. (4.3)], we obtain $a'_h \simeq 8$. For the sake of completeness, we will keep a'_h in the following formulae but use $a'_h \simeq 8$ for the numerical applications. The electron anisotropy ratio follows from the constraint of current neutrality: $a'_e \simeq (2-R_h)^2 m_e v_c^2/T_e$, where $R_h = n_h/(n_c+n_h) \simeq 0.2$ is the relative density of the hot ion beam. Consequently, $k_{\rm sat}$ verifies

$$\frac{k_{\rm sat}c}{\omega_{pe}} \simeq \eta_i\sqrt{\frac{Z_i m_e n_h}{m_i n_e}a'_h + (2-R_h)^2\frac{m_e v_c^2}{Z_i T_e}} \simeq \eta_i\sqrt{\frac{Z_i m_e}{m_i}}\sqrt{a'_h R_h + (2-R_h)^2\frac{m_i v_c^2}{Z_i T_e}}\,. \tag{4.10}$$

Two unknown plasma parameters involved in the above equation are the electron temperature T_e and the incoming ion velocity v_c.

The simplified quasilinear equations (3.17)-(3.19) relate the plasma parameters to the evolution of the magnetic spectrum. In Chapter 3, one of the main simplifications allowed by the symmetric character of the interaction was to get rid of the $\mathcal{Z}$ function. The symmetry of the system gave us a simple formulation of ξ_i, independent of the plasma parameters. By contrast, Eq. (4.7) leads to ξ_i being strongly sensitive to the plasma parameters. The integration of the quasilinear equations therefore appears very complicated for the ions. The electron temperature, however, can be readily linked to the spectrum making use of Eq. (3.21) as in Chapter 3:

$$\partial_t T_{ey} \simeq \frac{a_e+1}{m_e}\partial_t S_p\,. \tag{4.11}$$

We remind the reader that this equation is valid for isotropic and very hot electrons ($a_e = 0$ and $|\xi_e| \ll 1$). In the case of Fig. 4.11(a), $|\xi_e| \leq 0.04 \ll 1$. In the assumption of isotropic electrons in

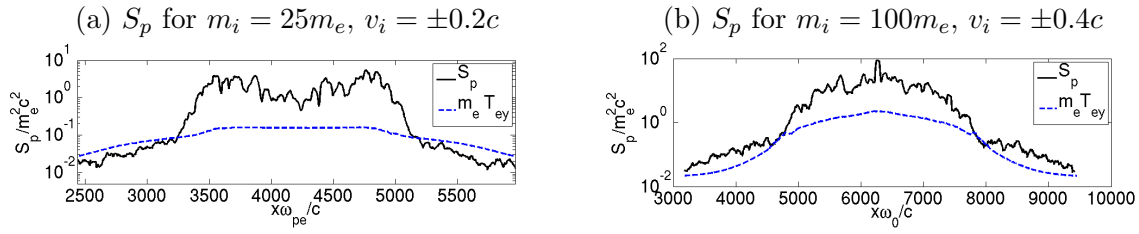

Figure 4.12. Profile of $S_p/m_e^2c^2$ in a propagating shock simulation of parameters $m_i = 25m_e$, $v_i = \pm 0.2c$ at $t\omega_{pe} = 8820$ (a) and $m_i = 100m_e$, $v_i = \pm 0.4c$ at $t\omega_{pe} = 4200$ (b) with $T^{(0)}_{i,ex,y} = 0.01m_ec^2$. The total transverse electron temperature T_{ey}/m_ec^2 is superposed as dashed blue lines.

the upstream region [verified in Fig. 4.8(d)], we obtain a very simple formulation:

$$m_e \Delta T_{ey} = \Delta S_p \,. \tag{4.12}$$

This relation is well satisfied in the upstream region ($x\omega_{pe}/c < 3300$ or $x\omega_{pe}/c > 5000$), as illustrated in Fig. 4.8(e). Moreover, Fig. 4.12(a,b) shows a good agreement between the variations of S_p and m_eT_{ey}. This relation stays valid as long as the magnetic spectrum remains transverse, which is not the case in the isotropic downstream region. Plugging Eq. (4.12) into Eq. (4.10) allows us to express the dominant wavevector as a function of S_p:

$$\frac{k_{\rm sat}c}{\omega_{pi}} \simeq 0.45\sqrt{a'_hR_h + (2-R_h)^2\frac{m_em_iv_c^2}{Z_i\Delta S_p}} \Leftrightarrow Z_i\Delta S_p \simeq (2-R_h)^2\frac{m_im_ev_c^2\lambda_{\rm sat}^2}{2\lambda_c^2 - a'_hR_h\lambda_{\rm sat}^2}\,, \tag{4.13}$$

where use is made of $\lambda_c = \sqrt{2}\pi c/\omega_{pi}\eta_i$. Figures 4.10(a,b) display the transverse magnetic spectrum and the S_p profile in the collisionless shock simulation at $t\omega_{pe} = 4830$ for $m_i = 25m_e$, $v_i = \pm 0.4c$. The PIC results are compared with the values deduced by plugging the simulated S_p (respectively $k_{\rm sat}$) in the expression of $k_{\rm sat}$ (respectively S_p) as black solid line of Fig. 4.10(a) (respectively red solid line of Fig. 4.10(b)). Good agreement is obtained, which validates Eq. (4.13).

Since the incoming ion population creates filaments in the upstream, their coalescence dynamics can be modeled as in Sec. 3.4.2. Note, however, in the present configuration, the current involved in the equation of dynamics is associated to the cold incoming ion population. Equation (3.66) then writes, in the frame of the incoming ions

$$d\left[\frac{3m_i}{2}(\partial_t\lambda_{\rm sat})^2\right] = Z_c\kappa v_c d\sqrt{S_p}\,. \tag{4.14}$$

Making use of Eq. (4.13) and of $\kappa \simeq 4c/\lambda_{\rm sat}\omega_{pe}$ of Eq. (3.61), one gets

$$\left[(\partial_t\lambda_{\rm sat})^2\right]^t_{t_*} = (2-R_h)\frac{8cZ_c}{3m_i\omega_{pe}}a'_h\sqrt{\frac{m_im_e}{Z_i}}\int_{\lambda_*}^{\lambda_{\rm sat}}\frac{v_c}{\lambda}\partial_\lambda\left(\frac{v_c\lambda}{\sqrt{2\lambda_c^2 - a'_hR_h\lambda^2}}\right)d\lambda\,. \tag{4.15}$$

A precise calculation would requires the knowledge of v_c as a function of $\lambda_{\rm sat}$. Yet, the profile of v_c plotted in Fig. 4.8(f) does not present any significant variation except very close to the shock front. We will then assume v_c constant, which will allow us to obtain an approximate solution of Eq. (4.15) To this goal, we recast the above equation as

$$\left[(\partial_t\lambda_{\rm sat})^2\right]^t_{t_*} = (2-R_h)\frac{8cZ_i}{3m_i\omega_{pe}}\sqrt{\frac{m_im_e}{Z_i}}v_c^2\int_{\lambda_*}^{\lambda_{\rm sat}}\frac{d\lambda}{\lambda}\partial_\lambda\left(\frac{\lambda}{\sqrt{2\lambda_c^2 - a'_hR_h\lambda^2}}\right)\,. \tag{4.16}$$

As in Sec. 3.4.3, we will suppose that, at the end of the linear phase at $t = t_*$, $\lambda_{\rm sat}(t_*) = \lambda_*$ and $\partial_t \lambda_{\rm sat}(t_*) = 0$. Integrating by parts and making use of

$$\int \frac{dx}{x\sqrt{1-ax^2}} = \ln(x) - \ln(1+\sqrt{1-ax^2})\,, \tag{4.17}$$

we obtain (to leading order in $\lambda/\lambda_c < \lambda_{\rm sat}/\lambda_c$):

$$\partial_t \lambda_{\rm sat} \simeq v_c \left(\frac{Z_i m_e}{m_i}\right)^{\frac{1}{4}} \sqrt{\frac{4\sqrt{2}c}{3\omega_{pe}\lambda_c}(2-R_h)} \left[\ln\left(\frac{\lambda_{\rm sat}}{\lambda_*}\right) + \frac{5}{4}a'_h R_h \frac{\lambda_{\rm sat}^2 - \lambda_*^2}{2\lambda_c^2}\right]^{\frac{1}{2}}. \tag{4.18}$$

There results

$$v_c \left(\frac{Z_i m_e}{m_i}\right)^{\frac{1}{4}} \sqrt{\frac{4\sqrt{2}c}{3\omega_{pe}\lambda_c}\frac{5}{4}a'_h R_h(2-R_h)\Delta t} = \frac{\lambda_c}{\lambda_*}\int_{\lambda_*}^{\lambda_{\rm sat}} \frac{d\lambda}{\sqrt{\frac{4}{5a'_h R_h}\frac{2\lambda_c^2}{\lambda_*^2}\ln\left(\frac{\lambda}{\lambda_*}\right) + \frac{\lambda^2}{\lambda_*^2} - 1}} \tag{4.19}$$

Assuming the ln term negligible, we obtain

$$v_c \left(\frac{m_e Z_i}{m_i}\right)^{\frac{1}{4}} \sqrt{\frac{8c}{3\omega_{pe}\lambda_c}\frac{5}{4}a'_h R_h(2-R_h)\Delta t} = \lambda_c \left[\operatorname{arccosh}\left(\frac{\lambda_{\rm sat}}{\lambda_*}\right)\right], \tag{4.20}$$

and therefore

$$\lambda_{\rm sat} = \lambda_* \cosh\left(\frac{\Delta t}{\tau_1}\right), \tag{4.21}$$

with

$$\tau_1 = \frac{\lambda_c}{v_c}\left(\frac{m_i}{Z_i m_e}\right)^{\frac{1}{4}} \sqrt{\frac{2\omega_{pe}\lambda_c}{10ca'_h R_h(2-R_h)}}\,, \tag{4.22}$$

and $\lambda_c\omega_{pi}/c = 2\pi/0.5$. We see that the typical coalescence time τ_1 does not depend on the initial condition λ_*, in contrast to the symmetric interaction regime. This stems from the neglect of the ln term in Eq. (4.18). However, λ_* is usually much lower than λ_c since $\lambda_c^2/\lambda_*^2 \gtrsim m_i/Z_i m_e \gg 1$. Hence, neglecting $\lambda^2/\lambda_*^2 - 1$ in front of $\lambda_c^2 \ln(\lambda/\lambda_*)/\lambda_*^2$ yields

$$v_c \left(\frac{Z_i m_e}{m_i}\right)^{\frac{1}{4}} \sqrt{\frac{4\sqrt{2}c}{3\omega_{pe}\lambda_c}(2-R_h)\Delta t} = \int_{\lambda_*}^{\lambda_{\rm sat}} \frac{d\lambda}{\sqrt{\ln\left(\frac{\lambda}{\lambda_*}\right)}} = -\sqrt{\pi}\left[\operatorname{erfi}\left(\sqrt{\ln\left(\frac{\lambda_{\rm sat}}{\lambda_*}\right)}\right)\right], \tag{4.23}$$

where erfi is the complex error function (see Nomenclature). This equation can be recast as

$$\lambda_{\rm sat} = \lambda_* \exp\left[\operatorname{erfi}^{-1}\left(\frac{\Delta t}{\tau_2}\right)^2\right], \tag{4.24}$$

$$\tau_2 = \frac{\lambda_*}{v_c}\left(\frac{m_i}{Z_i m_e}\right)^{\frac{1}{2}} \sqrt{\frac{4\pi^2}{8\eta_i(2-R_h)}}\,. \tag{4.25}$$

We have introduced erfi^{-1}, the inverse complex error function. We plotted in Fig. 4.13 the mathematical function $\exp[(\operatorname{erfi}^{-1})^2]$. Note that the above formulae are valid provided $\lambda_* \ll \lambda_c$, which is usually verified for realistic ions. Moreover, for $\lambda_* \propto c/\omega_{pe}$, τ_2 does not depend on the electron

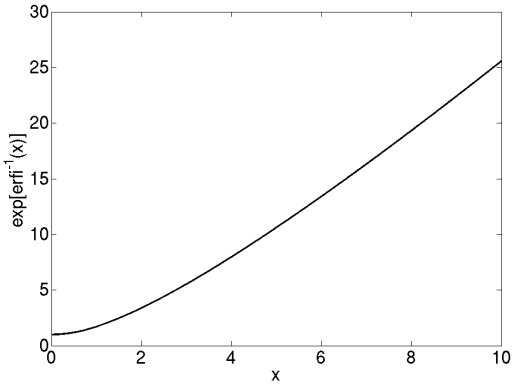

Figure 4.13. Function $x \to \exp[(\mathrm{erfi}^{-1}(x))^2]$

mass. For $\Delta t \ll \tau_2$, we obtain

$$\lambda_{\mathrm{sat}} \simeq \lambda_* \left(1 + \frac{\pi \Delta t^2}{4\tau_2^2}\right) . \tag{4.26}$$

For $\Delta t \gg \tau_2$, λ_{sat} is implicitly given by

$$\frac{\Delta t}{\tau_2} \simeq \frac{\lambda_{\mathrm{sat}}}{\lambda_* \sqrt{\pi \ln\left(\frac{\lambda_{\mathrm{sat}}}{\lambda_*}\right)}} . \tag{4.27}$$

Although Eq. (4.24) differs from its symmetric counterpart, Eq. (3.79), it predicts a qualitatively similar evolution of λ_{sat}: a plateau of typical duration τ_1 appears at the beginning of the saturation stage, followed by a strong increase of the wavelength while $\lambda < \lambda_c$. Combining Eqs. (4.13) and (4.24), the spectrum variable S_p evolves according to

$$S_p = \frac{(2 - R_h)^2}{Z_i} \frac{m_i m_e v_c^2 \lambda_*^2 \exp\left[2\mathrm{erfi}^{-1}\left(\frac{\Delta t}{\tau_2}\right)^2\right]}{2\lambda_c^2 - a_h' R_h \lambda_*^2 \exp\left[2\mathrm{erfi}^{-1}\left(\frac{\Delta t}{\tau_2}\right)^2\right]} . \tag{4.28}$$

4.3.4 Shock profile

Equations (4.24) and (4.28) give the explicit temporal evolution of the spectral parameters at a given position in the upstream region, assuming that the Weibel instability has entered its nonlinear phase at time t_*. In order to obtain the spatial profile of the spectral parameters in front of the shock, we will make use of a simple argument. In the downstream framework, the shock is formed at the center of the system x_{center} at time t_{form}. The velocity of the shock front v_{shock} is given by the Rankine-Hugoniot conditions (Drury 1983)

$$v_{\mathrm{shock}}^{\mathrm{2D}} = \frac{v_c}{2} , \tag{4.29}$$

$$v_{\mathrm{shock}}^{\mathrm{3D}} = \frac{v_c}{3} . \tag{4.30}$$

For the parameters $m_i = 25 m_e$ and $v_i = 0.4c$, a shock velocity $v_{\mathrm{shock}} = 0.2c$ is then predicted, in agreement with the simulation results [Fig. 4.8(g)]. The shock front therefore reaches a given

position x in the upstream plasma at the approximate time

$$t_{\rm front}(x) = t_{\rm form} + \frac{|x - x_{\rm center}|}{v_{\rm shock}}\,. \tag{4.31}$$

Therefore, we need to estimate the values of S_p or $\lambda_{\rm sat}$ at the shock front (or close to it) in order to obtain the spectrum spatial profile. At the shock front, the value of $\lambda_{\rm sat}$ will be defined as $\lambda_{\rm front}$ and verifies

$$\lambda_{\rm front} \equiv \lambda_{\rm sat}(t_{\rm front}) = \lambda_* \exp\left[{\rm erfi}^{-1}\left(\frac{t_{\rm front}(x) - t_*(x)}{\tau_2}\right)^2\right]\,, \tag{4.32}$$

The above formulation can be greatly simplified if we assume that the time needed to achieve isotropization at a given position is very long: $t_{\rm front}(x) - t_*(x) \gg \tau_2$. Making use of Eq. (4.27), we obtain:

$$\lambda_* \frac{t_{\rm front} - t_*}{\tau_2} = \frac{\lambda_{\rm front}}{\sqrt{\pi \ln\left(\frac{\lambda_{\rm front}}{\lambda_*}\right)}}\,. \tag{4.33}$$

Assuming $\lambda_{\rm front}$ is known, the profile of $\lambda_{\rm sat}$, independently of t_*:

$$\lambda_{\rm sat} = \lambda_* \exp\left[{\rm erfi}^{-1}\left(\frac{t - t_{\rm form}}{\tau_2} - \frac{|x - x_{\rm center}|}{\tau_2 v_{\rm shock}} - {\rm erfi}\left(\sqrt{\ln\left(\frac{\lambda_{\rm front}}{\lambda_*}\right)}\right)\right)^2\right]\,, \tag{4.34}$$

where $t - t_{\rm form} > 0$ and $\lambda_* \leq \lambda_{\rm sat} \leq \lambda_{\rm front}$.

The dominant wavevector $\lambda_{\rm sat}$ at the shock front can be qualitatively related to a fraction of the largest wavelength in the equations: λ_c. The relation between the dominant magnetic wavevector and the plasma parameters (Eq. (4.10)) reads

$$k_{\rm sat} \simeq \eta_i \frac{\omega_{pe}}{c}\sqrt{\frac{Z_i m_e}{m_i}}\sqrt{a'_h R_h + (2 - R_h)^2 \frac{m_i v_c^2}{Z_i T_e}}\,. \tag{4.35}$$

A way to estimate $\lambda_{\rm front}$, is to assume that the anisotropy ratio of the incoming ions has dropped down to the large-ion-anisotropy validity limit ($a_i = 2 > 1$) at the shock front. We remind that this argument has been used to estimate shock formation time in Sec. 4.2. In the present case, the ion-anisotropy ratio is not predicted analytically by our model which make this criterion hard to apply. Another criterion which estimates $\lambda_{\rm front}$ can be worked out, assuming equipartition of electron and ion energies in Eq. (4.35), $T_e(t_{\rm front}) \sim m_i v_c(t_{\rm front})^2 + T_{ix}(t_{\rm front})$. At the shock front, the ions are close to isotropisation, hence we estimate $m_i v_c(t_{\rm front})^2 \sim T_{ix}(t_{\rm front})$ which yields, $m_i v_c(t_{\rm front})^2 / T_e(t_{\rm front}) \sim 0.5$. We then obtain

$$\lambda_{\rm front} = \lambda_{\rm sat}(t_{\rm front}) \simeq \frac{c}{\omega_{pi}} \frac{2\pi}{\eta_i \sqrt{(2 - R_i)^2/2Z_i + a'_h R_h}} \simeq 0.8\lambda_c\,. \tag{4.36}$$

There follows the spectral profile S_p

$$S_p = \frac{(2 - R_h)^2}{Z_i} \frac{m_i m_e v_c^2 \lambda_*^2 \exp\left[{\rm erfi}^{-1}\left(\frac{t - t_{\rm form}}{\tau_2} - \frac{|x - x_{\rm center}|}{\tau_2 v_{\rm shock}} - {\rm erfi}\left(\sqrt{\ln\left(\frac{\lambda_{\rm front}}{\lambda_*}\right)}\right)\right)^2\right]^2}{2\lambda_c^2 - a'_h R_h \lambda_*^2 \exp\left[{\rm erfi}^{-1}\left(\frac{t - t_{\rm form}}{\tau_2} - \frac{|x - x_{\rm center}|}{\tau_2 v_{\rm shock}} - {\rm erfi}\left(\sqrt{\ln\left(\frac{\lambda_{\rm front}}{\lambda_*}\right)}\right)\right)^2\right]^2}\,. \tag{4.37}$$

Our model assumes that the shock profile, defined by S_p and $\lambda_{\rm sat}$, is stationary in a frame mov-

ing at $v_{\rm shock}$. In Eqs. (4.34) and (4.37), the sharpness of the profile increases with the factor $\mathrm{erfi}\left(\sqrt{\ln\left(\frac{\lambda_{\rm front}}{\lambda_*}\right)}\right)$. The thickness of the Weibel magnetic saturation zone can be easily deduced: it is the length needed for $\lambda_{\rm sat}$ to increase from λ_* to $\lambda_{\rm front} \simeq 0.8\lambda_c$. For large ion masses (so that $\lambda_* \ll \lambda_c$), we can multiply Eq. (4.33) by $v_{\rm shock}$ to obtain the length of the magnetic turbulence L_B in the upstream flow:

$$L_B = v_{\rm shock}(t_{\rm shock} - t_*) = 5\frac{c}{\omega_{pi}}\left(\frac{m_i}{Z_i m_e}\right)^{\frac{1}{2}}\sqrt{\frac{2\pi}{2(2-R_h)\ln\left(\frac{\lambda_{\rm front}}{\lambda_*}\right)}}\,, \tag{4.38}$$

where use has been made of $\lambda_c = \sqrt{2}\pi c/\eta_i\omega_{pi}$. We emphasize that it represents the length of the upstream plasma over which the magnetic saturation takes place, not necessarily the length of variation of the hydrodynamic plasma parameters (n_i, T_i). Consequently, the size of the upstream magnetic turbulence does not depend on the initial velocity of the plasma slabs, which confirms the result, obtained by Kato & Takabe (2008). Moreover, this length is weakly sensitive to the initial filament size λ_*, and is proportional to the ion mass (and not to $m_i^{1/2}$ as the ion skin depth). Moreover, since the typical time τ_2 depends on the electron mass m_e (for fixed λ_*), the length of the turbulent spatial scale L_B does depend on m_e.

We now compare our analytical predictions with the results of various shock simulations. In Figs. 4.15(a-d) are plotted the $\lambda_{\rm sat}$ (top) and S_p (bottom) profiles measured in simulations run with the parameters $v_i = \pm 0.2c$ (left) and $v_i = \pm 0.4c$ (right) for an ion mass of $m_i = 25m_e$. Overall, the theoretical predictions correctly match the simulated spectra. Moreover, the simulated spectra evidence a slight evolution of the spectrum far from the shock front for both $\lambda_{\rm sat}$ and S_p. However, close to the shock front, the profiles are very similar up to the noise level. This is also consistent with the analytical model which predicts a dependence on the parameter λ_* of the spectra far from the shock front. Its value can be estimated the same way than in Chapter 3, making use of Eq. (3.95). We thus show that k_* should be a fraction of ω_{pe}/c which has been used in Figs. 4.14. The qualitative influence described earlier of λ_* on the profiles is thus confirmed.

Qualitatively, the larger is the overlapping region between the cold incoming and hot reflected ion populations, the longer is the interaction region which should strengthen the heating effects of the various instabilities developing prior to the Weibel growth. The later an element of the upstream region turns Weibel-unstable, the hotter are its electron and ion components, yielding a larger saturated wavelength, λ_* an thus a smoother shock profile.

Close to the shock front, the analytical spectrum depends mainly on the value of the wavelength at the shock front, $\lambda_{\rm sat}(t_{\rm shock}) \simeq 0.6\lambda_c \simeq 0.84c/\omega_{pi}$ [Eq. (4.32)]. The corresponding value of S_p reads

$$S_p(x = x_{\rm shock}(t)) = (2-R_h)^2\frac{m_e m_i v_c^2}{Z_i}\frac{0.8^2}{2 - R_h a_h' 0.8^2} \simeq 2.1\frac{m_e m_i v_c^2}{Z_i}\,. \tag{4.39}$$

We remind the reader that we have neglected the variations of the mean incoming ion velocity v_c, an invalid assumption close to the shock front. The decrease in v_c close to the shock front will be estimated numerically from the ion-quasilinear equations in next section.

4.3.5 Evolution of the ion parameters

In the symmetric interaction regime, the Weibel wavevector is linked to the ion anisotropy ratio, hence solving the problem required to know the ion population parameters. In the present asymmetric case, by contrast, the wavevector only involves (to first order) the incoming ion velocity, which is assumed constant. This approximation could be relaxed in a refined version of our model The quasilinear equations (Eqs. (3.28)-(3.30)) can be applied to the cold incoming ion population

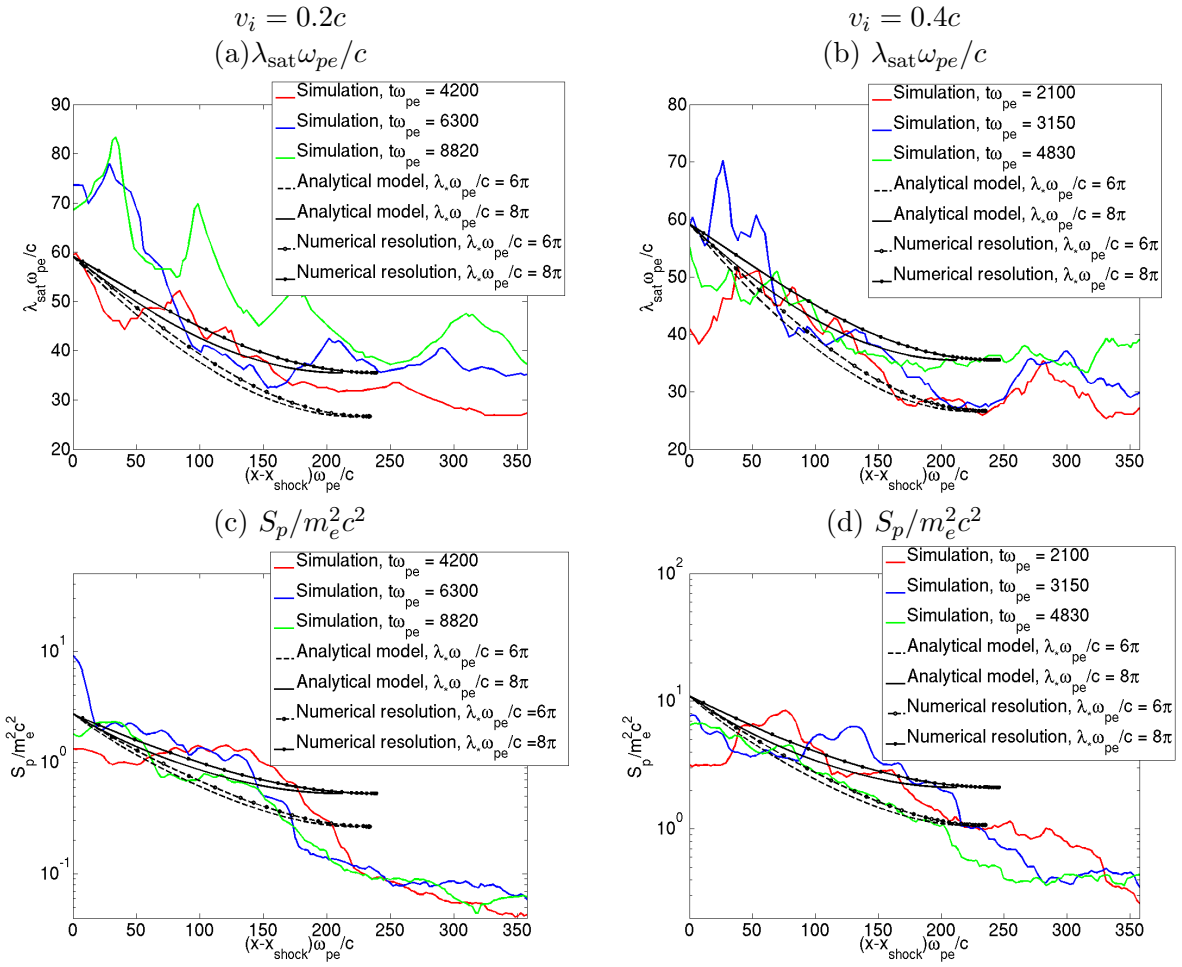

Figure 4.14. Spatial profile of the Weibel wavelength $\lambda_{\rm sat}\omega_{pe}/c$ (a,b) and $S_p/m_e^2c^2$ (c,d) for two shock propagation simulations: $m_i = 25m_e, v_i = 0.2c$ (a,c) and $m_i = 25m_e, v_i = 0.4c$ (b,d). The abscissa is measured from the shock front position $(x - x_{\rm shock})\omega_{pe}/c$ given by Eq. (4.31). The shock formation time of Eq. (4.31) is $t_{\rm form}\omega_{pe} = 1800$ for the cases (a,c) and $t_{\rm form}\omega_{pe} = 800$ for the cases (b,d). The analytic formula Eqs. (4.34), (4.36) and (4.37) have been superposed as black dashed and plain lines for respectively $\lambda_* = 6\pi c/\omega_{pe}$ and $\lambda_* = 8\pi c/\omega_{pe}$. The exact numerical resolution from Eqs. (4.46), (4.41)-(4.45) are superposed as circled black dashed and plain lines for respectively $\lambda_* = 8\pi c/\omega_{pe}$ and $\lambda_* = 6\pi c/\omega_{pe}$.

and solved numerically. Therefore, assuming that the temporal evolution of S_p is known, the ξ_i parameter can be estimated from Eq. (4.7). We have simplified the spectrum function as detailed in Sec. 3.3.2. The only difference being that the parameter $\alpha_i = 1 + \xi_i^{\rm sat}\mathcal{Z}(\xi_i^{\rm sat})$ now depends strongly on the plasma properties. We thus obtain the following set of equations for fixed position

x:

$$t_{\rm front}(x) = t_{\rm form} + \frac{|x - x_{\rm center}|}{v_{\rm shock}}\,, \tag{4.40}$$

$$\partial_t v_c \simeq -\frac{Z_i^2}{m_i}\left[1 + \xi_c^{\rm sat}\mathcal{Z}(\xi_c^{\rm sat})\right]\frac{v_c}{T_{cy}}\partial_t S_p\,, \tag{4.41}$$

$$\partial_t T_{cy} \simeq +\frac{Z_i^2}{m_i}\left[1 + \xi_c^{\rm sat}\mathcal{Z}(\xi_c^{\rm sat})\right]\frac{K_{cy}}{T_{cy}}\partial_t S_p\,, \tag{4.42}$$

$$\partial_t K_{cx} \simeq -\frac{Z_i^2}{m_i}\{2\left[1 + \xi_c^{\rm sat}\mathcal{Z}(\xi_c^{\rm sat})\right]\frac{K_{cy}}{T_{cy}} - 1\}\partial_t S_p\,, \tag{4.43}$$

$$\xi_c^{\rm sat} \simeq i(1-\eta_i^2)\sqrt{\frac{m_i}{2\pi T_{cy}}}\frac{R_h a_h' + (2-R_h)^2\frac{m_i m_e v_c^2}{Z_i S_p}}{\sqrt{\frac{m_i}{2T_{cy}}} + R_h\frac{a_h'+1}{v_c} + ((2-Ri)^2\frac{m_i m_e v_c^2}{Z_i S_p} + \frac{m_i}{m_e})\frac{m_e}{\sqrt{2S_p}}}\,, \tag{4.44}$$

$$\partial_t S_p = S_p\partial_t\lambda_{\rm sat}\left[\frac{2}{\lambda_{\rm sat}} + \frac{2R_h a_h'\lambda_{\rm sat}}{2\lambda_c^2 - R_h a_h'\lambda_{\rm sat}^2}\right]\,, \tag{4.45}$$

where $R_h \simeq 0.2$, $a_h' \simeq 8$, $\eta_i = 0.5$, and $\lambda_c = \sqrt{2}\pi c/\eta_i\omega_{pi}$. In order to be solved, the above set of equations need to be coupled to the coalescence model. For this purpose, we take the time derivative of Eq. (4.15)

$$\frac{3\omega_{pe}}{4c}\sqrt{\frac{m_i}{Zim_e}}\frac{\lambda_{\rm sat}}{v_c}d_{tt}^2\lambda_{\rm sat} = \frac{(2-R_h)v_c}{\sqrt{\lambda_c^2 - a_h' R_h\lambda_{\rm sat}^2}}\left[1 + \frac{a_h' R_h\lambda_{\rm sat}^2}{2\lambda_c^2 - a_h' R_h\lambda_{\rm sat}^2} + \frac{\lambda_{\rm sat}}{v_c}\frac{d_t v_c}{d_t\lambda_{\rm sat}}\right]\,. \tag{4.46}$$

The above second order differential equations closes the set of Eqs. (4.41)-(4.45) and can be solved with the initial conditions $\lambda(t_*) = \lambda_*$ and $\partial_t\lambda_{\rm sat}(t_*) = 0$. We also use the plasma conditions $T_{x,yc}(t_*) = T_{x,yc}^{(0)}$ and $v_c(t_*) = v_c^{(0)}$. We obtain the position of the shock front, as in previous analytical developments, making use of $\lambda_{\rm sat}(t_{\rm front}) = \lambda_{\rm front} \simeq 0.8\lambda_c$. Hence the shock propagation magnetic spectral and plasma parameters can be reduced to a set of differential equations given by, Eqs. (4.46), (4.41)-(4.45) which open the way to an accurate numerical resolution.

On Figs. 4.14(a,b,c,d), S_p and $\lambda_{\rm sat}$ from the numerical resolution of the above set of equations (circled plain and dashed lines) agree well with the analytical formulae of Eqs. (4.34) and (4.37) (plain and dashed lines). This validates the analytical developments derived for the spectral parameters S_p and $\lambda_{\rm sat}$. We will now compare the ion temperature, anisotropy and velocity profiles extracted from the two different simulations of shock propagation [Fig. 4.15]. Overall the tendencies of the numerical resolution are fairly well reproduced by simulations results. The ion parameter profile evolve slightly with time. Both simulations show that once the shock is formed the temperature profiles smoothen with time. This can be explained qualitatively. The size of the overlap region between the incoming ions and reflected ions increases with time. Thus, the incoming plasma flow can have experienced many instabilities and undergone a strong heating before the Weibel instability saturates. Consequently, at fixed location in the moving shock frame, the Weibel wavelength should increase with time. This parameter λ_* could be estimated from Eq. (4.35) if the electron temperature, and reflected ion density ratio R_h were known at the beginning of the non-linear Weibel instability. An accurate description of the various instabilities taking place in the upstream region and of their impact upon the plasma's species is a formidable task, well outside the scope of this thesis.

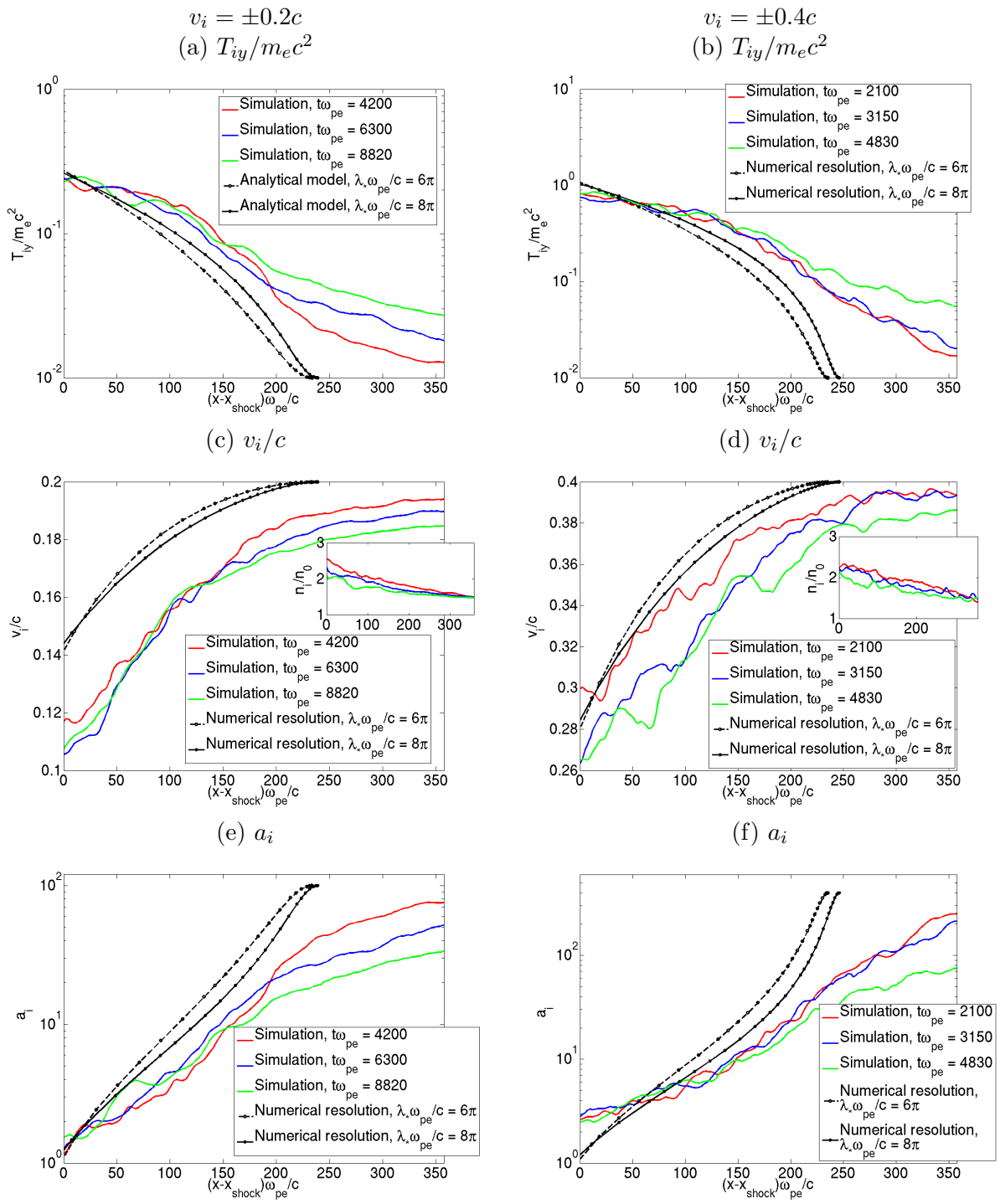

Figure 4.15. Spatial profiles of the ion plasma parameters at different times for two 2D simulations of shock-propagation: $m_i = 25m_e, v_i = \pm 0.2c$ (a,c,e) and $m_i = 25m_e, v_i = \pm 0.4c$ (b,d,f). The position (abscissa) is measured in respect to the position of the shock front. The shock formation time of Eq. (4.31) is $t_{\rm form}\omega_{pe} = 1800$ for (a,c) and $t_{\rm form}\omega_{pe} = 800$ for the case (b,d). (a,b) Transverse ion temperature profiles. (c,d) Mean longitudinal velocity and ion density (inset). (e,f) Ion anisotropy ratio. The theoretical predictions from Eqs. (4.41)-(4.45), (4.46) (numerical resolution) using $\lambda_* = 8\pi c/\omega_{pe}$ and $\lambda_* = 6\pi c/\omega_{pe}$ are superposed in (a-f).

4.3.6 Assumptions of the model

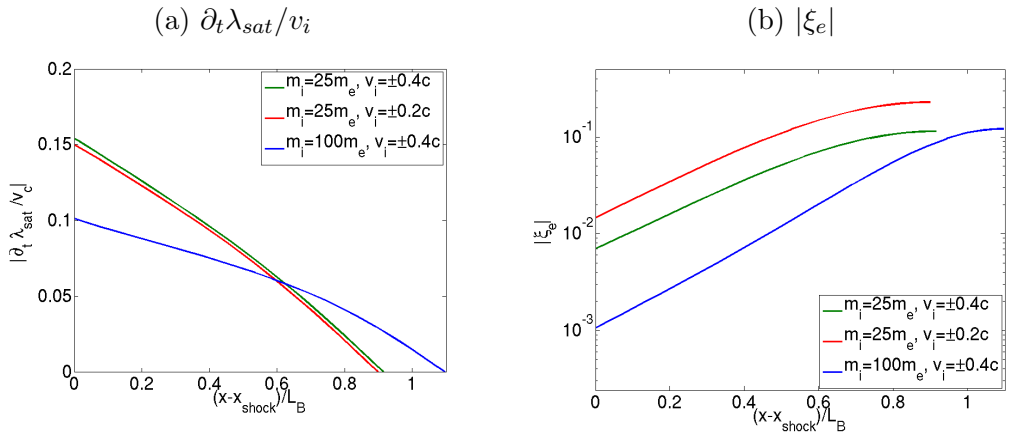

Figure 4.16. (a) Ratio $\partial_t \lambda_{sat}/v_i$ as a function of the distance to the shock front normalized to L_B from numerical resolution. (b) Temporal evolution (normalized to ω_{pe}^{-1}) of $|\xi_e|$ [Eq. (4.47)] with S_p and v_c from the numerical resolution of Eqs. (4.41)-(4.45), (4.46). The green, red and blue sold lines correspond to the case $m_i = 25m_e$, $v_i = \pm 0.4c$, $v_i = \pm 0.2c$ and $m_i = 100m_e$, $v_i = \pm 0.4c$ respectively.

At a given position of the upstream, the variation of S_p should be given by the above relations. The quasilinear equations of Davidson *et al.* (1972) are valid in a homogeneous system which is not the case in upstream of the shock. The insets of Figs. 4.17(d,e,f) evidence an ion density profile which increase from its far upstream value, $n_i/n_0 = 1$, to a compressed value of $n_i/n_0 \simeq 2$. Note that in the core the downstream, density jump ratio verifies the Rankine-Hugoniot conditions $n_i/n_0 \simeq 3$. Our model may remain valid if the variation of $\lambda_{\rm sat}$ is faster than that of the ion velocity. Consequently, for a small ratio $\partial_t \lambda_{sat}/v_c$, the spatial gradients should be negligible and the local equations used in the model should be valid. The spatial profile of $\partial_t \lambda_{\rm sat}/v_c$ is illustrated in Fig. 4.16(a) for three cases. For a broad range of parameters the Weibel wavelength is found to evolve much faster than the ion plasma parameters. Consequently, the spatial profiles can be neglected in the upstream up to the shock front.

Another critical assumption underlying our model is the hot electron approximation, $|\xi_e| \ll 1$, which allows us to neglect $\xi_e \mathcal{Z}(\xi_e)$ in the quasilinear equations. Its validity can be easily checked by comparing the value of $|\xi_e|$ computed from Eqs. (4.7) and of $S_p \simeq m_e T_e$ [Eq. (4.12)]. We obtain the temporal evolution of $|\xi_e|$,

$$|\xi_e|(t) \simeq (1-\eta_i^2)\sqrt{\frac{m_e^2}{2\pi S_p(t)}}\frac{\frac{R_h}{m_i}a_h' + (2-R_h)^2\frac{m_e v_c^2(t)}{S_p(t)}}{\frac{1-R_h}{m_i}+\frac{R_h}{m_i}(1+a_h')+(2-R_h)^2\frac{m_e v_c^2(t)}{S_p(t)}+1}\,, \tag{4.47}$$

where S_p is given by Eq. (4.28) with $a_h' \simeq 8$, $R_h \simeq 0.2$, $\alpha_i = 0.5$, $\eta_i = 0.5$. This equation is plotted in 4.16(b) for three sets of parameters. In all cases $|\xi_e| \ll 1$ over the non-linear Weibel region.

We will now focus on the plasma properties at $t = t_*$ (or $x - x_{\rm shock} \simeq L_B$). We remind the reader that, in the case of symmetric ion beams (Sec. 3.4.3), the plasma properties at $t = t_*$ could be easily related to the initial plasma parameters at $t = 0$ by the choice of λ_* combined with the dominant wavevector, $k_{\rm sat} = \eta_i \omega_{pi}/c\sqrt{a_i}$, [Eq. (3.10)]. We thus obtained Eqs. (3.87)-(3.90) which give the plasma properties at $t = t_*$, given the parameters at $t = 0$ and λ_*. This contrasts with the present asymmetric case, where no simple relations have been given between the plasma properties at $t = 0$ (unperturbed) and at $t = t_*$. Therefore, use has been made of the unperturbed plasma properties for the plasma conditions at $t = t_*$ ($T_{iy}(t_*) \simeq T_{iy}^{(0)}$, $v_i(t_*) \simeq v_i^{(0)}$ and $a_i(t_*) \simeq a_i^{(0)}$) during

the numerical resolution of Eqs. (4.41)-(4.45), (4.46) [Fig. 4.15]. This results in the discrepancy between the theoretic and simulation results at $x - x_{\rm shock} \simeq 250c/\omega_{pe}$, of a factor $\sim 2-4$ for T_{iy}. We will now estimate the influence of the plasma properties at $t = t_*$ for a fixed value of λ_*, in the case a 2D simulations of shock-propagation: $m_i = 100m_e, v_i = \pm 0.4c$, $T^{(0)}_{i,ex,y} = 0.01 m_e c^2$. The simulated plasma and spectral profiles (blue and red lines) are compared to the numerical resolution of Eqs. (4.41)-(4.45), (4.46) [Fig. 4.17] for two set of plasma properties at $t = t_*$, a cold ($T_{iy}(t = t_*) = 0.01 m_e c^2$ and $v_i = \pm 0.4c$, plain black line) and a hot one ($T_{iy}(t = t_*) = 0.5 m_e c^2$ and $v_i = \pm 0.39c$, dashed black line). We evidence no significant difference in the spectral profiles S_p and $\lambda_{\rm sat}$, for initially hot or cold plasma properties, moreover, both curves agree very well with the analytical predictions [Fig. 4.17(a,b)]. As for the plasma profiles, a discrepancy of about a factor ~ 20 of magnitude on $T_{iy}(x \simeq 900c/\omega_{pe})$, or a position shift of $\Delta x \simeq 200c/\omega_{pe}$ [Fig. 4.17(d)] are shown between the simulated curves and the initially cold plasma conditions. This discrepancy is mitigated, for the hot initial conditions. We highlight that no significant difference between the initially hot and cold curves are evidenced close to the shock front, for the three plasma profiles v_i, T_{iy} and a_i.

4.4 Conclusions

The formation of Weibel-mediated shocks results from the long-time non-linear evolution of the Weibel-filamentation instability. The model of collective filament dynamics worked out in previous chapter is based on equations of filament merging coupled with quasilinear relations of the ion populations. It can be applied to Weibel-unstable system during the non-linear stage of the instability when the two overlapping ion populations are symmetric. It has been shown to be valid during the collision of two non-relativistic plasma slabs. Comparison with various simulations has confirmed its ability to predict the non-linear evolution of the system until quasi-shock formation. Moreover, its predictions have been shown to be consistent with the evolution of filamented structures measured in recent experiments of plasma collision of Kugland *et al.* (2012b); Fox *et al.* (2013). This has highlighted the importance of the electron screening effect and therefore of the electron mass in the ion-Weibel dynamic. The proton radiographs of Fox *et al.* (2013)'s are analyzed in light of a 2D simulation where the ion mass has a physical value but where the electron mass is artificially increased. Only qualitative agreement is found between the experimental and simulation values. However, we showed that the nonphysical electron mass can explains the discrepancy between the experiment and the large scale simulation illustrated in Fig. 4.7(b). The shock formation time of our model scales as $\Delta t_{\rm form} \propto \omega_{pi}^{-1}/(m_e/m_i)^{1/4}$. Consequently, increasing the simulated electron mass by a factor 37, as in Fox *et al.* (2013), artificially speeds up the filament dynamics by a factor ~ 3. Our theoretical predictions are also consistent with the experimental data of Kugland *et al.* (2012b), under the assumption that the observed structures stem from the the Weibel-filamentaton instability.

In a second part, we have addressed the propagation of a fully formed collisionless shock. Its propagation is due to the non-linear Weibel filamentation instability taking place in the upstream, in front of the shock discontinuity. The instability is triggered by the overlapping of the cold incoming ions, propagating in the direction of the shock, and the hot out-coming ions, generated at the shock front and propagating in the opposite direction. The stability properties of the upstream plasma have been analyzed by means of the numerical techniques presented in Chapter 1 and via analytical approximations of the dominant modes. A simple relation has been obtained between the potential vector energy and the dominant wavevector in the upstream. This relation has been combined with the coalescence model of Chapter 3 in order to obtain an analytical formulation of the magnetic spectrum profile. The predicted profiles have been successfully compared with PIC simulations. We also obtained estimate of the amplitude and periods of the magnetic modulations at the shock front.

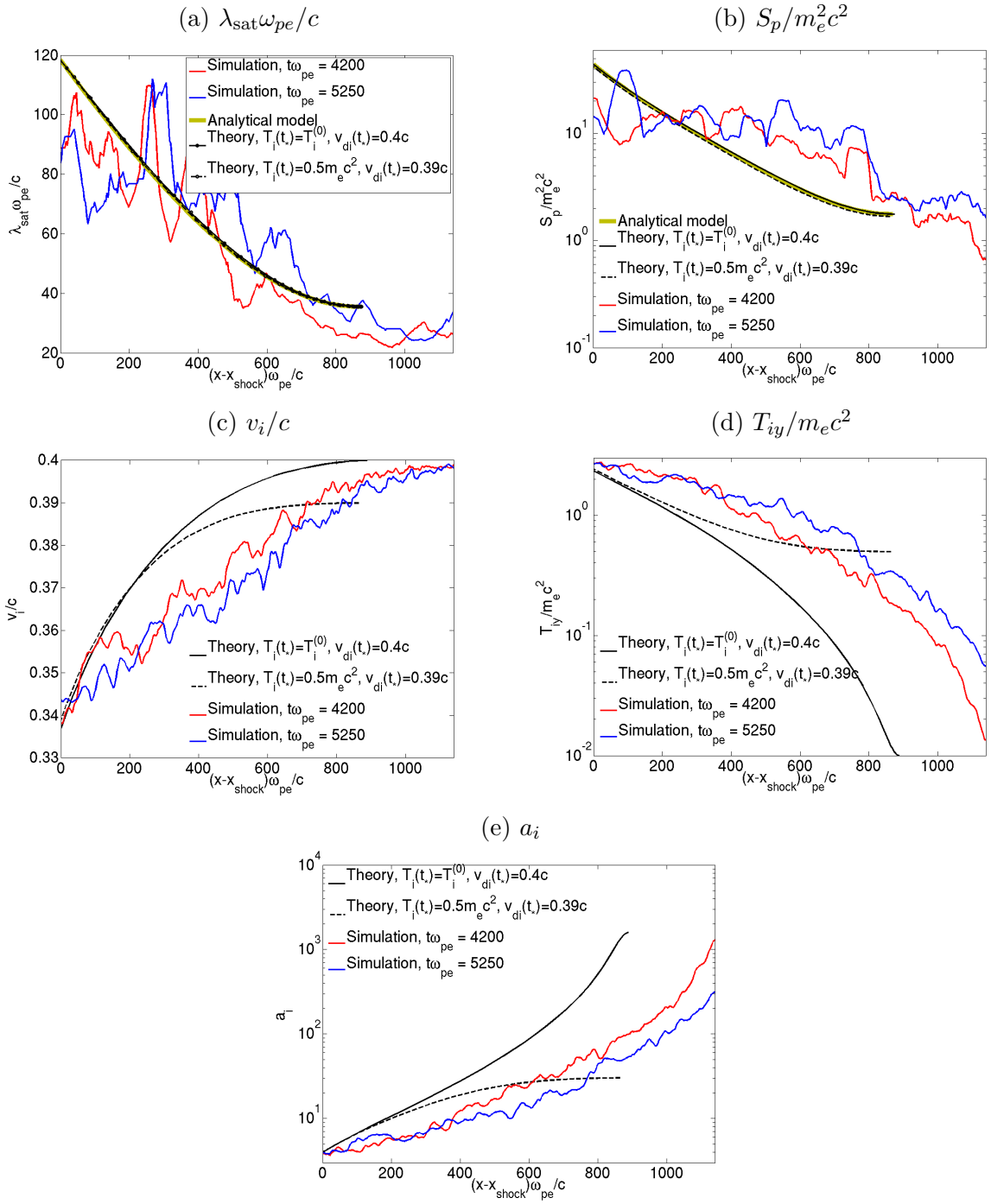

Figure 4.17. Spatial profiles of the ion plasma parameters at different times for a 2D simulations of shock-propagation: $m_i = 100m_e, v_i = \pm 0.4c$ for the two times $t\omega_{pe} = 4200$ (blue) and $t\omega_{pe} = 7140$ (red). The position (abscissa) is measured in respect to the shock front position given by Eq. (4.31) for $t_{\rm form}\omega_{pe} = 2000$. The theoretical predictions from Eqs. (4.41)-(4.45), (4.46) (numerical resolution) using $\lambda_* = 8\pi c/\omega_{pe}$ are superposed for two set of plasma parameters at $t = t_*$ (or $x - x_{\rm shock} \simeq 900c/\omega_{pe}$): $T_{ix}(t_*) = T_{iy}(t_*) = T_{iy}^{(0)} = 0.01m_ec^2$ and $v_i(t_*) = v_i^{(0)} = 0.4c$ (plain black line) and $T_{ix}(t_*) = T_{iy}(t_*) = 0.5m_ec^2$ and $v_i(t_*) = 0.39c$ (dashed black line). The analytical profiles of $\lambda_{\rm sat}$ [Eq. (4.34)] and S_p [Eq. (4.37)] are superposed as yellow plain lines on (a) and (b) respectively.

Moreover, we derived set of differential equations predicting both the spectral and ion profiles in the shock front, in fair agreement with PIC results. The wavelength λ_* at the end of the Weibel linear phase is found to affect the sharpness of the magnetic profile. In the case of shock propagation, this parameter have an impact on the sharpness of the magnetic profile. Its value could depend on all the instabilities preceding the Weibel saturation.

The analytical equations of $\lambda_{\rm sat}$ and S_p depends on some approximated parameters. The reflected ion density ratio R_h has been assumed equal to 0.2, whereas our simulations show a possible range of $0.05 \lesssim R_h \lesssim 0.3$. The temperature and drift velocity of the reflected ions have been also grossly estimated. Care has been taken to keep these parameters explicit in all the equations to open the way to future refinements. Finally, our model predicts that the length of the magnetic turbulence is independent of the plasma velocity and nearly independent of λ_*.

Chapter 5

Laser-induced Weibel-mediated collisionless shocks: theory and PIC simulations

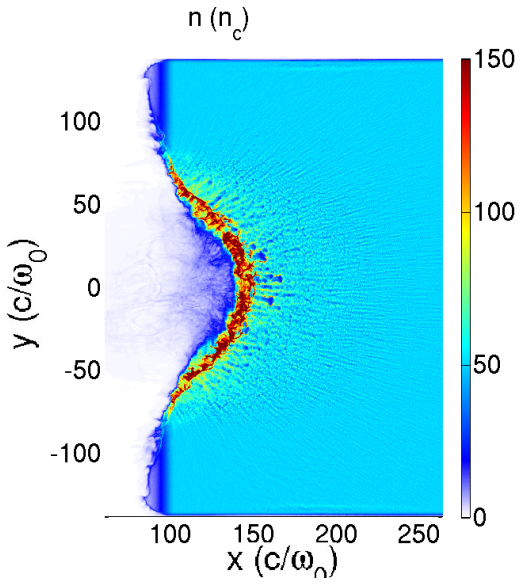

Figure 5.1. Weibel-mediated collisionless shock induced during the irradiation of an hydrogen plasma by a laser of intensity $I_0 \simeq 1.8\,10^{21}\mathrm{W.cm}^{-2}$, focused on a 16μm spot size.

5.1 Introduction

Theoretical and numerical modeling of electron-ion collisionless shocks is important for understanding various high-energy astrophysical environments, where they are held responsible for the generation of nonthermal particles and radiation Drury (1983); Malkov & O'C Drury (2001); Bykov & Treumann (2011). The formation and evolution of these structures can now be simulated numerically from first principles as shown previously, over significant spatio-temporal scales using state-of-the-art particle-in-cell (PIC) codes Kato & Takabe (2008); Spitkovsky (2008b); Keshet *et al.* (2009); Martins *et al.* (2009); Nishikawa *et al.* (2009); Haugbølle (2011); Sironi & Spitkovsky (2011); Stockem *et al.* (2014). These numerical studies have demonstrated that, for initially unmagnetized flows of high enough velocities, the well-known Weibel/filamentation instability Medvedev & Loeb (1999); Achterberg & Wiersma (2007); Achterberg *et al.* (2007) provides the small-scale magnetic turbulence needed for efficient dissipation of the bulk flow energy and Fermi-type acceleration of suprathermal particles Sagdeev (1966); Lemoine *et al.* (2006).

According to simulations (see chapter 3 and 4), shock formation occurs along the following 'standard' scenario: electron-driven Weibel/filamentation instabilities Bret *et al.* (2010b); Lemoine & Pelletier (2011) grow and saturate first, leaving the electrons mostly thermalized over the overlap region; for fast enough flows, an ion-driven Weibel/filamentation instability subsequently develops at larger scales, causing enhanced ion scattering off amplified magnetic fluctuations; the deflected ions then accumulate in the turbulent region, until satisfying the shock hydrodynamic jump conditions Blandford & McKee (1976).

These numerical advances go along with rapid experimental progress towards the generation of collisionless, self-magnetized shocks by intense lasers Takabe *et al.* (2008); Kuramitsu *et al.* (2011); Ross *et al.* (2013); Fox *et al.* (2013). Two main configurations are currently investigated to this goal. The first one relies upon the interaction of two counter-propagating plasma flows generated from the ablation of foil targets by high-energy ($\sim 0.1 - 1\,\mathrm{MJ}$), nanosecond-duration laser pulses Drake & Gregori (2012). Such flows are of relatively low density ($n \ll n_c$, where $n_c \sim 10^{21}\,\mathrm{cm}^{-3}$ is the critical density of a $1\,\mu$m-wavelength laser), temperature ($T_e \sim 1\,\mathrm{keV}$) and drift velocity ($v_i \sim 1000\,\mathrm{km\,s}^{-1}$).

An alternate approach, proposed by Fiuza *et al.* (2012) and further studied in this chapter, hinges upon the irradiation of an overdense plasma ($n \gg n_c$) by a relativistic-intensity ($I_0 > 10^{20}\,\mathrm{Wcm}^{-2}$), picosecond-duration laser pulse (Fig. 5.2). During this interaction, copious amounts of electrons are heated to relativistic energies and injected into the target. The ensuing strong charge separation and pressure gradients accelerate the surface ions to a velocity $v_i \sim 2v_p$, where v_p is the laser-driven piston ('hole boring') velocity (Wilks & Kruer 1992). According to Fiuza *et al.* (2012), the various filamentation instabilities triggered in the ion beam-plasma region may lead to the formation of a collisionless shock for intense enough lasers and/or dilute enough targets.

An electrostatic to Weibel-mediated shock transition will be evidenced by mean of two-dimensional (2-D) PIC simulations. Since the ion isotropization results from the instability-generated magnetic turbulence, we will present a quantitative analysis of the filamentation instability, assuming either relativistic Maxwell-Jüttner or relativistic multi-waterbags distribution functions. In particular, we will assess the influence of the hot electron population upon the instability's properties and the resulting saturated magnetic field.

As in Fiuza *et al.* (2012), the capability of ultra-intense laser pulses to drive self-magnetized shocks into overdense plasmas has been investigated by means of 2-D PIC (CALDER) simulations. The process of shock formation is studied (rather than the propagation of the shock), which is inaccessible in astrophysical contexts.

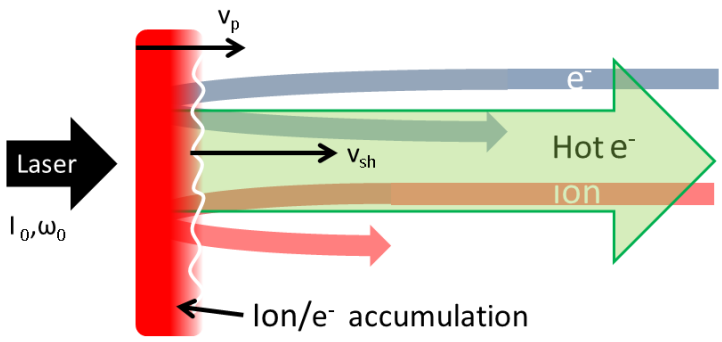

Figure 5.2. Sketch of the relativistic laser-driven shock formation (in the laser piston frame): electromagnetic instabilities are triggered in the upstream by counter-streaming electron-ion flows. The magnetic fluctuations isotropize the incoming ions over a time scale $\Delta t_{\rm iso}$, at which point the shock Rankine-Hugoniot jump conditions are fulfilled across the turbulent region.

5.2 PIC simulations: results and analysis

5.2.1 Numerical setup

The simulations have been performed using the CALDER code, run in 2-D geometry. The laser pulse is modeled as an electromagnetic plane wave linearly polarized along the y-axis, with a $1\,\mu$m wavelength and an intensity of $I_0 = 3.6\times10^{21}\,\mathrm{Wcm^{-2}}$. This corresponds to a normalized field amplitude $A_0 = eE_0/m_e c\omega_0$ (where ω_0 is the laser frequency) of $A_0 = 60$. The laser intensity is held constant after a linear ramp of $30\omega_0^{-1}$ duration. The wave propagates along the $x>0$ direction and interacts with a fully-ionized, overdense plasma slab located at $x = 40c/\omega_0$ and of maximum electron density $n_e^{(0)}$. The plasma is made of protons ($m_i/m_e = 1836$, $Z_i = 1$, $n_e^{(0)} = 50-100n_c$, where $n_c \simeq 10^{21}\,\mathrm{cm^{-3}}$ is the critical density). The initial electron and ion temperatures are $T_{e,i}^{(0)} = 5\,\mathrm{keV}$. A $63c/\omega_0$ ($10\,\mu$m) scale-length density ramp is added on the front surface to mimic the effect of the laser pedestal. The simulation grid comprises 8600×1536 cells with mesh sizes $\Delta x = \Delta y = 0.25c/\omega_{pe}$. The time step is taken to be $\Delta t = 0.95\Delta x/c\sqrt{2}$. Each cell contains 50 macro-particles per species, yielding a total of 6.6×10^8 macro-particles. To reduce the numerical noise, 3rd-order weight factors are used. The boundary conditions are absorbing in x and periodic in y for both particles and fields. We have checked in the hydrogen case that increasing the number of macroparticles to 100 macro-particles per species per cell or shortening the plasma ramp does not alter significantly the results.

5.2.2 Shock formation in a hydrogen plasma

General description

Let us first analyse the generation of a collisionless shock in a H^+ plasma for the parameters $A_0 = 60$ and $n_e^{(0)} = 50n_c$. These parameters are identical to those considered in Fiuza *et al.* (2012). Figure 5.3(a) shows that, by $\omega_0 t = 480$, the Weibel/filamentation instability induced by the laser-accelerated particles flowing through the bulk plasma has given rise to strong magnetic channels parallel to the x-axis. From Fig. 5.3(b), we see that these channels are associated to pronounced modulations in the ion density ($\delta n_i/n_i \sim 1$). As a result of successive coalescences and decreasing anisotropy of the particle momentum distributions (see below), the field amplitude and filament size grow from $eB_z/m_e\omega_0 \simeq 1$ and $\lambda \simeq 3c/\omega_0$ ($\simeq 21c/\omega_p$) to $eB_z/m_e\omega_0 \simeq 10$ and $\lambda \simeq 12c/\omega_0$ ($\simeq 85c/\omega_p$) when moving from $\omega_0 x/c \simeq 300$ to $\omega_0 x/c \simeq 200$. Closer to the target front

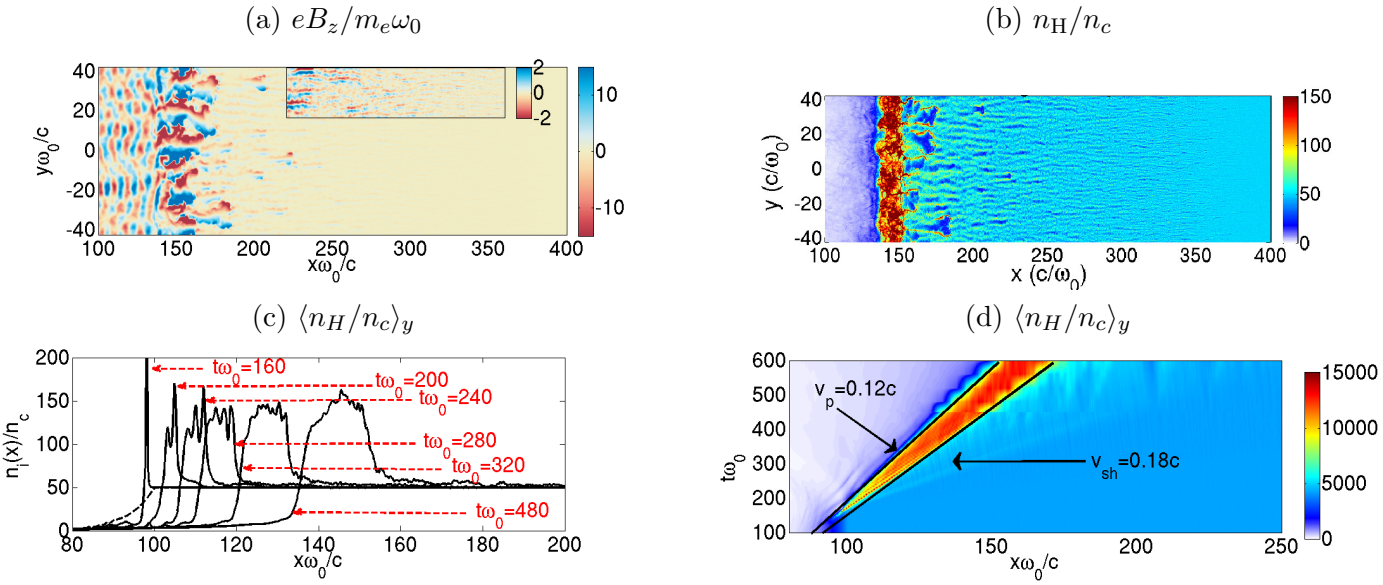

Figure 5.3. Shock formation in a H^+ plasma with $A_0 = 60$ and $n_e^{(0)} = 50n_c$. (a) Magnetic field B_z at $t\omega_0 = 480$. (b) Proton density n_H at $\omega_0 t = 480$. (c) y-averaged proton density *vs* x at successive times. (d) y-averaged proton density *vs* (x, t).

($150 \lesssim \omega_0 x/c \lesssim 200$), the filaments exhibit kink-like oscillations, while further growing in amplitude and size (up to $eB_z/m_e\omega_0 \simeq 25$ and $\lambda\omega_0/c \simeq 20$) (Milosavljević & Nakar 2006). They eventually decay into a compressed turbulent layer (further referred to as the downstream) in the interval $140 \lesssim \omega_0 x/c \lesssim 150$. The spatio-temporal evolution of this shock-like structure is displayed in Figs. 5.3(c,d). The compression ratio relative to the unperturbed (upstream) plasma stabilizes to a value $n_d/n_u \simeq 3$ (where u and d stand for upstream and downstream, respectively) by $\omega_0 t \simeq 240$, and remains constant at later times. The right side of the compressed layer propagates at a velocity $v_{\rm sh} \simeq 0.175c$, while its left (irradiated) side is pushed by the laser radiation pressure at a velocity $v_p \simeq 0.125c$ [Fig. 5.2]. These values are consistent with a strong hydrodynamic shock induced by the laser-driven motion of the target surface at a piston (or 'hole boring') velocity Wilks & Kruer (1992)

$$v_p = c\sqrt{\frac{(1+R_L)Z_i A_0^2}{4n_e^{(0)} m_i}}\,, \tag{5.1}$$

where R_L denotes the laser reflectivity. This expression directly follows from equating the photon and ion momentum fluxes across the laser-plasma interface (in the non-relativistic limit $v_p \ll 1$). In the present simulation, we have $R_L \simeq 0.4$, so that $v_p \simeq 0.12c$, which closely agrees with the measured value. The theoretical compression ratio, n_d/n_u, and velocity, $v_{\rm sh}$, of a non-relativistic strong hydrodynamic shock are

$$\frac{n_d}{n_u} = \frac{\Gamma_{\rm ad}+1}{\Gamma_{\rm ad}-1}\,, \tag{5.2}$$

$$v_{\rm sh} = v_p\frac{\Gamma_{\rm ad}+1}{2}\,, \tag{5.3}$$

with $\Gamma_{\rm ad}$ the adiabatic index Blandford & McKee (1976). In the present 2-D case, we have $\Gamma_{\rm ad} = 2$, and hence $n_d/n_u = 3$ and $v_{\rm sh} = 0.18$, which match the simulated values. As first discussed in Fiuza *et al.* (2012), these features bear much resemblance to those observed in simulations of Weibel-mediated electron-ion shocks (Kato & Takabe 2008).

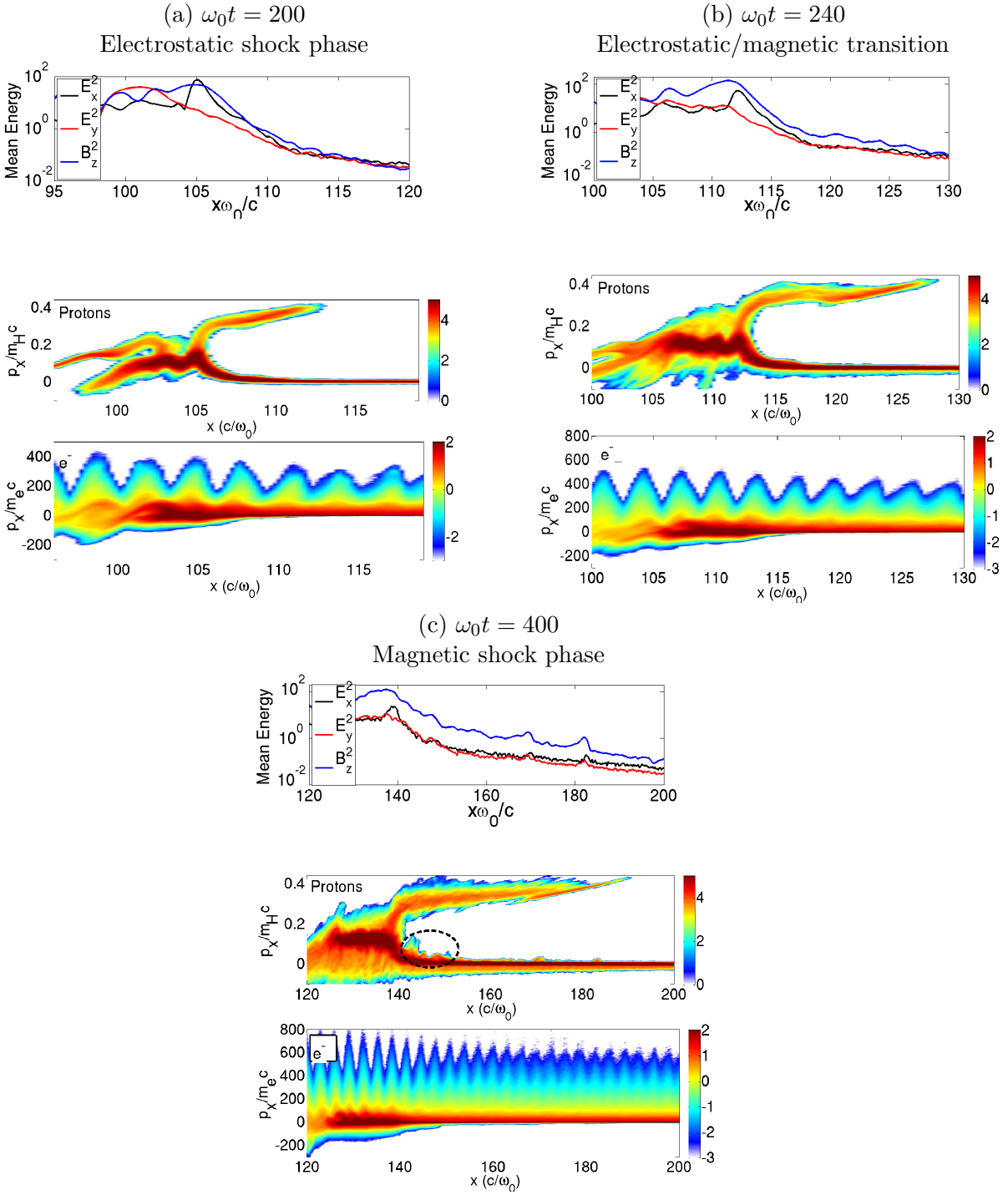

Figure 5.4. Shock formation in a hydrogen plasma with $A_0 = 60$ and $n_e^{(0)} = 50 n_c$. Upper panels: y-averaged electromagnetic energies normalized to $m_e c^2 n_c$. Middle and lower panels: respectively proton and electron $x - p_x$ phase spaces at (a) $t\omega_0 = 200$, (b) $t\omega_0 = 240$ and (c) $t\omega_0 = 400$.

Instability development and shock formation

The ion and electron $x - p_x$ phase spaces around the shock front are displayed in the middle and lower panels respectively at successive times in Figs. 5.4(a-c). The electrons accelerated in the $x > 0$ direction have a large momentum dispersion ($\Delta p_x \sim 100 m_e c$), with $2\omega_0$-modulations typical

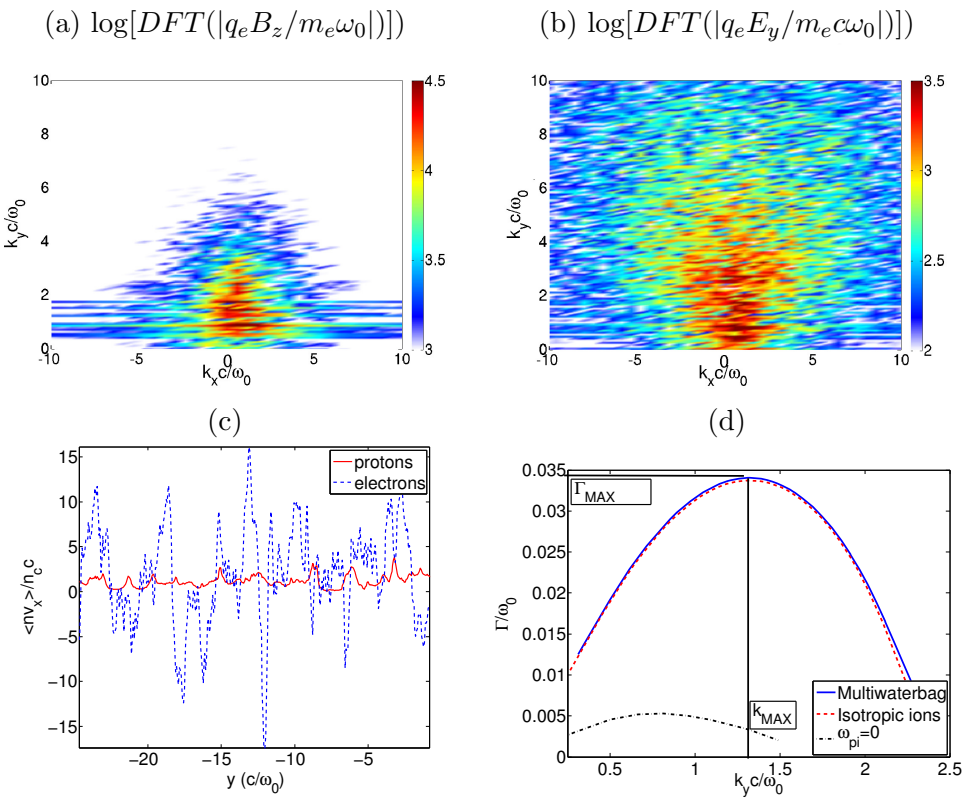

Figure 5.5. Spatial Fourier transforms of B_z (a) and E_y (b) at $t\omega_0 = 240$ and $x\omega_0/c = 120$ (in $\log_{10}$ scale). (c) y-profile of the normalized current density $\langle nv_x\rangle/n_c c$ of the electrons (blue) and protons (red). (d) Normalized filamentation growth rate Γ/ω_0 solution of Eq. (1.21). The blue line corresponds to a multi-waterbag model of the electron and proton distributions [Figs. 5.6(c,d)]; the red line corresponds to isotropic Maxwellian protons with $T_H = 5\,\mathrm{keV}$; the black line corresponds to immobile protons.

of ponderomotive laser acceleration. Later on, the electron distribution broadens with time, with maximum p_x increasing from $\sim 400 m_e c$ at $\omega_0 t = 200$ to $\sim 800 m_e c$ at $\omega_0 t = 480$.

At $\omega_0 t = 200$, partial ion reflection ($n_{i,r}/n_i^{(0)} \sim 0.1$) occurs off a shock front located at $\omega_0 x/c \simeq 105$. This gives birth to a diluted beam of velocity range $2v_{\rm sh} \lesssim v_x \lesssim 0.4c$, and extending up to $\omega_0 x/c \simeq 112$. In the downstream region, the ions are, on average, accelerated to the piston velocity v_p, while exhibiting velocity oscillations. The upper panel of Fig. 5.4(a) further shows that the y-averaged electrostatic energy due to E_x then slightly dominates the magnetic energy. All of these features suggest a transient electrostatic, rather than magnetic, collisionless shock driven by the laser radiation pressure Denavit (1992); Silva *et al.* (2004); Zhang *et al.* (2007). At $\omega_0 t = 240$, the reflected and upstream ion populations overlap over the space interval $112 \lesssim \omega_0 x/c \lesssim 128$. The peak E_x energy, however, has decreased by 50% in the vicinity of the shock front. Meanwhile, the magnetic energy has increased so that it prevails in both the shock foot and downstream regions. Figures 5.5(a,b) plot the 2-D spatial Fourier transforms $|B_z(k_x, k_y)|$ and $|E_y(k_x, k_y)|$ in the overlap region ($x\omega_0/c = 120$) at $t\omega_0 = 240$. Both spectra are mostly peaked around $k_x c/\omega_0 \sim 0$ and $k_y c/\omega_0 \sim 1-2$, consistently with dominant Weibel/filamentation modes in the shock foot region.The transition into a magnetic shock is complete by $\omega_0 t = 400$, at which time the magnetic energy exceeds the electric energy by more than one order of magnitude. The shock front has then moved to $\omega_0 x/c \simeq 140$. Note that the E_x and E_y energies exhibit similar profiles in the shock foot region, except at the shock front ($\omega_0 x/c \sim 140$), where the E_x energy becomes larger by a factor of ~ 2.5.

Figure 5.5(c) plots transverse lineouts of the electron and ion current density, $\langle nv_x\rangle$, at $\omega_0 t = 240$

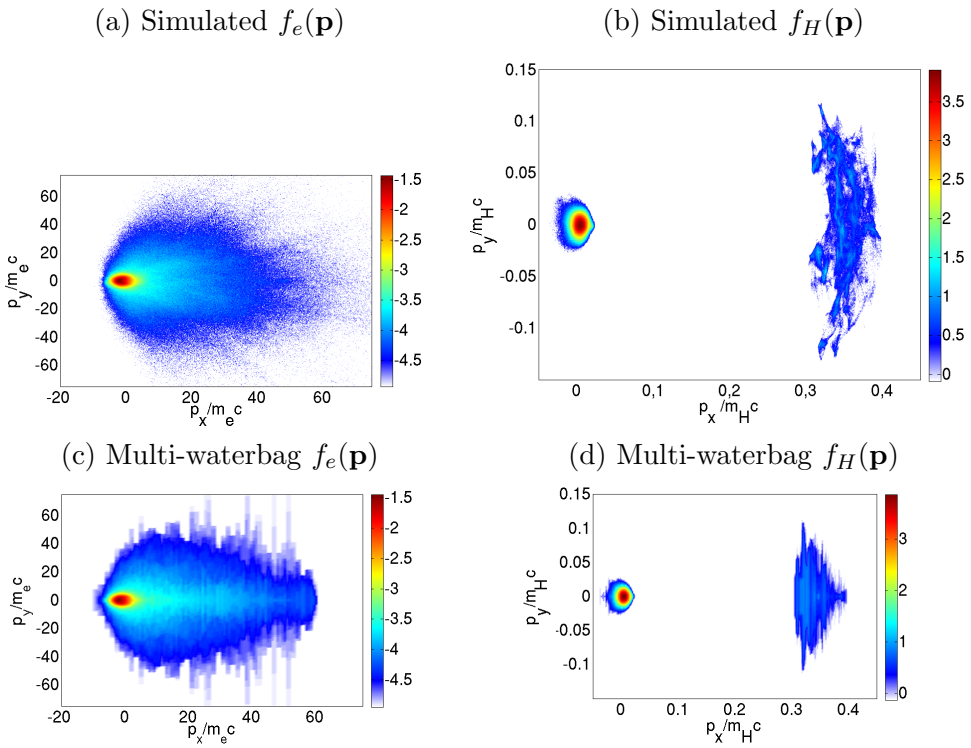

Figure 5.6. $p_x - p_y$ phase space (in $\log_{10}$ scale) of the electrons (a) and protons (b) at $\omega_0 x/c = 240$ and $\omega_0 t = 120$. Panels (c,d) show the corresponding multi-waterbag fits used for the stability analysis (see text).

in the shock foot region ($\omega_0 x/c = 120$). The electron current fluctuations are seen to largely prevail over the ion current fluctuations. This feature, which holds on both sides of the shock front for the time scales considered, implies that the magnetic filaments, and the resulting shock, are mostly driven by the electrons.

This important observation is corroborated by a linear stability analysis of the particle momentum distributions in the shock foot, displayed in Figs. 5.6(a,b). As expected Ren *et al.* (2006), the electron distribution is comprised of a diluted, high-energy tail (extending up to $|\mathbf{p}| > 100 m_e c$) and of a denser part carrying moderately-relativistic laser-accelerated electrons as well as non-relativistic return current electrons. The ion phase space exhibits two clearly-separated structures associated to the upstream target ions (around $v = 0$) and the reflected ions (around $v_x/c \simeq 0.35$). The latter present a weakly-varying, anisotropic ($\Delta p_y \simeq 0.2 m_H c \simeq 3\Delta p_x$) distribution, much broader than that of the upstream ions (of temperature close to the initial value of 5 keV). In order to solve the dispersion relation of the Weibel/filamentation instability, it is convenient to approximate the measured distributions using the multi-waterbag decomposition scheme introduced in chapter 1 (Gremillet *et al.* 2007; Bret *et al.* 2010b). The resulting multiwaterbag distribution reads [Eq. (1.99)]

$$f_{MW}(\mathbf{p}) = \sum_{j=1}^{N} \alpha_j f_j^{(0)}(\mathbf{p}) \,. \tag{5.4}$$

where α_j is the weight of the jth waterbag component and $f_j^{(0)}(\mathbf{p})$ is the jth waterbag distribution given by Eq. (1.81), which reads

$$f_j^{(0)}(\mathbf{p}) = \frac{1}{4 P_{jx} P_{jy}} H(P_{jx} - |p_x - P_{jd}|) H(P_{jy} - |p_y|) \delta(p_z) \,. \tag{5.5}$$

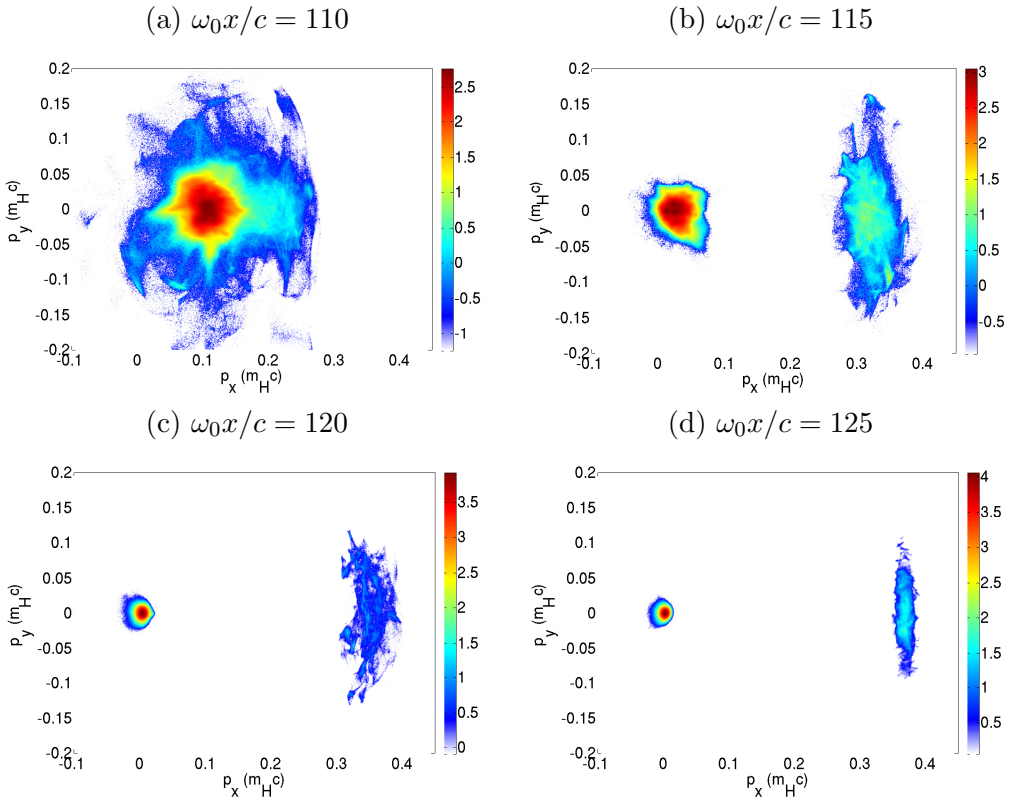

Figure 5.7. Proton $p_x - p_y$ phase space at $t\omega_0 = 240$ and various locations: $x\omega_0/c = 110$ (a), 115 (b), 120 (c) and 125 (d) (in $\log_{10}$ scale).

We remind the reader that H is the Heaviside function and P_{jd}, P_{jx}, P_{jy} are adjustable parameters. Figures 5.6(c,d) display the best-fitted multi-waterbag approximations (with $N = 10^4$) of the electron (c) and ion (d) momentum distributions. The multi-waterbag distributions reproduce the momentum fluxes of the original distributions (a,b) to within an error $< 10\%$. The susceptibility tensor associated to these waterbag distributions is detailed in Sec. 1.4 of Ref. Bret *et al.* (2010b). Using the resolution scheme of Sec. 1.1.2 procedure, the filamentation growth rate $\Gamma = \Im\omega$ is plotted as a function of the transverse wave number k_y (for $k_x = 0$) in Fig. 5.5(d). The maximum value $\Gamma_{\max}/\omega_0 \simeq 0.035$ is obtained at the wave number $k_{\max}c/\omega_0 \simeq 1.3$. To assess the contribution of the ions to the instability, we have replaced their multi-waterbag distribution by an isotropic non-drifting Maxwellian of temperature $T_H = 5\,\mathrm{keV}$. The resulting growth rate curve almost coincides with that obtained with the full ion distribution, which proves that the reflected ions are not responsible for the observed filamentation instability. As will be analyzed later on, because the electrons' mean energy is here comparable to the ions' (as measured in the piston frame), the electrons can induce magnetic fluctuations strong enough to scatter the ions and entail shock formation. This contrasts with the standard scenario of Weibel-mediated astrophysical shocks Lyubarsky & Eichler (2006), where the unstable two-stream ion distribution is considered as the key player in generating magnetic turbulence. Although, in our case, the ion anisotropy is not the driving force behind the magnetic buildup, the thermal bulk ions, while stable, may significantly enhance the electron-driven instability by mitigating space-charge effects. This destabilizing mechanism, previously discussed in Refs. Tzoufas *et al.* (2006); Ren *et al.* (2006), is demonstrated by computing the growth rate upon assuming infinite-mass ions. As seen in Fig. 5.5(d), this yields a maximum growth rate lowered by a factor ~ 6, and a dominant wave number down-shifted to $k_{\max}c/\omega_0 \sim 0.7$.

Figures 5.7(a-d) plot the proton $p_x - p_y$ phase space at various locations in the upstream region

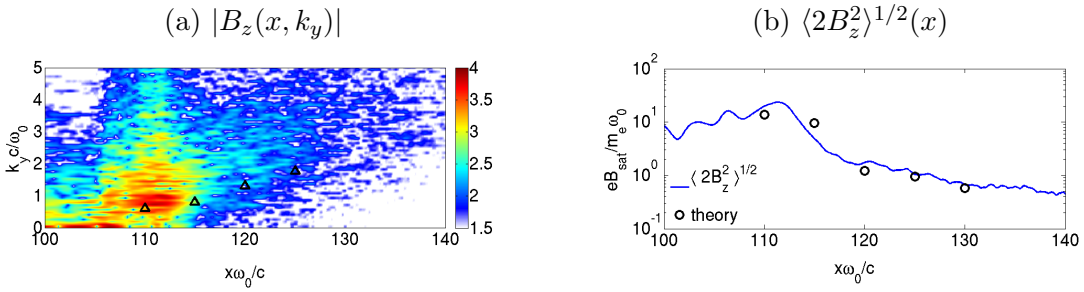

Figure 5.8. (a) Magnetic spectrum $|B_z(x,k_y)|$ (in $\log_{10}$ scale) in the upstream region at $t\omega_0 = 240$. The triangles plot the fastest-growing wave numbers, $k_{\max}$, predicted from linear theory at the locations of Fig. 5.7(a-d). (b) Spatial profile of the transversely averaged magnetic field $\langle 2B_z^2\rangle^{1/2}$ at $t\omega_0 = 240$ (blue solid line). The black circles plot Eq. (5.9), where $k_{\rm sat}$ and $\gamma_{e,\rm eff}$ are measured from the simulation.

at time $t\omega_0 = 240$. Both the bulk and reflected proton distributions broaden as one moves closer to the shock front as a result of growing magnetic scattering. At the shock front ($x\omega_0/c = 110$), they have merged into a relatively isotropized population [Fig. 5.7(a)]. In Fig. 5.8(a) the magnetic spectrum $|B_z(x,k_y)|$ in the upstream region is displayed and compared to the fastest-growing wave number predicted from linear theory using the particle distributions of Figs. 5.7(a-d). Overall, a correct agreement is obtained between linear theory and the simulated spectrum.

The spatial profile of the transversely-averaged magnetic field amplitude, $\langle 2B_z^2\rangle^{1/2}$, at $\omega_0 t = 240$ (i.e., the approximate formation time of the magnetic shock) is plotted in Fig. 5.8(b). The amplitude varies by aboyt two orders of magnitude over the upstream region $110 \lesssim \omega_0 x/c \lesssim 140$. Note that at this time, the reflected ions extend to $x\omega_0/c \simeq 128$ [Fig. 5.4(b)]. At the shock front ($x\omega_0/c \simeq 112$), the magnetic field reaches a value $\langle B_z^2\rangle^{1/2} \simeq 25 m_e\omega_0/e$, comparable to the laser field strength.

In order to analyze this magnetic profile, we have assessed the effectiveness of the various parts of the electron distribution in driving the Weibel instability. A similar evaluation was made in Ref. Ren *et al.* (2006), yet within the simplifying assumption of a purely transverse instability. Here, we adopt an alternative approach based on our multi-waterbag model. The condition for instability of a multi-waterbag system reads $\Delta = AB - C^2 > 0$, where the factors A,B,C, given in Appendix B of Ref. Bret *et al.* (2010b), take the form of a sum over the waterbag components. For instance, we have

$$C = \sum_j \omega_{pj}^2 P_{jd}/P_{jy}^2 \,. \tag{5.6}$$

Let us now define

$$C_i = \sum_{j\neq i} \omega_{pj}^2 P_{jd}/P_{jy}^2 \,, \tag{5.7}$$

where the index i labels a given waterbag component. Likewise, we introduce A_i, B_i, $\Delta_i = A_iB_i - C_i$ and $S_i = 1 - \Delta_i/\Delta$. The latter expression then quantifies the stabilizing ($S_i < 0$) or destabilizing ($S_i > 0$) influence of the ith waterbag component. Figure 5.9 displays $\sum_j S_j f_j^{(0)}(\mathbf{p})(\mathbf{p})$ using the electron distribution measured at $\omega_0 t = 240$ and $\omega_0 x/c = 120$ It appears that the electrons mostly responsible for the late-stage instability have moderate energies ($\gamma \simeq 3$) and, on average, negative x-momenta ($p_x < 0$). These particles are therefore associated to the background return current induced by the higher-energy, laser-driven electrons propagating in the $x > 0$ direction. This feature was first pointed out in Ref. Ren *et al.* (2006) under similar laser-plasma conditions. The relativistic energies attained by the return current electrons stem from the various (electromagnetic Weibel/filamentation, electrostatic longitudinal/oblique) beam-plasma instabilities induced in the upstream region.

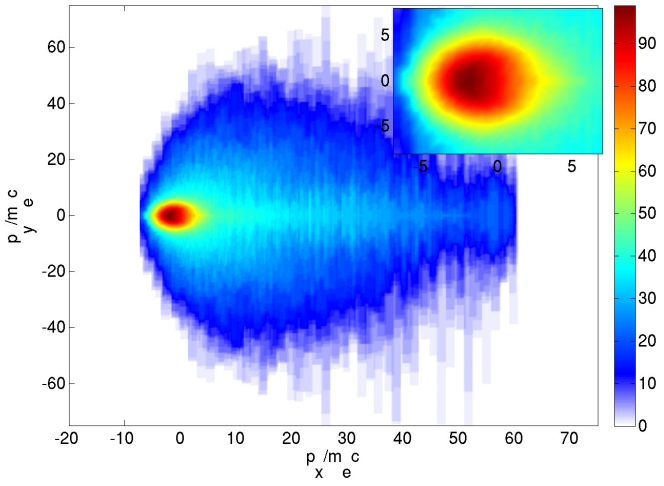

Figure 5.9. Map of $\sum S_i W_i(\mathbf{p})$, which measures the local contribution to the Weibel instability in the electron $p_x - p_y$ phase space. The subpanel zooms in on the most destabilizing electrons.

Let us now confront the simulated magnetic profile of Fig. 5.8(b) to simple models of the saturated field accounting for the Weibel-effective part of the electron distribution. According to the widely-used transverse-trapping model Davidson *et al.* (1972); Yang *et al.* (1994); Silva *et al.* (2002); Kaang *et al.* (2009), saturation occurs when the electron bounce frequency inside a magnetic filament is equal to the maximum growth rate . This yields the magnetic field amplitude

$$\frac{eB_{\rm sat}}{m_e\omega_0} \simeq \left\langle \frac{\gamma}{\beta_x} \right\rangle_{\rm eff} \left(\frac{\Gamma_{\rm max}}{\omega_0} \right)^2 \frac{\omega_0}{k_{\rm max}c}\,, \tag{5.8}$$

where $\langle\gamma/\beta_x\rangle_{\rm eff}$ denotes the average of γ/β_x over the Weibel-effective electrons. We have typically $\langle\gamma/\beta_x\rangle_{\rm eff} \simeq 5-10$. As a result, formula (5.8) predicts relatively weak amplitudes ($eB_{\rm sat}/m_e\omega_0 \simeq 0.01$), which match the simulation results only in the far upstream region. This suggests that the magnetic profile of Fig. 5.8(b) corresponds to a more strongly nonlinear regime than is assumed in the transverse-trapping model. A second estimate of $B_{\rm sat}$ may therefore be derived supposing that the Weibel-effective electrons are magnetized Moiseev & Sagdeev (1963); Lyubarsky & Eichler (2006). Equating the typical filament size, $2\pi/k_{\rm sat}$ to the Larmor radius of the effective electrons, $\langle\gamma\rangle_{\rm eff}/eB$, gives the lower limit

$$\frac{eB_{\rm sat}}{m_e\omega_0} \simeq \langle\gamma\rangle_{\rm eff} \frac{k_{\rm sat}c}{\pi\omega_0}\,. \tag{5.9}$$

For a numerical application, the saturated wave number $k_{\rm sat}$ is extracted from the spectrum of Fig. (5.8)(a), while the Weibel-effective electrons are defined as that part of the electron phase space satisfying $\sum_j S_j W_j(\mathbf{p}) > \frac{1}{2}\max_{\mathbf{p}}(\sum_j S_j W_j)$. The resulting $B_{\rm sat}$ values are plotted at different locations as black circles in Fig. 5.8(b), where they are found to capture to a good accuracy the simulated magnetic profile.

In summary, a perturbative analysis of the local plasma distribution functions shows that the magnetic turbulence in the upstream region mostly results from the interplay between the laser-accelerated and background electrons. More precisely, the dominant destabilizing effect comes from the moderate-energy return current electrons. While the reflected ions have a negligible influence, the background ions strengthen the instability by weakening its inhibiting, electrostatic component Tzoufas *et al.* (2006); Ren *et al.* (2006). Although the typical wave numbers compare satisfactorily with linear theory, the magnetic field profile in the shock-foot region is indicative of the magnetiza-

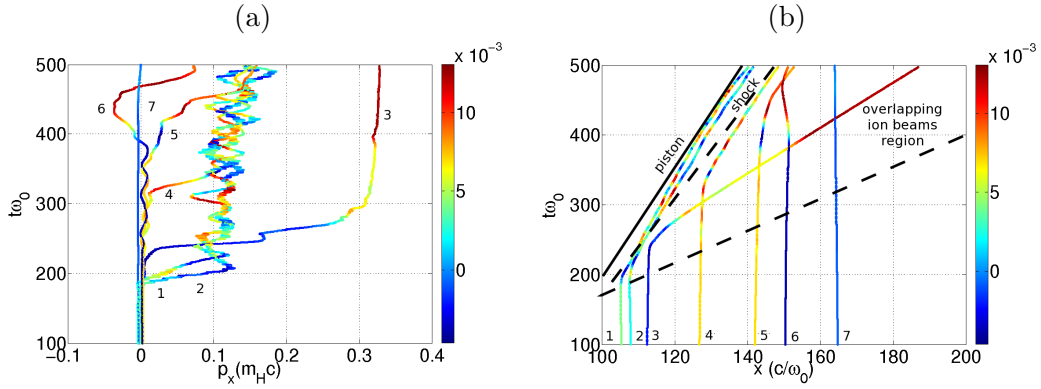

Figure 5.10. Typical proton trajectories for various initial x-locations: (a) $p_x(t)$ and (b) $x(t)$. The color of each curve is indexed by $p_y(t)/m_H c$. In (b) are also plotted the trajectories of the laser-driven piston (black solid line), of the shock front (black dashed line) and of the reflected proton front (black dotted-dashed line).

tion of the Weibel-effective part of the electron distribution.

Proton trajectories

To gain insight into the dynamics of the upstream protons, we plot in Figs. 5.10(a,b) seven typical proton trajectories $(x(t), p_x(t))$, originating from increasing target depths. The color of each trajectory (labeled by the particle number) is indexed by the instantaneous value of the normalized y-momentum, $p_y(t)/m_H c$. In Fig. 5.10(b), the trajectories of the laser-driven piston, of the shock front and of the reflected ion front are also plotted.

Particles 1 and 2 are rapidly (over the time interval $190 \lesssim t\omega_0 \lesssim 220$) accelerated forward by the electrostatic field set up by the electron pressure gradient at the (then mainly electrostatic) shock front. After reaching the downstream (piston) velocity ($v_x/c \simeq 0.12$), they remain confined in the downstream region where they experience an increasing level of electromagnetic turbulence. The latter makes them oscillate in both v_x and v_y, with similar amplitudes $\Delta v_x \sim \Delta v_y/c \sim 0.02$. Particle 3 is more strongly accelerated by the electrostatic shock potential: it attains a velocity $v_x/c \simeq 0.3$, which corresponds to reflection in the shock frame. During its main acceleration phase ($220 \lesssim \omega_0 t \lesssim 300$), its y-velocity hardly varies due to a weak magnetic turbulence in the shock foot region. Later on, however, the magnetic fluctuations get strong enough to induce velocity variations $\Delta v_y/c \sim 0.02$.

Particles 4-6 exemplify the ion dynamics in the magnetic shock regime. Because the upstream electromagnetic turbulence has grown in amplitude and spatial extent, they undergo an increasing number of oscillations in v_x and v_y while being, on average, accelerated along x by the electrostatic field. The effective range of the turbulence can be assessed by noting that particle 7, initially located at $x\omega_0/c \simeq 165$, does not exhibit any significant acceleration up to $t\omega_0 = 500$, at which time the shock front has moved to $x\omega_0/c \simeq 145 - 150$.

Late-time evolution: magnetic vortices

Figure 5.3(a) shows the formation of depleted ion 'bubbles' in the shock foot region. As displayed in Fig. 5.3(b) and in the zoom of Fig. 5.11, these structures are associated with magnetic dipole vortices.

The long term evolution of the shock shows the development of 'bubbles' in which is maintained a static magnetic loop. Those bubbles significantly develops in both hydrogen ($n_H = 50n_c$, $A_0 = 60$) and carbon ($n_C = 50n_c$, $A_0 = 60$) simulations after the Weibel-induced shock is being formed.

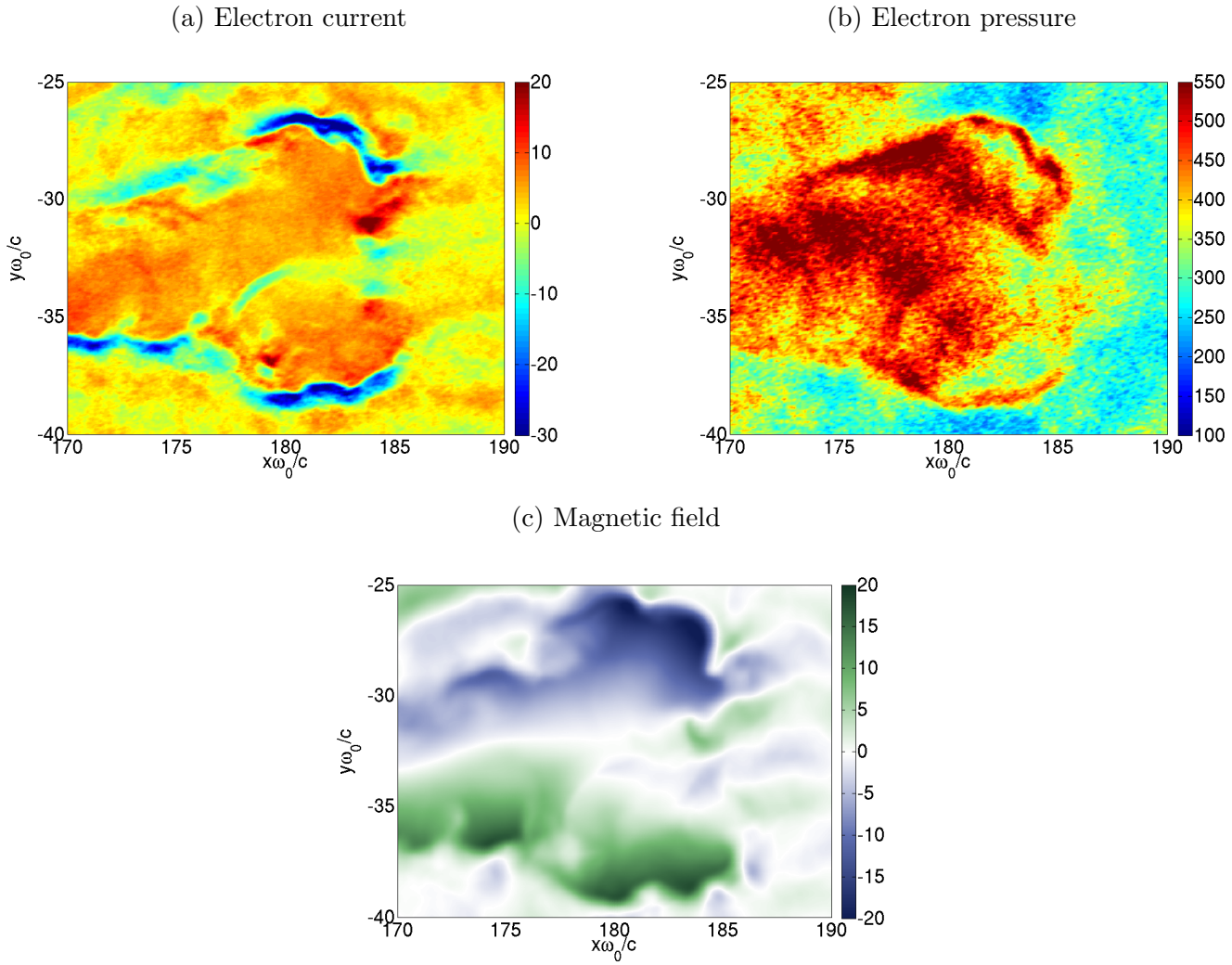

Figure 5.11. Magnetic vortex: (a) electron current density $\langle nv_x \rangle / n_c c$, (b) y-component of electron pressure tensor $\langle nv_y p_y / n_c m_e c^2 \rangle$ and (c) magnetic field $q_e B_z / m_e \omega_0$.

Figures 5.3(a,b) evidence those magnetic vortexes in the shock-foot region. The electron current in the bubble at $t\omega_0 = 480$ situated around $x\omega_0/c = 170$ and $y\omega_0/c = -30$ of Fig. 5.3(a) is illustrated on Figs. 5.11(a) showing that a strong electron current of $-j_e \sim 6n_c c$. This current is maintained on the size of the shell $l_y \sim 7c/\omega_0$ which corresponds to a magnetic field variation of $B \sim \Delta B/2 \sim l_y j_e/2 \sim 21 m_e \omega_0/e$ in a good agreement with Fig. 5.11(c) giving $B \sim 20 m_e \omega_0/e$. This magnetic field induced by the hot electron filaments ($< v_x >_e > 0$ on Fig. 5.11(a)) coming from the downstream is able to pinch the cold electron filaments [$< v_x >_e < 0$ on Fig. 5.11(a)]. The filaments transverse sizes $l_y^{\pm}$ are then asymmetric: $l_y^- \omega_0/c \sim 0.5$ for the cold electrons $< v_x >_e < 0$ and $l_y^+ \omega_0/c \sim 7$ for the hot electrons $< v_x >_e > 0$. This mechanism is able to trigger the formation of a strong magnetic loop. References Kutznetov *et al.* (2001); Bulanov *et al.* (2005) evidence the formation of magnetic vortex and Nakamura *et al.* (2010) studies the influence of plasma density-gradient on the magnetic laser-induced loops. It is shown that their sizes increase while they undergo a decreasing density. In our case, the loops are not laser-generated but induced by the electronic filaments in their highly nonlinear stage dominated by the electron pressure in the shock-front region as illustrated by Fig. 5.8(a,b). But the effect of the plasma density-gradient on the magnetic loop is the same: the vortex size increases while it undergoes a decreasing density from the downstream

to the upstream.

The electron pressure in the vortex illustrated on Fig. 5.11(b) gives $P_e = 500 n_c m_e c^2$ which is of the same order of the magnetic pressure $P_B = 0.5B^2/\mu_0 \sim 200 n_c m_e c^2$. Figure 5.3(a) shows an ion under-density in the bubbles which indicates that the protons are repulsed from the bubble creating an ion shell. The expansion velocity of the magnetic vortex in the shock foot region can be obtained from the equation of ion motion and yield a velocity close to the Alfvén velocity estimated here at $v_a \sim B/\sqrt{n_i m_i} \sim 0.1c$. The circled region of the ion phase space Fig. 5.4(c) presents a local velocity jump of $\Delta v \sim 0.1c \sim v_a$ close to the Alfven speed and corresponds to the location of the magnetic bubble at $t\omega_0 = 400$. Those magnetic vortex develops significantly after ions get isotropised and start to accumulate in the downstream so that the shock formation should not be affected. A few magnetic vortices at early stage of their development are also visible in Fiuza *et al.* (2012).

5.2.3 Influence of a finite laser spot-size

We have run a 2D simulation with a 16μm (FWHM) Gaussian laser profile (propagating on the $y = 0$ axis), with the same intensity and temporal profile as before (Sec. 5.2.1). The simulation grid has been enlarged up to 16800×9216 cells with unchanged mesh sizes of $\Delta x = \Delta y = 0.25c/\omega_{pe}$ and plasma parameters. The number of macroparticles per mesh has been reduced to 20, so that their total number in the simulation is 3.1×10^9.

The simulated ion density and magnetic field at $t\omega_0 = 480$ are displayed in Fig. 5.12(a,b) and compared to the plane-wave results. Because of the Gaussian shape of the laser beam, the piston velocity peaks on the $y = 0$-axis and decreases away from it, resulting in a curved laser-plasma interface. However, the proton density of Fig. 5.12(a) shows a relatively flat transverse profile (independent of y), close to the laser propagation axis ($y = 0$): the plasma is roughly three times more dense close to the laser piston (downstream) than far from it. The Rankine-Hugoniot conditions are verified in the region $-20 < y\omega_0/c < 20$ and the Weibel-mediated collisionless shock is formed. Its shock front is located at $x\omega_0/c \simeq 150$ as in Fig. 5.3(b), which yields similar piston velocity for both cases. The magnetic field profile of Fig. 5.12 evidences only 4 or 5 magnetic periods in the region $x\omega_0/c \sim 150$ and $|y\omega_0/c| < 20$. This relatively small extension of effective magnetic turbulence seams to be large enough to form the shock.

The y-averaged ion density profiles at $t\omega_0 = 240$, $t\omega_0 = 480$ and $t\omega_0 = 620$ are illustrated in Fig. 5.3(c) for the two cases considered, a 16μm-spot size (plain red line) and a plane-wave laser (black dashed line). At $t\omega_0 = 240$ and $t\omega_0 = 480$, the location of the laser-piston is identical in the two laser configurations. Although the black and red curves are very close to each other at $t\omega_0 = 240$, at later times ($t\omega_0 = 480$) the downstream is of thickness $\sim 50\%$ smaller for a finite focal spot than for a plane wave. This can be explained by the curvature of the laser-plasma interface [Fig. 5.3(a)], which allows the ions and electrons of the downstream to "leak" off the $y = 0$ axis. To ensure a stable front shock over a duration Δt, the laser spot size should be larger than $\beta_p \Delta t$. Otherwise, the downstream will be significantly distorted by the Gaussian piston which may hamper the shock propagation. In the case of a $\lambda_f = 16\mu$m-focal spot, the shock should be stable up to $\Delta t \lesssim \lambda_f/v_p \simeq 800\omega_0^{-1}$. The decreasing trend exhibited by the ion density profile extracted at $t\omega_0 = 620$ (corresponding to an effective interaction time of $520\omega_0^{-1}$) supports qualitatively this estimate.

5.3 Conclusions

In contrast to the currently explored experimental setup (Kugland *et al.* 2013; Fox *et al.* 2013; Yuan *et al.* 2013; Huntington *et al.* 2013) which requires 10kJ-class laser facilities, we found that only $1-2$kJ of intense-enough laser pulses should be able to drive Weibel-mediated shocks which confirms

the results of Fiuza *et al.* (2012). Their mechanism of formation is as follow. Rapidly after laser plasma interaction, an electrostatic shock forms and propagates. The high intensity laser creates a fast electron population of energy comparable to the ion kinetic energy, which is able to trigger a strong Weibel-mediated magnetic turbulence in the shock front region. The critical role of the return-current electrons in driving the Weibel-filamentation instability has been shown, making use of the multiwaterbag decomposition scheme introduced in chapter 1. Unlike the usual framework (Moiseev & Sagdeev 1963; Sagdeev 1966; Lyubarsky & Eichler 2006) studied in chapter 4, the ion heating and isotropization results from an electron-Weibel and not an ion-Weibel instability. Care has been taken to verify that a large enough laser spot-size does not affect the formation of the collisionless shock for time scales smaller than $\sim \lambda_f/v_p$.

Many points have yet to be clarified to ensure the feasibility of an experiment of Weibel-mediated laser-induced collisionless shock. The influence of collisions, ionization, radiative losses as well as 3D effects could be important. One of the most critical issue is linked to the diagnostics of such experiments. A major drawback of such shocks is that they develop in dense plasmas over very short space and time scales, a few μm and 100fs, which greatly complicates their experimental characterization unless one disposes of an intense, short-duration x-ray probe as provided by a free-electron-laser.

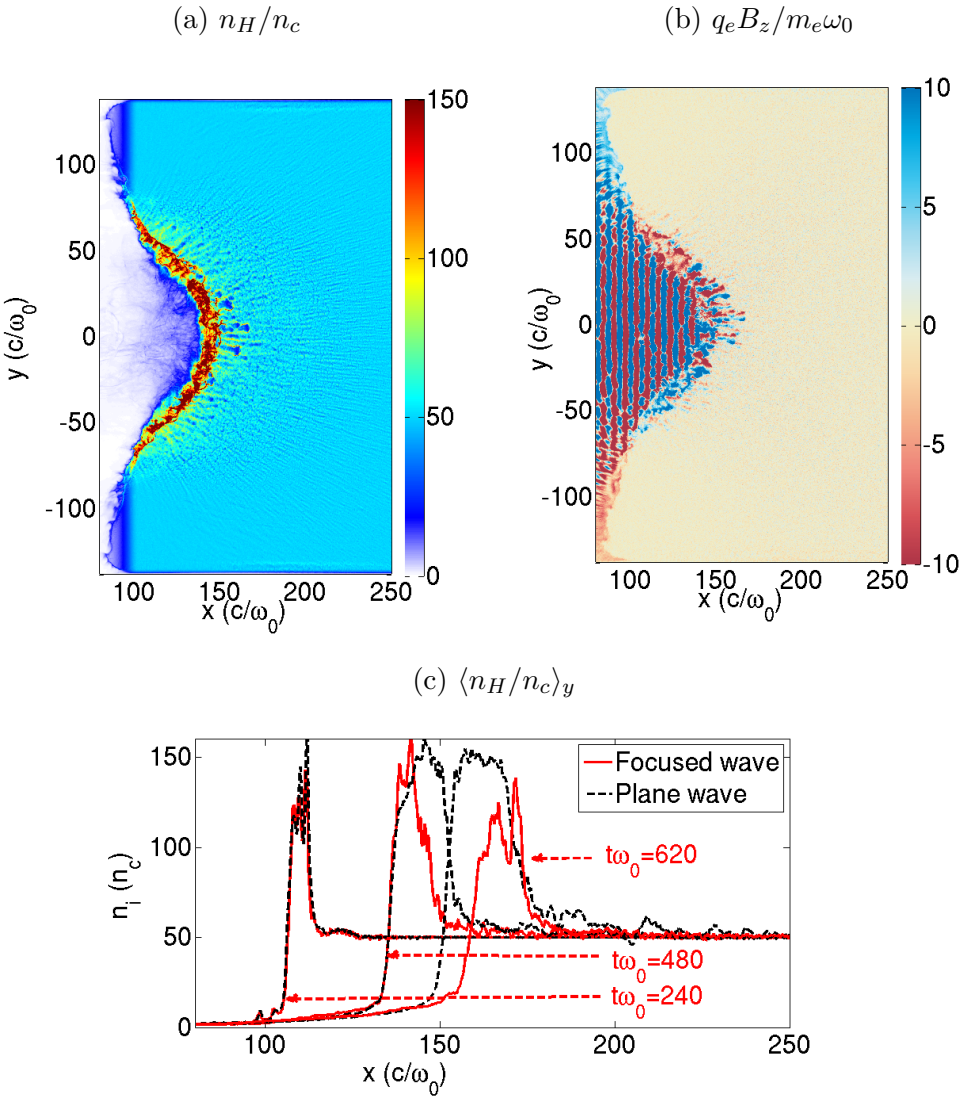

Figure 5.12. (a) Hydrogen density, (b) magnetic field at $t\omega_0 = 480$ and (c) ion density profiles averaged over the transverse direction in the region $|y\omega_0/c| < 10$ (red solid line) for a Weibel-mediated collisionless shock induced during the irradiation of an hydrogen plasma by a laser of intensity $I_0 \simeq 1.8\,10^{21}\mathrm{W.cm}^{-2}$, focused on a 16$\mu$m spot size. (c) The y-averaged density profiles of a plane-wave laser pulse is superposed in dashed black lines.

Conclusions and prospects

Conclusions and synthesis

This thesis work has begun with an apparently simple question. What is the spectral equilibrium of a relativistic plasma? How can we evaluate its field-energy? Most of the instability analyses are based on the linear dispersion relations, and thus on deformation of an equilibrium. However, this equilibrium is poorly known in the relativistic regime. We studied the relativistic field fluctuations in the beginning of this thesis. For this purpose, we generalized the Fried and Gould scheme to the Maxwell-Jüttner electrostatic dispersion relations and then to the transverse dispersion relations. We then evidenced the role of supraluminal normal modes on the fluctuation spectra in the adiabatic regime. In this assumption, the plasma had been existing at the equilibrium for a very long time. We thus get rid of any initial conditions in the plasma, especially on the supraluminal part of the spectrum. Any sharp initial condition would have an impact on the undamped supraluminal part of the spectrum and leaves a physically meaningless imprint on the evolution of the spectrum. A careful comparison between theory and PIC simulations have validated the theoretical electromagnetic spectra in the subluminal region. The eigenmode dispersion relations are accurately captured, yet with somewhat underestimated energy in the supraluminal domain. Only the non-relativistic regime had been studied up to recently (Dieckmann *et al.* 2004; Drouin 2009). This work represents the first comparison (and validation), to our knowledge, of the thermal fluctuations of a PIC code in the relativistic regime.

Analytical formulations of the fluctuation spectra resolved in frequency and wavevector (ω, k) have been proposed for various field polarizations. An exact resolution of the spatial fluctuations (integration over ω) has been demonstrated and applied to the longitudinal and transverse configurations. We thus extended the longitudinal non-relativistic fluctuation formulation of Akhiezer *et al.* (1975) to the relativistic regime. Care have been taken to study the Weibel-like configuration, *i.e.*, when the drift velocity is perpendicular to the wavevector. In the context of an international collaboration, we made use of these calculations to estimate analytically the saturation time of the electron-positron Weibel instability. The theoretical predictions were supported by PIC simulations over three decades of initial flow energy (Bret *et al.* 2013).

The Maxwell-Jüttner distribution function considered thus far is too restrictive to study various kinetic instabilities, for which a temperature anisotropy $T_x \neq T_y$ is critical. As an example, the electron two-stream instability and the transition to the electron-Weibel and ion-Weibel instabilities studied in Chapter 2 requires a two-temperature distribution in order to be accurately analyzed. In this respect, we solved the non-relativistic bi-Maxwellian dispersion relation and generalized the Fried and Gould scheme to any combination of distribution functions with a common symmetric axis and for any wavevector orientation. This allowed us to solve the growth rate map in the (k_x, k_y)-plane and to follow the evolution of the oblique instability. Moreover, care has been taken to locate the electron two-stream instability in its parametric space.

Up to this point, only the equilibrium or the linear regime of instabilities had been addressed. Various saturation criteria of the Weibel instability had been studied in Sec. 2.6 (Bret *et al.* 2013),

but only in order to estimate the duration of the linear phase. Regarding the non-linear regime, there exists an extensive literature on the current filament dynamics (Gremillet 2001; Polomarov *et al.* 2008), or within a quasi-equilibrium framework (Suzuki 2008; Suzuki & Shigeyama 2009; Gedalin *et al.* 2010; Abraham-Shrauner 2010), the kink-like instability (Milosavljević & Nakar 2006) and filament coalescence (Medvedev *et al.* 2005). However, none of these studies led to a predictive model of the particle population evolution in the non-linear stage of the instability. This illustrates the complexity of the Weibel non-linear stage. We simplified the quasilinear theory of Davidson in the large ion anisotropy limit, assuming hot and isotropic electrons. We obtained simple analytical relations between the ion and spectral parameters. The robustness of this simplified quasilinear theory was evidenced by a comparison with 1D, 2D and 3D PIC simulations in various ion-electron plasma configurations. We extended the validity of our relations to the non-linear regime.

We then worked out a model of collective ion filament coalescence based on Medvedev *et al.* (2005) and taking into account the refinement of Achterberg *et al.* (2007). The physical processes leading to the coalescence of two filaments can be easily understood. Two filaments with a net current of same sign and verifying charge neutrality attract each other and merge when they are sufficiently close. Each coalescence is a non-linear event which results in internal energy modifications. Achterberg *et al.* (2007) took into account the critical effect of electron current screening on the long-term evolution of the collective filament dynamics. The larger the filaments are, the stronger the electron screening effect is, and the weaker the magnetic interactions between filaments. This is why accounting carefully for the electrons screening is essential. In addition, many coalescence events result in a significant ion heating and slowing down, which brings the system closer to the equilibrium. This further slows down the filament dynamics. Hence, combining the quasilinear relations with the filament dynamics yields a predictive model of the non-linear stage of the Weibel instability. Note that this predictive model involves a scalar initial condition (the magnetic wavelength λ_*) at the end of the linear phase, which could be difficult to predict precisely. An estimate of λ_* have been given for sake of completeness. However, we demonstrated that this initial condition does not impact the late-evolution of the system. This model has been successfully compared with PIC simulations in various geometries and configurations. Moreover, it can be compared to very recent experiments of colliding flows (Kugland *et al.* 2012b; Fox *et al.* 2013). It also provides an explanation for the discrepancy between the experimental data and some simulation results using non-physical mass ratios.

Our predictive model takes the form of a second order differential equation on the transverse magnetic period for which an approximate solution can be obtained. The comparison with collisionless shock formation demonstrated the validity of the model until quasi-isotropization of the ion population. This leads us to an analytical formulations of the shock formation time in the non-relativistic regime. Moreover, generalizing the model to the asymmetric case open the possibility to model the magnetic turbulence taking place in the shock front. Theoretical formulations of the magnetic spectrum and ion temperature profiles have been given and compared with PIC simulation results, giving a fairly good agreement. As for the shock formation, the initial magnetic period λ_* at saturation of the Weibel instability has no significant impact on the spectrum value at the shock front. However it can affect the ion parameter profiles. The prediction of this parameter requires to take into account all of the instabilities preceding the Weibel-filamentation along with their impact on the plasma parameters.

An alternative approach (Fiuza *et al.* 2012) to produce a Weibel-mediated collisionless shocks, studied in Chapter 5, hinges upon the irradiation of a dense plasma ($n \gg n_c$) by a relativistic-intensity ($> 10^{20}\,\mathrm{W.cm^{-2}}$), picosecond-duration laser pulse (Fig. 5.1). During this interaction, part of the electrons are heated to relativistic energies and pushed into the target. The electron populations in the target have been estimated and proven to induce the magnetic turbulence responsible of the collisionless shock formation. More specifically, the electrons from the returning are crucial

in driving the Weibel-filamentation instability. This contrasts with the usual astrophysical scenario where ions usually drive the instability. We highlight that such experiments are already seriously considered at the LCLS facility in Stanford (USA).

Prospective remarks

Although the dispersion relations can be solved exactly for any distribution function, the different instabilities preceding the ion Weibel saturation remain poorly known. Predicting these instabilities and their effects on the particle populations up to the phase ruled by the Weibel instability would be a critical achievement. Even if the parametric location of the electrostatic and electromagnetic collisionless shocks have been recently studied in Stockem *et al.* (2014) many questions remain unanswered. The growth and saturation of the oblique instability require further understanding and parametric location. The instabilities preceding the ion-Weibel instability has been shown to have a marginal effect on the collisionless shock formation if the Weibel saturation lasts long enough (according to the model of Chapter 4). The distance between filaments at the beginning of the nonlinear Weibel instability does not impact the late-time Weibel evolution, in contrast with the propagation of the collisionless shock. The study of the upstream magnetic turbulence has evidenced an impact of the state of the plasma at the beginning of the non-linear Weibel stage (far from the shock discontinuity) on the sharpness of the magnetic turbulence.

As for the relativistic regime, can we build a model of non-linear Weibel instability in the relativistic regime? Is it ruled by the dynamics of filament coalescence as the symmetric non-relativistic regime? Highly relativistic pair shocks (Spitkovsky 2008b) seem to show weak coalescence effects in the upstream region. In this case, what are the non-linear effects ruling the propagation of the shock?

We note that the astrophysicists are not so much interested in the collisionless shock formation as they are on their long-term propagation, their radiative signature and their ability to accelerate particles to ultra-relativistic energies. The long-time evolution of the shock propagation is very challenging to study by numerical simulations. However our theoretical shock-front profiles may open the way to more astrophysically relevant systems and time evolutions. Is there a steady-state of Weibel-mediated collisionless shocks? If it is the case, how long does it take to reach such conditions? Is it possible to run a simulation of a "steady-state Weibel-mediated collisionless shock"?

On the experimental point of view, diagnostics are among the main problems. The magnetic field is one of the main ingredient of the Weibel-mediated collisionless shocks. However, no diagnostics are able, for the moment, to probe magnetic turbulence of hundreds or thousands of Tesla. This also poses the question of the experimental demonstration of the Weibel instability. How can we demonstrate in an experiment that the growing turbulent fields observed in a system are non-propagating and mainly magnetic, therefore potentially due to the Weibel instability?

Chapter 6

Appendix

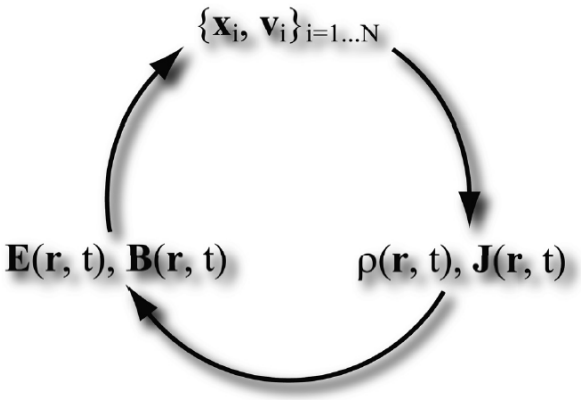

Figure 6.1. Scheme of a PIC code

6.1 Scheme of a PIC code

6.1.1 Numerical scheme

The PIC simulation scheme (Birdsall & Langdon 1985) aims to describe the evolution of charged macroparticles (which represent pieces of the distribution function) which undergoes self-generated or external fields. We then solve Maxwell's set of equations

$$\frac{\partial \mathbf{B}}{\partial t} = -\nabla \times \mathbf{E}\,, \tag{6.1}$$

$$\frac{1}{c^2}\frac{\partial \mathbf{E}}{\partial t} = \nabla \times \mathbf{B} - \mu_0 \mathbf{J}\,, \tag{6.2}$$

$$\nabla \cdot \mathbf{E} = \frac{\rho}{\varepsilon_0}\,, \tag{6.3}$$

$$\nabla \cdot \mathbf{B} = 0\,, \tag{6.4}$$

combined with the equations of motion

$$\frac{d\mathbf{p}_\alpha}{dt} = q_\alpha \left[\mathbf{E}(\mathbf{r}_\alpha, t) + \mathbf{v}_\alpha \times \mathbf{B}(\mathbf{r}_\alpha, t)\right]\,, \tag{6.5}$$

$$\frac{d\mathbf{r}_\alpha}{dt} = \mathbf{v}_\alpha\,, \tag{6.6}$$

where α is the macroparticle-subscript. The PIC scheme is repeated at each time-steps and is illustrated on Fig. 6.1.

The finite difference scheme of Yee (1966) is used to discretize the Maxwell equations and to compute the electromagnetic fields. It is based on a leapfrog scheme and descretizes the fields and current densities on Cartesian meshes (see Fig. 6.2):

$$\begin{aligned}
(E_x)^n_{i+1/2,j,k} &= \widehat{\mathbf{x}}.\mathbf{E}((i+1/2)\Delta x, j\Delta y, k\Delta z, n\Delta t)\\
(E_y)^n_{i,j+1/2,k} &= \widehat{\mathbf{y}}.\mathbf{E}(i\Delta x, (j+1/2)\Delta y, k\Delta z, n\Delta t)\\
(E_z)^n_{i,j,k+1/2} &= \widehat{\mathbf{z}}.\mathbf{E}(i\Delta x, j\Delta y, (k+1/2)\Delta z, n\Delta t)
\end{aligned} \tag{6.7}$$

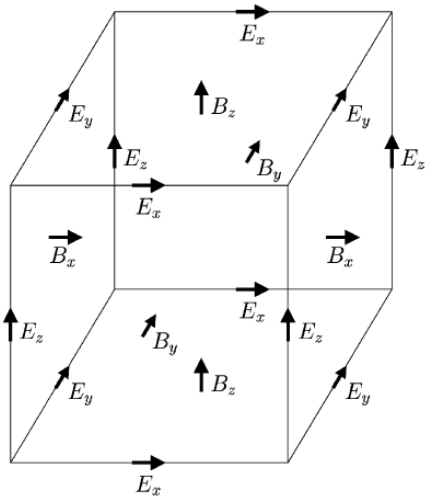

Figure 6.2. Field mesh for the Yee scheme used in CALDER.

and

$$\begin{aligned}
(B_x)^{n+1/2}_{i,j+1/2,k+1/2} &= \widehat{\mathbf{x}}.\mathbf{B}(i\Delta x,(j+1/2)\Delta y,(k+1/2)\Delta z,(n+1/2)\Delta t)\\
(B_y)^{n+1/2}_{i+1/2,j,k+1/2} &= \widehat{\mathbf{y}}.\mathbf{B}((i+1/2)\Delta x,j\Delta y,(k+1/2)\Delta z,(n+1/2)\Delta t)\\
(B_z)^{n+1/2}_{i+1/2,j+1/2,k} &= \widehat{\mathbf{z}}.\mathbf{B}((i+1/2)\Delta x,(j+1/2)\Delta y,k\Delta z,(n+1/2)\Delta t)
\end{aligned} \tag{6.8}$$

The current density elements **J** are centered as the field **E**. We then update the **E**-field, making use of Maxwell-Ampère equation and the **B**-field with Maxwell-Faraday (written in Eqs. (6.9) for the parallel components ($\parallel \widehat{\mathbf{x}}$) only).

$$\begin{aligned}
\frac{(E_x)^{n+1}_{i+\frac{1}{2},j,k}-(E_x)^{n}_{i+\frac{1}{2},j,k}}{\Delta t} &= c^2\left[\frac{(B_z)^{n+\frac{1}{2}}_{i+\frac{1}{2},j+\frac{1}{2},k}-(B_z)^{n+\frac{1}{2}}_{i+\frac{1}{2},j-\frac{1}{2},k}}{\Delta y}\right]\\
&\quad - c^2\left[\frac{(B_y)^{n+\frac{1}{2}}_{i+\frac{1}{2},j+\frac{1}{2},k}-(B_y)^{n+\frac{1}{2}}_{i+\frac{1}{2},j-\frac{1}{2},k}}{\Delta z}\right]-\frac{1}{\varepsilon_0}(J_x)^{n+\frac{1}{2}}_{i+\frac{1}{2},j,k},
\end{aligned} \tag{6.9}$$

$$\frac{(B_x)^{n+\frac{1}{2}}_{i,j+\frac{1}{2},k+\frac{1}{2}}-(B_x)^{n-\frac{1}{2}}_{i,j+\frac{1}{2},k+\frac{1}{2}}}{\Delta t} = -\frac{(E_z)^{n}_{i,j+1,k+\frac{1}{2}}-(E_z)^{n}_{i,j,k+\frac{1}{2}}}{\Delta y}+\frac{(E_y)^{n}_{i,j+\frac{1}{2},k+1}-(E_y)^{n}_{i,j+\frac{1}{2},k}}{\Delta z} \tag{6.10}$$

The formulae of the other components can be deduced from a circular permutation (see Sec. 6.1.3). Hence, all the derivatives are centered which implies a precision to the second order in Δx of the Yee Scheme. Moreover the discretized ∇-operator verifies *exactly* the relations $\nabla\cdot\nabla\times = 0$ et $\nabla\times\nabla = 0$.

When the fields are updated at all mesh-points $\mathbf{X}_{i,j,k} = (i\Delta x, j\Delta y, k\Delta z)$, the equations of motion for each macroparticle have to be resolved in order to update the positions and momenta at the next time-step (Fig. 6.1). Therefor, the force undergone by a macroparticle has to be estimated with the fields defined at the neighboring mesh-points. We thus introduce the interpolation-function

(or form-factor) S which gives:

$$\mathbf{E}(\mathbf{r}_\alpha) = \sum_{j=1}^{N_g} \mathbf{E}(\mathbf{X}_j) S(\mathbf{X}_j - \mathbf{r}_\alpha)\,, \tag{6.11}$$

$$\mathbf{B}(\mathbf{r}_\alpha) = \sum_{j=1}^{N_g} \mathbf{B}(\mathbf{X}_j) S(\mathbf{X}_j - \mathbf{r}_\alpha)\,, \tag{6.12}$$

where N_g is the number of mesh-points in the system. Any form-factor would be valid if it is used for both field and current interpolation and if its sum over the mesh is equal to unity. The simplest form-factor of the n-th order is defined as the n-th convolution of the rectangular function with itself (Birdsall & Langdon 1985):

$$S_0(x) = \begin{cases} 1\,, & \text{si } |x| < \Delta x/2 \\ 0\,, & \text{sinon} \end{cases}\,, \tag{6.13}$$

Hence, the form-factor S is a polynomial function of the n-th order by part. The multidimensional form-factor is the tensorial product of its mono-dimensional counterpart. For a d dimensional geometry, the form-factor extends on $(n+1)^d$ meshpoints. Hence, a high-order form-factor tends to filter the high frequencies (Birdsall & Langdon 1985). This spatial averaging can reduce the numerical heating inherent with the PIC scheme (Drouin 2009).

The current density update is done so as to verify charge conservation. Charge density at time $n\Delta t$ is computed making use of

$$\rho^n(\mathbf{X}_j) = \sum_{\alpha=1}^{N_p} q_\alpha S(\mathbf{X}_j - \mathbf{r}_\alpha^n)\,, \tag{6.14}$$

where N_p is the number of macroparticles. The numerical counterpart of charge conservation equation reads:

$$\begin{aligned} &\frac{(J_x)^{n+1/2}_{i+1/2,j,k} - (J_x)^{n+1/2}_{i-1/2,j,k}}{\Delta x} + \frac{(J_y)^{n+1/2}_{i,j+1/2,k} - (J_y)^{n+1/2}_{i,j-1/2,k}}{\Delta y} + \frac{(J_x)^{n+1/2}_{i,j,k+1/2} - (J_z)^{n+1/2}_{i,j,k-1/2}}{\Delta z} \\ &= -\frac{(\rho)^{n+1}_{i,j,k} - (\rho)^n_{i,j,k}}{\Delta t}\,. \end{aligned} \tag{6.15}$$

The simulation code CALDER makes use of the Esirkepov (2001) scheme to compute the current $\mathbf{J}^{n+1/2}$ from the above equation. More details are given in Drouin (2009).

6.1.2 Electromagnetic dispersion relations in vacuum

The understanding of the PIC-scheme stability can be easily understood with the numerical dispersion relation of electromagnetic wave in an empty simulation box (no macroparticles). For a wave following $(\mathbf{E}, \mathbf{B}) \propto \exp(i\mathbf{k}\cdot\mathbf{X} - \omega t)$ in a one-dimensional simulation box, Maxwell-Faraday and Maxwell-Ampère (Eqs.(6.9) and (6.10)) gives:

$$(E_y)^n_{i,j+\frac{1}{2},k} \frac{e^{-i\omega\Delta t/2} - e^{i\omega\Delta t/2}}{\Delta t} e^{-i\omega\Delta t/2} = c^2 (B_z)^{n+\frac{1}{2}}_{i,j+\frac{1}{2},k} \frac{e^{ik_x\Delta x/2} - e^{-ik_x\Delta x/2}}{\Delta x} \tag{6.16}$$

and

$$(B_z)^{n+\frac{1}{2}}_{i+\frac{1}{2},j+\frac{1}{2},k}\frac{e^{-i\omega\Delta t/2}-e^{i\omega\Delta t/2}}{\Delta t}=-(E_y)^{n}_{i+\frac{1}{2},j+\frac{1}{2},k}\frac{e^{ik_x\Delta x/2}-e^{-ik_x\Delta x/2}}{\Delta x}e^{-i\omega\Delta t/2}\,. \tag{6.17}$$

Combining those two equations gives:

$$\left[\frac{\sin(\omega\Delta t/2)}{c\Delta t}\right]^2=\left[\frac{\sin(k_x\Delta x/2)}{\Delta x}\right]^2. \tag{6.18}$$

In the general case of a three-dimensional simulation box, the above equation reads:

$$\left[\frac{\sin(\omega\Delta t/2)}{c\Delta t}\right]^2=\left[\frac{\sin(k_x\Delta x/2)}{\Delta x}\right]^2+\left[\frac{\sin(k_y\Delta y/2)}{\Delta y}\right]^2+\left[\frac{\sin(k_z\Delta z/2)}{\Delta z}\right]^2, \tag{6.19}$$

and will be compared to the physical dispersion relation in vacuum:

$$\left(\frac{\omega}{c}\right)^2=|\mathbf{k}|^2\,. \tag{6.20}$$

The scheme stability requires ω to be real hence $\sin^2(\omega\Delta t/2)<1$. Consequently, the general stability condition of Courant-Friedrich-Levy (CFL) reads:

$$\Delta t\leq\Delta t_{\max}=\left(c\sqrt{\Delta x^{-2}+\Delta y^{-2}+\Delta z^{-2}}\right)^{-1}. \tag{6.21}$$

6.1.3 Discretized Maxwell-Ampère and Maxwell-Faraday set of equations: the general case

In the general case with three spatial dimensions (x,y,z), the discretized equations of Maxwell-Ampère and Maxwell-Faraday at mesh-point (i,j,k) and time-step n reads:

$$\frac{(E_x)^{n+1}_{i+\frac{1}{2},j,k}-(E_x)^{n}_{i+\frac{1}{2},j,k}}{\Delta t}=c^2\left[\frac{(B_z)^{n+\frac{1}{2}}_{i+\frac{1}{2},j+\frac{1}{2},k}-(B_z)^{n+\frac{1}{2}}_{i+\frac{1}{2},j-\frac{1}{2},k}}{\Delta y}-\frac{(B_y)^{n+\frac{1}{2}}_{i+\frac{1}{2},j+\frac{1}{2},k}-(B_y)^{n+\frac{1}{2}}_{i+\frac{1}{2},j-\frac{1}{2},k}}{\Delta z}\right]-\frac{1}{\varepsilon_0}(J_x)^{n+\frac{1}{2}}_{i+\frac{1}{2},j,k} \tag{6.22}$$

$$\frac{(E_y)^{n+1}_{i,j+\frac{1}{2},k}-(E_y)^{n}_{i,j+\frac{1}{2},k}}{\Delta t}=c^2\left[\frac{(B_x)^{n+\frac{1}{2}}_{i,j+\frac{1}{2},k+\frac{1}{2}}-(B_x)^{n+\frac{1}{2}}_{i,j+\frac{1}{2},k-\frac{1}{2}}}{\Delta z}-\frac{(B_z)^{n+\frac{1}{2}}_{i+\frac{1}{2},j+\frac{1}{2},k}-(B_z)^{n+\frac{1}{2}}_{i-\frac{1}{2},j+\frac{1}{2},k}}{\Delta x}\right]-\frac{1}{\varepsilon_0}(J_y)^{n+\frac{1}{2}}_{i,j+\frac{1}{2},k} \tag{6.23}$$

$$\frac{(E_z)^{n+1}_{i,j,k+\frac{1}{2}} - (E_z)^{n}_{i,j,k+\frac{1}{2}}}{\Delta t} = c^2 \left[\frac{(B_y)^{n+\frac{1}{2}}_{i+\frac{1}{2},j,k+\frac{1}{2}} - (B_y)^{n+\frac{1}{2}}_{i-\frac{1}{2},j,k+\frac{1}{2}}}{\Delta x} - \frac{(B_x)^{n+\frac{1}{2}}_{i,j+\frac{1}{2},k+\frac{1}{2}} - (B_x)^{n+\frac{1}{2}}_{i,j-\frac{1}{2},k+\frac{1}{2}}}{\Delta y} \right] - \frac{1}{\varepsilon_0}(J_z)^{n+\frac{1}{2}}_{i,j,k+\frac{1}{2}} \tag{6.24}$$

$$\frac{(B_x)^{n+\frac{1}{2}}_{i,j+\frac{1}{2},k+\frac{1}{2}} - (B_x)^{n-\frac{1}{2}}_{i,j+\frac{1}{2},k+\frac{1}{2}}}{\Delta t} = -\frac{(E_z)^{n}_{i,j+1,k+\frac{1}{2}} - (E_z)^{n}_{i,j,k+\frac{1}{2}}}{\Delta y} + \frac{(E_y)^{n}_{i,j+\frac{1}{2},k+1} - (E_y)^{n}_{i,j+\frac{1}{2},k}}{\Delta z} \tag{6.25}$$

$$\frac{(B_y)^{n+\frac{1}{2}}_{i+\frac{1}{2},j,k+\frac{1}{2}} - (B_y)^{n-\frac{1}{2}}_{i+\frac{1}{2},j,k+\frac{1}{2}}}{\Delta t} = -\frac{(E_x)^{n}_{i+\frac{1}{2},j,k+1} - (E_x)^{n}_{i+\frac{1}{2},j,k}}{\Delta z} + \frac{(E_z)^{n}_{i+1,j,k+\frac{1}{2}} - (E_z)^{n}_{i,j,k+\frac{1}{2}}}{\Delta x} \tag{6.26}$$

$$\frac{(B_z)^{n+\frac{1}{2}}_{i+\frac{1}{2},j+\frac{1}{2},k} - (B_z)^{n-\frac{1}{2}}_{i+\frac{1}{2},j+\frac{1}{2},k}}{\Delta t} = -\frac{(E_y)^{n}_{i+1,j+\frac{1}{2},k} - (E_y)^{n}_{i,j+\frac{1}{2},k}}{\Delta x} + \frac{(E_x)^{n}_{i+\frac{1}{2},j+1,k} - (E_x)^{n}_{i+\frac{1}{2},j,k}}{\Delta y} \tag{6.27}$$

6.2 Field and plasma fluctuations in the adiabatic assumption

We start from the density correlation tensor of a non-interacting (ballistic) assembly of particles $\langle N_s(\mathbf{v},\mathbf{r},t)N_{s'}(\mathbf{v}',\mathbf{r}',t')\rangle$ (Sitenko 1982; Ichimaru 1992). This quantity gives the correlation between the sth spicies particles with a velocity $\mathbf{v}$ at position $\mathbf{r}$ and time t with the s'th spicy particles with a velocity $\mathbf{v}'$ at position $\mathbf{r}'$ and time t' for non-interacting particles. If the system is stable, $\langle N_s(\mathbf{v},\mathbf{r},t)N_{s'}(\mathbf{v}',\mathbf{r}',t')\rangle$ is a function of s, s', $t-t'$ and $\mathbf{r}-\mathbf{r}'$ and can be linked to the velocity statistical distribution function $f_s^0(v)$ by

$$\langle N_s(\mathbf{v},\mathbf{r},t)N_{s'}(\mathbf{v}',\mathbf{r}',t')\rangle = \delta_{s,s'}f_s^0(\mathbf{v})\delta(\mathbf{v}-\mathbf{v}')\delta[(\mathbf{r}-\mathbf{r}')-v(t-t')]\,. \tag{6.28}$$

We then use a spatial and temporal Fourier transform on the variables $T=t-t'$ and $\mathbf{R}=\mathbf{r}-\mathbf{r}'$ to obtain $\langle N_s(\mathbf{v})N_{s'}^*(\mathbf{v}')\rangle_{\mathbf{k},\omega}$.

$$\langle N_s(\mathbf{v})N_{s'}^*(\mathbf{v}')\rangle_{\mathbf{k},\omega} = \iiint_{\mathbb{R}^3} d\mathbf{R}\int_{-\infty}^{+\infty} dT e^{-i\mathbf{k}\cdot\mathbf{R}+i\omega T}\langle N_s(\mathbf{v},\mathbf{r},t)N_{s'}(\mathbf{v}',\mathbf{r}',t')\rangle\,. \tag{6.29}$$

Note that this step assumes that the system exists for all time and for all positions. We obtain:

$$\langle N_s(\mathbf{v})N_{s'}^*(\mathbf{v}')\rangle_{k,\omega} = \delta_{s,s'}f_s^0(\mathbf{v})\delta(\mathbf{v}-\mathbf{v}')\delta(\omega-\mathbf{k}\cdot\mathbf{v})\,. \tag{6.30}$$

This represents the ballistic source tensor in the Fourier space.

Given the definition of the density, the current density or the sth spicies:

$$\rho_s = \iiint_{\mathbb{R}^3} d\mathbf{v}N_s(\mathbf{v})\,, \tag{6.31}$$

$$\mathbf{j}_s = q_s\iiint_{\mathbb{R}^3} d\mathbf{v}\mathbf{v}N_s(\mathbf{v})\,, \tag{6.32}$$

and following the steps of Eqs. (6.28), (6.29) and (6.30), we obtain the current density and density fluctuation source tensor. They read:

$$\langle j_\alpha j_\beta^*\rangle_{\mathbf{k},\omega} = 2\pi\epsilon_0\sum_s m_s\omega_{ps}^2\int_{\mathbb{R}^3} d^3p\, v_\alpha v_\beta f_s^{(0)}(\mathbf{p})\delta(\omega-\mathbf{k}\cdot\mathbf{v})\,, \tag{6.33}$$

$$\langle \rho\rho^*\rangle_{\mathbf{k},\omega} = 2\pi\epsilon_0\sum_s m_s\omega_{ps}^2\int_{\mathbb{R}^3} d^3p\, f_s^{(0)}(\mathbf{p})\delta(\omega-\mathbf{k}\cdot\mathbf{v})\,. \tag{6.34}$$

Making use of Eq. (1.5) and (1.6) we obtain $\mathbf{j}_{\mathbf{k},\omega} = \mathbf{Z}_{\mathbf{k},\omega}^{-1}\cdot\mathbf{E}_{\mathbf{k},\omega}$ where the tensor $\mathbf{Z}_{\mathbf{k},\omega}^{-1}$ reads

$$\mathbf{Z}_{\mathbf{k},\omega}^{-1} = -i\sum_s\frac{q_s^2 n_s}{m_s}\int d\mathbf{p}\frac{\mathbf{p}}{\gamma}\otimes\frac{\delta_{\mathbf{p}}f_s^{(1)}}{\mathbf{k}\cdot\mathbf{v}-\omega}\cdot(\mathbf{1}+\mathbf{v}\times\frac{\mathbf{k}}{\omega}\times)\,. \tag{6.35}$$

Making use of the definition of $\boldsymbol{\epsilon}$ of Eq. (2.5) and proceeding to an inversion of the tensor, we obtain the equation (2.4) which gives the formulation of $\mathbf{Z}_{\mathbf{k},\omega}$. It also verifies:

$$\langle\mathbf{E}\mathbf{E}^\dagger\rangle_{\mathbf{k},\omega} = \mathbf{Z}_{\mathbf{k},\omega}\cdot\langle\mathbf{j}\mathbf{j}^\dagger\rangle_{\mathbf{k},\omega}\cdot\mathbf{Z}_{\mathbf{k},\omega}^\dagger\,. \tag{6.36}$$

6.3 Oblique to filamentation transition

It can be seen from Fig. 2.18 that the growth rate at large $Z_\perp$ reaches a limit $\delta_{Z_\perp,\infty}$ which is function of $Z_\parallel$. For $\gamma_0 = 1.1$, $\delta_{Z_\perp,\infty}(Z_\parallel)$ reaches an extremum for $Z_\parallel \neq 0$, which corresponds to a spectrum governed by oblique modes. Then, for $\gamma_0 = 10$, the extremum is reached at $Z_\parallel = 0$, and filamentation dominates. The first derivative $\partial\delta_{Z_\perp,\infty}/\partial Z_\parallel$ always vanishes for $Z_\parallel = 0$. The transition from one regime to the other occurs then when the second derivative vanishes at $Z_\parallel = 0$.

The asymptotic dispersion equation for $Z_\perp = \infty$ can be determined and reads,

$$4(1-\gamma_0^2) - 2(x^2 + Z_\parallel^2)\gamma_0 + (x^2 - Z_\parallel^2)^2\gamma_0^4 = 0. \tag{6.37}$$

This equation can be solved, and the growth rate for $Z_\perp = \infty$ is,

$$\delta^2_{Z_\perp,\infty} = Z_\parallel^2 + \frac{1 - \sqrt{1 + 4\gamma_0^3(Z_\parallel^2 + \beta^2\gamma_0)}}{\gamma_0^3}. \tag{6.38}$$

Deriving twice the expression above with respect to $Z_\parallel$ gives the Lorentz factor for the transition from the oblique to the filamentation regime,

$$\begin{aligned} \gamma_0 &= \sqrt{\frac{3}{2}} \sim 1.22, \\ \beta_0 &= \frac{1}{\sqrt{3}} \sim 0.57\ . \end{aligned}$$

6.4 Application to a 2D PIC plasma

Care must be taken when using the formula (2.101) for a 2D PIC-modeled plasma. The plasma is then composed of macro-particles with charge and mass equal, respectively, to $Q_p = W_p q$ and $M_p = W_p m$, where q and m denote the real particles' charge and mass, and W_p is the statistical weight. In a 3D plasma, W_p is a dimensionless quantity, whereas it is a lineic density in 2D. For the numerical plasma to behave collectively as its physical counterpart, the plasma frequencies of the two systems must be equal, which implies

$$W_p = n_e \frac{\Delta x \Delta y}{N_p}\,, \tag{6.39}$$

where N_p is the number of macro-particles per cell and $\Delta x = \Delta y$ is the cell size.

In a 2D geometry, the fluctuation field is then given by

$$\begin{aligned} B_i^2 &\sim \int_{k_\perp,min}^{k_\perp,max} dk_\perp \int_{-k_\parallel,max}^{k_\parallel,max} dk_\parallel \int_{-\delta\omega}^{\delta\omega} B^2_{k,\omega=0} \\ &\sim \frac{12}{\sqrt{3}}\frac{\gamma_0}{\mu}\left(\frac{\omega_p}{c}\right)^2 W_p m c^2\,. \end{aligned} \tag{6.40}$$

Note that the normalized inverse temperature μ is also an invariant. Substitution of Eq. (6.39) and $\Delta x = 0.05\sqrt{\gamma_0}c/\omega_p$ into (6.40) readily yields

$$B_i^2 = \frac{2.5\times10^{-3}}{N}\sqrt{\frac{3}{\pi}}\frac{\gamma_0^2}{\mu}\left(\frac{mc\omega_p}{q}\right)^2\,. \tag{6.41}$$

There follows the ratio

$$\frac{B_f^2}{B_i^2} = 4 \times 10^2 \sqrt{\frac{\pi}{3}} \frac{\mu}{\gamma_0} N \tag{6.42}$$

and the saturation time given by Eq. (2.126).

Bibliography

Abraham-Shrauner, B. (2010). *Weibel instability and quasi-equilibria for collisionless plasmas.* Plasma Phys. Control. Fusion **52**, p. 025003.

Abramowitz, M. & Stegun, I. A. (1964). *Handbook of Mathematical Functions With Formulas, Graphs and Mathematical Tables.* Milton Abramowitz and Irene A. Stegun.

Achterberg, A. & Wiersma, J. (2007). *The Weibel instability in relativistic plasmas. I. Linear theory.* A & A **475**, p. 1–18.

Achterberg, A., Wiersma, J. & Norman, C. A. (2007). *The Weibel instability in relativistic plasmas. II. Nonlinear theory and stabilization mechanism.* A & A **475**, p. 19–36.

Akhiezer, A. I., Akhiezer, I. A., Polovin, R. V., Sitenko, A. G. & Stepanov, K. N. (1975). *Plasma electrodynamics. Volume 2 - Non-linear theory and fluctuations.* Pergamon Press.

Allen, B., Yakimenko, V., Babzuen, M., Fedurin, M., Kusche, K. & Muggli, P. (2012). *Experimental study of current filamentation instability.* Phys. Rev. Lett. **109**, p. 185007.

Axford, W. I., Leer, E. & Skadron, G. (1977). *The acceleration of cosmic rays by shock waves.* International Cosmic Ray Conference **11**, p. 132.

Begelman, M. C., Blandford, R. D. & Rees, M. J. (1984). *Theory of extragalactic radio sources.* Reviews of Modern Physics **56**, p. 255.

Bell, A. R. (1978a). *The acceleration of cosmic rays in shock fronts. I.* Mon. Not. R. Astron. Soc **182**, p. 147.

Bell, A. R. (1978b). *The acceleration of cosmic rays in shock fronts. II.* Mon. Not. R. Astron. Soc **182**, p. 443.

Birdsall, C. K. & Langdon, A. B. (1985). *Plasma physics via computer simulation.* McGraw-Hill, New York.

Blandford, R. D. & McKee, C. F. (1976). *Collective electromagnetic modes for beam-plasma interaction in the whole k space.* Phys. Fluids **19**, no. 8, p. 1130.

Blandford, R. D. & Ostriker, J. P. (1978). *Particle acceleration by Astrophysical shocks.* Astrophys. J. **221**, p. L29–L32.

Bludman, S. A., Watson, K. M. & Rosenbluth, M. N. (1960). *Statistical mechanics of relativistic streams. ii.* Phys. Fluids **3**, p. 747.

Bohm, D. & Gross, E. P. (1949). *Theory of plasma oscillations. a. origin of medium-like behavior.* Phys. Rev. **75**, no. 12, p. 1851.

Bret, A. (2009). *Weibel, two-stream, filamentation, oblique, Bell, Buneman... which one grows faster ?* Astrophys J. **699**, p. 990–1003.

Bret, A. & Deutsch, C. (2005). *Hierarchy of beam plasma instabilities up to high beam densities for fast ignition.* Phys. Plasmas **12**, p. 082704.

Bret, A., Firpo, M. C. & Deutch, C. (2004). *Collective electromagnetic modes for beam-plasma interaction in the whole k space.* Phys. Rev. E **70**, p. 046401.

Bret, A., Gremillet, L. & Bellido, J. C. (2007). *How really transverse is the filamentation instability ?* Phys. Plasmas **14**, p. 032103.

Bret, A., Gremillet, L. & Bénisti, D. (2010a). *Exact relativistic kinetic theory of the full unstable spectrum of an electron-beam-plasma system with Maxwell-Jüttner distribution functions.* Phys. Rev. E **81**, no. 3, p. 036402.

Bret, A., Gremillet, L., Bénisti, D. & Lefebvre, E. (2008). *Exact relativistic kinetic theory of an electron beam-plasma system: Hierarchy of the competing modes in the system parameter space.* Phys. Rev. Lett. **100**, p. 205008.

Bret, A., Gremillet, L. & Dieckmann, M. E. (2010b). *Multidimensional electron beam-plasma instabilities in the relativistic regime.* Phys. Plasmas **17**, no. 12, p. 120501.

Bret, A., Stockem, A., Fiuza, F., Ruyer, C., Gremillet, L., Narayan, R. & Silva, L. O. (2013). *Collisionless shock formation, spontaneous electromagnetic fluctuations, and streaming instabilities.* Phys. Plasmas **20**, no. 4, p. 042102.

Bret, A., Stockem, A. & Silva, L. O. (2014). *Collective Weibel shocks: Full formation mechanism and timing.* Phys. Plasmas **21**, p. 072301.

Bulanov, S., Dylov, D., Esirkepov, T., Kamenets, F. & Sokolov, D. (2005). *Ion acceleration in a dipole vortex in a laser plasma corona.* Plasma Phys. Rep. **31**, no. 5, p. 409–421.

Buneman, O. (1959). *Dissipation of currents in ionized media.* Phys. Rev. **115**, p. 503–517.

Bykov, A. M. & Treumann, R. A. (2011). *Fundamentals of collisionless shocks for astrophysical application, 2. Relativistic shocks.* Astron. Astrophys. Rev. p. 19–42.

Califano, F., Pegoraro, F., Bulanov, S. V. & Mangeney, A. (1998). *Kinetic saturation of the weibel instability in a collisionless plasma.* Phys. Rev. E **57**, no. 6, p. 7048.

Chang, P., Spitkovsky, A. & Arons, J. (2008). *Long-term evolution of magnetic turbulence in relativistic collisionless shocks: Electron-positron plasmas.* Astrophys J. **674**, no. 1, p. 378–387.

Cottrill, L. A., Langdon, A. B., Lasinski, B. F., Lund, S. M., Molvig, K., Tabak, M., Town, R. P. J. & Williams, E. A. (2008). *Kinetic and collisional effects on the linear evolution of fast ignition relevant beam instabilities.* Phys. Plasmas **15**, p. 082108.

Cubero, D., Casado-Pascual, J., Dunkel, J., Talkner, P. & Hänggi, P. (2007). *Thermal equilibrium and statistical thermometers in special relativisty.* Phys. Rev. Lett. **99**, no. 17, p. 170601.

Davidson, R. C., Hammer, D. A., Haber, I. & Wagner, C. E. (1972). *Nonlinear development of electromagnetic instabilities in anisotropic plasmas.* Phys. Fluids **15**, no. 2, p. 317.

Denavit, J. (1992). *Absorption of high-intendity subpicosecond lasers on solid density targets.* Phys. Rev. Lett. **69**, p. 3052.

Dieckmann, M. E., Bret, A. & Shukla, P. K. (2007). *Comparing electrostatic instabilities driven by midly and highly relativistic proton beams.* Plasma Phys. Control. Fusion **49**, p. 1989–2004.

Dieckmann, M. E., Chapman, S. C., McClements, K. G., Dendy, R. O. & Drury, L. O. (2000). *Electron acceleration due to high frequency instabilities at supernova remnant shocks.* Astronomy & Astrophysics **356**, p. 377–388.

Dieckmann, M. E., Kourakis, I., Borghesi, M. & Rowlands, G. (2009). *One-dimensional particle simulation of the filamentation instability: Electrostatic field driven by the magnetic pressure gradient force.* Phys. Plasmas **16**, no. 7.

Dieckmann, M. E., Meli, A., Shukla, P. K., Drury, L. O. C. & Mastichiadis, A. (2008). *Two-dimensional pic simulations of ion-beam instabilities in supernova-driven plasma flows.* arXiv .

Dieckmann, M. E., ans S. C. Chapman, A. Y., Rowlands, G. & Andersson, N. (2004). *Simulating thermal noise.* Physica Scripta **69**, p. 456–460.

Dieckmann, M. E., Sarri, G., Doria, D., Pohl, M. & Borghesi, M. (2013). *Modification of the formation of high-mach number electrostaic shock like structures in the ion acoustic instability.* Phys. Plasmas **20**, p. 102112.

Drake, R. P. & Gregori, G. (2012). *Design consideration for unmagnetized collisionless-shock measurements in homologous flows.* Astrophys J. **179**, p. 171.

Drouin, M. (2009). *Vers la simulation particulaire réaliste de l'interaction laser-plasma surcritique : conception d'un schéma implicite avec amortissement ajustable et fonctions de forme d'ordre élevé.* Thèse de doctorat, École normale supérieure de Cachan.

Drury, L. O. (1983). *An introduction to the theory of diffusive shock acceleration of energetic particles in tenuous plasmas.* Rep. Prog. Phys. **46**, p. 973–1027.

Esirkepov, T. Z. (2001). *Exact charge conservation scheme for Particle-in-Cell simulation with an arbitrary form-factor.* Comp. Phys. Comm. **135**, p. 144–153.

Faĭnberg, Y. B., Shapiro, V. D. & Shevchenko, V. (1970). Soviet Phys. JETP **30**, p. 528.

Felten, T., Schlickeiser, R., Yoon, P. H. & Lazar, M. (2013). *Spontaneous electromagnetic fluctuations in unmagnetized plasmas ii: Reltativistic form factors of aperiodic thermal modes.* Phys. Plasmas **20**, p. 052113.

Fiuza, F., Fonseca, R., Tonge, J., Mori, W. & Silva, L. (2012). *Weibel-instability-mediated collisionless shocks in the laboratory with ultraintense lasers.* Phys. Rev. Lett. **108**, no. 24, p. 235004.

Fonseca, R. A., Martins, S. F., Silva, L. O., Tonge, J. W., Tsung, F. S. & Mori, W. B. (2008). *One-to-one direct modeling of experiments and astrophysical scenarios: pushing the envelope on kinetic plasma simulations.* Plasma Phys. Controlled Fusion **50**, p. 124034.

Fonseca, R. A., Silva, L. O., Tonge, J. W., Mori, W. B. & Dawson, J. M. (2003). *Three-dimensional Weibel instability in astrophysical scenarios.* Phys. Plasmas **10**, no. 5, p. 1979.

Fonseca, R. A., Silva, L. O., Tsung, F. S., Decyk, V. K., Lu, W., Ren, C., Mori, W. B., Deng, S., Lee, S., Katsouleas, T. & Adam, J. C. (2002). *OSIRIS: A Three-Dimensional, Fully Relativistic Particle in Cell Code for Modeling Plasma Based Accelerators*, tome 3231. P. Sloot and A. Hoekstra and C. Tan and J. Dongarra (Springer-Verlag, Heidelberg, 2002).

Fonseca, R. A., Vieira, J., Fiuza, F., Davidson, A., Tsung, F. S., Mori, W. B. & Silva, L. O. (2013). *Exploring multi-scale parallelism for large scale numerical modeling of laser wakefield accelerators.* Plasma Phys. Control. Fusion **55**, p. 124011.

Forslund, D. W. & Shonk, C. R. (1970). *Numerical simulation of electrostatic counter-streaming instabilities in ion beams.* Phys. Rev. Lett. **25**, no. 5, p. 281.

Fox, W., Fiksel, G., Bhattacharjee, A., Chang, P.-Y., Germaschewski, K., Hu, S. X. & Nilson, P. M. (2013). *Filamentation instability of counter-streaming laser-driven plasmas.* Phys. Rev. Lett. **111**, p. 225002.

Fried, B. D. (1959). *Mechanism for instability of transverse plasma waves.* Phys. Fluids **2**, no. 3, p. 337–337.

Fried, B. D., Gell-Mann, M., Jackson, J. D. & Wyld., H. W. (1960). *Longitudinal plasma oscillation in an electric field.* J. Nuclear Energy: Part C **1**, p. 190.

Fried, B. D. & Gould, W. (1961). *Longitudinal ion oscillations in a hot plasma.* Phys. Fluids B **4**, no. 1, p. 139–147.

Fuchs, J., Cowan, T. E., Audebert, P., Ruhl, H., Gremillet, L., Kemp, A., Allen, M., Blazevic, A., Gauthier, J.-C., Geissel, M., Hegelich, M., Karsch, S., Parks, P., Roth, M., Sentoku, Y., Stephens, R. & Campbell, E. M. (2003). *Spatial uniformity of laser-accelerated ultra-high current MeV electron propagation in metals and insulators.* Phys. Rev. Lett. **91**, p. 255002.

Gary, S. P., Tokar, R. L. & L., R. (1985). *The electron acoustic mode.* Physics of Fluids (1958-1988) **28**, no. 8.

Gedalin, M., Medvedev, M., Spitkovsky, A., Krasnoseskikh, V., Balikhin, M., Vaivads, A. & Perri, S. (2010). *Growth of filaments and saturation of the filamentation instability.* Phys. Plasmas **17**, p. 032108.

Gedalin, M., Smolik, E., Spitkovsky, A. & Balikhin, M. (2012). *Electron heating by filamentary instability.* Eur. Phys. Lett. **97**, p. 35002.

Gremillet, L. (2001). *Étude théorique et expérimentale du transport des électrons rapides dans l'interaction laser-solide à très haut flux.* Thèse de doctorat, École Polytechnique.

Gremillet, L., Bénisti, D. & Lefebvre, E. (2007). *Linear and nonlinear development of oblique beam-plasma instabilities in the relativistic kinetic regime.* Phys. Plasmas **14**, p. 040704.

Harris, D. & Krawczynski, H. (2006). *X-ray emission from extragalactic jets.* Annual Review of Astronomy and Astrophysics **44**, p. 463.

Haugbølle, T. (2011). *Three-dimensional modeling of relativistic collisionless ion-electron shocks.* Astrophys. J. Lett. **739**, p. 42.

Hededal, C. B., Haugbølle, T., Frederiksen, J. T. & Nordlund, Å. (2004). *Non-fermi power-Law acceleration in astrophysical plasma shocks.* Astrophys. J. Lett. **617**, p. L107–L110.

Hellinger, P., Passot, T., Sulem, P. L. & Trávníček, P. (2013). *Quasi-linear heating and acceleration in bi-Maxwellian plasmas.* Phys. Plasmas **20**, p. 122306.

Honda, M., Meyer-ter-Vehn, J. & Pukhov, A. (2000). *Collective stopping and ion heating in relativistic-electron-beam transport for fast ignition.* Phys. Rev. Lett. **85**, no. 10, p. 2128.

Huntington, C. M., Fiuza, F., Ross, J. S., Zylstra, A. B., Drake, R. P., Froula, D. H., Gregory, G., Kugland, N. L., Kuranz, C. C., Levy, M. C., Li, C. K., Meinecke, J., Morita, T., Petrasso, R., Plechaty, C., Remington, B. A., Ryutov, D. D., Sakawa, Y., Spitkovsky, A., Takabe, H. & Park, H.-S. (2013). *Observation of magnetic field generation via the Weibel instability in interpenetrating plasma flows.* arXiv .

Ichimaru, S. (1973). *Basic Principles of Plasma Physics.* Benjamin, Reading, MA.

Ichimaru, S. (1992). *Statistical Plasma Physics. Volume I: Basic Principles*, chapitre 7, p. 229–292. Addison-Wesley, Tokyo.

Kaang, H. H., Ryu, C.-M. & Yoon, P. H. (2009). *Nonlinear saturation of relativistic Weibel instability driven by thermal anisotropy.* Phys. Plasmas **16**, no. 8, p. 082103.

Kato, T. N. & Takabe, H. (2008). *Nonrelativistic collisionless shocks in unmagnetized electron-ion plasmas.* Astrophys. J. Lett. **681**, no. 2, p. L93–L96.

Kato, T. N. & Takabe, H. (2010a). *Electrostatic and electromagnetic instablities associated with electrostatic shocks: Two-dimensional particle-in-cell simulation.* Phys. Plasmas **17**, p. 032114.

Kato, T. N. & Takabe, H. (2010b). *Nonrelativistic collisionless shocks in weakly magnetized electron-ion plasmas: two-dimensional particle-in-cell simulation of perpendicular shock.* Astrophys. J. Lett. **721**, no. 1, p. 828–842.

Keshet, U., Katz, B., Spitkovsky, A. & Waxman, E. (2009). *Magnetic field evolution in relativistic unmagnetized collisionless shocks.* Astrophys. J. Lett. **693**, no. 2, p. L127–L130.

Klimontovich, Y. L. (1982). *Kinetic Theory of Nonideal Gases & Nonideal Plasmas.* Pergamon Press.

Koyama, K., Petre, R., Gotthelf, E. V., Hwang, U., Matsuura, M., Ozaki, M. & Holt, S. S. (1995). *Evidence for shock acceleration of high-energy electrons in the supernova remnant SN1006.* Nature **378**, p. 255–258.

Kugland, N. L., nd C. Plechaty, D. D. R., Ross, J. S. & Park, H.-S. (2012a). *Invited article: Relation between electric and magnetic field structures and their proton-beam images.* Rev. Sci. Instrum. **83**, p. 101301.

Kugland, N. L., Ryutov, D. D., Chang, P.-Y., Drake, R. P., Fiskel, G., Froula, D. H. & Glenzer, S. H. (2012b). *Self-organized electromagnetic field structures in laser-produced counter-streaming plasmas.* Nature Physics **8**, p. 809.

Kugland, N. L., Ryutov, D. D., Chang, P.-Y., Drake, R. P., Fiskel, G., Froula, D. H. & Glenzer, S. H. (2013). *Visualizing electromagnetic fields in laser-produced counter-streaming plasma experiments for collisionless shock laboratory astrophysics.* Phys. Plasmas **20**, p. 056313.

Kuramitsu, Y., Sakawa, Y., Morita, T., Gregory, C. D., Waugh, J. N., Dono, S., Aoki, H., Tanji, H., Koenig, M., Woolsey, N. & Takabe, H. (2011). *Time evolution of collisionless shock in counter-streaming laser-produced plasmas.* Phys. Rev. Lett. **106**, no. 17, p. 175002.

Kutznetov, A., Esirkepov, T., Kamenets, F. & Bulanov, S. (2001). *Efficiency of ion acceleration by a relativistically strong laser pulse in an underdense plasma.* Plasma Phys. Rep. **25**, no. 3, p. 225–234.

Laing, E. W. & Diver, D. A. (2006). *Relativistic Landau damping of longitudinal waves in isotropic pair plasmas.* Phys. Plasmas **13**, p. 092115.

Langdon, A. B. (1979). *Kinetic theory for fluctuations and noise in computer simulation of plasma.* Phys. Fluids **22**, no. 1, p. 163–171.

Lazar, M., Yoon, P. H. & Schlickeiser, R. (2012). *Spontaneous electromagnetic fluctuations in unmagnetized plasmas iii: Generalized kappa distributions.* Phys. Plasmas **19**, p. 122108.

Lefebvre, E., Cochet, N., Frizler, S., Malka, V., Aléonard, M.-M., Chemin, J.-F., Darbon, S., Disdier, L., Faure, J., Fedotoff, A., Landoas, O., Malka, G., Méot, V., Morel, P., Rabec Le Goahec, M., Rouyer, A., Rubbelynck, C., Tikhonchuk, V., Wrobel, R., Audebert, P. & Rousseaux, C. (2003). *Electron and photon production from relativistic laser-plasma interactions.* Nucl. Fusion **43**, p. 629–633.

Lemoine, M. (2013). *Synchrotron signature of a relativistic blast wave with decaying microturbulence.* Mon. Not. R. Astron. Soc. **428**, p. 846–866.

Lemoine, M. & Pelletier, G. (2011). *Dispersion and thermal effects on electromagnetic instabilities in precursor of relativistic shocks.* Mon. Not. R. Astron. Soc. **417**, p. 1148–1161.

Lemoine, M., Pelletier, G. & Revenu, B. (2006). *On the efficiency of fermi acceleration at relativistic shocks.* Astrophys. J. Lett. **645**, p. L129–L132.

Lerche, I. (1968a). *Enhanced bremsstrahlung from supraluminous, and subluminous, waves in an isotropic, homogeneous plasma.* Phys. Fluids **11**, p. 2459–2471.

Lerche, I. (1968b). *Supra-luminous waves and the power spectrum of an isotropic, homogeneous plasma.* Phys. Fluids **11**, p. 413–422.

Lerche, I. (1969). *Landau poles, branch cuts and supra-luminous waves in a one-dimensional plasma.* Plasma Phys. **11**, p. 849.

Lerche, I. (1969a). *Reply to Comments by Norman Rostoker.* Phys. Fluids **12**, p. 1955–1956.

Lerche, I. (1969b). *Reply to the Comments by Kulsrud, Oberman, Dawson, and Rosenbluth.* Phys. Fluids **12**, p. 1959.

Lund, E. J., Treumann, R. A. & LaBelle, J. (1995). *Quasi-thermal fluctuations in a beam-plasma system.* Phys. Plasmas **3**, no. 4, p. 1234–1240.

Lyubarsky, Y. & Eichler, D. (2006). *Are gamma-ray burst shocks mediated by Weibel instability ?* Astrophys. J. **647**, no. 2, p. 1250.

Macchi, A., Cattani, F., Liseykina, T. V. & Cornolti, F. (2005). *Laser acceleration of ion bunches at the front surface of overdense plasmas.* Phys. Rev. Lett. **94**, p. 165003.

Macchi, A., Nindrayog, A. S. & Pegoraro, F. (2012). *Solitary versus shock waves acceleration in laser-plasma interactions.* Phys. Rev. E **85**, no. 4, p. 046402.

Mackinnon, A. J., Patel, P. K., Town, R. P., Edwards, M. J., Phillips, T., Lerner, S. C., Price, D., Hicks, D., Key, M. H. & Hatchett, S. (2004). *Invited article: Relation between electric and magnetic field structures and their proton-beam images.* Rev. Sci. Instrum. **75**, p. 3531.

Malkov, M. A. & O'C Drury, L. (2001). *Nonlinear theory of diffusive acceleration of particles by shock waves.* Rep. Prog. Phys. **64**, p. 429–481.

Manheimer, W. M., Colombant, D. G. & Gardner, J. H. (1982). *Steadystate planar ablative flow.* Phys. Fluids **25**, no. 9, p. 1644.

Martins, S. F., Fonseca, R. A., Silva, L. O. & Mori, W. B. (2009). *Ion Dynamics and Acceleration in Relativistic Shocks.* Astrophys. J. Lett. **695**, p. 189–193.

McKee, C. F. (1971). *One-dimensional simulation of relativistic streaming instabilities.* Phys. Fluids **14**, no. 10, p. 2164.

Medvedev, M. V., Fiore, M., Fonseca, R. A., Silva, L. O. & Mori, W. B. (2005). *Long-time evolution of magnetic fields in relativistic gamma-ray burst shocks.* Astrophys. J. **618**, p. L75–L78.

Medvedev, M. V. & Loeb, A. (1999). *Generation of Magnetic Fields in the Relativistic Shock of Gamma-Ray Burst Sources.* Astrophys. J. Lett. **526**, p. 697–706.

Michno, M. & Schlickeiser, R. (2010). *On the magnetization of cosmic outflows: Plasma modes and instabilities of unmagnetized plasma beams.* Astrophysical Journal **714**, p. 868.

Milosavljević, M. & Nakar, E. (2006). *Weibel filament decay and thermalization in collisionless shocks and gamma-ray burst afterglows.* Astrophys J. **641**, p. 978–983.

Moiseev, S. S. & Sagdeev, R. Z. (1963). *Collisionless shock waves in a plasma in a weak magnetic field.* Plasmas Phys. **5**, p. 43–47.

Montgomery, D. & Joyce, G. (1969). *Shock-like solutions of the electrostatic vlasov equation.* Journal of Plasma Physics **3**, p. 1–11.

Nakamura, T., Bulanov, S., Esirkepov, T. & M.Kando (2010). *High-energy ions from near-critical density plasmas via magnetic vortex acceleration.* Phys. Rev. Lett. **105**, p. 135002.

Nakar, E. (2007). *Short-hard gamma-ray bursts.* Phys. Rep. **442**, p. 166.

Nishikawa, K.-I., Hardee, P., Richardson, G., Preece, R., Sol, H. & Fishman, G. J. (2005). *Particle acceleration and magnetic field generation in electron-positron relativistic shocks.* The Astrophysical Journal **622**, no. 2, p. 927.

Nishikawa, K.-I., Niemiec, J., Hardee, P. E., Medvedev, M., Sol, H., Mizuno, Y., Zhang, B., Pohl, M., Oka, M. & Hartmann, D. H. (2009). *Weibel Instability and Associated Strong Fields in a Fully Three-Dimensional Simulation of a Relativistic Shock.* Astrophys. J. Lett. **698**, p. L10–L13.

Opher, M. & Opher, R. (1996). *Was the electromagnetic spectrum a blackbody in the early universe?* Phys. Rev. Lett. **79**, no. 14, p. 2628–2631.

Park, H.-S., Ryutov, D. D., Ross, J. S., Kugland, N. L., Glenzer, S. H., Plechaty, C., Pollaine, S. M., Remington, B. A., Spitkovsky, A., Gargate, L., Gregori, G., Bell, A., Murphy, C., Sakawa, Y., Kuramitsu, Y., Morita, T., Takabe, H., Froula, D. H., Fiksel, G., Miniati, F., Koenig, M., Ravasio, A., Pelka, A., Liang, E., Woolsey, N., Kuranz, C. C., Drake, R. P. & Grosskopf, M. J. (2012). *Studying astrophysical collisionless shocks with counter-streaming plasmas from high power lasers.* High Energy Density Physics **8**, p. 38–45.

Piran, T. (2004). Rev. Mod. Phys. **76**, p. 1143.

Pokhotelov, O. A. & Amariutei, O. A. (2011). *Quasi-linear dynamics of the Weibel instability.* Ann. Geophys. **29**, p. 1997–2001.

Polomarov, O., Kaganovich, I. & Shvets, G. (2008). *Merging of Super-Alfénic current filaments during collisionless Weibel instability of relativistic electron beams.* Phys. Rev. Lett. **101**, no. 17, p. 175001.

Ren, C., Tzoufras, M., Tonge, J., Mori, W. B., Tsung, F. S., Fiore, M., Fonseca, R. A., Silva, L. O., Adam, J. C. & Héron, A. (2006). *A global simulation for laser-driven MeV electrons in 50-μm Fast Ignition targets.* Phys. Plasmas **13**, p. 056308.

Romanov, D. V., Bychenkov, V. Y., Rozmus, W., Capjack, C. E. & Fedosejevs, R. (2004). *Self-organisation of a plasma due to 3d evolution of the Weibel instability.* Phys. Rev. Lett. **93**, p. 215004.

Ross, J. S., Park, H.-S., Berger, R., Divol, L., Kugland, N. L., Rozmus, W., Ryutov, D. & Glenzer, S. H. (2013). *Collisionless coupling of ion and electron temperatures in counter-streaming plasma flows.* Phys. Rev. Lett. **110**, p. 145005.

Rostoker, N. & Rosenbluth, M. N. (1960). *Test Particles in a Completely Ionized Plasma.* Phys. Fluids **3**, p. 1–14.

Ruyer, C., Gremillet, L., Bénisti, D. & Bonnaud, G. (2013). *Electromagnetic fluctuations and normal modes of a drifting relativistic plasma.* Phys. Plasmas **20**, no. 4, p. 112104.

Ruyer, C., Gremillet, L., Bénisti, D. & Bonnaud, G. (2014). *Laser-induced Weibel-mediated collisionless shock: theory and PIC simulations.* Phys. Plasmas **20**, no. 4, p. 112104.

Sadovskiĭ, A. M. & Galeev, A. A. (2001). *Quasilinear theory of the ion Weibel instability in the earth's magnetoshperic tail.* Plasma Phys. Rep. **27**, no. 6, p. 490–496.

Sagdeev, R. Z. (1966). *Cooperative phenomena and shock waves in collisionless plasmas.* Reviews of Plasma Physics **4**, p. 23.

Schlickeiser, R. (2004). *Covariant kinetic dispersion theory of linear waves in anisotropic plasmas. i. general dispersion relations, bi-Maxwellian distributions and nonrelativistic limits.* Phys. Plasmas **11**, no. 12.

Schlickeiser, R. & Yoon, P. H. (2012). *Spontaneous electromagnetic fluctuations in unmagnetized plasmas i: General theory and nonrelativistic limit.* Phys. Plasmas **19**, p. 022105.

Shaisultanov, R., Lyubarsky, Y. & Eichler, D. (2012). *Stream instabilities in relativistically hot plasma.* Astrophysical Journal **744**, p. 182.

Silva, L. O., Fonseca, R. A., Tonge, J. W., Dawson, J. M., Mori, W. B., & Medvedev, M. V. (2003). *Interpenetrating plasma shells: Near-equipartition magnetic field generation and nonthermal particle acceleration.* Astrophys. J. **596**, p. L121–L124.

Silva, L. O., Fonseca, R. A., Tonge, J. W., Mori, W. B. & Dawson, J. M. (2002). *On the role of the purely transverse Weibel instability in fast ignitor scenarios.* Phys. Plasmas **9**, p. 2458.

Silva, L. O., Marti, M., Davies, J. R., Fonseca, R. A., Ren, C., Tsung, F. S. & Mori, W. B. (2004). *Proton shock acceleration in laser-plasma interactions.* Phys. Rev. Lett. **92**, no. 1, p. 015002.

Sironi, L. & Spitkovsky, A. (2011). *Particle acceleration in relativistic magnetized collisionless electron-ion shocks.* Astrophys. J. **726**, no. 2.

Sitenko, A. G. (1982). *Fluctuations & Non-linear Wave Interactions in Plasmas*, tome 107. Pergamon Press, Kiev.

Spitkovsky, A. (2005). *Simulations of relativistic collisionless shocks: shock structure and particle acceleration.* Dans *Astrophysical Sources of High Energy Particles and Radiation*, edité par T. Bulik, B. Rudak & G. Madejski, tome 801 de *American Institute of Physics Conference Series*, p. 345–350.

Spitkovsky, A. (2008a). *On the structure of relativistic collisionless shocks in electron-ion plasmas.* Astrophys J. Lett. **673**, no. 1, p. L39–L42.

Spitkovsky, A. (2008b). *Particle acceleration in relativistic collisionless shocks: Fermi process at last?* Astrophys. J. Lett. **682**, no. 1, p. L5–L8.

Stewart, P. (1973). *Relativistically induced interstellar density fluctuations.* Astrophys. Space Sci. **24**, p. 269–277.

Stockem, A., Fiuza, F., Bret, A., Fonseca, R. A. & Silva, L. O. (2014). *Exploring the nature of collisionless shocks under laboratory conditions.* Sci. Rep. **4**, no. 3934.

Stockem, A., Grismpayer, T., Fonseca, R. A. & Silva, L. O. (2014). *Electromagnetic field generation in the downstream of electrostatic shocks due to electron trapping.* Phys. Rev. Lett. **113**, p. 105002.

Strickland, D. & Mourou, G. (1985). *Compression of amplified chirped optical pulses.* Opt. commun. **55**, no. 6, p. 447–449.

Suzuki, A. (2008). *A novel method to construct stationary solutions of the Vlasov-Maxwell system: The relativistic case.* Phys. Plasmas **15**, p. 072107.

Suzuki, A. & Shigeyama, T. (2009). *Detailed analysis of filamentary structure in the Weibel instability.* Astrophys J. **695**, p. 1550–1558.

Tajima, T. & Cable, S. (1992). *On zero-frequency magnetic fluctuation in plasmas.* Phys. Fluids B **4**, no. 7, p. 2338–2345.

Takabe, H., Kato, T. N., Sakawa, Y., Kuramitsu, Y., Morita, T., Kadono, T., Shigemori, K., Otani, K., Nagatomo, H., Norimatsu, T., Dono, S., Endo, T., Miyanishi, K., Kimura, T., Shiroshita, A., Ozaki, N., Kodama, R., Fujioka, S., Nishimura, H., Salzman, D., Loupias, B., Gregory, C., Koenig, M., Waugh, J. N., Woolsey, N. C., Kato, D., Li, Y.-T., Dong, Q.-L., Wang, S.-J., Zhang, Y., Zhao, J., Wang, F.-L., Wei, H.-G., Shi, J.-R., Zhao, G., Zhang, J.-Y., Wen, T.-S., Zhang, W.-H., Hu, X., Liu, S.-Y., Ding, Y. K., Zhang, L., Tang, Y.-J., Zhang, B.-H., Zheng, Z.-J., Sheng, Z.-M. & Zhang, J. (2008). *High-Mach number collisionless shock and photo-ionized non-LTE plasma for laboratory astrophysics with intense lasers.* Plasma Phys. Control. Fus. **50**, no. 12, p. 124057.

Tautz, R. C. & Schlickeiser, R. (2007). *Spontaneous emission of Weibel fluctuations by anisotropic distributions.* Phys. Plasmas **14**, p. 102102.

Tzoufas, M., Ren, C., Tsung, F., Tonge, J., Mori, W., Fiore, M., Fonseca, R. & Silva, L. (2006). *Space-charge effects in the current-filamentation or weibel instablility.* Phys. Rev. Lett. **96**, p. 105002.

Tzoufras, M., Ren, C., Tsung, F. S., Tonge, J. W., Mori, W. B., Fiore, M., Fonseca, R. A. & Silva, L. O. (2006). *Space charge effects in the current filamentation or Weibel instability.* Phys. Rev. Lett. **96**, p. 105002.

Watson, K. M., Bludman, S. A. & Rosenbluth, M. N. (1960a). *Statistical mechanics of relativistic streams I.* Phys. Fluids **3**, no. 5, p. 741.

Watson, K. M., Bludman, S. A. & Rosenbluth, M. N. (1960b). *Statistical mechanics of relativistic streams. i.* Phys. Fluids **3**, p. 741.

Watson, K. M., Bludman, S. A. & Rosenbluth, M. N. (1960c). *Statistical mechanics of relativistic streams II.* Phys. Fluids **3**, no. 5, p. 747.

Weibel, E. S. (1959). *Spontaneous growing transverse waves in a plasma due to an anisotropic velocity distribution.* Phys. Rev. Lett. **2**, no. 3, p. 83–84.

Weideman, J. A. C. (1995). *Computation of the complex error function.* SIAM J. Numer. Anal. **13**, no. 5, p. 1497–1518.

Wilks, S. C. & Kruer, W. L. (1992). *Absorbtion of ultra-intense laser pulses.* Phys. Rev. Lett. **69**, no. 9, p. 1383–1386.

Wright, T. P. & Hadley, G. R. (1975). *Relativistic distribution functions and applications to electron-beams.* Phys. Rev. A **12**, no. 2, p. 686–697.

Yang, T.-Y. B., Arons, J. & Langdon, A. B. (1994). *Evolution of the weibel instability in relativistically hot electron-positron plasmas.* Phys. Plasmas **1**, no. 9, p. 3059–3077.

Yee, K. (1966). *Numerical solution of inital boundary value problems involving Maxwell's equations in isotropic media.* IEEE Trans. Antennas Propag. **14**, p. 302–307.

Yoon, P. H. (2005). *Effects of spontaneous fluctuations on generalized weak turbulence theory.* Phys. Plasmas **12**, p. 042306.

Yoon, P. H. (2007). *Spontaneous thermal magnetic field fluctuation.* Phys. Plasmas **14**, p. 064504.

Yuan, D. W., Li, Y. T., Liu, X., Zhang, Y., Zhong, J. Y., Zheng, W. D., Dong, Q. L., Chen, M., Sakawa, Y., Morita, T., Kuramitsu, Y., Kato, T. N., Takabe, H., Rhee, Y.-J., Zhao, J. Q. & Zhang, J. (2013). *Shockwaves and filaments induced by counter-streaming laser-produced plasmas.* High Energy Density Physics **9**, p. 239–242.

Zhang, X., Shen, B., Yu, M. Y., Li, X., Jin, Z., Wang, F. & Wen, M. (2007). *Effect of plasma temperature on electrostatic shock generation and ion acceleration by laser.* Phys. Plasmas **14**, no. 11, p. 113108.